

RICE UNIVERSITY

**Search, Discovery, Synthesis and Characterization of
Itinerant Magnets Composed of Non-magnetic Constituents**

by

Eteri Svanidze

A THESIS SUBMITTED
IN PARTIAL FULFILLMENT OF THE
REQUIREMENTS FOR THE DEGREE

Doctor of Philosophy

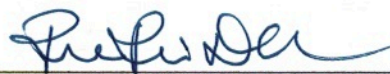
APPROVED, THESIS COMMITTEE:



Emilia Morosan, *Chair*
Professor of Physics and Astronomy, Rice
University



Junichiro Kono
Professor of Physics and Astronomy, Pro-
fessor of Electrical and Computer Engi-
neering, Rice University



Rui - Rui Du
Professor of Physics and Astronomy, Rice
University

HOUSTON, TEXAS
APRIL 3, 2015

ABSTRACT

Search, Discovery, Synthesis, and Characterization of Itinerant Magnets Composed
of Non-magnetic Constituents

by

Eteri Svanidze

The origin of magnetism in metals has been traditionally discussed in two diametrically opposite limits: itinerant and local. Itinerant magnetism, caused by conduction electrons, has been of interest due to intriguing phenomena that frequently accompany it: heavy fermion behavior, co-existence of superconductivity and magnetism, metamagnetic transitions, spin- and cluster-glass behavior, multisublattice magnetism, non-Fermi liquid behavior, and quantum criticality. Surprisingly, while many systems exhibit both local and itinerant magnetism, only two are known to contain no local moment ions – Sc_3In and ZrZn_2 . Doping experiments on Sc_3In were used to investigate the effects of both magnetic (Er) and non-magnetic (Lu) substitutions within the itinerant matrix. While the former induces a cluster-glass state, the latter drives the system through a quantum phase transition. A novel Arrott-Noakes scaling indicates that Sc_3In cannot be described by the mean-field theory, contrary to what has been seen in ZrZn_2 . This indicates that ZrZn_2 and Sc_3In are drastically different, which is likely associated with the dimensionality of spin fluctuations. Given these disparities between two seemingly analogous systems, more itinerant compounds containing non-magnetic elements are needed.

While the Stoner criterion for band ferromagnetism calls for high density of states at the Fermi level together with strong electron correlations, more conditions are likely at play. A systematic search among $3d$ systems resulted in the discovery of the first itinerant antiferromagnet composed of non-magnetic elements – TiAu. The spin-density wave antiferromagnetic ordering separates this compound from the previously reported ferromagnetic ones. Furthermore, perturbation of TiAu lattice with doping resulted in an antiferromagnetic quantum critical point, which can provide insights on the validity of the self-consistent renormalization theory of spin fluctuations in itinerant magnets.

ACKNOWLEDGEMENTS

A large number of people have helped me in numerous ways along my PhD path during the last 5 years at Rice University. First of all, I would like to thank my advisor Emilia Morosan for guidance and encouragement. My committee members Junichiro Kono and Rui-Rui Du for their interest in my research and for serving on both my Masters and PhD committees. My labmates Jiakui Wang, Liang Zhao, Chih-Wei Chen, Binod Rai, Andrea Marcinkova and Chris Georgen for useful discussions, reading of my manuscripts and assistance with measurements.

During my tenure at Rice I have been fortunate enough to have collaborated with a large number of truly amazing people. Their expertise has widened my horizons and has contributed significantly to my projects. I am very grateful to Tiglet Besara and Theo Siegrist (Florida State University) for x-ray measurements and structural characterization of arc-melted samples, necessary for our $\text{Sc}_{3.1}\text{In}$ and TiAu projects. Single crystal x-ray diffraction of ScGa_3 and LuGa_3 samples would not have been possible without Julia Chan and Gregory McCandless (University of Texas, Dallas)

I would like to thank Monika Gamża and Meigan Aronson for high-temperature magnetization measurements, necessary for the TiAu project. I am grateful to the Brian Maple group (UCSD) for low temperature AC magnetic susceptibility measurements (Ben White) and pressure-dependent resistivity measurements (Colin McElroy) of TiAu .

I thoroughly enjoyed my time at the the NCNR summer school, which led to many wonderful collaborations. In particular, I would like to acknowledge Jeff Lynn (NIST) and Qingzhen Huang (NIST) for neutron diffraction experiments and their expertize in data analysis. Their contribution was invaluable to the TiAu project.

High-field data was taken by John Singleton and Vivien Zapf (Los Alamos National Laboratory) and was incredibly helpful for the TiAu project. I am grateful for the TDO data that provided by Jeon Leotin (Laboratoire National des Champs Magnetiques Intenses).

I would like to thank Yasutomo Uemura, Lian Liu, Ben Frandsen (Columbia University), and Tim Munsie (McMaster University) for training and teaching me during my stay at TRIUMF. Their assistance, discussions, and data analysis of μ SR measurements was invaluable for the $(\text{Sc}_{1-x}\text{Lu}_x)_{3.1}\text{In}$ and TiAu projects.

The $\text{Ti}_{1-x}\text{Au}_x$ project has benefited greatly from the hardness, SEM and TEM measurements performed by Yan Xin and Ke Han (Florida State University). As well as wear and TEM analysis done by Hong Liang and Fevzi Ozaydin (Texas A&M University).

Theoretical analysis in the form of band structure calculations would not have been possible without Jiakui Wang and Andriy Nevidomskyy (Rice University).

I would like to acknowledge support from the National Science Foundation DMR 0847681.

Contents

Abstract	ii
Acknowledgements	iv
1 Outline	2
2 Background	7
2.1 Magnetism	7
2.1.1 Origin of Magnetism in Free Ions	8
2.1.2 Non-interacting Magnetic Moments: Curie Law	15
2.1.3 Interacting Magnetic Moments: Curie-Weiss Law	19
2.1.4 Magnetism of Conduction Electrons	23
2.1.5 Itinerant Ferromagnetism: Stoner Criterion	28
2.1.6 Itinerant Antiferromagnetism	32
2.1.7 Itinerant <i>vs.</i> Local Magnetism	36
2.1.8 Itinerant Magnets without Magnetic Elements: Sc_3In and ZrZn_2	38
2.1.9 Search for New Itinerant Magnets	41
2.2 Phase Transitions	44
2.2.1 Classical <i>vs.</i> Quantum Phase Transitions	44
2.2.2 Critical Exponents and Critical Scaling	45
2.2.3 Arrott and Arrott-Noakes Analysis	49
2.3 Spin-Glass Systems	53
2.3.1 Physical Properties of Spin- and Cluster-glasses	57
2.3.2 Theoretical Description of Spin-glass Systems	63

2.4	Superconductivity	71
3	Experimental and Theoretical Techniques	81
3.1	Sample Preparation	82
3.2	Crystallography and X-ray Diffraction	91
3.3	Magnetization Measurements	98
3.4	Specific Heat Measurements	104
3.5	Resistivity Measurements	108
3.6	X-ray Photoemission Spectroscopy	112
3.7	Hardness Measurements	116
3.8	Muon Spin Relaxation, Rotation, and Resonance	120
3.9	Tunnel Diode Oscillation Measurements	126
3.10	Neutron Scattering	130
3.11	Band Structure Calculations	135
4	Doping-induced Quantum Critical Point in $(\text{Sc}_{1-x}\text{Lu}_x)_{3.1}\text{In}$	138
4.1	Motivation and Background	139
4.2	Physical Properties	142
4.2.1	Temperature-Dependent Magnetization Measurements	143
4.2.2	Arrott and Arrott-Noakes Analysis	145
4.2.3	Non-Fermi Liquid Behavior	153
4.2.4	Muon Spin Relaxation Measurements	156
4.3	Discussion	161
5	Doping-induced Cluster-glass Behavior in $(\text{Sc}_{1-x}\text{Er}_x)_{3.1}\text{In}$	164
5.1	Motivation and Background	165
5.2	Physical Properties	166
5.3	Cluster-Glass Analysis	172
5.4	Conclusions and Open Questions	179
6	Novel Itinerant Antiferromagnet TiAu	181
6.1	Motivation and Background	182
6.2	Physical Properties	183
6.2.1	Structural and Composition Analysis	183
6.2.2	Magnetization, resistivity, and specific heat	187
6.2.3	Muon Spin Relaxation and Neutron Diffraction Measurements	192
6.2.4	Tunnel Diode Oscillator Measurements	201

6.2.5	High Field Magnetization Measurements	203
6.2.6	High Pressure measurements	205
6.3	Band Structure Calculations	206
6.4	Conclusion and Open Questions	210
7	Doping-induce Quantum Critical Point in $\text{Ti}_{1-x}\text{Sc}_x\text{Au}$	212
7.1	Motivation and Background	213
7.2	Physical Properties	215
7.3	Band Structure Calculations	225
7.4	Conclusion and Open Questions	230
8	Mechanical Properties of Ti-Au Alloys	232
8.1	Introduction	233
8.2	Material Selection and Ashby Diagrams	234
8.3	Designing and Improving Hard Materials	236
8.4	Properties of Ti and its Alloys	243
8.5	Ti - Au Alloys	246
8.5.1	Previous Work: From Dental Implants to "Iron Man"	246
8.5.2	Current Study	247
8.5.3	Effects of Heat Treatment	258
8.5.4	Conclusion and Future Endeavors	259
9	Type I Superconductivity in ScGa_3 and LuGa_3	260
9.1	Motivation and Background	261
9.2	Physical Properties	263
9.3	Band Structure Calculations	272
9.4	Conclusion	273
10	Summary	276
	Bibliography	278

List of Figures

2.1	Electron orbitals s , p , d , and f [3].	8
2.2	Representation of the total angular momentum.	10
2.3	Various contributions to the magnetic susceptibility of a metal. Relative magnitudes are not drawn to scale.	13
2.4	The mass susceptibility for the first 60 elements in the periodic table at room temperature as function of the atomic number [42].	14
2.5	Comparison of paramagnetic moment μ_{PM} , obtained from experiment with that expected based on Hund's rules [133].	17
2.6	Graphical solution of Eqs. 2.34.	21
2.7	Temperature dependence of $1/(\chi - \chi_0)$ for the paramagnetic (orange), antiferromagnetic (blue), and ferromagnetic (green) cases.	23
2.8	(a) Without external field, the number of electrons in both sub-bands is the same. (b) After a field has been applied, the Fermi energy shifts, resulting in Pauli paramagnetism.	25
2.9	The density of spin-up and spin-down electrons exhibit a spontaneous spin splitting without any external magnetic field.	29
2.10	Schematic incommensurate spin density wave in bcc Cr. The arrows indicate the amplitude of the spin density wave at the lattice sites [404].	34
2.11	Physical properties near T_N in Cr: linear thermal expansion (α), resistivity ρ , specific heat C_p , and thermoelectric power S as a function of temperature [108].	35

2.12	The evolution of magnitude of magnetic moment with temperature for the (a) local and (b) itinerant scenarios in zero field. Reproduced from Ref. [261].	37
2.13	Rhodes-Wohlfarth ratio for local magnets (open symbols) and itinerant magnets (full symbols), reproduced from Ref. [261].	38
2.14	Physical properties of ZrZn_2 : (a) inverse susceptibility as a function of temperature [44], (b) magnetization as a function of field [299], temperature-dependent (c) resistivity and (d) specific heat [412]. . . .	40
2.15	Physical properties of Sc_3In : (a) Variation of the size of the magnetic moment as a function of Sc:In ratio [246], (b) susceptibility and inverse susceptibility as a function of temperature [140], (c) magnetization as a function of field [124], (d) temperature-dependent magnetization derivative and specific heat scaled by temperature [355].	41
2.16	In Sc_3In and ZrZn_2 , Sc and Zr are located across from Zn and In. . .	42
2.17	Arrott plot with the critical isotherm represented by a red line passing through the origin.	50
2.18	Two examples of frustrated lattices: (a) a triangular lattice with antiferromagnetic coupling and (b) a square lattice with ferromagnetic nearest neighbor and antiferromagnetic next nearest neighbor coupling.	54
2.19	Different types of magnetic behavior for various concentration regimes in a canonical spin-glass [273].	55
2.20	Spin-glass with micromagnetic clusters in a 2D square lattice [273]. .	56
2.21	A schematic $T - x$ phase diagram for a dilute magnetic alloy [273]. .	56
2.22	The inverse susceptibility fits for various concentrations of Fe in Au. The dashed lines are linear extrapolations of the Curie-Weiss fit, from which values of θ_W are extracted. Negative values of θ_W indicate antiferromagnetic coupling while those for ferromagnetic coupling are positive [259].	58
2.23	(a) ZFC and FC magnetization data for spin-glass $\text{Mn}_{1-x}\text{Cu}_x$ alloys [277]. (b) ZFC and FC magnetization data for $\text{La}_{1-x}\text{Ca}_x\text{CoO}_3$ cluster-glass [56]. The bifurcation at the freezing temperature is one of a characteristics features of a spin- or cluster-glass materials.	59
2.24	(a) Evolution of cusp in AC susceptibility with application of field for $\text{Au}_{1-x}\text{Fe}_x$ [63]. (b) Temperature dependent χ' and χ'' for $\text{Eu}_{0.2}\text{Sr}_{0.8}\text{S}$ in various frequencies [165]. (c) Shift in the position of the cusp as a function of frequency for $\text{Cu}_{99.06}\text{Mn}_{0.94}$ [272].	59

2.25	(a) Specific heat in various external fields for $\text{Cu}_{99.7}\text{Mn}_{0.3}$ [53]. (b) Specific heat per Eu atom divide by $k_B T$ as a function of temperature T . The inset shows the behavior on a log-log plot [255].	63
2.26	(a) Susceptibility and (b) specific heat versus reduced temperature calculated from the Edwards and Anderson model for two spin values [112].	66
2.27	(a) Magnetic phase diagram for Ising spins interacting <i>via</i> an infinite-ranged gaussian distribution of exchange forces with variance Δ and mean J_0 . (b) The AC susceptibility as a function of temperature, calculated from the Sherrington-Kirkpatrick model: J_0/Δ is 0 and 0.5 for upper and lower curves, respectively. The field $H = 0$ for solid curves and $H = 0.1J_0$ for the dashed ones [330].	68
2.28	(a) The AT line or the $H - T$ phase diagram illustrating the stability limits of the Sherrington-Kirkpatrick solution for the case of $J_0 = 0$ [91]. (b) Phase diagram for vector spins interacting with infinite-ranged distribution (J_0 is the mean and Δ is the width of variance) [121]. . .	69
2.29	Resistivity of a typical conductor (dashed line) and a superconductor (solid line) [231].	72
2.30	(a) Schematic diagram of the exclusion of magnetic flux from interior of a superconductor [372]. (b) Distribution of magnetic field lines around the superconductor below and above the critical temperature T_c . (c) A Nd-based magnet levitating above a $\text{YBa}_2\text{Cu}_3\text{O}_7$ pellet, cooled with liquid N.	73
2.31	Typical field-dependent magnetization $M(H)$ curves of (a) Type I and (b) Type II superconductors. Temperature dependence of critical field(s) for a (c) Type I and (d) Type II superconductor [20]. . . .	75
2.32	The distribution of magnetic field lines around a sample for a long, thin cylinder ($\eta = 0$) (a) and a sphere ($\eta = 1/3$) (b) [372].	77
2.33	Progress in development of superconducting materials [286].	78
3.1	Phase diagram of ScGa_3 [389] with a few features specified on the plot. The growth recipe for the ScGa_3 compound is marked by a red line [357].	84
3.2	Packing scenario for a flux growth: constituents are combined in an alumina crucible, sealed in quartz ampoule.	85
3.3	Single crystal growth of Sc_3In is complicated by high melting temperatures and short liquedus line [389].	87

3.4	Single crystal growth of TiAu is complicated by a large width of formation and high melting temperature [389].	88
3.5	The arc melter, along with a TiAu sample prepared using it (inset). .	90
3.6	The fourteen Bravais lattices [86].	92
3.7	Planes in a cubic lattice and their Miller indices [144].	93
3.8	(a) The schematic for the Bragg-Brentano diffractometer configuration. (b) Adjustable slits that control the intensity of incident and diffracted beams. (c) The path of the x-ray beam in a diffractometer, equipped with a monochromator [144].	94
3.9	An example of a powder diffraction pattern for ScGa ₃ with Miller indices for all peaks [357]. Asterisks represent flux, present on the surface of single crystals. Inset: the $Pm\bar{3}m$ crystal structure of ScGa ₃ [389]. .	95
3.10	(a) QD MPMS instrument along with the (b) sample holder.	99
3.11	(a) Main components of the MPMS system along with (b) the MPMS magnet [340].	100
3.12	A schematic showing how magnetic properties of a sample are recorded using a second derivative gradient coil configuration [340].	101
3.13	AC magnetic susceptibility coils configuration and sample insert [236].	102
3.14	(a) QD PPMS instrument along with the (b) ³ He insert.	105
3.15	(a) Exploded view of the specific heat puck [236] along with (b) top and (c) bottom perspectives.	106
3.16	(a) Four-probe resistivity measurement. (b) Interface of the resistivity puck. (c) The bottom view of the resistivity puck features 12 pin connections, identical to those seen in the specific heat puck in Fig. 3.15 [236]. (d) A set of three samples, prepared for a resistivity measurement.	109
3.17	(a) Experimental layout of XPS Phi Quantera. (b) The mechanism of a peak doublet formation. (c) Deconvolution of a peak with elements whose binding energies are very similar. (d) Background subtraction fit. (e) A peak doublet of Ca [235].	113
3.18	Scales for various hardness measurement methods compared to each other and the yield strength [26].	116
3.19	Shapes of various hardness indenters: (a) spherical, (b) trigonal pyramid, (c) square pyramid, and (d) elongated pyramid [134].	117
3.20	Geometry of the indenter for the Vickers hardness test.	118

3.21	(a) The mechanism of muon production. (b) Muon-spin precession in a magnetic field B applied at an angle θ [43]. (c) The transverse field μ SR setup. (d) The zero-field μ SR setup.	122
3.22	(a) Samples mounted on a silver plate for the M15 beamline. The area necessary for μ SR experiments is equivalent to the area of a penny. (b) The top view of the M20 experiment at TRIUMF. The main components include three orthogonal pairs of Helmholtz coils, a cryostat and various detectors. (c) The silver tape and holder used for the M20 beamline.	123
3.23	(a) Schematic representation of the tunnel diode oscillator circuit [99]. (b) Low temperature stage platform diagram along with an expanded view of the sample tube [28].	126
3.24	(a) A broad peak is observed close to T_C in an itinerant ferromagnet ZrZn_2 [386]. (b) A sharp cusp is visible around T_C in a local moment ferromagnet CeAgSb_2 [386].	128
3.25	Penetration depth as a function of atomic number for neutron (red), x-rays (blue), and electrons (yellow). The penetration depth is taken as the depth at which the intensity has been reduced to about 37 % of its original value [304].	131
3.26	Types of interactions depending on the incoming beam type – neutrons (red), x-rays (blue), and electrons (yellow) [304].	132
3.27	(a) Elastic ($k' = k$) and (b) inelastic ($k' > k$ or $k' < k$) scattering events [304]. In both cases, the neutron is scattered through the angle 2θ with a scattering vector is Q	133
3.28	Pictorial representation of a muffin-tin potential [2].	136
4.1	Measured X-ray diffraction pattern for $(\text{Sc}_{1-x}\text{Lu}_x)_{3.1}\text{In}$ (black line) where $x = 0$, with calculated peak positions marked by vertical lines, based on space group $\text{P6}_3/\text{mmc}$ and lattice parameters $a = 6.42 \text{ \AA}$ and $c = 5.18 \text{ \AA}$. The crystal structure of $\text{Sc}_{3.1}\text{In}$ (left inset) exhibits quasi-1D chains of Sc-In. Right inset: evolution of lattice parameters a and c and the unit cell volume V with composition x	140

-
- 4.2 (a) $\text{Sc}_{3.1}\text{In}$ susceptibility (left) and inverse susceptibility $1/(\chi - \chi_0)$ (right) for $H = 0.1$ T, where $\chi_0 = C/T^*$ (see text). (b) The magnetization derivative dM/dT (left) and specific heat C_p/T (right) for $\text{Sc}_{3.1}\text{In}$ with the vertical arrow marking the Curie temperature T_C . (c) $(\text{Sc}_{1-x}\text{Lu}_x)_{3.1}\text{In}$ AC susceptibility $\chi'(T)$. The Curie temperature T_C is estimated from the peak position (solid line), indicated by the vertical arrow. 144
- 4.3 $M^{1/\beta}$ vs. $(H/M)^{1/\gamma}$ isotherms for $\text{Sc}_{3.1}\text{In}$ with (a) mean field exponents $\beta = \beta_{MF} = 0.5$ and $\gamma = \gamma_{MF} = 1$, $T_C = 9.75$ K (solid line) and (c) non-mean-field exponents $\beta = 0.26$ and $\gamma = 1.03$, $T_C = 4.45$ K (solid line). (b) Log-log plot of $\text{Sc}_{3.1}\text{In}$ $M(H)$ isotherms, with the straight line representing the fit for the critical isotherm. (d) Arrott-Noakes scaling plots $M|t|^{-\beta}$ vs. $H|t|^{-\delta\beta}$. The scaled $M(H)$ data collapses onto two diverging branches, one below T_C ($t < 0$, open symbols) and one above T_C ($t > 0$, full symbols). 146
- 4.4 Log-log $(\text{Sc}_{1-x}\text{Lu}_x)_{3.1}\text{In}$ $M(H)$ isotherms for (a) $x = 0.005$, (b) $x = 0.008$ and (c) $x = 0.01$ with linear fits (solid lines) at the critical ($T = T_C$) isotherm. (d) Log-log $M(H)$ curve for $x = 0.02$ and $T = 1.8$ K, with a linear fit above $H = 0.05$ T. 147
- 4.5 $(\text{Sc}_{1-x}\text{Lu}_x)_{3.1}\text{In}$ Arrott-Noakes $M^{1/\beta}$ vs. $(H/M)^{1/\gamma}$ isotherms for (a) $x = 0.005$, (b) $x = 0.008$, and (c) $x = 0.01$ with linear fits (solid lines) at T_C 150
- 4.6 (a) Spontaneous magnetization $M_0(T)$ for $(\text{Sc}_{1-x}\text{Lu}_x)_{3.1}\text{In}$ where $0 \leq x \leq 0.02$. (b) The critical exponents scaled by their mean-field values δ/δ_{MF} (triangles), γ/γ_{MF} (squares) and β/β_{MF} (circles) as a function of composition x 151
- 4.7 Scaling plots $M|t|^{-\beta}$ vs. $H|t|^{-\delta\beta}$ for (a) $x = 0.005$, (b) $x = 0.08$ and (c) $x = 0.01$ in $(\text{Sc}_{1-x}\text{Lu}_x)_{3.1}\text{In}$ 152
- 4.8 (a) Semi-log plot of the specific heat C_p/T (symbols) and the linear fits (lines) at low temperatures. The data for $x > 0$ are shifted vertically for clarity by 30 mJ/mol_{F.U.} K². Inset: Specific heat for $(\text{Sc}_{0.98}\text{Lu}_{0.02})_{3.1}\text{In}$ in various magnetic fields: $H = 0, 0.01, 1$ and 3 T. (b) Temperature-dependent resistivity for $(\text{Sc}_{1-x}\text{Lu}_x)_{3.1}\text{In}$ ($0 \leq x \leq 0.04$). The data are shifted vertically for clarity. Inset: the whole range of $\rho(T)$ from which RRR is determined. 154

- 4.9 Time spectra of zero field and longitudinal field μ SR of $(\text{Sc}_{1-x}\text{Lu}_x)_{3.1}\text{In}$ where $x = 0$ (squares), 0.01 (downward-facing triangles) and 0.025 (leftward-facing triangles). The background sample holder contribution in the two Lu-doped samples was subtracted. The solid lines represent fits to Eqs. 4.3 and 4.4. 156
- 4.10 (a) The muon spin precession frequencies ν_1 (full squares) and ν_2 (open squares), and (b) the volume fraction V_M of the magnetically ordered regions, obtained from zero field μ SR of $\text{Sc}_{3.1}\text{In}$ 158
- 4.11 (a) Muon spin relaxation rate σ for $x = 0.01$ (downward-facing triangles) and $x = 0.025$ (leftward-facing triangles) for $(\text{Sc}_{1-x}\text{Lu}_x)_{3.1}\text{In}$ (left axis) along with the average static internal field H_{av} for $x = 0$ (right axis), obtained from the fits of zero field μ SR measurements. The vertical axes are scaled with γ_μ , the gyromagnetic ratio of a positive muon. (b) The longitudinal relaxation rate $1/T_1$, obtained from the longitudinal field μ SR measurements. 158
- 4.12 (a) $T - x$ phase diagram for $(\text{Sc}_{1-x}\text{Lu}_x)_{3.1}\text{In}$ for $0 \leq x \leq 0.10$, with the Weiss-like temperature T_C^* (squares, left axis), the Curie temperature T_C (circles, left axis) and paramagnetic moment μ_{PM} (diamonds, right axis). (b) Enlarged $T - x$ phase diagram for $x \leq 0.04$ [shaded area in (a)], with the ab plane projection of the $\text{Sc}_{3.1}\text{In}$ unit cell shown in the inset. The horizontal line at $T = 1.17$ K denotes the minimum experimental temperature, with the open symbols representing T_C estimates extrapolated from accessible measurements. 162
- 5.1 (a) X-ray diffraction pattern for $\text{Sc}_{3.1}\text{In}$, obtained from an arc-melted polycrystalline specimen (see text). Vertical marks correspond to the $\text{P6}_3/\text{mmc}$ phase. (b) Nearly one-dimensional bipyramidal Sc-In chains. (c) Evolution of the lattice parameters a (triangles), c (circles) and the unit cell volume V (squares) with composition x 168
- 5.2 (a) zero field cooled (full) and field cooled (open) DC susceptibility for $(\text{Sc}_{1-x}\text{Er}_x)_{3.1}\text{In}$ ($0 \leq x \leq 0.10$). (b) Inverse susceptibility for $(\text{Sc}_{1-x}\text{Er}_x)_{3.1}\text{In}$ where $0 \leq x \leq 0.10$. The $x = 0$ data is scaled by a factor of $1/4$. Inset: composition dependence of measured (triangles) and calculated (line) paramagnetic moments μ_{PM}^{exp} and μ_{PM}^{calc} 169

5.3	$T = 2$ K magnetization as a function of field for $(\text{Sc}_{1-x}\text{Er}_x)_{3.1}\text{In}$ with $0 \leq x \leq 0.10$. Inset: calculated saturated moment μ_{sat}^{calc} (line) and measured magnetic moment $\mu_{5.6T}$ (diamonds).	170
5.4	Frequency-dependence of the real component $\chi'(T)$ of the AC susceptibility data for $(\text{Sc}_{1-x}\text{Er}_x)_{3.1}\text{In}$ with $0 \leq x \leq 0.10$. An example of fit used to determine the freezing temperature $T_f(f)$ is shown in panel (d) for $f = 10$ Hz.	173
5.5	(a) - (e) Frequency f versus freezing temperature $T_f(f)$ for $0 \leq x \leq 0.10$ in $(\text{Sc}_{1-x}\text{Er}_x)_{3.1}\text{In}$. Insets: $T_f(f)$ vs. $1/\ln(f_0/f)$ along with the fits (solid lines) to the Vogel-Fulcher law (see text).	174
5.6	C_p/T vs. T^2 for $(\text{Sc}_{1-x}\text{Er}_x)_{3.1}\text{In}$ ($0 \leq x \leq 0.10$), with open symbols corresponding to the freezing temperature $T_f(0)$, as determined from $\chi'(T)$	176
5.7	(a) The freezing temperature $T_f(0)$ (open squares), the irreversibility temperature T_{irr} (full squares) and the Weiss-like temperature θ (full diamonds) as a function of x in $(\text{Sc}_{1-x}\text{Er}_x)_{3.1}\text{In}$. (b) Rhodes-Wohlfarth plot for local-moment compounds (triangles), itinerant-moment compounds (full circles) and $(\text{Sc}_{1-x}\text{Er}_x)_{3.1}\text{In}$ ($0 \leq x \leq 0.10$) (open circles). The red line indicates the local limit for $q_c/q_s \approx 1$. Inset: the Rhodes-Wohlfarth ratio for $(\text{Sc}_{1-x}\text{Er}_x)_{3.1}\text{In}$ ($0 \leq x \leq 0.10$).	178
6.1	Neutron diffraction data: a high resolution diffraction pattern for $T = 5$ K is indexed with the orthorhombic $Pmma$ TiAu phase, denoted by blue vertical marks. The inset shows a portion of the high-intensity diffraction data (solid circles) taken on BT-7 at $T = 2.5$ K. Fig. 6.5(d) shows the observed counts (solid circles) for the magnetic peak, with the solid curves representing fits to Gaussian (instrumental) peaks.	183
6.2	Magnetic peak data at $T = 2.5$ K: The symbols are measured data, with the Gaussian fit shown as a solid line.	184
6.3	X-ray photoemission spectroscopy: (a) survey scan along with elemental scans for Au (b) and Ti (c).	186
6.4	Temperature-dependent magnetization of TiAu. Left axis: zero-field cooled magnetic susceptibility as a function of temperature for $\mu_0 H = 0.1$ T applied field. Right axis: inverse susceptibility H/M along with a Curie-Weiss-like fit (solid line), with $\theta \approx -37$ K. Inset: the crystal structure of TiAu with Ti (small) and Au (large) atoms.	187

6.5	Specific heat and resistivity of TiAu. $H = 0$ temperature-dependent resistivity (a) and specific heat (b). (c) The ordering temperature T_N (vertical dotted line) for TiAu determined from peaks in the temperature derivatives of resistivity, $d\rho/dT$ (black triangles), and MT , $d(MT)/dT$ (red squares), and in C_p/T (blue circles). The entropy S_m (solid blue line, right axis) is calculated by subtracting a polynomial non-magnetic component (dashed line) from the measured specific heat data.	188
6.6	Field-dependent magnetization of TiAu. The magnetization isotherms $M(H)$ (solid, left axis) and the derivative dM/dH (open, right axis) for $T = 2$ K (circles) and 60 K (triangles). No saturation is achieved for magnetic fields up to 7 T. A metamagnetic transition is observed around 4 T in the $T = 2$ K isotherm, but not in the one above the magnetic order.	190
6.7	Spin chain: quasi one-dimensional $S = 1/2$ spin chain [210].	193
6.8	μ SR asymmetry analysis: Comparison of the fit with the LSF line shape (Eq. 6.3, blue line) and the two-exponential phenomenological line shape (Eq. 6.1, black line). The difference is subtle, and the choice between these two functions does not alter the essential part of the presented conclusions. The reasoning for using LSG function is described below.	195
6.9	Muon spin relaxation and neutron diffraction. (a) Time dependence of the asymmetry, fit with Eq. 6.4 (solid lines). (b) A small applied longitudinal field $\mu_0 H = 0.01$ T eliminates the relaxation response. (c) Relaxation rate a (black circles, left) and volume fraction (red circles, right) as a function temperature. (d) Integrated intensity of the $(0, \pi/b, 0)$ TiAu magnetic Bragg peak as a function of temperature with mean-field fit ($T_N = 36(2)$, black curve). Inset: net counts normalized for 2 min. counting time between 2.5 K and 60 K, showing the $(0, \pi/b, 0)$ magnetic peak fit with a resolution-limited Gaussian (red line). Uncertainties are statistical in origin and represent one standard deviation.	196

6.10	(a) Temperature-dependent DC resistivity of TiAu along with the derivative (inset). (b) Frequency shift Δf of the tunnel diode oscillator resonance as a function of temperature for TiAu. Inset: the derivative of the frequency shift with respect to temperature $d(\Delta f)/dT$ reveals a peak around 27 K.	202
6.11	(a) Field-dependent magnetization data taken using the VSM option. Inset: high-field data exhibits a remarkably linear behavior. (b) Pulsed field magnetization data for TiAu at various temperatures. Combined high-field magnetization data: (c) the $M(10\text{ T})$ decreases with increasing temperature while the derivative dM/dH , shown in (d), exhibits a feature around 5 T which is suppressed for $T > 36\text{ K}$	204
6.12	(a) Temperature-dependent resistance for various pressure values. Inset: the value of T_N , determined from dR/dT . (b) The transition is more visible in the derivative of resistance with respect to temperature dR/dT	206
6.13	Band structure calculations for TiAu. (a) The non-magnetic density of states (thin black line) exhibits a peak close to the Fermi surface, similar to that seen in other itinerant magnets. For the AFM1 ground state, the finite total density of states (thick red line) at the Fermi energy is flanked by two peaks around 0.1 eV (inset), which explains the metamagnetic transition at low T (see text). (b) The electron spin density shows a modulation along the b axis, consistent with the $k = 2\pi/(3b)$ nesting shown in (c). Fermi surface with nesting vector $Q_{calc} = (0, 2\pi/3b, 0)$ is shown in (c). Separated Fermi surface plot is shown in Fig. 6.14.	207
6.14	Separated Fermi surface for different bands. Color is used for the ease of viewing only.	208
7.1	Evolution of lattice parameters a (triangles, left axis), b (circles, left axis), and c (squares, left axis) along with the unit cell volume V (diamonds, right axis) with doping x in $\text{Ti}_{1-x}\text{Sc}_x\text{Au}$ ($0 \leq x \leq 0.25$). .	214
7.2	(a) Inverse susceptibility $H/(M - M_0)$ (symbols) along with respective Curie-Weiss fits (lines) for $\text{Ti}_{1-x}\text{Sc}_x\text{Au}$ with $0 \leq x \leq 0.25$. (b) Magnetic susceptibility M/H as a function of temperature T for $\text{Ti}_{1-x}\text{Sc}_x\text{Au}$ with $0 \leq x \leq 0.25$. (c) The Néel temperature T_N is determined from the peak in $d(MT)/dT$, which is reduced below $T = 2\text{ K}$ for $x \geq 0.12$. .	216

7.3	(a) non-Fermi liquid behavior is evident from $C_p/T \propto -\log T$ for $0.09 \leq x \leq 0.20$ in $\text{Ti}_{1-x}\text{Sc}_x\text{Au}$. (b) A Fermi liquid specific heat temperature dependence $C_p/T \propto T^2$ is recovered away from the quantum critical point for $0 \leq x \leq 0.07$ and $x = 0.25$ in $\text{Ti}_{1-x}\text{Sc}_x\text{Au}$	217
7.4	(a) Temperature-independent contribution to the susceptibility χ_0 as a function of doping x in $\text{Ti}_{1-x}\text{Sc}_x\text{Au}$. (b) Sommerfeld coefficient γ as a function of $T_N^{3/4}$ (symbols), line is a guide to the eye.	220
7.5	(a) - (l) Resistivity as a function of temperature T for $\text{Ti}_{1-x}\text{Sc}_x\text{Au}$ where $0 \leq x \leq 0.25$. Solid lines represent fit to $\rho = \rho_0 + A_n T^n$	221
7.6	(a) - (l) Resistivity as a function of temperature T^n for $\text{Ti}_{1-x}\text{Sc}_x\text{Au}$ where $0 \leq x \leq 0.25$. The value of the exponent n achieves a minimum for $x = 0.13$, consistent with the breakdown of the Fermi liquid regime for which $n = 1$. On either side of the critical point, Fermi liquid resistivity is regained with n values close to 2.	223
7.7	Magnetic Grüneisen ratio Γ_{mag} for $\text{Ti}_{1-x}\text{Sc}_x\text{Au}$ where $0 \leq x \leq 0.25$: the value of Γ_{mag} at lowest temperature diverges as $x \rightarrow x_c$	224
7.8	The total (solid lines) and partial (dashed lines) density of states in paramagnetic state for $\text{Ti}_{1-x}\text{Sc}_x\text{Au}$ where $x = 0, 0.2$ and 0.4 . In the $x = 0$ case, Ti bands (maroon) contribute more to the density of states at the Fermi level than the Au bands (cyan). The dashed densities of state are divided by a factor of two for ease of viewing. Inset: both position and magnitude of the peak at the Fermi level are affected by doping.	226
7.9	The evolution of the Fermi surface in TiAu with doping. While four bands contribute to the Fermi level in $x = 0$, only three bands are present for the $x = 0.4$ compound.	228
7.10	(a) Evolution of the Néel temperature T_N and (b) paramagnetic moment $\mu_{\text{P.M.}}$ with doping x . (c) Left axis: the Sommerfeld coefficient γ extracted from C_p/T vs. T^2 (Fermi liquid region, full circles) and from C_p/T vs. $\log T$ (non-Fermi liquid region, open circles). Right axis: The Grüneisen ratio Γ_{mag} . (d) Wilson's ratio R_W . (e) Left axis: The exponent n , extracted from $\Delta\rho$ vs. T^n (open triangles) and $\log\Delta\rho$ vs. $\log T$ (full triangles). Right axis: The resistivity coefficient A_n for varied n (full diamonds) and $n = 2$ (open diamonds).	229
8.1	Cutting speed as a function of time [134].	233

8.2	An example of Ashby plots [26] for (a) Young's modulus <i>vs.</i> density and (b) strength <i>vs.</i> relative cost per unit volume. The guide lines are used to select materials better suited for minimum weight design and minimum cost for desired strength, respectively.	235
8.3	Hardness as a function of inverse grain diameter d for various metals and alloys [147].	237
8.4	An example of an annealing process for cold-worked nickel [58, 334]. The energy released on annealing was compared with that of a non-deformed sample.	239
8.5	The effects of various precipitation hardening methods on hardness of the Al-4%Cu alloy [58]	241
8.6	Binary phase diagram of Ti-Au with the open circles representing the compositions of the $\text{Ti}_{1-x}\text{Au}_x$ alloys for the current study ($0 \leq x \leq 1$) [389].	248
8.7	Hardness as a function of composition (top axis) and density (bottom axis) for $\text{Ti}_{1-x}\text{Au}_x$ and other medical alloys. Current study is represented by red circles. Previous studies of $\text{Ti}_{1-x}\text{Au}_x$ alloys are shown in full black symbols while other medical alloys are represented by open symbols.	249
8.8	(a) In an SEM image, arrows indicate second phase particles which form between the dendrites of the material. Those particles are a Ti-rich solid solution. (b) The dark contrasted features in the TEM bright field image are the second phase Ti particles, one of which is indicated by an arrow. (c) X-ray diffraction pattern indicates that the $\alpha\text{Ti}_3\text{Au}$ phase (blue vertical symbols) main phase accompanied by small inclusions of $\beta\text{Ti}_3\text{Au}$ and αTi (marked by asterisks).	252
8.9	(a) Coefficient of friction as a function of time for $\text{Ti}_{1-x}\text{Au}_x$ with $x = 0, 0.25, 0.30$ and 0.50 . Inset: the $x = 0.25$ sample used for wear tests. (b) Wear volumes of the $\text{Ti}_{1-x}\text{Au}_x$ pin (dashed bars) and a SiC disk (full bars).	254
8.10	SEM images of the pin and disk wear test: (a) Ti reference ingot, (b), (d), (f) and (h) SiC disk. $\text{Ti}_{1-x}\text{Au}_x$ pins for $x = 0.25$ (c), $x = 0.30$ (e) and $x = 0.50$ (g) samples.	255
8.11	(a) Density of states as a function of energy for TiAu (black), TiAu_2 (yellow), TiAu_4 (blue) and Ti_3Au (red). Ti_3Au exhibits a pronounced valley around the Fermi energy, marked by a dashed gray line in (b).	256

9.1	(a) Powder x-ray diffraction pattern for ScGa_3 (black), with calculated peak positions (vertical red marks) for space group $Pm\bar{3}m$ and lattice parameter $a = 4.0919 \text{ \AA}$. Minute amounts of residual Ga flux are marked by asterisks. Inset: a picture of a single crystal of ScGa_3 . (b) A cluster of ScGa_3 crystals, prepared from a molten solution.	261
9.2	(a) Zero-field cooled temperature-dependent susceptibility data, scaled by 4π and corrected for demagnetizing effects (see text), for ScGa_3 in applied magnetic fields up to 80 Oe. (b) $H = 5$ Oe zero-field cooled (full symbols) and field-cooled (open symbols) scaled susceptibility $4\pi\chi_{eff}$ data for ScGa_3 (squares) and LuGa_3 (triangles).	264
9.3	(a) ScGa_3 and (b) LuGa_3 $M(H_{eff})$ for temperatures between 1.8 K and 2.3 K. Open squares: $M(H)$ isotherms for $T = 1.8$ K, where H is the applied magnetic field.	265
9.4	Specific heat data for (a) ScGa_3 and (b) LuGa_3 in applied magnetic fields up 240 Oe. (c) and (d) Normal ($H = 240$ Oe) and superconducting ($H = 0$) electronic specific heat C_e , scaled by temperature T . The entropy conservation construct gives the ratio $\Delta C_{es}/\gamma_n T_c \approx 1.44$ for both ScGa_3 and LuGa_3 , with the dashed line representing a fit of C_e/T to the expected BCS electronic specific heat.	267
9.5	$H = 0$ temperature-dependent resistivity for ScGa_3 (full black symbols) and LuGa_3 (open gray symbols), with Bloch-Grüneisen-Mott fits (solid lines) for $n = 2$ (ScGa_3) and $n = 3$ (LuGa_3). Left inset: low-temperature $\rho(T)$ around T_c . Right inset: $\Delta\rho = \rho - \rho(0)$ vs. T^2 , with solid lines representing linear fits up to 80 K for ScGa_3 and 70 K for LuGa_3	269
9.6	Density of states for ScGa_3 exhibits a peak at the Fermi surface. Inset: the Fermi surface of ScGa_3	272
9.7	$H - T$ phase diagram for ScGa_3 (open black symbols) and LuGa_3 (full red symbols). The values of the critical fields H_c are determined from $\chi(T)$ data (squares), $M(H)$ data (triangles) and $C_p(T)$ data (circles).	273
9.8	Doping of ScGa_3 with C and B shifts the peak away from the Fermi surface (a) and (c). The respective Fermi surface is plotted in (b).	274

List of Tables

2.1	Comparison of calculated and measured Pauli susceptibility values χ_{Pauli} [27].	28
2.2	Critical exponents for various models [42].	48
2.3	Critical exponents for itinerant systems at the critical point [268]. . .	49
2.4	Critical exponents for itinerant systems near a quantum critical point [268].	49
2.5	Frequency shifts δ for various spin-glasses [273].	61
5.1	Cluster-glass parameters for $(\text{Sc}_{1-x}\text{Er}_x)_{3.1}\text{In}$ ($0 \leq x \leq 0.10$).	179
6.1	Crystallographic information for $Pmma$ TiAu extracted from neutron diffraction data.	185
6.2	Crystallographic information for $Pmma$ TiAu extracted from x-ray diffraction analysis.	185
6.3	Comparison of μSR results for itinerant helimagnetic, ferromagnetic, spin density wave, spin glass, and charge density wave systems.	194
6.4	Comparison of μSR results for itinerant helimagnetic, ferromagnetic, spin density wave, spin glass, and charge density wave systems.	197
7.1	Summary of the band structure calculations for $\text{Ti}_{1-x}\text{Sc}_x\text{Au}$ with $x =$ $0, 0.2$ and 0.4 with paramagnetic, ferromagnetic, and spin density wave configuration.	227
8.1	Crystal structure for the Mohs's scale reference materials [157, 333]. .	236

8.2	Temperature range and time typically used for stress relief in Ti and Ti-based alloys [307].	244
8.3	Summary of parameters for as-cast $\text{Ti}_{1-x}\text{Au}_x$ alloys.	250
8.4	Summary of composition analysis for as-cast $\text{Ti}_{1-x}\text{Au}_x$ alloys.	253
8.5	Wear parameters of the $\text{Ti}_{1-x}\text{Au}_x$ alloys.	257
8.6	Crystallographic and pseudogap parameters for Ti-Au phases.	257
8.7	Comparison of hardness for different annealing profiles of $\text{Ti}_{1-x}\text{Au}_x$ alloys.	258
9.1	Summary of parameters describing properties of ScGa_3 and LuGa_3	271

Outline

The breakthroughs in the field of quantum mechanics in the beginning of the 20th century allowed for an immense progress in understanding of the origin of magnetism and long range magnetic order [156,221,261,397], as summarized in Chapter 2. This, however, is only true for the case of local moment magnetism, where magnetic ions are fixed on lattice sites. It was later realized that another type of magnetism, now referred to as itinerant, can arise from conduction electrons [350]. This realization came after non-integer values of magnetic moment per atom were experimentally observed for simple metals like Fe, Ni, and Co, different from what was expected from the Hund's rules. Stoner suggested that the extra moment arises from conduction electrons and postulated a condition for the emergence of itinerant magnetism in a metal: unpolarized sea of conduction electrons spontaneously creates a spin imbalance between spin-up and spin-down population, resulting in non-zero overall magnetization. Most importantly, this is possible even when constituent elements are non-magnetic. Itinerant magnetism is observed in a large number of systems, but it is almost always accompanied by local moment magnetism. However, this is not the case in Sc_3In [246] and ZrZn_2 [245], both of which do not contain any magnetic constituents. Both order

ferromagnetically and exhibit Curie-Weiss-like behavior, and while ZrZn_2 has been studied extensively, this is not the case for Sc_3In .

Since attempts to drastically alter the overall magnetization of Sc_3In *via* pressure [124, 140] and magnetic field [167] were unsuccessful, the effects of doping on Sc_3In were investigated. The addition of local moment ions in the itinerant matrix was investigated by doping $\text{Sc}_{3.1}\text{In}$ with Er, as summarized in Chapter 5. This could provide an insight into the interplay between the two types of magnetism: the itinerant moment is expected to have a weak variation with the composition, but the overall magnetic moment should increase with increasing amounts of local moment. It was found that Er doping of $\text{Sc}_{3.1}\text{In}$ [358] results in cluster-glass behavior below the characteristic freezing temperature, which is enhanced by the increasing doping amount x . The crystallographic frustration and site disorder, induced by Er doping on the bipyramidal sites, induces a cluster-glass state that originates from a metallic ferromagnetic ground state. Mixing of itinerant and local magnetism produces intermediate values of the Rhodes-Wohlfarth ratio [309], signaling a transition from the itinerant to the local limit. The effect of local moment ion doping in Sc_3In is drastically different from that in ZrZn_2 , for which the addition of Gd^{3+} into the itinerant matrix resulted in complete suppression of magnetism [25].

The effects of non-magnetic ion doping of $\text{Sc}_{3.1}\text{In}$ are presented in Chapter 4. By partial substitution of Sc with Lu, it was possible to achieve a quantum critical point [355]. While quantum critical points are observed in a large number of strongly correlated electron systems, including high temperature superconductors [45, 291, 314], low-dimensional compounds [90, 132, 158], and heavy fermions [54, 96, 260, 322, 348, 375], the number of quantum critical points in itinerant magnets is small. Perhaps this explains the lack of associated theoretical understanding. Remarkable for a system with no local moments, the quantum critical point is accompanied by non-Fermi

liquid behavior, manifested in the logarithmic divergence of the specific heat both in the ferro- *and* the paramagnetic states, as well as linear temperature dependence of the low temperature resistivity. Through application of Arrott-Noakes analysis [17], unusual critical scaling is observed close to the quantum critical point, yielding non-mean-field values of critical exponents δ , γ and β . This is in stark contrast to the mean-field nature of ZrZn_2 [341]. It was established that the quantum critical scaling of Sc_3In is more similar to a heavy fermion URu_2Si_2 [57]. Possible explanation lies within the dimensionality of spin fluctuations, since nearly 1D Sc_3In is more similar to the 2D URu_2Si_2 rather than the 3D ZrZn_2 [355].

Given these discrepancies between seemingly analogues systems Sc_3In and ZrZn_2 , additional itinerant magnets are needed to develop a comprehensive understanding of itinerant phenomena. Compounds without local moment are particularly convenient for studying itinerant magnetism as they lack complexity associated with the interplay between local and itinerant moments. Unfortunately, a theoretical basis for a systematic way of finding said compounds does not exist. Spontaneous magnetization according to the Stoner criterion [350] is more likely to occur in d band metals with high density of states at the Fermi level. Additionally, a peak in the density of states near the Fermi surface is indicative of instability towards a magnetic ground state and has been suggested to lead to magnetism [266]. From these considerations, analysis of band structure calculations for intermetallic compounds was employed to discover new itinerant magnets. This search was successful in finding the first itinerant antiferromagnet, composed of non-magnetic constituents – TiAu [359]. Given the small number of known itinerant magnets, the discovery of the novel itinerant antiferromagnet TiAu provides long-sought insights into the physics of itinerant magnets in general, and of itinerant antiferromagnets in particular. A number of physical property measurements including magnetization, resistivity, specific heat, neutron and x-ray diffraction as well as muon spin relaxation were implemented to confirmed the

spin-density wave ground state of TiAu below the Néel temperature $T_N \simeq 36$ K, as summarized in Chapter 6. The long range static order is further confirmed by neutron diffraction data, which, together with μ SR experiments, indicate small moment ordering in the whole sample volume. In addition to the overwhelming experimental evidence for the itinerant moment antiferromagnetic order in TiAu, density functional theory calculations confirm the spin-density wave small moment ordering.

As summarized in Chapter 7, the suppression of the antiferromagnetic order in TiAu to $T = 0$ in a quantum critical regime was possible *via* partial substitution of Ti with Sc in $\text{Ti}_{1-x}\text{Sc}_x\text{Au}$. The critical doping estimate $x_c = 0.13 \pm 0.01$ is consistent across all measurements, indicating collective quantum critical phenomenon. Moreover, the scaling behavior of $\text{Ti}_{1-x}\text{Sc}_x\text{Au}$ clearly indicates the 2D antiferromagnetic nature of magnetic spin fluctuations [268]. Divergent specific heat along with linear dependence of resistivity and diverging Grüneisen parameter are consistent with a 2D antiferromagnetic non-Fermi liquid, previously only observed in f electron systems [129, 206, 207]. Moreover, non-Fermi liquid behavior associated with the quantum critical point is more pronounced than that observed in Sc_3In and ZrZn_2 . The suppression of the spin density wave - paramagnetic transition to absolute zero with Sc doping is also confirmed *via* band structure calculations, where a gradual shift of the peak in the density of states at the Fermi level as well as the loss of the Fermi surface nesting are expected. While the critical doping level extracted from the band structure calculations is larger than $x_c = 0.13 \pm 0.01$, the quantitative discrepancy is expected to decrease if the effects of disorder are taken into account. Understanding the properties of this system will serve as a stepping stone towards explaining anomalous properties of solids in general and itinerant magnets in particular.

An unexpectedly high hardness of arc-melted TiAu samples prevented typical powder diffraction experiments but led to a startling discovery – hardness of the

$\text{Ti}_{0.75}\text{Au}_{0.25}$ alloy was found to be four times higher than that of pure Ti, as presented in Chapter 8. The $\text{Ti}_{1-x}\text{Au}_x$ ($0.22 \leq x \leq 0.8$) alloys exhibit extreme hardness values, elevated melting temperatures (compared to those of constituent elements), reduced density compared to Au, high malleability, bulk metallicity, high biocompatibility, low wear, reduced friction, potentially high radio opacity, as well as osseointegration. All these properties render the $\text{Ti}_{1-x}\text{Au}_x$ alloys particularly useful for orthopedic, dental, and prosthetic applications, where they could be used as both permanent and temporary components. Additionally, the ability of $\text{Ti}_{1-x}\text{Au}_x$ alloys to adhere to ceramic parts could reduce the weight and cost of these components. Since the search for new hard materials is often challenging from both theoretical and experimental points of view, a discovery of a hard biocompatible alloy is likely to benefit both fundamental research and everyday applications.

In Chapter 9, superconductive properties of single crystals of ScGa_3 and LuGa_3 are characterized. As evidenced by magnetization, specific heat and resistivity measurements, these compounds have a Type I superconducting ground state: low critical temperatures $T_c = 2.1 - 2.2$ K, field-induced second-to-first order phase transition in the specific heat, critical fields less than 240 Oe and low Ginzburg-Landau coefficients ($\kappa \approx 0.23$ and 0.30 for ScGa_3 and LuGa_3 , respectively) are observed. These properties render ScGa_3 and LuGa_3 two of only several Type I superconducting compounds, with most other superconductors being Type II (compounds and alloys) or Type I (elemental metals and metaloids). Despite the large number of known conventional and unconventional superconductors, new findings still emerge even from simple, binary intermetallic systems. Valuable insights into the rare occurrence of Type I superconductivity in binary or ternary systems can pave the way towards better understanding of superconducting phenomena.

Background

2.1 Magnetism

While the first accounts of magnetism date back to ancient Greece, where the term "magnet" was first introduced, not much was understood about the nature of magnetism until the 19th century. However, this did not prevent magnets from being widely used as part of the compass as early as the 16th century. Hans Christian Oersted noticed that an electric current in a coil could deflect a compass needle, observing for the first time the correlation between the magnetic and electric fields. This gave birth to the first electromagnet in 1825. Other scientists such as Ampere, Faraday, Gauss and Maxwell made significant contributions to the subject, but it was mostly the twentieth century physicists who have established proper theoretical models for the origin of magnetism and long range magnetic order. Curie, Langevin, Weiss and Néel described these phenomena, building the foundation for the field.

2.1.1 Origin of Magnetism in Free Ions

In order to understand the ionic origin of magnetism, it is necessary to recall the fact that electricity and magnetism are deeply intertwined – all magnetic phenomena are due to electric charges in motion. Since the dynamics of an electron in a nucleus can be separated into two parts, two contributions to overall magnetic moment exist – *orbital* (l) and *spin* (s). By convention, the electrons can either be "spin-up" ($m_s = 1/2$) or "spin-down" ($m_s = -1/2$). The total spin quantum number S for all electrons in an ion can therefore be represented as:

$$S = n_{\uparrow} \frac{1}{2} - n_{\downarrow} \frac{1}{2} \quad (2.1)$$

where n_{\uparrow} and n_{\downarrow} is the number of electrons in the spin-up and spin-down state.

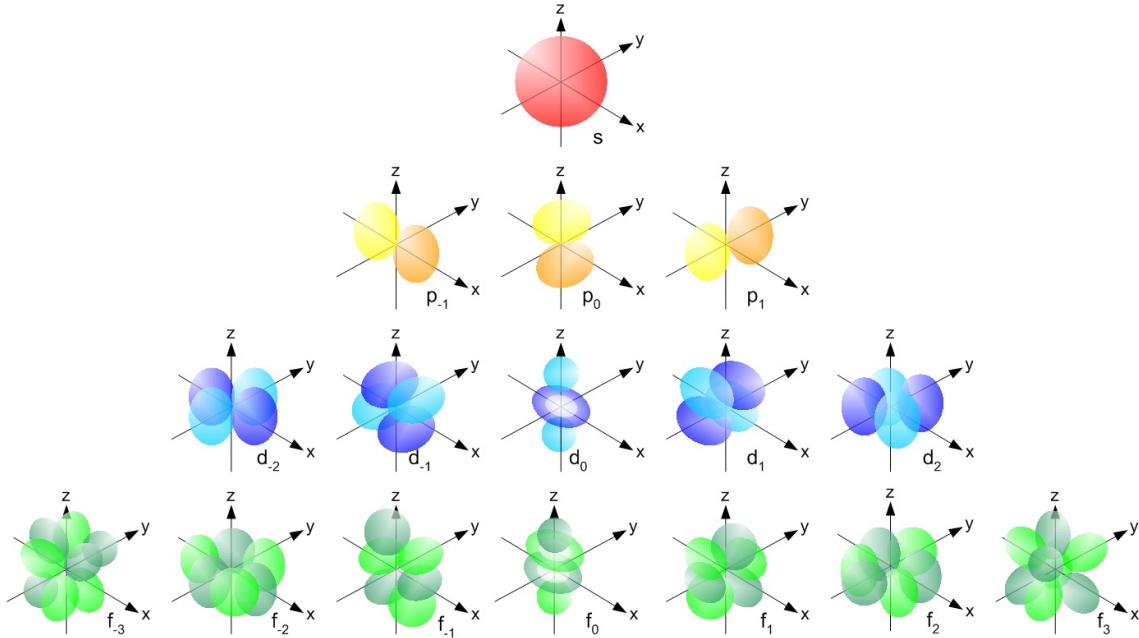


Figure 2.1: Electron orbitals s , p , d , and f [3].

The wave-like nature of the electron only allows for the calculation of the probability of finding it around the nucleus, providing a three dimensional map of

the electron's likely location. These possible quantum states of a single or a group of electrons are known as *atomic orbitals* (since motion of an electron cannot be described as that of a solid particle, its path can no longer be called *orbit* but rather *orbital* in order to differentiate their wave-like nature). Depending on the angular momentum quantum number, $l = 0, 1, 2, 3$, electrons can occupy different types of orbitals: *s* (sharp), *p* (**p**rincipal), *d* (**d**iffuse), *f* (**f**undamental). These names, derived from the characteristics of their spectroscopic lines, describe the shape of the orbitals, depicted in Fig. 2.1. Subsequently, the magnetic quantum number m_l is equal to $-l, -l+1, \dots, +l-1, +l$, and thus the total orbital quantum number L of an ion can be found as:

$$L = \sum_l m_l \quad (2.2)$$

Pauli's exclusion principle, Coulomb repulsion, and spin-orbit coupling govern the distribution of electrons among these orbitals. In order to determine the ground state, Hund's rules must be followed in the following sequence:

1. Maximum possible S consistent with Pauli's exclusion principle.
2. For maximum S , choose configuration which maximizes L .
3. Since S and L are coupled, $J = S + L$ (orbitals are more than half-filled) or $J = |L - S|$ (orbitals are less than half-filled).

In the absence of an applied magnetic field, electron spins are randomly oriented, hence no net magnetization is observed. However, when a magnetic field is applied, the magnetic spins will experience a torque, aligning them and giving rise to a net magnetization. Similar to the free ion case, the magnetic moment of an atom has two contributions, which result in the orbital μ_L , and spin μ_S magnetic moments:

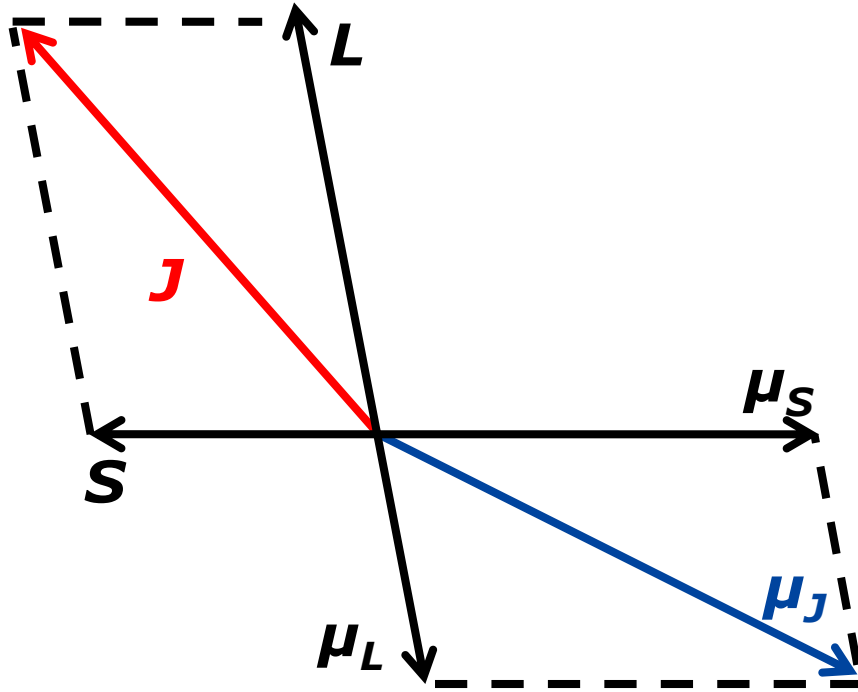


Figure 2.2: Representation of the total angular momentum.

$$\vec{\mu}_L = -g_L \mu_B \vec{L} \quad (2.3)$$

$$\vec{\mu}_S = -g_S \mu_B \vec{S} \quad (2.4)$$

where μ_B is the Bohr magneton and $g_L = 1$ and $g_S = 2$ are the orbital and spin Landé g -factors, respectively. Combining the two as a vector sum, the total angular momentum $\vec{\mu}_J$ is shown in Fig. 2.2 and can be found as:

$$\vec{\mu}_J = \vec{\mu}_L + \vec{\mu}_S \quad (2.5)$$

Introducing the total Landé g -factor g_J allows for μ_J to be written in a form similar to that of μ_L and μ_S :

$$\mu_J = g_J \mu_B J \quad (2.6)$$

Additionally, g_J can be written in the following form:

$$g_J = \frac{3}{2} + \frac{1}{2} \frac{S(S+1) - L(L+1)}{J(J+1)} \quad (2.7)$$

As mentioned earlier, a magnetic moment will tend to align with the field when an external magnetic field is applied. From the classical point of view, since the electron is constantly in motion, the magnetic field will result in a force perpendicular to electron's velocity. Because no work is being done, this means that the energy of the system does not depend on the applied field, yielding zero magnetization [42]. A more formal proof can be derived using classical statistical mechanics as follows. For a system of N electrons, the magnetic moment μ is a linear function of the position with the following form [11]:

$$\mu = \sum_{i=1}^N a_i \frac{\partial r_i}{\partial t} \quad (2.8)$$

The vector coefficients a_i depend on the position coordinates r_i ($i = 1 \dots N$), but not on the momentum p_i . The canonical equations of classical motion for a charged particle are given as [11]:

$$\frac{\partial r_i}{\partial t} = \frac{\partial \mathcal{H}_{\text{CL}}}{\partial p_i} \quad \text{and} \quad \frac{\partial p_i}{\partial t} = -\frac{\partial \mathcal{H}_{\text{CL}}}{\partial r_i} \quad (2.9)$$

$$\mathcal{H}_{\text{CL}} = \frac{1}{2m_e} \sum_{i=1}^N \left(p_i - \frac{e}{c} A_i \right)^2 + e\phi(q) \quad (2.10)$$

where m_e is the electron mass, A_i is the magnetic vector potential and $\phi(q)$ is the electric scalar potential. Substituting the expression for $\partial r_i / \partial t$ into the total magnetic moment equation yields:

$$\mu = \sum_{i=1}^N a_i \frac{\partial \mathcal{H}_{\text{CL}}}{\partial p_i} \quad (2.11)$$

The classical statistical average that will be measured can be found as:

$$M = \frac{\int \mu e^{-\beta \mathcal{H}_{\text{CL}}} dr_1 \dots dr_N dp_1 \dots dp_N}{\int e^{-\beta \mathcal{H}_{\text{CL}}} dr_1 \dots dr_N dp_1 \dots dp_N} \quad (2.12)$$

with $\beta = 1/k_B T$. The numerator of the above expression is a sum of terms, each proportional to:

$$\int_{-\infty}^{\infty} \frac{\partial \mathcal{H}_{\text{CL}}}{\partial p_i} e^{-\beta \mathcal{H}_{\text{CL}}} dp_i = [-k_B T e^{-\beta \mathcal{H}_{\text{CL}}}]_{p_i=-\infty}^{\infty} \quad (2.13)$$

According to Eq. 2.10, $\mathcal{H}_{\text{CL}} \propto p_i^2$. Therefore, the sum M vanishes, yielding zero magnetization for any applied field [46]. This relationship is known as the Bohr-Van Leeuwen theorem [46], stating that electrons behaving according to the classical laws of physics do not interact with an applied magnetic field. This problem can be addressed by treating electrons as a quantum mechanical phenomena, which will be presented in Section 2.1.2.

As noted earlier, in order to probe the magnetic character of a given material, an external magnetic field must be applied. The response of the material is known as the magnetic susceptibility χ . In some materials the spins will align in the direction

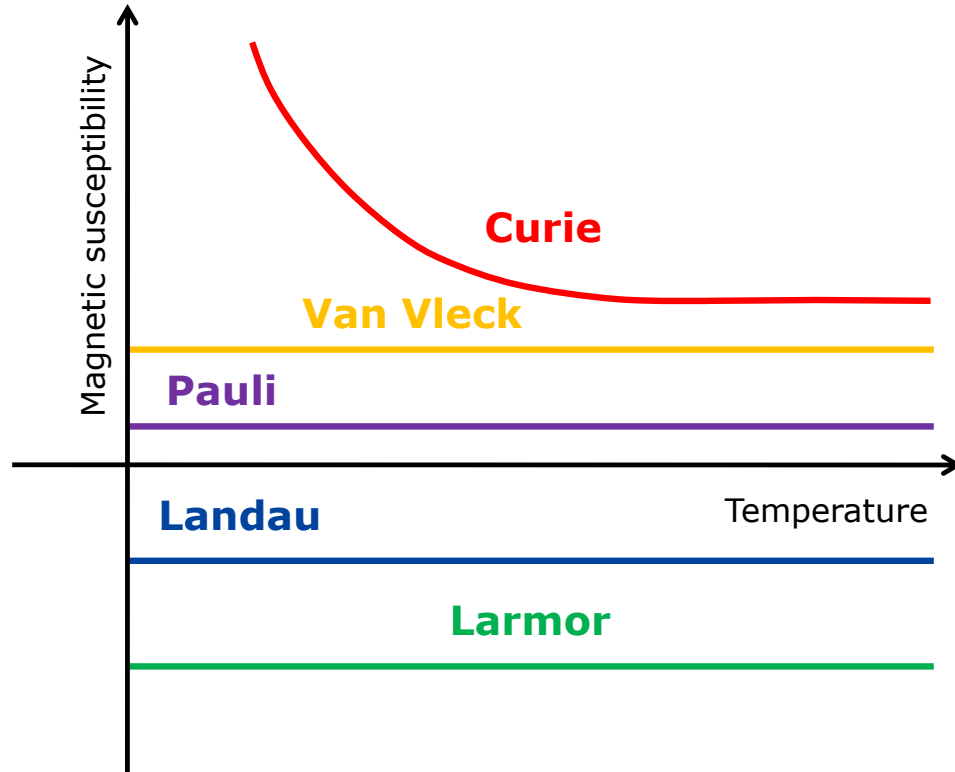


Figure 2.3: Various contributions to the magnetic susceptibility of a metal. Relative magnitudes are not drawn to scale.

of the field, yielding a positive value of χ (paramagnets, $\chi > 0$), while in other cases spins will have a direction opposite to that of the field, resulting in a negative χ (diamagnets, $\chi < 0$). The different contributions to the overall magnetic susceptibility χ arise from various orbital filling configurations. Their relative strengths ultimately dictate the material's behavior:

1. Electrons in filled atomic orbitals ($L = S = 0$):
 - Larmor diamagnetism typically results in a very small contribution to the susceptibility, $\chi_L \approx -10^{-6} - 10^{-8}$ emu/mole [27].
2. Electrons in partially filled atomic orbitals:
 - If $J = 0$, the Van Vleck paramagnetism arises with $\chi_V \approx 10^{-6} - 10^{-8}$ emu/mole

[81].

- If $J \neq 0$, Curie paramagnetism (Sections 2.1.2 and 2.1.3) will be the dominant contribution to the susceptibility since $\chi_{\text{Curie}} \approx 10^{-2} - 10^{-3}$ emu/mole [27].

3. Conduction electrons:

- Electron's spin contribution to susceptibility χ is known as Pauli paramagnetism (Section 2.1.4), $\chi_{\text{Pauli}} \approx 10^{-4} - 10^{-6}$ emu/mole [27, 346].
- Electron's orbital motion results in Landau diamagnetism, the value of which is approximately $1/3\chi_{\text{Pauli}}$ [27, 81, 295].

It is important to note that, except for the Curie paramagnetism, all of the above contributions are temperature-independent (Fig. 2.3). Combinations of various contributions present in a material will dictate overall susceptibility χ . An example of mass susceptibility for several pure elements is shown in Fig. 2.4.

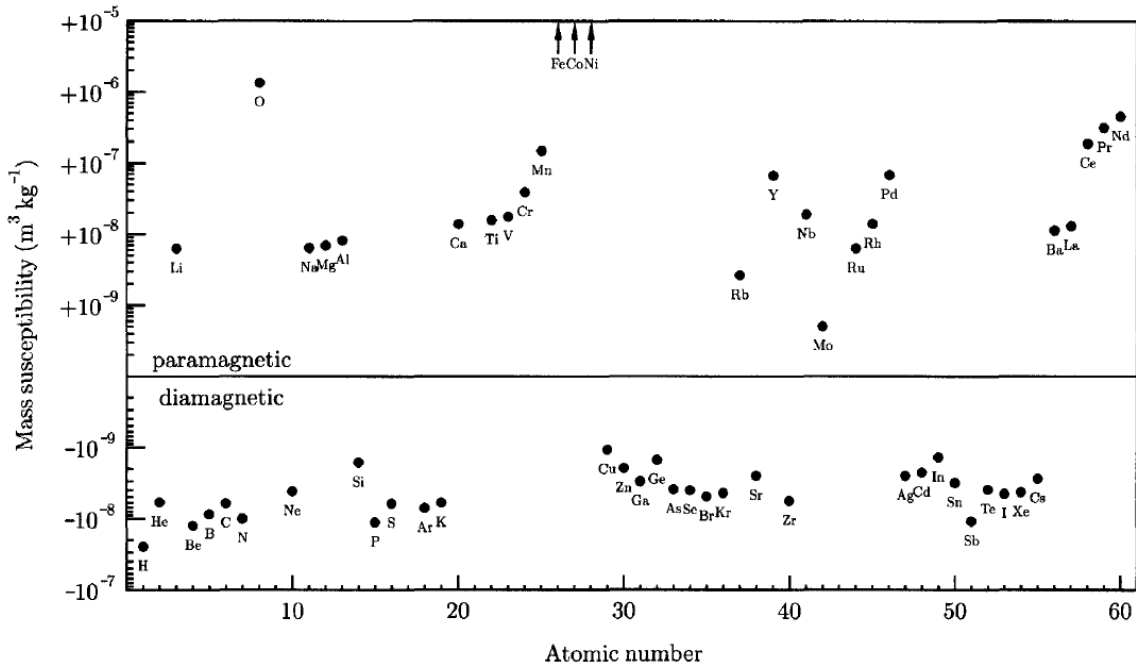


Figure 2.4: The mass susceptibility for the first 60 elements in the periodic table at room temperature as function of the atomic number [42].

2.1.2 Non-interacting Magnetic Moments: Curie Law

Besides being material-dependent, magnetic susceptibility χ also depends on the magnitude of the applied magnetic field:

$$\chi = \frac{dM}{dH} = -\frac{1}{V} \frac{\partial^2 F}{\partial H^2} \quad (2.14)$$

where F is the free energy given by:

$$F = -k_B T \ln Z \quad (2.15)$$

where k_B is Boltzman's constant and Z is the partition function. The free energy is temperature-dependent since the temperature-induced motion of ions in solids competes with the magnetic field's tendency to align them. The partition function Z can be calculated as follows:

$$Z = \sum_{m_J=-J}^J e^{\frac{-E_{J,m_J}}{k_B T}} = \sum_{m_J=-J}^J e^{\frac{-g_J m_J \mu_B H}{k_B T}} \quad (2.16)$$

with E_{J,m_J} being the energy eigenvalues of a magnetic ion in a magnetic field H for a system of non-interacting magnetic moments, described by \mathcal{H}_{NI} :

$$E_{J,m_J} = g_J \mu_B m_J H \quad \text{with} \quad m_J = -J, \dots, J \quad (2.17)$$

$$\mathcal{H}_{NI} = -g_J \mu_B \sum_j \vec{J}_j \cdot \vec{H} \quad (2.18)$$

Therefore, the magnetization can be determined as:

$$M = \frac{k_B T}{V} \frac{\partial}{\partial H} \left(\sum_{m_J=-J}^J e^{\frac{-g_J m_J \mu_B H}{k_B T}} \right) \quad (2.19)$$

which yields:

$$M = M_0 \left[\frac{2J+1}{J} \coth \left(\frac{2J+1}{2J} x \right) - \frac{1}{2J} \coth \left(\frac{1}{2J} x \right) \right] \quad (2.20)$$

$$x = \frac{g_J J \mu_B H}{k_B T} \quad \text{and} \quad M_0 = n g_J J \mu_B \quad (2.21)$$

Thus

$$M = M_0 B_J(x) \quad (2.22)$$

where $B_J(x)$ is the Brillouin function that depends on the values of the quantum numbers S , L and J . For small values of x , a series expansion can be used to approximate the Brillouin function:

$$B_J(x) = \frac{(J+1)x}{3J} + O(x^3) \quad (2.23)$$

Because M is linear in H for low H values, when $k_B T \gg g \mu_B H$ the magnetic susceptibility χ can be approximated as:

$$\chi \approx \frac{M}{H} \quad (2.24)$$

Using the expansion for $B_J(x)$ from the Eq. 2.23 (with higher order terms

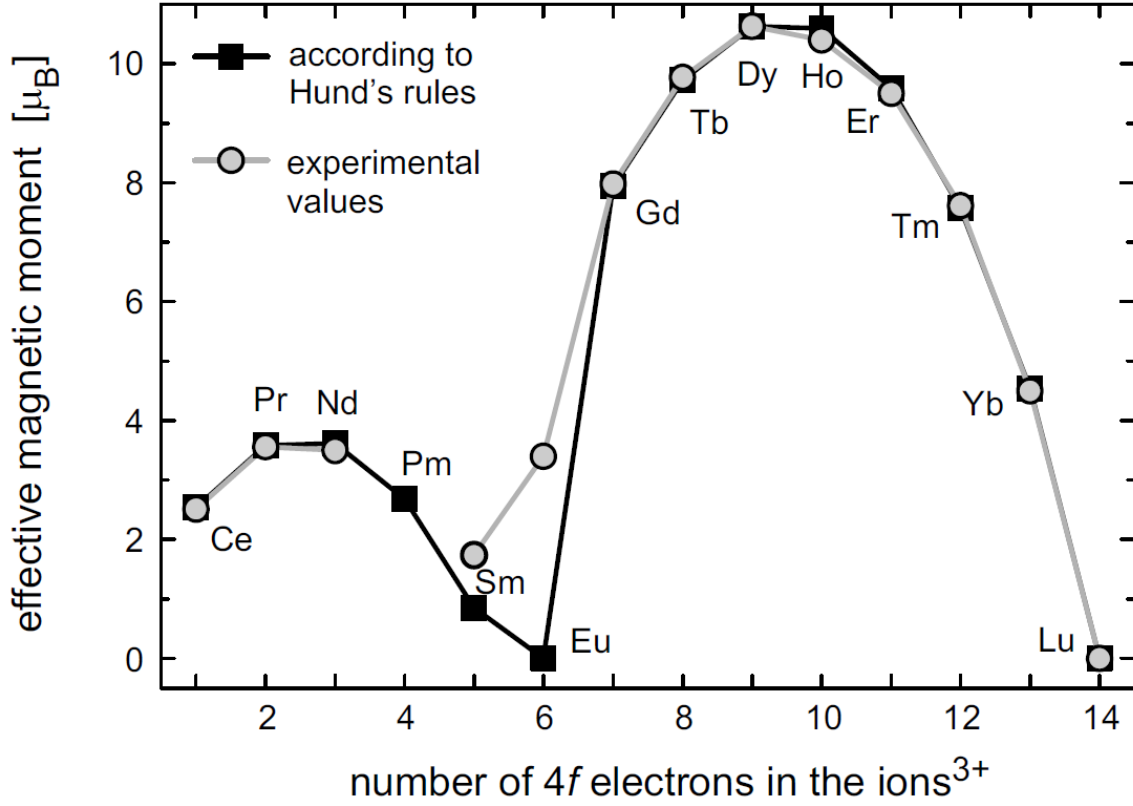


Figure 2.5: Comparison of paramagnetic moment μ_{PM} , obtained from experiment with that expected based on Hund's rules [133].

discarded) and the expression for the magnetization from the Eqs. 2.22 and 2.21, the magnetic susceptibility χ can be found as:

$$\chi = \frac{ng_J^2\mu_B^2J(J+1)}{3k_BT} \quad (2.25)$$

The dependence on the particular magnetic ion (through the values of the quantum numbers S , L and J) can be summarized by the quantity called the paramagnetic moment μ_{PM} , defined as:

$$\mu_{PM} = g_J\sqrt{J(J+1)}\mu_B \quad (2.26)$$

This allows for the susceptibility to be rewritten as:

$$\chi = \frac{n\mu_{PM}^2}{3k_B T} = \frac{C}{T} \quad \text{where} \quad C = \frac{n\mu_{PM}^2}{3k_B} \quad (2.27)$$

The above expression describes the relationship between temperature and magnetic susceptibility of a given material, ignoring correlations between ions, and is known as the Curie law (C is the Curie constant). Since there is typically a temperature-independent component of the susceptibility χ_0 that can arise from various contributions (Section 2.1.1), the Curie law is typically written as:

$$\chi = \frac{C}{T} + \chi_0 \quad (2.28)$$

Upon subtraction of the χ_0 term, the linear temperature dependence of the inverse susceptibility is evident. It was first noticed experimentally by P. Curie [87] and was later derived theoretically by P. Langevin [221]. The values of μ_{PM} , extracted from the fit to the Curie law, are compared with those obtained from Eq. 2.26 (Fig. 2.5) [133]. The agreement is generally fair for $4f$ elements with the exceptions of Eu and Sm, for which the $L - S$ coupling is small resulting in level mixing as a function of temperature or field [133]. For compounds containing $3d$ electrons, the orbital momentum is frequently quenched due to interactions between electrons, yielding $L = 0$.

In the following Section, the Curie law will be expanded to include interactions between spins, which result in a collective behavior, known as long range magnetic order. Depending on the type of the spin-spin interaction, the material will order ferromagnetically (parallel) or antiferromagnetically (antiparallel).

2.1.3 Interacting Magnetic Moments: Curie-Weiss Law

The Curie law, derived for a system of non-interacting magnetic moments, indicates that susceptibility χ is inversely proportional to the temperature T . In order to derive the temperature dependence of a system with spin-spin interactions, an extra term must be added to the Hamiltonian in Eq. 2.18. If the coupling constant between spins i and j is denoted by J_{ij} , the Hamiltonian will have the following form:

$$\mathcal{H}_{IN} = g_J \mu_B \sum_j \vec{J}_j \cdot \vec{H} - \sum_{ij} J_{ij} \vec{J}_i \cdot \vec{J}_j \quad (2.29)$$

Further, the Hamiltonian can be written in an equivalent form:

$$\mathcal{H}_{IN} = g_J \mu_B \sum_j \vec{J}_j \cdot \left(-\frac{1}{g_J \mu_B} \sum_{ij} J_{ij} \vec{J}_i + \vec{H} \right) \quad (2.30)$$

where the sum in parentheses represents the effective molecular field at the i^{th} spin site (\mathcal{H}_{MF}), given by:

$$\vec{H}_{MF} = -\frac{1}{g_J \mu_B} \sum_i J_{ij} \vec{J}_i \quad (2.31)$$

This allows for the Hamiltonian to be written in a simplified form:

$$\mathcal{H}_{IN} = g_J \mu_B \sum_i \vec{J}_i \cdot (\vec{H}_{MF} + \vec{H}) \quad (2.32)$$

The molecular field tends to align neighboring magnetic moments parallel or antiparallel to each other, depending on whether the coupling constant J_{ij} is positive (ferromagnetic case) or negative (antiferromagnetic case). In the case of a ferromagnetic order, the strength of the molecular field was postulated by Weiss [397] as part

of his molecular field model, giving:

$$H_{MF} = \lambda M \quad (2.33)$$

with λ representing the molecular field constant.

As mentioned earlier, temperature effects compete with field's spin alignment. If the temperature is raised, the magnetization will be gradually reduced by thermal fluctuations, and the magnetic order will be suppressed at the critical temperature. The Brillouin function, defined in previous section by Eqs. 2.21 – 2.23, now has an additional term:

$$M = M_0 B_J(x) \quad \text{with} \quad x = \frac{g_J \mu_B J (H + \lambda M)}{k_B T} \quad (2.34)$$

Since it is necessary to solve the above equations simultaneously, a graphical solution is shown in Fig. 2.6. A non-zero solution, $M > 0$, exists only if the slope of the line from Eq. 2.34 is smaller than the initial slope of the Brillouin function. This means that the magnetization M is finite and positive only for temperatures below the transition temperature T_C , known as the Curie temperature:

$$T_C = \frac{g_J \mu_B (J + 1) \lambda M_0}{3k_B} = \frac{n \lambda \mu_{PM}^2}{3k_B} \quad (2.35)$$

The magnetization is zero for temperatures $T \geq T_C$, and non-zero for $T < T_C$. If a small magnetic field $\mu_B H \ll k_B T$ is applied at $T \geq T_c$, then the linear expansion from Eq. 2.34 can be used to determine the magnetization M :

$$\frac{M}{M_0} \approx \frac{g_J \mu_B (J + 1)}{3k_B} \left(\frac{H + \lambda M}{T} \right) \quad (2.36)$$

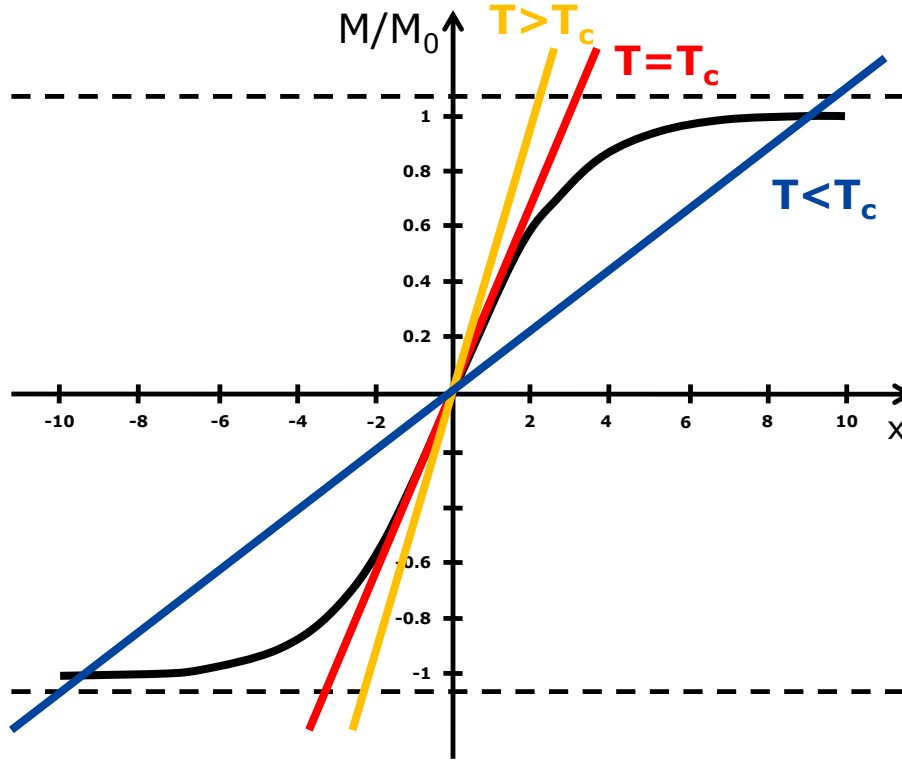


Figure 2.6: Graphical solution of Eqs. 2.34.

resulting in:

$$\frac{M}{M_0} \approx \frac{T_C}{\lambda M_0} \left(\frac{H + \lambda M}{T} \right) \quad (2.37)$$

$$\frac{M}{M_0} \left(1 - \frac{T_C}{T} \right) \approx \frac{T_C H}{\lambda M_0} \quad (2.38)$$

Therefore, the magnetic susceptibility, χ can be written as:

$$\chi \approx \frac{C}{T - T_C} \quad (2.39)$$

including the temperature-independent susceptibility contribution χ_0 , the Curie-Weiss

law becomes:

$$\chi = \chi_0 + \frac{C}{T - \theta_W} \quad (2.40)$$

In the above equation, C is the same Curie constant as that in the Curie law (Eq. 2.28), χ_0 represents a small, temperature-independent susceptibility contribution, and θ_W is the Weiss temperature. It follows from Eq. 2.40 that $1/(\chi - \chi_0)$ *vs.* T is linear, from which the values of μ_{PM} and θ_W can be extracted. In order to account for inter-atomic coupling, the magnetic field in the Eq. 2.28 must be rewritten as:

$$\frac{M}{H + \lambda M} = \frac{C}{T} \quad (2.41)$$

The susceptibility can now be expressed as:

$$\chi = \frac{M}{H} = \frac{C}{T - \lambda C} \quad (2.42)$$

Therefore $\theta_W = \lambda C$, and the sign of θ_W indicates whether or not the molecular field is acting in the same direction as the applied field. Thus, $\theta_W = 0$ indicates paramagnetic behavior, while non-zero values signal ferromagnetic ($\theta_W > 0$) or antiferromagnetic ($\theta_W < 0$) coupling, as shown in Fig. 2.7. Furthermore, the absolute value of θ_W is close to the value of the ordering temperature T_C or T_N , since according to Eqs. 2.35 and 2.27:

$$T_C = \frac{n\lambda\mu_{PM}^2}{3k_B} = C\lambda = \theta_W \quad (2.43)$$

Experimentally, the value of the ordering temperature and θ_W are sometimes found to be different as the effects of short-range order above T_C are neglected in the

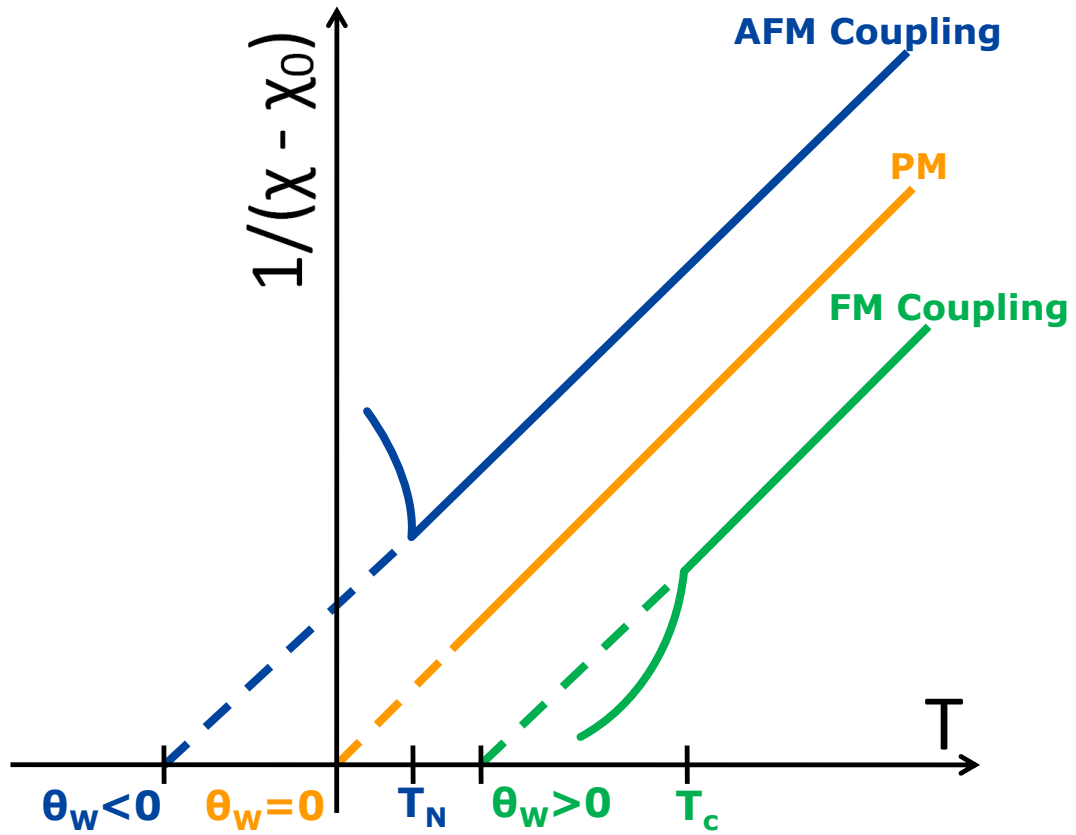


Figure 2.7: Temperature dependence of $1/(\chi - \chi_0)$ for the paramagnetic (orange), antiferromagnetic (blue), and ferromagnetic (green) cases.

simple molecular field treatment [138].

2.1.4 Magnetism of Conduction Electrons

In previous sections, susceptibility contributions of both interacting and non-interacting *localized* electrons have been discussed. For local moment magnets, the magnetic moments are fixed on lattice sites and the magnitude of the overall magnetization can be predicted according to Hund's rule. The driving interaction is the inter-atomic exchange, therefore the coupling between the neighboring atoms is strong [258]. However, magnetism can also arise from conduction or valence electrons (also called *itinerant* due to delocalized character) that move nearly free inside the material. The driv-

ing interaction in this case is the intra-atomic exchange and the size of the magnetic moment can no longer be predicted by the Hund's rules. The Landau diamagnetism, caused by conduction electrons, is rarely of interest as its magnitude is much smaller than that of the Pauli paramagnetism, which will be discussed in this section. Ferro- and antiferromagnetism can arise under certain conditions, as will be presented in Section 2.1.5.

Since motion of conduction electrons is not restrained, it is suitable to treat them as a free electron gas. The energy of an electron when no external magnetic field is applied is given by:

$$E = \frac{\hbar^2 k^2}{2m} \quad (2.44)$$

Each k -state in a metal can be doubly occupied because of the two possible spin values (up and down, Fig. 2.8(a)). An applied magnetic field will either raise (spin-down) or lower (spin-up) the energy of an electron by $\mu_B H$:

$$E_{\downarrow\uparrow} = \frac{\hbar^2 k^2}{2m} \pm \mu_B H \quad (2.45)$$

The increase and decrease in the energies of the spin-down and spin-up electrons will result in different Fermi energy E_F values in the two sub-bands, Fig. 2.8(b). In order to achieve a physical state with the same Fermi energy E_F and minimize the overall energy of the system, electrons from the "down" sub-band flip to the "up" states until the Fermi energies in the two sub-bands match, as shown in Fig. 2.8(b). Because the magnetic moment of an electron is equal to $1\mu_B$, the imbalance of up

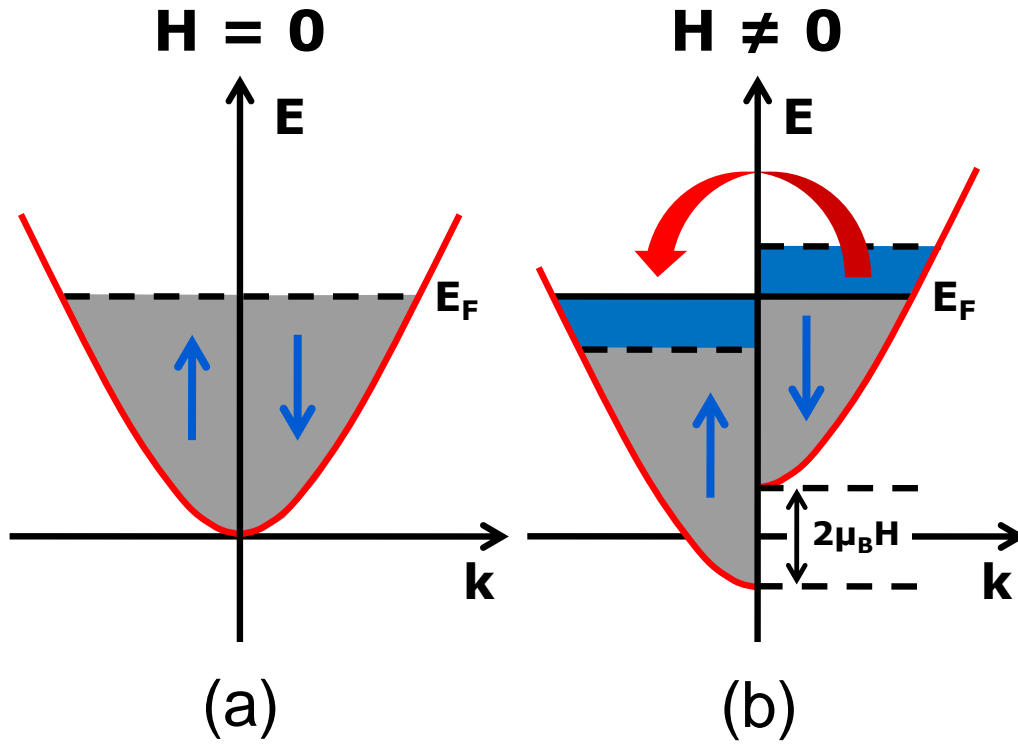


Figure 2.8: (a) Without external field, the number of electrons in both sub-bands is the same. (b) After a field has been applied, the Fermi energy shifts, resulting in Pauli paramagnetism.

and down electrons will result in a net magnetization:

$$M = -(n_{\uparrow} - n_{\downarrow})\mu_B \quad (2.46)$$

The number of up and down spins (n_{\uparrow} and n_{\downarrow}) can be written in terms of the density of states $g(E)$:

$$n_{\downarrow} = \int g_{\downarrow}(E)f(E)dE \quad (2.47)$$

$$n_{\uparrow} = \int g_{\uparrow}(E) f(E) dE \quad (2.48)$$

where $f(E)$ is the Fermi-Dirac distribution given by:

$$f(E) = \frac{1}{e^{(E-\mu)/kT} + 1} \quad (2.49)$$

A Taylor expansion can be applied for the density of states if the magnetic field is small ($\mu_B H \ll E_F$), and the above equation becomes:

$$g_{\uparrow}(E) \approx \frac{1}{2}g(E - \mu_B H) \approx \frac{1}{2}\left(g(E) - \mu_B H g'(E)\right) \quad (2.50)$$

$$g_{\downarrow}(E) \approx \frac{1}{2}g(E + \mu_B H) \approx \frac{1}{2}\left(g(E) + \mu_B H g'(E)\right) \quad (2.51)$$

Therefore:

$$n_{\uparrow} = \frac{1}{2} \int g(E) f(E) dE - \frac{1}{2} \mu_B H \int g'(E) f(E) dE \quad (2.52)$$

$$n_{\downarrow} = \frac{1}{2} \int g(E) f(E) dE + \frac{1}{2} \mu_B H \int g'(E) f(E) dE \quad (2.53)$$

Thus, from Eq. 2.46, the magnetization can be found as:

$$M = \mu_B^2 H \int g'(E) f(E) dE = \mu_B^2 H \int g(E) f'(E) dE \quad (2.54)$$

For the low temperature limit, $f'(E) \approx \delta(E - E_F)$:

$$M = \mu_B^2 H \int g(E) \delta(E - E_F) dE = \mu_B^2 H g(E_F) \quad (2.55)$$

The resulting Pauli susceptibility χ_{Pauli} is positive and does not depend on temperature:

$$\chi_{Pauli} = \mu_B^2 g(E_F) \quad (2.56)$$

Which, using the density of states for the free electron case ($g(E_F) = mk_F/\hbar^2\pi^2$), gives [27]:

$$\chi_{Pauli} = \left(\frac{e^2}{2\pi\hbar c} \right)^2 (a_0 k_F) = \left(\frac{2.59}{r_s/a_0} \right) 10^{-6} \quad (2.57)$$

where a_0 and r_s are Bohr and elemental radii, respectively. Significant discrepancies between measured and theoretical values, listed in Table 2.1, are the result of neglected electron-electron interactions [27]. Both theoretical and experimental values of χ_{Pauli} reveal that while Pauli paramagnetism is the dominant temperature-independent susceptibility contribution, it has a rather weak effect, as compared to the local moment magnetism. This can be explained by the fact that, while for the localized picture at least one electron per magnetic atoms contributes to the overall magnetization, in the itinerant case only electrons close to the Fermi surface play a role [42]. Therefore, features in resistivity and specific heat (Figs. 2.14(c, d) and 2.15(d)), corresponding to the transition from ordered to the disordered state are much weaker for itinerant magnets, as compared with the local ones.

Table 2.1: Comparison of calculated and measured Pauli susceptibility values χ_{Pauli} [27].

Metal	r_s/a_0	$10^6 \chi_{Pauli}$ (from Eq. 2.57)	$10^6 \chi_{Pauli}$ (measured)
Li	3.25	0.80	2.0 [325]
Na	3.93	0.66	1.1 [326]
K	4.86	0.53	0.8 [324]
Rb	5.20	0.50	0.8 [185]
Cs	5.62	0.46	0.8 [185]

2.1.5 Itinerant Ferromagnetism: Stoner Criterion

Itinerant ferromagnetism is often referred to as band ferromagnetism because it is caused by spontaneously split electron bands: unpaired electrons are delocalized which broadens the original energy levels. This broadening W depends on the inter-atomic separation r :

$$W \propto r^{-5} \quad (2.58)$$

Under the influence of an applied magnetic field, a portion of electrons is transferred from the spin-down to the spin-up band, the kinetic energy of the system $E_{K.E.}$ will then increase by:

$$\Delta E_{K.E.} = \frac{1}{2} g(E_F) (\delta E)^2 \quad (2.59)$$

As previously stated, the overall magnetization will be given by:

$$M = -\mu_B(n_\uparrow - n_\downarrow) = \mu_B \left(\frac{1}{2} \left[n + g(E_F)(\delta E) \right] - \frac{1}{2} \left[n - g(E_F)(\delta E) \right] \right) \quad (2.60)$$

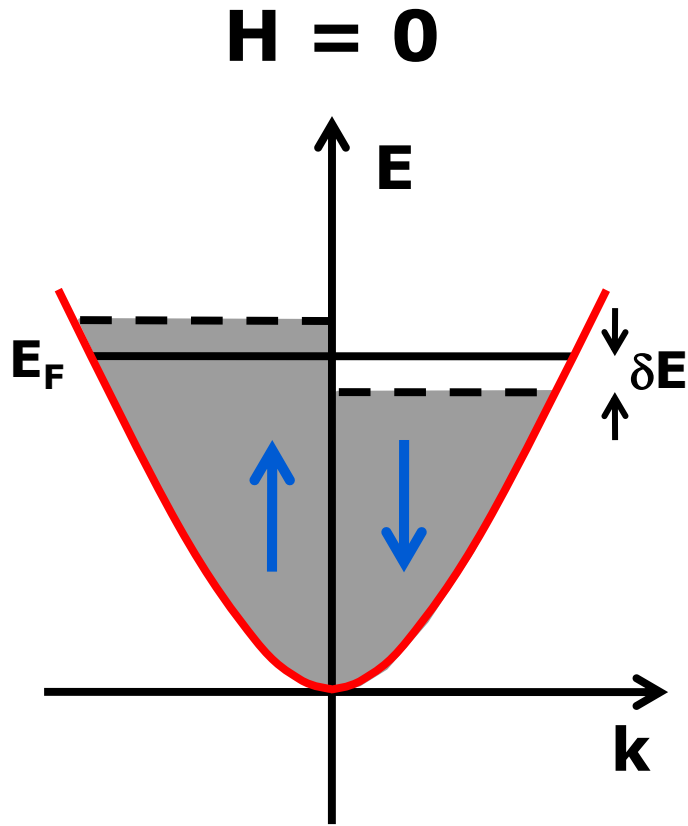


Figure 2.9: The density of spin-up and spin-down electrons exhibit a spontaneous spin splitting without any external magnetic field.

$$M = \mu_B \left(\frac{1}{2}n + \frac{1}{2}g(E_F)(\delta E) - \frac{1}{2}n + \frac{1}{2}g(E_F)(\delta E) \right) \quad (2.61)$$

$$M = \mu_B g(E_F)(\delta E) \quad (2.62)$$

The gain in the potential energy $E_{P.E.}$ can be expressed as:

$$\Delta E_{P.E.} = -\frac{1}{2}\mu_B^2\lambda(n_\uparrow - n_\downarrow)^2 \quad (2.63)$$

where λ is the molecular field constant as stated earlier.

For interacting electrons, the effective exchange energy per pair of $3d$ electrons is known as U_{eff} and is the measure of the Coulomb energy:

$$U_{eff} = \mu_B^2\lambda \quad (2.64)$$

Thus from Eq. (55 – 57) it follows that:

$$\Delta E_{P.E.} = -\frac{1}{2}U_{eff}\left[g(E_F)(\delta E)\right]^2 \quad (2.65)$$

Therefore, the total change in the energy that arises from the electron transfer between the up and down sub-bands is:

$$\Delta E = \Delta E_{K.E.} + \Delta E_{P.E.} = \frac{1}{2}g(E_F)(\delta E)^2(1 - U_{eff}g(E_F)) \quad (2.66)$$

If $1 - U_{eff}g(E_F) > 0$, then the fraction of electrons that move from the spin-down to spin-up band is zero and the system is non-magnetic. On the other hand if $1 - U_{eff}g(E_F) < 0$, then $\Delta E < 0$ and the $3d$ band will be split, leading to ferromagnetism. Therefore, the following condition, known as the Stoner criterion, is obtained:

$$U_{eff}g(E_F) \geq 1 \quad (2.67)$$

For spontaneous ferromagnetism, the spin-up and spin-down bands will be split by an energy Δ if the Coulomb effects are strong (large U_{eff}) and the density of states at the Fermi level $g(E_F)$ is large. The density of states of the s - and p -electron bands is much smaller than that of the d band, favoring spontaneous magnetization according to the Stoner criterion in the d band materials.

If the Stoner criterion is met, the susceptibility will exceed the value expected based on the Hund's rules (Section 2.1.1). A phenomenon known as the Stoner enhancement is caused by strong Coulomb interactions between the electrons. The energy shift described above will produce magnetization, thus in an applied magnetic field H the total change in energy is given by:

$$\Delta E = \frac{1}{2}g(E_F)(\delta E)^2 \left[1 - U_{eff}g(E_F)\right] - MH = \frac{M^2}{2\mu_B^2g(E_F)} \left[1 - U_{eff}g(E_F)\right] - MH \quad (2.68)$$

The equilibrium condition is given by:

$$\frac{d\Delta E}{dM} = \frac{M}{\mu_B^2g(E_F)} \left[1 - U_{eff}g(E_F)\right] - H = 0 \quad (2.69)$$

and therefore the resulting susceptibility is:

$$\chi = \frac{M}{H} \approx \frac{\mu_B^2g(E_F)}{1 - U_{eff}g(E_F)} = \frac{\chi_0}{1 - U_{eff}g(E_F)} = S\chi_0 \quad (2.70)$$

where $S = \frac{1}{1 - U_{eff}g(E_F)}$ is known as the Stoner enhancement factor.

Therefore, the susceptibility is enhanced compared to that of systems without interactions between the band electrons. In materials that are on the verge of ferromagnetism (*i. e.* $\chi(T = 0) = \inf$, the Fermi level is located immediately above

a sharp peak in the density of states, and the system can be driven into magnetic order with doping [258]), the Stoner enhancement factor will significantly increase the magnetic susceptibility. This will not, however, cause spontaneous ferromagnetism. Examples of these systems are Pd and Pt metals that have susceptibility roughly one order of magnitude greater than that of Zr metal [42].

2.1.6 Itinerant Antiferromagnetism

An electron traveling through an antiferromagnetic crystal experiences exchange-correlation forces that point in opposite directions on two sublattices, and that polarize each sublattice in such a way that on one sublattice the magnetization is positive, and on the other it is negative [214]. Using the approach developed for the ferromagnetic case, the antiferromagnetic material should be thought of as being composed of two sublattices A and B , whose lattice points are denoted by j and l , respectively [261]:

$$M_A = \frac{1}{2} \sum_j (n_{j\downarrow} - n_{j\uparrow}) \quad (2.71)$$

$$M_B = \frac{1}{2} \sum_l (n_{l\downarrow} - n_{l\uparrow}) \quad (2.72)$$

Staggered magnetization M_s can then be found as:

$$M_s = M_A - M_B \quad (2.73)$$

This, in turn, can be used to calculate the free energy within the Hartree-Fock

approximation [261]:

$$F_{HF}(M_s, T) = F_0(M_s, T) - IM_s^2 \quad (2.74)$$

The above expression can be expanded as:

$$F_{HF}(M_s) = \left(\frac{1}{2\chi_s^0} - I \right) M_s^2 + \dots \quad (2.75)$$

yielding the condition for the appearance of antiferromagnetism in a localized moment scenario:

$$2I\chi_s^0 > 1 \quad \text{and} \quad 2I\chi_s^0(T_N) = 1 \quad (2.76)$$

A similar approach can be applied for the itinerant case, where a spin density wave is formed. Possible existence of such an antiferromagnetic ground state in an itinerant electron system was first proposed by Slater [335], and then generalized by Overhauser [293], who used it in order to explain magnetic properties of Cr. The free energy shown in Eq. 2.75 will now depend on the amplitude of the spin density wave with the wave vector Q [261]. This results in a modified condition for the appearance of an antiferromagnetic ground state:

$$2I\chi_0(Q) > 1 \quad (2.77)$$

From the above equation it is obvious that the criterion for instability of the paramagnetic ground state is more complex than the Stoner criterion, evoked for ferromagnetic metals (Eq. 2.67). The dependence of susceptibility $\chi(Q)$ on the wave vector Q indicates that the criterion can be satisfied even if I is small, provided Fermi

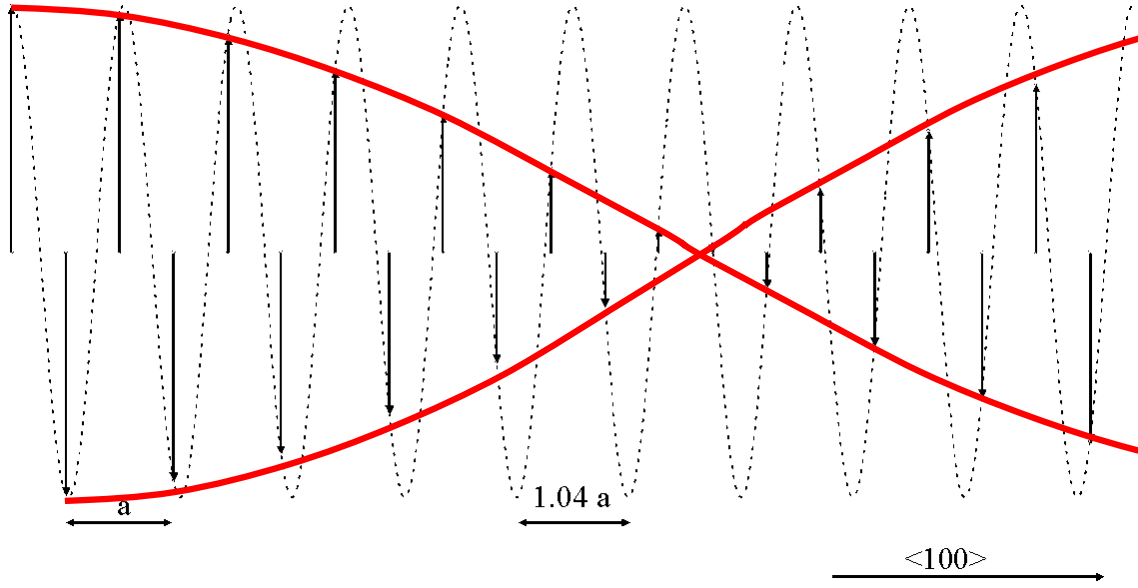


Figure 2.10: Schematic incommensurate spin density wave in bcc Cr. The arrows indicate the amplitude of the spin density wave at the lattice sites [404].

surface is nested [261] and $Q \approx 2k_f$ (where k_f is the diameter of the Fermi sphere) [404]. Various types of spin density waves have been reported experimentally [108], with examples including commensurate and incommensurate in both two and three dimensions [30]. In Cr, a static incommensurate spin density wave is formed, showing a sinusoidal variation with position (Fig. 2.10) [404].

Cr metal remains the archetypical example of a spin density wave in a metal. Interestingly enough, the 3d character of Cr has been shown to be of fundamental importance to its being magnetic, given that both Mo and W whose Fermi surfaces are very similar to that of Cr are non-magnetic [108]. The temperature dependence of various physical properties in the neighborhood of the Néel temperature ($T_N = 311$ K [108]) is shown in Fig. 2.11. The discontinuity signals transition from ordered into disordered state in a first order manner.

Cr has also of high interest since it is one of the very few non-Kondo systems that can be driven through an antiferromagnetic quantum critical point [227]. Quan-

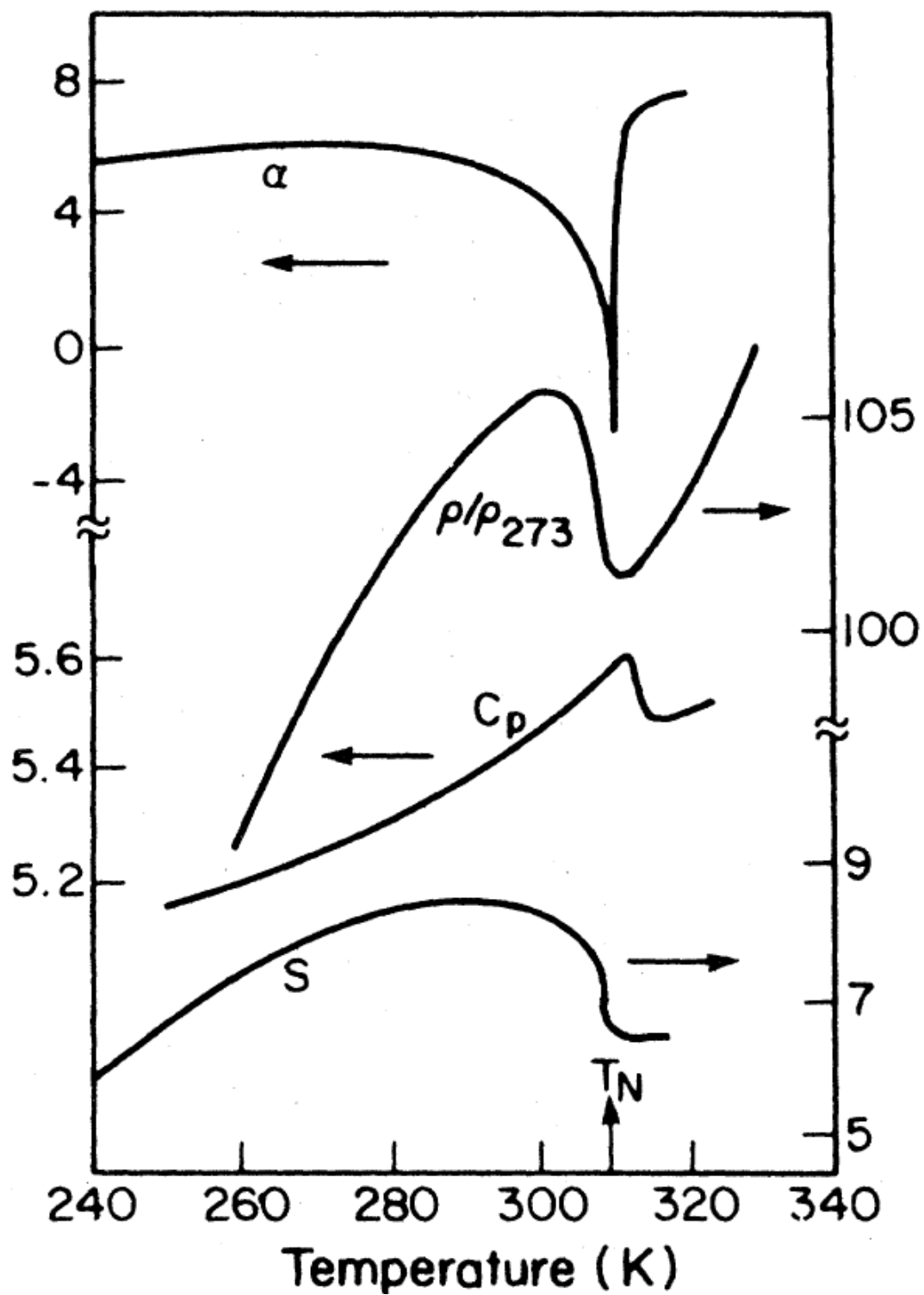


Figure 2.11: Physical properties near T_N in Cr: linear thermal expansion (α), resistivity ρ , specific heat C_p , and thermoelectric power S as a function of temperature [108].

tum critical points were achieved in Cr with both pressure [223] and doping [411] with scaling properties and critical exponents in both cases consistent with a 3D antiferromagnetic quantum critical point [227]. This type of quantitative analysis of quantum critical points in Cr has been invaluable for testing the self-consistent renormalization theory in itinerant antiferromagnets [227]. However, many open questions still remain, calling for additional systems.

2.1.7 Itinerant *vs.* Local Magnetism

As mentioned earlier, local moment magnetism arises from magnetic ions fixed at lattice positions. The magnitude of the individual spins remains the same for the whole temperature range, while the competition between temperature fluctuations and inter-atomic coupling results in mis-alignment of magnetic moments above $T = 0$ K (Fig. 2.12(a)). As $T \rightarrow 0$ K, an increasing number of spins becomes co-aligned, resulting in the maximum overall magnetization. This is in stark contrast to the itinerant case, for which the size of magnetic moments grows as a function of temperature (Fig. 2.12), yielding maximum magnetic moment at $T = 0$ K. For that reason, the ratio of the number of magnetic moment carriers below and above the transition can be used to differentiate between itinerant and local magnets. The paramagnetic moment μ_{PM} and the saturated moment estimates μ_{sat} can be used to determine the magnetic carrier per atom q_C (since it is derived from the Curie constant) and q_{sat} , respectively [309]. The quantity q_C describes the behavior of the system for temperatures above the ordering temperature, and is determined from the paramagnetic moment μ_{PM} [309], using:

$$q_C(q_C + 1) = \frac{(\mu_{PM})^2}{4} \quad (2.78)$$

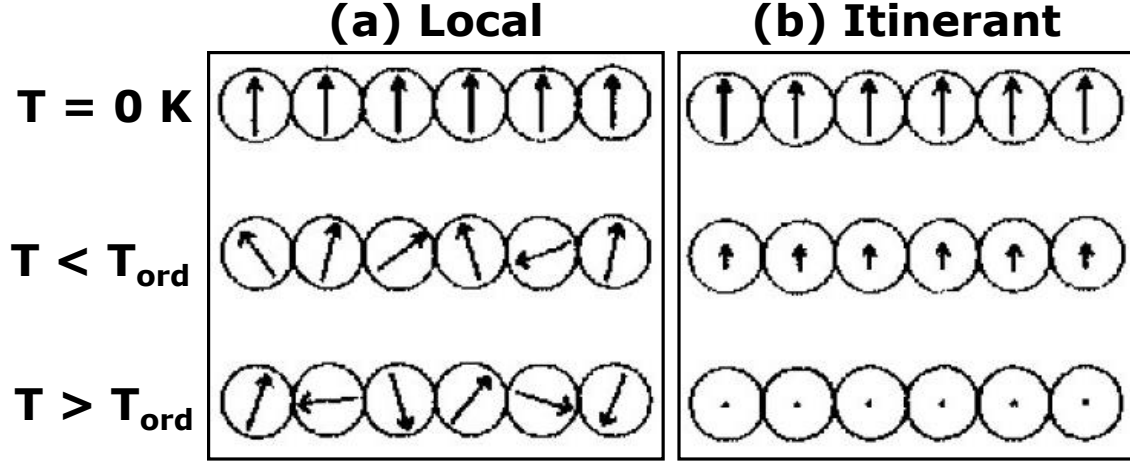


Figure 2.12: The evolution of magnitude of magnetic moment with temperature for the (a) local and (b) itinerant scenarios in zero field. Reproduced from Ref. [261].

Similarly, q_{sat} is obtained from the saturation magnetization at temperatures below the transition temperature:

$$q_{\text{sat}} = \frac{\mu_{\text{sat}}^{\text{exp}}}{2} \quad (2.79)$$

The ratio of q_C and q_{sat} is known as the Rhodes-Wohlfarth ratio: if the number of carriers below the transition temperature (q_{sat}) is the same as the one above the transition temperature (q_C) the ratio is:

$$\frac{q_C}{q_{\text{sat}}} \approx 1 \quad (2.80)$$

indicating a local-moment system. The other limiting case is that when:

$$\frac{q_C}{q_{\text{sat}}} > 1 \quad (2.81)$$

observed in delocalized or itinerant magnets [309]. The values of the Rhodes-Wohlfarth ratio for local (triangles) and itinerant (circles) moment compounds, together with

those for ZrZn_2 (green square) and Sc_3In (blue square), are shown in Fig. 2.13. While the the Rhodes-Wohlfarth ratio of magnetic carries [309] is generally used to differentiate between local and itinerant mechanisms in ferromagnetic materials, similar analysis has been applied to antiferromagnetic systems [31, 288, 301].

2.1.8 Itinerant Magnets without Magnetic Elements: Sc_3In and ZrZn_2

Heisenberg's theory for localized electrons [156] has been used to explain many phenomena associated with local-moment magnetism, including the linearity of the inverse susceptibility, as predicted by the Curie-Weiss law [261] in accordance with

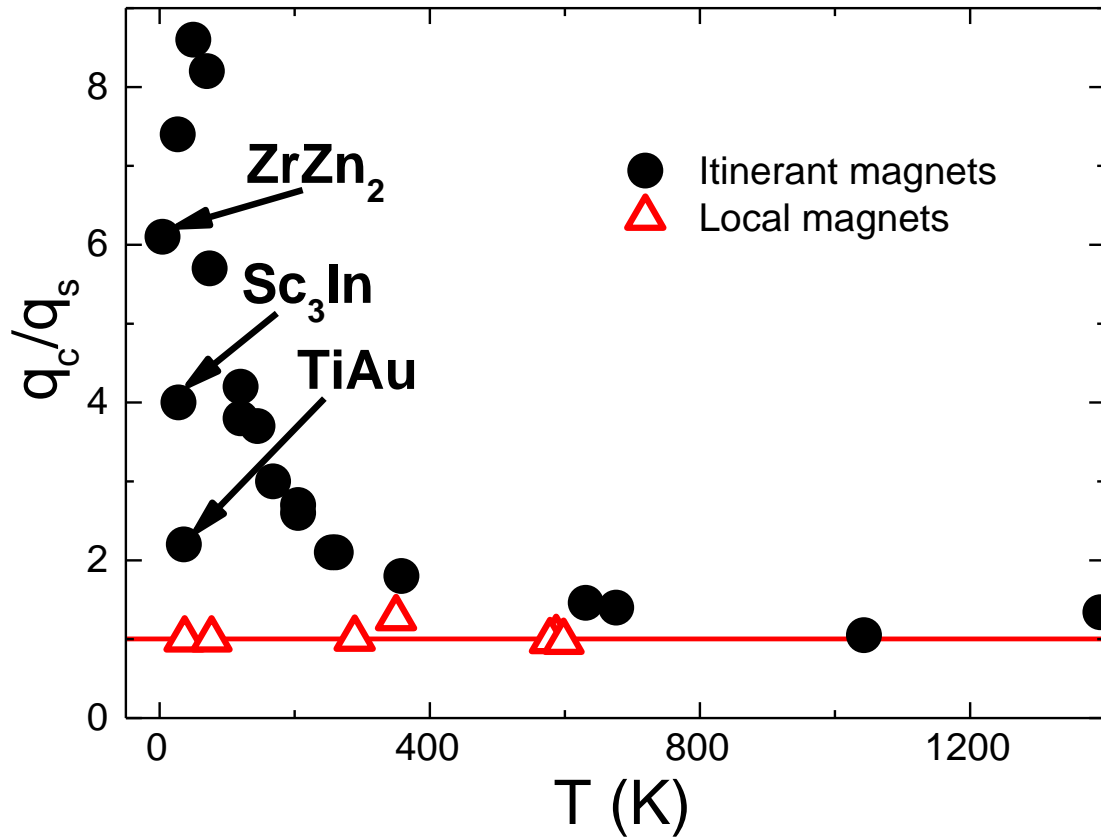


Figure 2.13: Rhodes-Wohlfarth ratio for local magnets (open symbols) and itinerant magnets (full symbols), reproduced from Ref. [261].

the Langevin and Weiss theory [220, 221, 397]. In metals, a separate contribution to magnetism is due to the conduction electrons, yielding non-integer values of magnetic moment per atom in Bohr magnetons even in simple elemental magnets such as Fe, Ni, and Co. The Stoner model [350] (Section 2.1.5) qualitatively accounts for this discrepancy in metals with large interaction constant I and high density of states at the Fermi level $g(E_F)$, but falls short in correctly predicting the Curie temperature and the Curie-Weiss-*like* magnetic susceptibility.

When a new family of weakly ferromagnetic materials was discovered, application of both Stoner and Heisenberg theories was not successful in estimating the magnitude of the paramagnetic moment [263]. Moreover, Curie-Weiss-*like* susceptibility in ZrZn_2 [245] (Fig. 2.14(a)) and Sc_3In [246] (Fig. 2.15(b)), previously thought to indicate presence of localized magnetic moments [365], was puzzling since both compounds are composed of non-magnetic elements. This indicated that a different mechanism is responsible for the Curie-Weiss-*like* behavior in weakly ferromagnetic materials [103].

Consequently, it has been determined that the effect of spin fluctuations is rather important for the thermodynamic properties of itinerant ferromagnets, and thus needs to be accounted for theoretically. The solution came with the theory of self-consistent renormalization theory of spin fluctuations [264, 265], unifying the local and itinerant pictures of magnetism and postulating a new cause for the Curie-Weiss-*like* susceptibility as the interactions of the spatially extended modes of spin fluctuations [261]. As for the itinerant antiferromagnets, a spin-density-wave model, based on the Hartree-Fock approximation, has been initially proposed as the underlying principle for the observed magnetic and physical properties [293]. However, when the importance of spin-fluctuations was realized for the case of ferromagnetic coupling [264, 265], similar considerations were investigated for antiferromagnets [151].

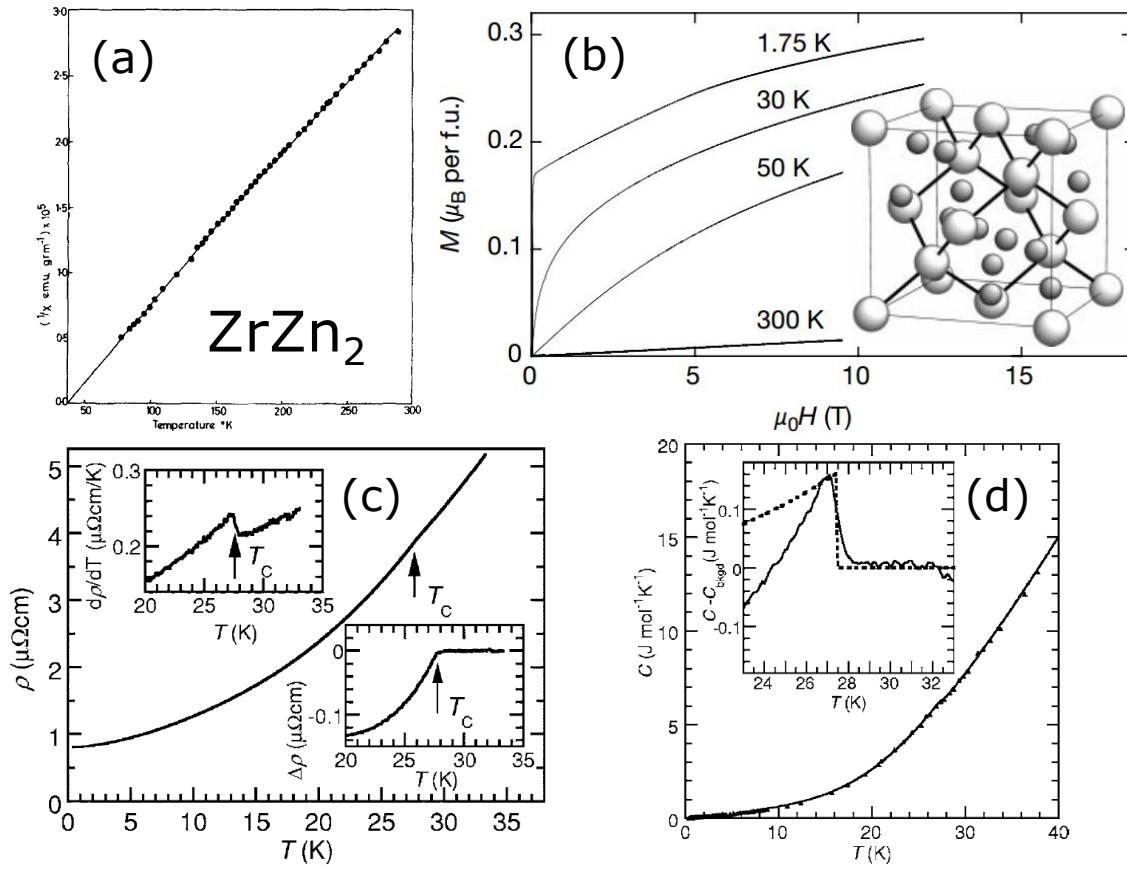


Figure 2.14: Physical properties of ZrZn_2 : (a) inverse susceptibility as a function of temperature [44], (b) magnetization as a function of field [299], temperature-dependent (c) resistivity and (d) specific heat [412].

While the self-consistent renormalization theory has been successful in explaining the majority of the phenomena seen in experiments, it includes a number of approximations [289], some of which are not easily justifiable [266, 289, 365]. While additional theoretical attempts have been put forth [214, 289], a systematic, mathematically rigorous theory that quantitatively explains all compounds that lie between the localized and itinerant limits is still lacking. This can be aided by discovery and characterization of new itinerant systems.

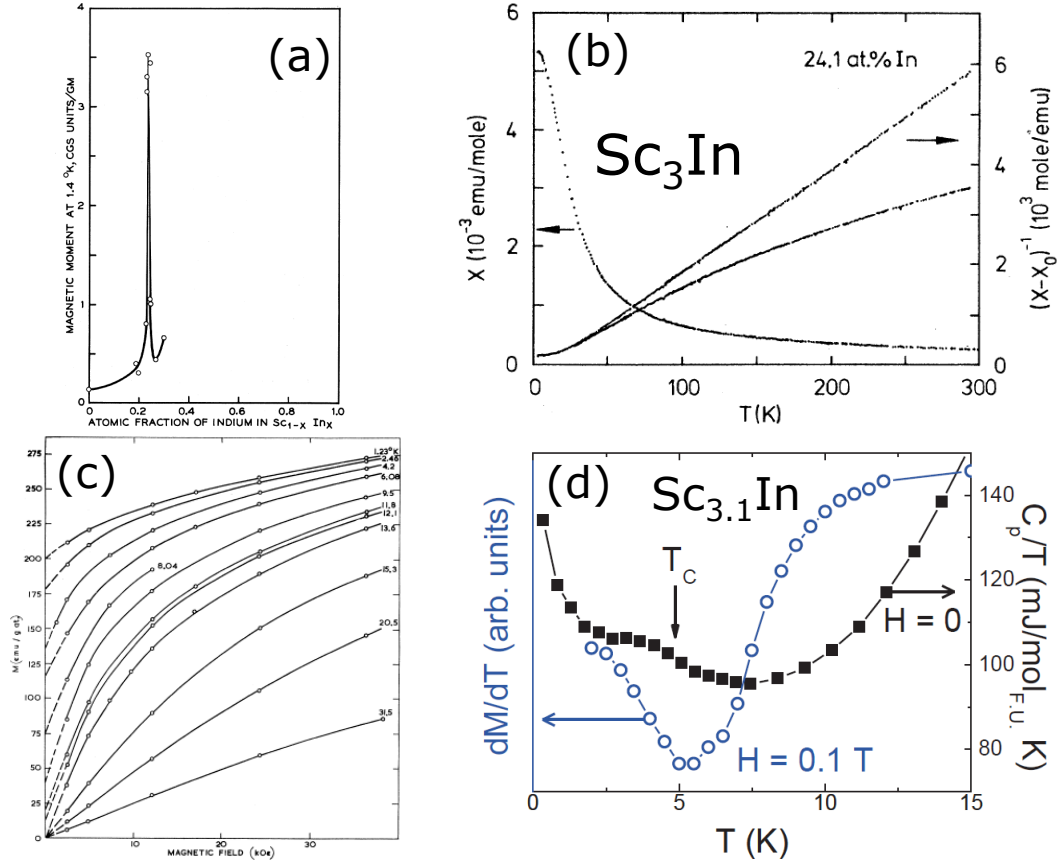


Figure 2.15: Physical properties of Sc_3In : (a) Variation of the size of the magnetic moment as a function of Sc:In ratio [246], (b) susceptibility and inverse susceptibility as a function of temperature [140], (c) magnetization as a function of field [124], (d) temperature-dependent magnetization derivative and specific heat scaled by temperature [355].

2.1.9 Search for New Itinerant Magnets

The search for new itinerant magnets is complicated by the drastic differences in properties of the known systems, which exhibit heavy fermion behavior [194, 306, 316], co-existence of superconductivity and magnetism [21, 312, 320, 417], metamagnetic transitions [5, 270, 385], chiral order [71, 148, 211, 380], multisublattice magnetism [59, 106], Fermi-liquid [64] as well as spin- and cluster-glass [29, 94, 212] behaviors. Furthermore, only two itinerant magnets do not contain magnetic elements – ZrZn_2 [245] and Sc_3In [246]. Quite surprisingly, while both ZrZn_2 and Sc_3In exhibit Curie-Weiss-like ferromagnetism [44, 124], they differ drastically in their dimensionality [176, 213], crit-

ical scaling behavior [341,355], and susceptibility to perturbations [25,140,341,355]. This will be described in more detail in Chapters 5 and 4.

Given these discrepancies between seemingly analogues systems, additional itinerant magnets are needed to develop a comprehensive understanding of itinerant phenomena. Compounds without local moment are particularly convenient for studying itinerant phenomena as they lack complexity associated with the interplay between local and itinerant moments. Additionally, ordering temperatures and size of magnetic moments are typically small, making these systems good candidates for a quantum phase transition.

Unfortunately, a theoretical basis for a systematic way of finding said compounds does not exist. As mentioned earlier, spontaneous magnetization according to

PERIODIC TABLE OF THE ELEMENTS

<http://www.kjgf.spd.it/periodic/en/>

The periodic table is organized into groups (I to VIII) and periods (1 to 7). It includes element symbols, names, and relative atomic masses. A legend identifies element types: Metal, Semimetal, Nonmetal, Alkali metal, Alkaline earth metal, Transition metals, Lanthanide, Actinide, Chalcogens element, Halogens element, and Noble gas. A box specifies standard states: Ne - gas, Fe - solid, Gs - liquid, and Tc - synthetic.

LANTHANIDE

57 138.91	58 140.12	59 140.91	60 144.24	61 (145)	62 150.36	63 151.96	64 157.25	65 158.93	66 162.50	67 164.93	68 167.26	69 168.93	70 173.04	71 174.97
La	Ce	Pr	Nd	Pm	Sm	Eu	Gd	Tb	Dy	Ho	Er	Tm	Yb	Lu
LANTHANUM	CERIU	PRASEODYMIUM	NEODYMIUM	PROMETHIUM	SAMARIUM	EUROPIUM	GADOLINIUM	TERBIUM	DYSPROSIUM	HOLMIUM	ERBIUM	THULIUM	YTTERIUM	LUTETIUM

ACTINIDE

89 (227)	90 232.04	91 231.04	92 238.03	93 (237)	94 (244)	95 (243)	96 (247)	97 (247)	98 (251)	99 (252)	100 (257)	101 (258)	102 (259)	103 (262)
Ac	Th	Pa	U	Np	Pu	Am	Cm	Bk	Cf	Es	Fm	Md	No	Lr
ACTINIUM	THORIUM	PROCTACTINIUM	URANIUM	NEPTUNIUM	PLUTONIUM	AMERICIUM	CURIUM	BERKELIUM	CALIFORNIUM	EINSTEINIUM	FERMIUM	Mendelevium	NOBELIUM	LAWRENCIUM

Editor: Ashya Vardhan (vardhan@rediffmail.com)

Figure 2.16: In Sc_3In and ZrZn_2 , Sc and Zr are located across from Zn and In.

the Stoner criterion is more likely to occur in d band metals (Section 2.1.5). Therefore, non-magnetic transition metals were surveyed. Additionally, existing itinerant magnets composed of non-magnetic elements (Sc_3In and ZrZn_2) are located across each other on the periodic table (Fig. 2.16), which can possibly lead to enhanced correlations I , necessary for the fulfillment of the Stoner criterion (Section 2.1.5). In general, the bigger the difference in electronegativity of two elements, the stronger the electron-electron correlation is [120]. Consequently, binaries of transition metal elements located across from each other in the periodic table were examined. For these, band structure calculations [88,89,328] were analyzed. According to the Stoner criterion (Section 2.1.5), high density of states at the Fermi level is desired. Additionally, a peak in the density of states near the Fermi surface is indicative of instability towards a magnetic ground state and has been suggested to lead to magnetism [266]. From these considerations, analysis of band structure calculations for binary intermetallic compounds is likely to yield new itinerant magnets. This search was successful in finding the *first itinerant antiferromagnet*, composed of non-magnetic constituents – TiAu – properties of which will be described in Chapter 6.

2.2 Phase Transitions

2.2.1 Classical *vs.* Quantum Phase Transitions

Paul Ehrenfest classified phase transitions according to the behavior of the free energy derivatives and the energy involved in the process:

1. First-order phase transitions: the first derivative is discontinuous, but the second one is continuous. Solid to liquid and liquid to gas transitions belong to this class, exhibiting discontinuous change in the density. These transitions include latent heat transfer – energy is either released or absorbed during the phase transition.
2. Second-order phase transitions: the first derivative is continuous but the second one is discontinuous. Examples include ferromagnetic phase transition during which the first derivative of free energy – magnetization varies continuously, while the second derivative – susceptibility – changes abruptly. Other examples include superconductor and superfluid transitions. A phenomenological theory of this type of transitions was given by Lev Landau.
3. Infinite-order phase transition: they are continuous, but there is no symmetry breaking. Some quantum phase transitions belong to this class.

The defining feature of quantum phase transitions is the fact that they occur at $T = 0$ K. Classical phase transitions – also referred to as the thermal phase transitions – are driven by the competition between the energy and the entropy of a given system. On the other hand, quantum phase transitions occur at absolute zero and classically the lack of entropy should imply no phase transition. Although thermal fluctuations cease to exist at absolute zero, quantum fluctuations come into play. The origin of quantum phase transitions is Heisenberg’s uncertainty principle –

if the atoms are placed precisely at the sites of a perfect crystalline lattice, then the momenta of the atoms are uncertain.

Since quantum phase transitions only occur at $T = 0$ K, the variation of physical parameter other than temperature will induce the transition. There are three quantities that can be varied in order to induce a quantum phase transition:

1. Magnetic field
2. Pressure
3. Chemical substitution – doping

The existence of quantum critical points – places where the quantum phase transition takes place – is hard to predict but could be observed based on physical properties of the system. Even though quantum phase transitions cannot be measured directly since the absolute zero is not achievable, the physical properties of materials at finite temperatures are determined by the properties for the system at absolute zero, and thus the presence of a quantum critical point can be inferred.

2.2.2 Critical Exponents and Critical Scaling

While Curie (Eq. 2.28) and Curie-Weiss (Eq. 2.40) Laws describe how susceptibility changes with temperature, behavior of other physical properties as a function of temperature and field is also of interest. Since changing temperature often results in a phase transition (from ferro- to paramagnetic state, for example),

Landau theory of phase transitions [390] is a mean-field theory in which an identical exchange field is experienced by all spins. The free energy for a ferromagnet

can be written as a power series in M :

$$F(M) = F_0 + a(T)M^2 + bM^4 + \dots \quad (2.82)$$

where F_0 and b are constants and $a(T) = a_0(T - T_c)$ is a function of temperature. In order to find the ground state energy it is necessary to minimize the free energy:

$$\frac{\partial F}{\partial M} = 0 \rightarrow 2M(a_0(T - T_c) + 2bM^2) = 0 \quad (2.83)$$

Therefore, the non-zero solution of the above equation is given by:

$$M = \pm \sqrt{\frac{a_0(T_c - T)}{2b}} \quad (2.84)$$

Eg. 1.66 shows that the magnetization below the phase transition behaves as $(T_c - T)^{1/2}$. The mean-field theory is the simplest type of theory that describes phase transitions, without taking into account correlations and fluctuations that become particularly important near the critical temperature above which the magnetic ordering vanishes. Therefore, in real systems, the magnetization behaves like $(T_c - T)^\beta$, where the exponent β is not necessarily equal to $1/2$. This exponent is one of the critical exponents which give important information about the nature of the phase transition. Other critical exponents characterize the temperature- and the field-dependence of the magnetization M , field H and reduced temperature:

$$t = \frac{T - T_c}{T_c} \quad (2.85)$$

$$M \propto t^\beta \text{ for } t < 0 \text{ } (\theta > 0) \quad (2.86)$$

$$M \propto H^{1/\delta} \text{ for } t = 0 \quad (2.87)$$

$$\chi \propto t^{-\gamma} \text{ for } t > 0 \ (\theta < 0) \quad (2.88)$$

where β , γ and δ are the critical exponents, whose values depend on the specific properties of a given system and satisfy following relation:

$$\delta - 1 = \frac{\gamma}{\beta} \quad (2.89)$$

The mean-field theory cannot provide an accurate description of systems with less than four dimensions, thus it is necessary to use the Ising or the Heisenberg models [42]. The list of the possible models is rather small due to the fact that the critical exponents are independent of the type of the phase transition, *i.e.* same for ferromagnetic-paramagnetic, liquid-gas or a quantum phase transition. For a continuous phase transition, the critical exponents must depend only on:

1. The dimensionality of the system, d .
2. The dimensionality of the order parameter, D .
3. Whether the forces are short- or long-ranged.

The above assumptions apply only to static critical exponents, *i.e.* critical exponents that do not change with time. By comparison, the dynamical critical exponents characterize time-dependent properties. It is possible to determine critical exponents for a few particular cases-set of different values of D and d for both short- and long-ranged forces. For some of the models, solutions already exist [42]:

1. Systems with $d = 1$ do not exhibit continuous phase transitions.

2. For systems with $d \geq 4$, the mean-field solution should be applied.
3. Most of the cases with long-ranged interactions can be solved with a mean-free solution.
4. The case with $d = 2$ and $D = 1$ is known as the 2D Ising model.
5. The case with $D = \infty$ for any d is known as the spherical model.

The values of critical exponents for those and some other cases are listed in Table 2.2.

Table 2.2: Critical exponents for various models [42].

Model	Mean - field	Ising (2D)	Ising (3D)	Heisenberg
D	any	1	1	3
d	any	2	3	3
β	1/2	1/8	0.326	0.367
γ	1	7/4	1.2378(6)	1.388(3)
δ	3	15	4.78	4.78

The most common real case corresponds to $d = 3$ with short-ranged interactions which has not been solved exactly. For this and other cases that cannot be solved directly, other methods should be used [42].

As mentioned previously, the self consistent renormalization theory took into account coupling among the spin fluctuation modes in a self-consistent manner [261]. This theory resolved the difficulties of the Stoner theory and predicted quantum critical exponents [268]. A summary of quantum critical exponents for both antiferromagnetic and ferromagnetic 2D and 3D systems is given in Table 2.3 and 2.4.

Table 2.3: Critical exponents for itinerant systems at the critical point [268].

	FM ($Q = 0$)		AFM ($Q \neq 0$)	
	3D	2D	3D	2D
$1/\chi_Q$	$T^{4/3} \rightarrow \text{C.W.}$	$-T \ln T \rightarrow \text{C. W.}$	$T^{3/2} \rightarrow \text{C.W.}$	$-T/\ln T \rightarrow \text{C.W.}$
C_m/T	$-\ln T$	$T^{-1/3}$	$-T^{1/2}$	$-\ln T$
$1/T_1$	$T\chi$	$T\chi^{3/2}$	$T\chi_Q^{1/2}$	$T\chi_Q$
ρ	$T^{5/3}$	$T^{4/3}$	$T^{3/2}$	T

Table 2.4: Critical exponents for itinerant systems near a quantum critical point [268].

	FM ($Q = 0$)		AFM ($Q \neq 0$)	
	3D	2D	3D	2D
C_m/T	$\ln S$	$S^{1/2}$	$-S^{1/2}$	$\ln S$
$1/T_1$	$T\chi$	$T\chi^{3/2}$	$T\chi_Q^{1/2}$	$T\chi_Q$
$(\rho - \rho_0)/T^2$	$S^{1/2}$	S	$S^{1/2}$	S

2.2.3 Arrott and Arrott-Noakes Analysis

The Curie temperature T_C at which the material orders ferromagnetically cannot be determined unambiguously. While an estimate (θ_W) can be extracted from Eq. 2.40 by fitting the $\chi(T)$ data to the Curie-Weiss law, fluctuations associated with the critical point do not allow for a good fit around T_C .

The Arrott-plot technique was first introduced by A. Arrott in 1957 [22], and is widely used to determine T_C from the field-dependent magnetization data. The method, derived independently by A. Arrott and K. Belov, is based on the Landau theory of phase transitions [23].

The free energy of a magnetic system will be decreased when a magnetic field is applied, as compared to the zero-field case (Eq. 2.82):

$$F(M) = F_0 + a(T)M^2 + bM^4 - MH \quad (2.90)$$

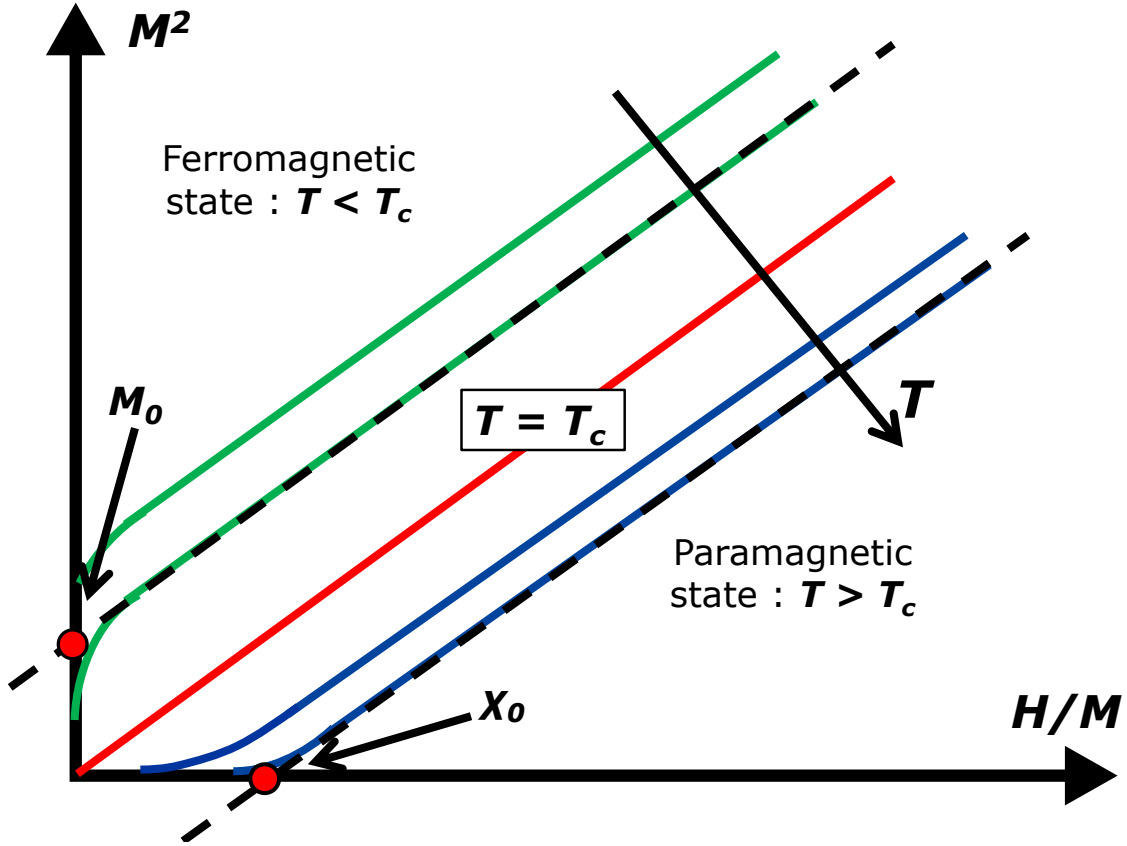


Figure 2.17: Arrott plot with the critical isotherm represented by a red line passing through the origin.

Minimizing the free energy results in the following temperature-magnetization relationship:

$$\frac{H}{M} = 4bM^2 + 2a_0(T_c - T) \quad (2.91)$$

It can be seen from the above equation, that plotting H/M as a function of M^2 for various T values, will result in parallel lines, all with the same slope of $4b$. Those isotherms are referred to as the Arrott plots. The isotherm that corresponds to the Curie temperature T_C should pass through the origin, yielding an accurate value of T_C (Fig. 2.17). Unfortunately, this method can only be applied to systems that exhibit the mean-field behavior. It relies on the fact that critical exponents,

mentioned in Section 2.2.2, have following values:

- $\beta = 0.5$, describing how the ordered moment grows below the Curie temperature
- $\delta = 3$, describing the curvature of $M(H)$ at T_C
- $\gamma = 1$, describing the divergence of magnetic susceptibility at T_C

In order to extend the Arrott technique to non-mean-field cases, it is necessary to modify the equation of state in the following manner:

$$\left(\frac{H}{M}\right)^{1/\gamma} = \frac{T - T_c}{T_1} + \left(\frac{M}{M_1}\right)^{1/\beta} \quad (2.92)$$

where T_1 , M_1 , β and γ are parameters to be determined from fitting the data and this is known as the Arrott-Noakes technique [24]. Similarly to the regular Arrott plot technique, the Arrott-Noakes procedure will yield values of T_C , spontaneous magnetization M_0 and critical exponents β , γ and δ . The relationships between M , H and the reduced temperature t are given for three separate regions by Eqs. 2.86 - 2.88, as before. However, in this case, exponents can have values different from those expected within mean-field description.

It is important to note, that in order for the Arrott-Noakes analysis to be consistent, it is necessary to satisfy following conditions simultaneously:

- The Arrott-Noakes isotherms must be linear at high fields and evenly spaced in reduced temperature t .
- In the Arrott-Noakes plot, the critical isotherm must pass through the origin and be linear for the whole field range.
- Scaling in $|M|/|t|^\beta$ vs. $H/|t|^{\delta\gamma}$ plot should occur, thus when plotting $|M|/|t|^\beta$ vs. $H/|t|^{\delta\gamma}$ the isotherms should collapse onto two diverging curves – one below the Curie temperature and one above the Curie temperature.

- The critical exponents must obey Eq. 2.89.
- The value for the Curie temperature T_C should be consistent between scaling, modified Arrott and power-law fitting methods [24].

An comparison between Arrott and Arrott-Noakes analysis in $\text{Sc}_{3.1}\text{In}$ is provided in Chapter 4. The Arrott-Noakes approach indicates non-mean field nature of $\text{Sc}_{3.1}\text{In}$, with critical exponents very different from those seen in another itinerant ferromagnet without magnetic constituents ZrZn_2 .

2.3 Spin-Glass Systems

A spin-glass is defined as a random, mixed-interacting, magnetic system characterized by a random, yet cooperative, freezing of spins at a well-defined temperature T_f below which a highly irreversible, metastable frozen state occurs without the usual long-range spatial magnetic order [273]. The name spin-glass was given because of the similarity with the ordinary glasses which freeze without any long range atomic order. Cluster-glass materials are glassy systems in which the spins exhibit short range correlations within a cluster, while the clusters themselves show the cooperative freezing characteristic of spin-glasses [40, 273].

The first ingredient necessary for glassiness is frustration. The term frustration has been introduced to describe systems in which a spin (or a number of spins) cannot find an orientation to fully satisfy all of the interactions between the neighboring spins [95]. A simple example of a frustrated lattice in two dimensions is a triangular one, shown in Fig. 2.18(a). Once two spin orientations are chosen, antiferromagnetic coupling cannot be satisfied for all three spins. Moreover, both choices have the same exchange energy, resulting in a degenerate ground state with a finite entropy even at zero temperature [273]. Similar problem occurs in the case of a square lattice with ferromagnetic nearest neighbor and antiferromagnetic next-nearest neighbor interactions, as shown in Fig. 2.18(b). Coupling for more than two spins cannot be satisfied, no matter which spin configuration is chosen. For three dimensional systems, frustration is observed in pyrochlore lattices, where antiferromagnetically coupled spins are located on the corners of a tetrahedron. Frustrated systems can present a wide range of physical properties due to many ground state configuration options, as compared with ordered systems [16].

While frustration can create degenerate and metastable ground states, it is not sufficient to generate a spin-glass. It must be accompanied by disorder or randomness.

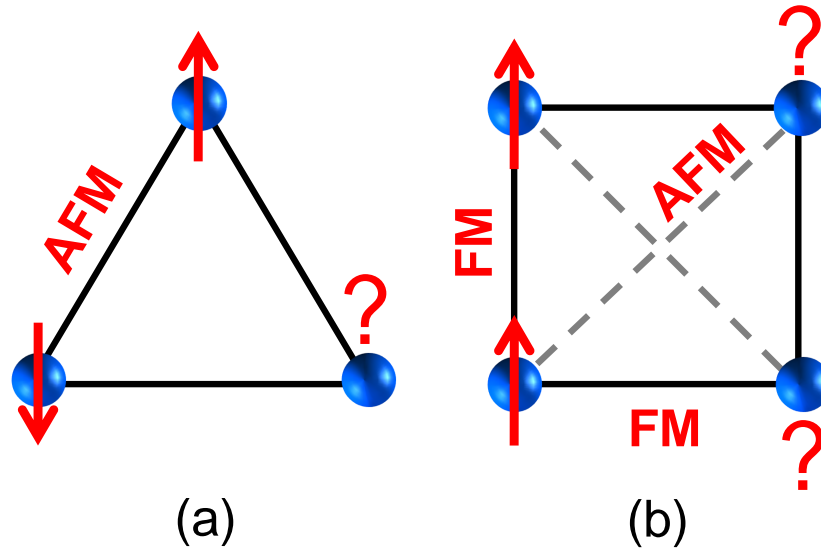


Figure 2.18: Two examples of frustrated lattices: (a) a triangular lattice with anti-ferromagnetic coupling and (b) a square lattice with ferromagnetic nearest neighbor and anti-ferromagnetic next nearest neighbor coupling.

Randomness is created either by a random site occupancy or by irregular bonds between magnetic ions. Mixed ferro- and anti-ferromagnetic interactions are essential to install the competition and to ensure cooperativeness of the freezing process [273].

First observations of spin-glass properties were made in dilute magnetic alloys such as CuMn [274,321], AgMn [230] and AuFe [63,275]. Random distribution of magnetic impurities in a non-magnetic matrix affects the sign and strength of interactions, giving rise to competing interactions and frustration. The physical properties depends greatly on the concentration regimes, shown in Fig. 2.19. For the very dilute region, there are isolated impurity-conduction electron couplings which result in a Kondo effect (WM region). The $T_K = T_f(x_0)$ is taken as the concentration limit x_0 , below which the Kondo effect plays a large role. For the next concentration region, conduction electron screening is eliminated and spins start to interact in pairs (SG region). Physical properties are universal functions of the concentration scaled pa-

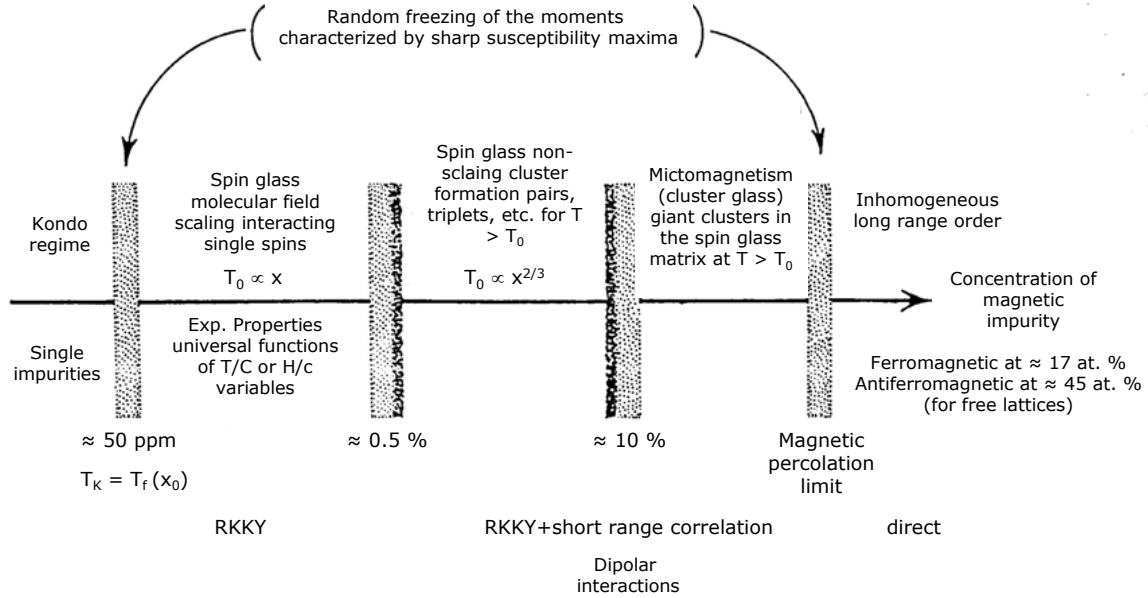


Figure 2.19: Different types of magnetic behavior for various concentration regimes in a canonical spin-glass [273].

rameters T/x and H_{ext}/x with $T_f \propto x$ [273]. The scaling laws breakdown around 0.5 %, where $T_f \propto x^{2/3}$. As the concentration of magnetic impurities is increased, there is a greater statistical chance of the impurity being first or second nearest neighbor to another impurity. Consequently, magnetic clusters can form as a result of concentration fluctuations in a random alloy [273]. When the magnetic behavior is dominated by the presence of such clusters, the material is referred to as a mictomagnet or a cluster-glass [273]. An example of clusters embedded in a spin-glass matrix is shown in Fig. 2.20.

For higher concentrations x , the percolation limit is reached: the concentration of magnetic ions is high enough to create a continuous path of nearest neighbor spins from one end of the system to another, resulting in long range magnetic order (LRO region). While Fig. 2.19 provides an estimate for the concentration limits for various regimes, it is important to note that those are not clear boundaries but rather gradual transitions.

For most dilute magnetic alloys, the dependence of magnetic behavior on the

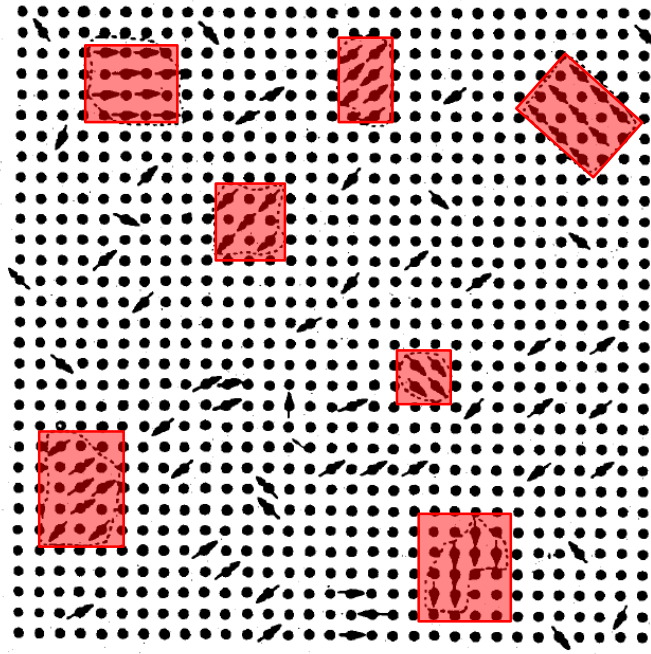


Figure 2.20: Spin-glass with micromagnetic clusters in a 2D square lattice [273].

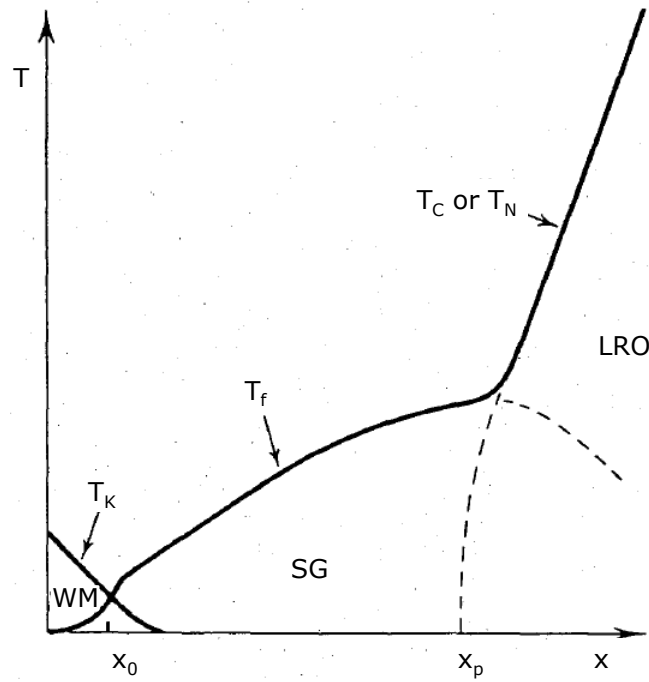


Figure 2.21: A schematic $T - x$ phase diagram for a dilute magnetic alloy [273].

concentration described above can be summarized in a phase diagram, shown in Fig. 2.21. The average Kondo temperature T_K decreases with concentration. For $T_K > T_f$, the Kondo effect prevents strong impurity-impurity interactions (WM region). For $x > x_0$, the spin-glass regime appears, developing T_f that is linearly dependent on x (SG region). When the percolation threshold is surpassed, there is a nearly linear increase of T_N or T_C with concentration as a long-range ordered state is formed and strengthened (LRO region) [273].

2.3.1 Physical Properties of Spin- and Cluster-glasses

As it is expected for a collection of randomly oriented spins, for $T \gg T_F$, a paramagnetic state is observed. It is followed by a region in which interactions between spins give rise to locally correlated clusters or domains which can rotate as a whole with the external field ($T > T_f$). In an applied magnetic field, a Curie-Weiss behavior is observed (Eq. 2.40). As $T \rightarrow T_f$, various spin components begin to interact with each other over a long range since thermal fluctuations are diminished [273]. Deviations from the Curie-Weiss law are observed, indicating the dominance of short-ranged correlations. The value of θ_W , extracted from the Curie-Weiss fit, identifies ferromagnetic and antiferromagnetic clustering, as shown in Fig. 2.22 [259]. For the alloys of Au and Fe, the coupling changes from antiferromagnetic to ferromagnetic as the Fe concentration increases [259].

Closer to $T = 0$ the system seeks its ground state configuration, resulting in a cooperative frozen state for $T < T_f$. As mentioned previously, a number of ground states is possible which means that the system can be trapped in a local rather than an absolute minimum [273]. One of the main signatures of spin-glass materials, a bifurcation between ZFC and FC magnetization, which occurs around the freezing temperature, is another indication of the ground state degeneracy [273]. This can

be seen in Fig. 2.23(a) for a Cu-doped Mn [277] and Fig. 2.23(b) for Ca-doped LaCoO_3 [56]. The FC magnetization is fully reversible while the ZFC one is not and is highly sensitive to the rate of temperature increase dT/dt [273]. These effects occur even when the applied field is small, confirming the existence of a multidegenerative ground state. For cluster- glasses, the value of the FC magnetization for $T < T_f$ is generally higher than the ZFC one [273]. This difference can be seen from Fig. 2.23, where the susceptibility data for a spin-glass are given in (a) while that for a cluster-glass compound are given in (b) [56, 277]. Another difference between the two is that the freezing temperatures, defined as maxima in the DC ZFC $\chi(T)$ data, are generally lower than the irreversibility temperatures T_{irr} between the ZFC and

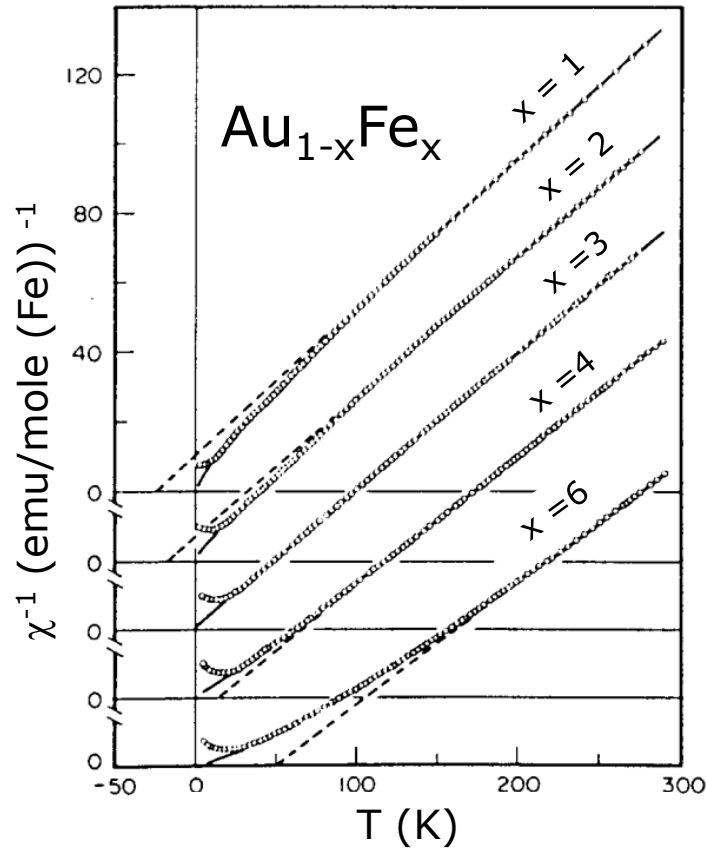


Figure 2.22: The inverse susceptibility fits for various concentrations of Fe in Au. The dashed lines are linear extrapolations of the Curie-Weiss fit, from which values of θ_W are extracted. Negative values of θ_W indicate antiferromagnetic coupling while those for ferromagnetic coupling are positive [259].

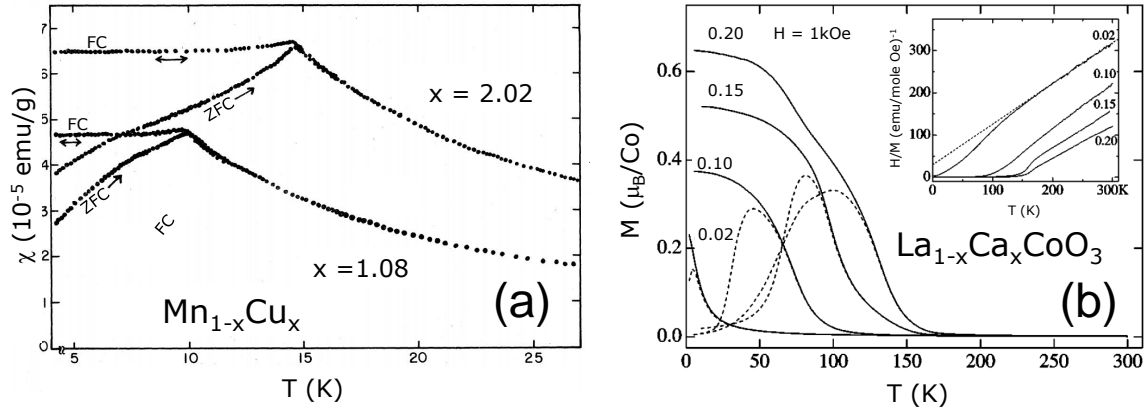


Figure 2.23: (a) ZFC and FC magnetization data for spin-glass $\text{Mn}_{1-x}\text{Cu}_x$ alloys [277]. (b) ZFC and FC magnetization data for $\text{La}_{1-x}\text{Ca}_x\text{CoO}_3$ cluster-glass [56]. The bifurcation at the freezing temperature is one of a characteristics features of a spin- or cluster-glass materials.

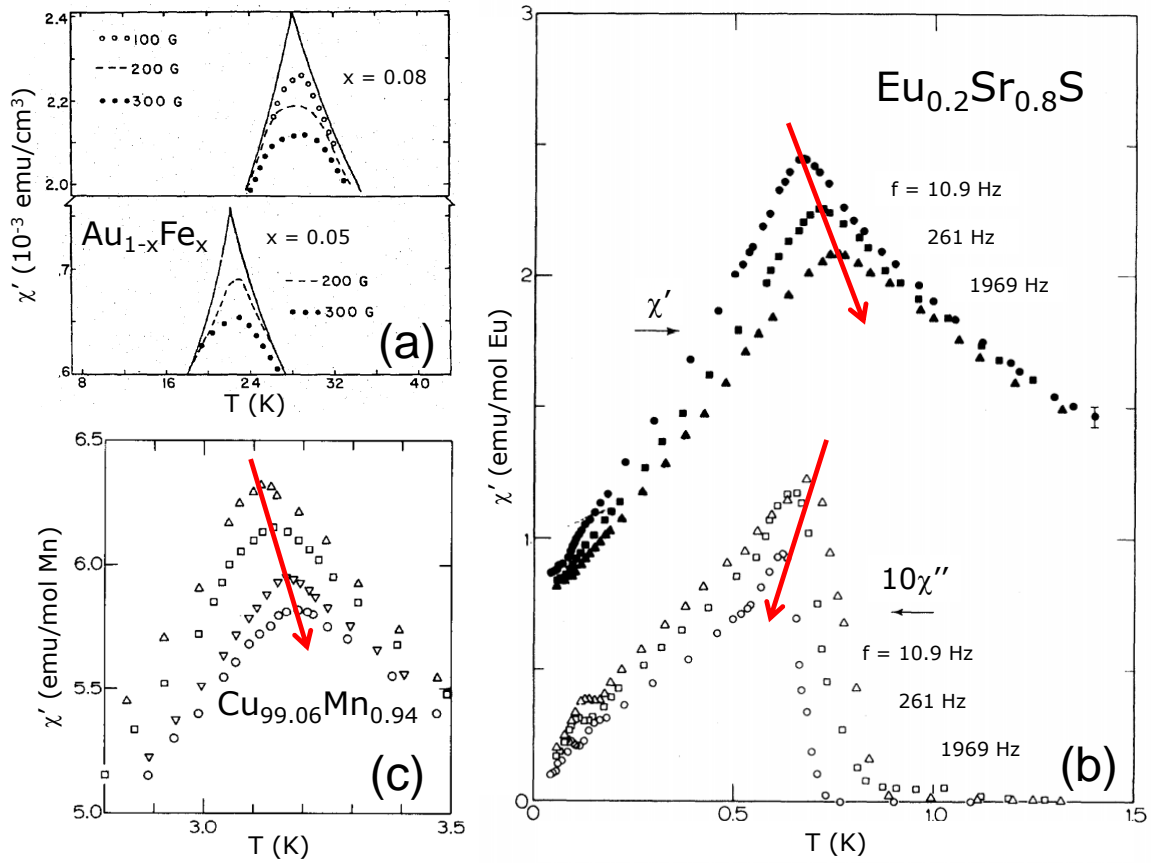


Figure 2.24: (a) Evolution of cusp in AC susceptibility with application of field for $\text{Au}_{1-x}\text{Fe}_x$ [63]. (b) Temperature dependent χ' and χ'' for $\text{Eu}_{0.2}\text{Sr}_{0.8}\text{S}$ in various frequencies [165]. (c) Shift in the position of the cusp as a function of frequency for $\text{Cu}_{99.06}\text{Mn}_{0.94}$ [272].

FC data for cluster-glasses. Additionally, lack of saturation in field-dependent $M(H)$ data at high magnetic fields is observed for the cluster-glass materials.

The value of the freezing temperature T_f is decreased with increasing field, as the field forces the spins to align with its direction, lifting the degeneracy caused by frustration, an example is given in Fig. 2.24(a) for $\text{Au}_{1-x}\text{Fe}_x$ [63]. To avoid erroneous T_f estimates, AC susceptibility measurements can be done instead. The AC susceptibility method (Section 3.3) requires very small applied field which will not affect the cusp, as the applied field smears the cusp to a broad maximum for DC susceptibility data [273]. An example of the imaginary and real component of the AC susceptibility for $\text{Eu}_{0.2}\text{Sr}_{0.8}\text{S}$ is shown in Fig. 2.24(b) [165]. For temperatures higher than T_f , χ' and DC susceptibility χ coincide. For low temperatures the AC susceptibility χ' is described by [273]:

$$\chi'(T) = \chi'(0) + bT^n \quad (2.93)$$

with $n \approx 2$ for metallic spin-glasses. Thus $\chi'(T)$ extrapolates to a finite value for $T \rightarrow 0$. Another characteristic of spin-glass materials is the frequency dependence of the cusp at T_f in the real part of the AC susceptibility [273]. As the frequency is increased, the freezing temperature T_f achieves higher values, since higher frequencies are frozen out at higher temperatures [273]. In order to quantify the frequency shift following expression is typically used:

$$\delta = \frac{\Delta T_f(f)}{T_f(f)\Delta(\log f)} \quad (2.94)$$

While a similar frequency dependence can also be found in superparamagnets, the δ values of 0.1 or less are typically observed for spin-glasses (Table 2.5), which are much smaller than those seen in superparamagnets [273]. Another way to differentiate

Table 2.5: Frequency shifts δ for various spin-glasses [273].

System	$\frac{\Delta T_f(f)}{T_f(f)\Delta(\log f)}$
$\text{Cu}_{1-x}\text{Mn}_x$	0.005
$\text{Au}_{1-x}\text{Mn}_x$	0.0045
$\text{Ag}_{1-x}\text{Mn}_x$	0.006
$\text{Pd}_{1-x}\text{Mn}_x$	0.013
$\text{Ni}_{1-x}\text{Mn}_x$	0.018
$\text{Au}_{1-x}\text{Fe}_x$	0.010
$\text{La}_{1-x}\text{Gd}_x\text{Al}_2$	0.06
$\text{Eu}_{0.2}\text{Sr}_{0.8}\text{S}$	0.06
$\text{Fe}_{1-x}\text{Mg}_x\text{Cl}_2$	0.08

spin-glasses and paramagnetic is to apply the Arrhenius law:

$$f = f_0 e^{-\frac{E_a}{k_B T_f}} \quad (2.95)$$

where f is the driving frequency of the AC measurements, k_B is the Boltzmann constant, f_0 is the characteristic relaxation frequency of a single spin (or cluster) and E_a is the activation energy or the energy barrier separating the states [273]. If the values of the freezing temperature T_f are recorded as the function of frequency f and fitted with the Arrhenius law, unphysical values of f_0 (10^{-200} s) and E_a (4400 K) are obtained. This distinguishes spin-glasses from superparamagnets, where the Arrhenius law does indeed hold and gives physically realistic values.

Since the increase of T_f with frequency mimics what happens if an ordinary glass becomes more viscous, another method of analysis is extracted from the theory describing real glasses. The Vogel-Fulcher law is empirical which characterizes the viscosity of supercooled liquids [119, 273, 343, 371]:

$$f = f_0 e^{-\frac{E_a}{k_B(T_f(f) - T_0)}} \quad (2.96)$$

here E_a is the activation energy and T_0 is the Vogel-Fulcher temperature that is often interpreted as a measure of intercluster interaction strength [15, 273, 332, 360]. A generally better agreement is seen for the Vogel-Furher fit.

Another analysis of the freezing temperature evolution with frequency is taken from the theory for dynamical scaling near a phase transition [273]. Conventionally, the critical relaxation time $\tau = 1/f$ is related to the correlation length ξ as $\tau \propto \xi^z$. Since ξ diverges with temperature, $\tau \propto \xi^z$ and $\xi \propto (T/(T - T_c))^\nu$. A power-law, established by Hohenberg *et. al.* [160], is frequently used to describe glassy materials [40, 273]:

$$\tau = \tau_0 \left(\frac{T_f(f)}{T_f(0)} - 1 \right)^{-z\nu} \quad (2.97)$$

where τ_0 is the characteristic relaxation time of a single spin (or cluster), ν is the critical exponent which describes the growth of the correlation length ξ [$\xi = (T_f(f)/T_f(0) - 1)^{-\nu}$], and z is the dynamic exponent which describes the evolution of the relaxation time. Typical values for the relaxation time are around 10^{-12} s, while $T_f(0)$ is slightly lower than the freezing temperature T_f , extracted from DC data. Empirically, the $z\nu$ values for glassy systems have been observed to fall within the range $2 \leq z\nu \leq 14$ [371].

While both DC and AC susceptibility display clear features corresponding to the transition into the frozen state, this is not the case for the specific heat data. While another estimate of $T_f(0)$ from specific heat would have been useful, the lack of a clear peak or singularity in the specific heat data does not allow for it. A broad cusp in the temperature-dependent specific heat $C_p(T)$ at $T \approx (1.2 - 1.4) T_f(0)$ is generally observed, as shown in Fig. 2.25(a). This clearly differentiates spin-glass freezing from a conventional phase transition. With the transition into the glassy

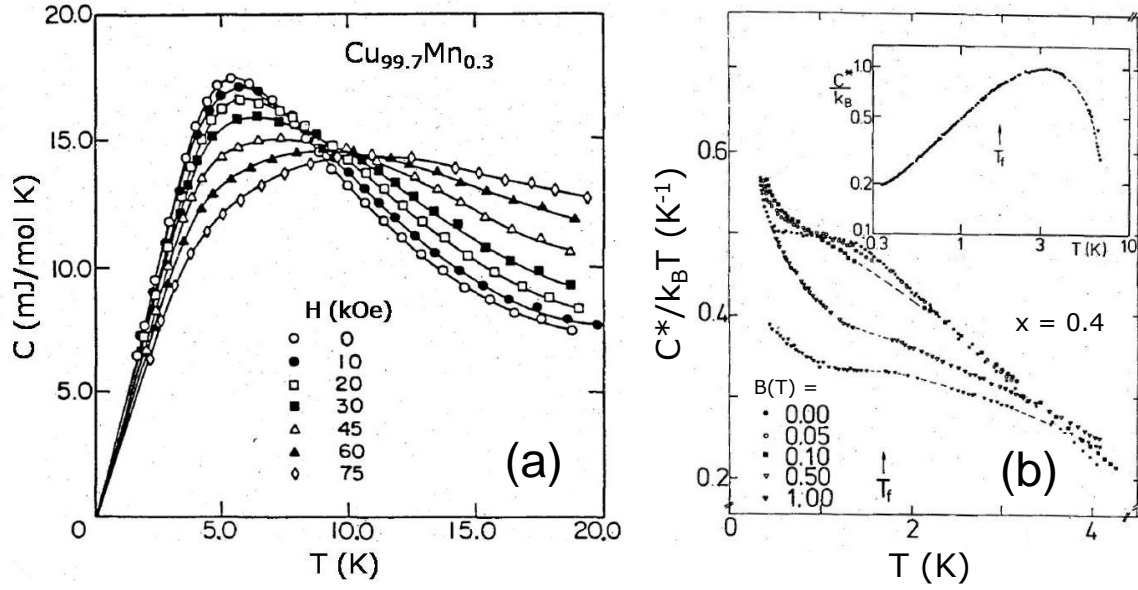


Figure 2.25: (a) Specific heat in various external fields for $\text{Cu}_{99.7}\text{Mn}_{0.3}$ [53]. (b) Specific heat per Eu atom divide by $k_B T$ as a function of temperature T . The inset shows the behavior on a log-log plot [255].

state, the entropy is removed as the temperature is decreased:

$$S_m = \int_0^T \frac{C_m}{T} dT = R \ln(2S + 1) \quad (2.98)$$

The constant amount of entropy S_m is drastically diminished even above the freezing temperature T_f . Even more is lost due to the formation of clusters, as the material enters the glassy state [273]. The loss of entropy explains the lack of a distinct feature at T_f .

2.3.2 Theoretical Description of Spin-glass Systems

It is important to note that the transformation of a spin-glass that occurs at the freezing temperature requires a different theoretical description, as compared with regular phase transitions. This process involves a complicated interplay between

randomly distributed and frustrated spins which has been the subject of extensive theoretical as well as experimental investigations.

The transition into a frozen state is inherently different from a typical phase transition, therefore a traditional order parameter can no longer be used. Instead, Edwards and Anderson focused on the time order. If each spin S_i becomes locked in to a preferred direction at site i , its orientation will remain the same tomorrow as it was today [273]. The time autocorrelation function was introduced:

$$q = \lim_{t \rightarrow \infty} \langle \langle S_i(0) \cdot S_i(t) \rangle_T \rangle_C \quad (2.99)$$

where the inner angular brackets represent a thermal averaging and the outer a configurational average over all spins. The evolution of q with temperature T can be determined using the condition $\partial F / \partial q = 0$, where $F(q)$ is the free energy. The derivation of the free energy starts with a hamiltonian for a random-bond 3D square lattice:

$$H = - \sum_i j J_{ij} S_i \cdot S_j - \sum_i H_i \cdot S_i \quad (2.100)$$

The spins on site i and j interact *via* exchange coupling J_{ij} and are randomly chosen using a Gaussian distribution with a variance Δ :

$$P(J_{ij}) = \frac{1}{\sqrt{2\pi\Delta^2}} e^{-\frac{J_{ij}^2}{2\Delta^2}} \quad (2.101)$$

Consequently, the free energy is given in terms of the partition function Z :

$$F = -k_B T \ln Z = -k_B T \text{Tr} \left(e^{\frac{-\mathcal{H}}{k_B T}} \right) \quad (2.102)$$

Now the free energy can be obtained in the mean-field approximation, assuming $\langle\langle S_i^\alpha S_j^\beta \rangle_T\rangle = 0$ and setting $q = \langle\langle S_i \rangle_T^2\rangle_C$ [273]. As mentioned above, $q(T)$ can be determined from $\partial F/\partial q = 0$, but it is only solvable in the limits $T \rightarrow 0$ and $T \rightarrow T_f$, resulting in:

$$q(T \rightarrow 0) = 1 - \left(\frac{2}{3\pi}\right)^{1/2} \frac{T}{T_f} \quad (2.103)$$

$$q(T \rightarrow T_f) = -\frac{1}{2} \left[1 - \left(\frac{T_f}{T}\right)^2 \right] \quad (2.104)$$

Using the fluctuation-dissipation theorem, the susceptibility can be written as:

$$\chi(T, H = 0) = \frac{(g\mu_B)^2}{3k_B T} \sum_{ij} \left[\langle\langle S_j^2 \rangle_T \rangle_C - \langle\langle S_i \rangle_T^2 \rangle_C \right] \quad (2.105)$$

Since there are no short- or long-range correlations, all $i \neq j$ terms must be set to zero [273]. This results in:

$$\langle\langle S_i^2 \rangle_T \rangle_C = 1 \quad (2.106)$$

$$\langle\langle S_i \rangle_T^2 \rangle_C = q \quad (2.107)$$

which in turn simplifies Eq. 2.105 as:

$$\chi(T, H = 0) = \frac{(g\mu_B)^2}{3k_B T} (1 - q(T)) \approx \chi_{ac}(T) \quad (2.108)$$

For $H = 0$, the limiting values of $q(T)$, taken from Eqs. 2.103 and 2.104, can

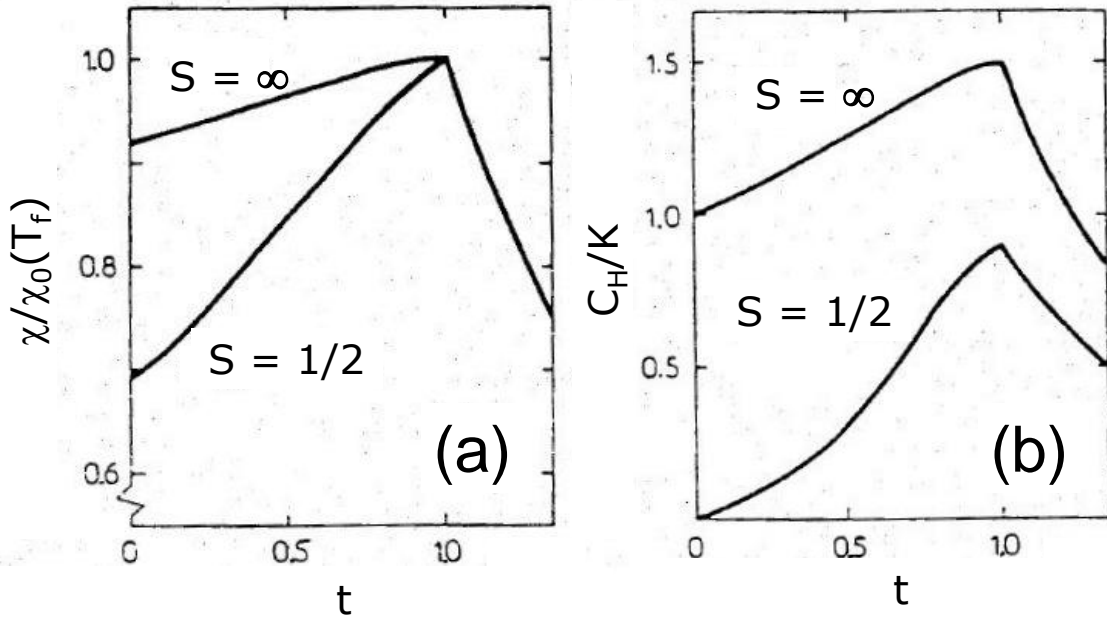


Figure 2.26: (a) Susceptibility and (b) specific heat versus reduced temperature calculated from the Edwards and Anderson model for two spin values [112].

be substituted into the above equation:

$$\chi_{ac}(T \leq T_f) = \frac{(g\mu_B)^2}{3k_B T} - O(T_f - T)^2 \quad (2.109)$$

$$\chi_{ac}(T \rightarrow 0) = \frac{(g\mu_B)^2}{3k_B T} \left(\frac{2}{3\pi} \right)^{1/2} \frac{T}{T_f} = \text{const} \quad (2.110)$$

This explains the asymmetric cusp in the susceptibility and the constant χ at very low temperatures. However, the Edwards and Anderson model also predicts a cusp in the specific heat at the T_f , which contradicts experimental observations [273]. The mean-field approximation, applied by Fischer [112], compared classical ($S = \infty$) and quantum ($S = 1/2$) spins. The results for the calculated susceptibility and specific heat are shown in Fig. 2.26: the $\chi(T)$ for $S = 1/2$ agrees with typical experimental results while $S = \infty$ is more reminiscent of a generic specific heat data [112]. This clearly indicates that there is a problem with the mean-field approximation

of the Edwards and Anderson model. Additionally, the Edwards-Anderson model is not solvable for the whole temperature region, away from $T = 0$ or $T = T_f$, leaving the description of the frozen state incomplete.

Another variation of the mean-field approximation was proposed by Sherrington and Kirkpatrick [330], who assumed that every spin couples equally with every other spin [273]. This means that the probability distribution $P(J_{ij})$ is assumed to be the same for all $i - j$ pairs of spins, independent of how far they are apart:

$$P(J_{ij}) = \frac{1}{\sqrt{2\pi\Delta'^2}} e^{-\frac{(J_{ij}-J'_0)^2}{2\Delta'^2}} \quad (2.111)$$

the scaling of variance $\delta' = \Delta/N^{1/2}$ and mean $J'_0 = J_0/N$ is required in order to account for infinite-range interactions [273]. The mean J'_0 has been included to reflect the possibility of ferromagnetism. Repeating some of the calculations done for the Edwards-Anderson model, expressions for the spin-glass order parameter q and the ferromagnetic order parameter m are obtained:

$$q = \frac{1}{\sqrt{2\pi}} \sum e^{-\frac{z^2}{2}} \tanh^2 \left(\frac{\Delta\sqrt{q}}{k_B T} z + \frac{J_0 m}{k_B T} \right) dz \quad (2.112)$$

$$m = \frac{1}{\sqrt{2\pi}} \sum e^{-\frac{z^2}{2}} \tanh \left(\frac{\Delta\sqrt{q}}{k_B T} z + \frac{J_0 m}{k_B T} \right) dz \quad (2.113)$$

For given ratios of J_0/Δ , $q(T)$ and $m(T)$, the above expressions are used to determine the magnetic phase diagram, shown in Fig. 2.27(a). Three possible phases are predicted from the Sherrington-Kirkpatrick model for Ising spins interacting *via* an infinite-ranged Gaussian distribution of exchange forces centered at J_0 with width

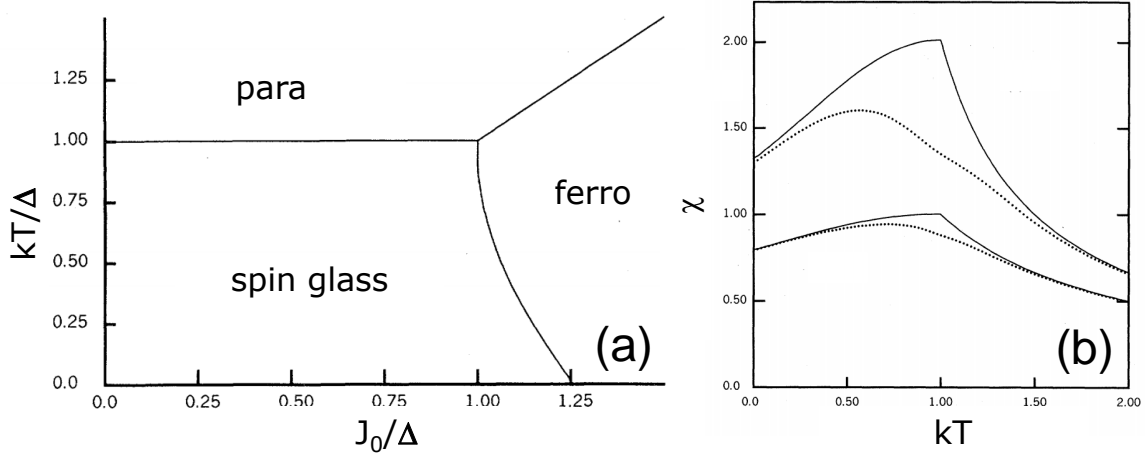


Figure 2.27: (a) Magnetic phase diagram for Ising spins interacting *via* an infinite-ranged gaussian distribution of exchange forces with variance Δ and mean J_0 . (b) The AC susceptibility as a function of temperature, calculated from the Sherrington-Kirkpatrick model: J_0/Δ is 0 and 0.5 for upper and lower curves, respectively. The field $H = 0$ for solid curves and $H = 0.1J_0$ for the dashed ones [330].

Δ [330]. The AC susceptibility can be computed from $q(T)$:

$$\chi(T) = \frac{1 - q(T)}{k_B T - J_0(1 - q(T))} \quad (2.114)$$

The evolution of χ with field can be calculated by including the applied field H in to the hamiltonian in Eq. 2.100. This behavior is shown in Fig. 2.27(b), for which $J_0/\Delta = 0$ and 0.5 as well as $H = 0$ and 0.1Δ are considered [273]. As observed in experiments, the AC susceptibility data show a cusp which becomes rounded and shifts downward in a DC field. The agreement for the specific heat case the agreement is not as good, as a cusp is predicted by the Sherrington-Kirkpatrick model along with an unphysical negative value of the entropy at $T = 0$.

The difficulties observed in the Sherrington-Kirkpatrick model called for additional investigations: Almeida and Thouless showed that the Sherrington-Kirkpatrick solution is unstable at low temperatures for both spin-glass and ferromagnetic phases [91]. The stability limit is given by a phase boundary, known as the AT line, which

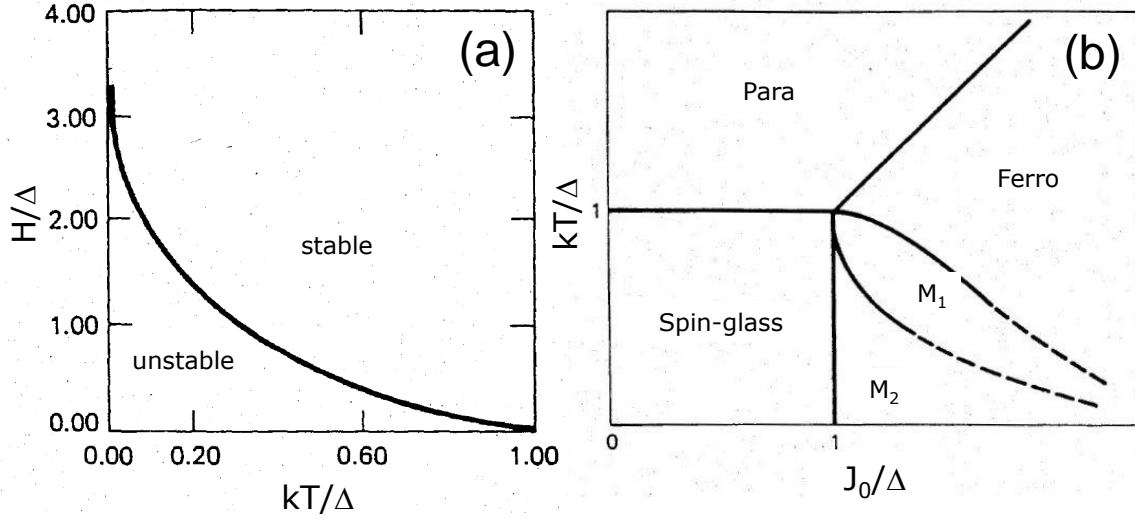


Figure 2.28: (a) The AT line or the $H - T$ phase diagram illustrating the stability limits of the Sherrington-Kirkpatrick solution for the case of $J_0 = 0$ [91]. (b) Phase diagram for vector spins interacting with infinite-ranged distribution (J_0 is the mean and Δ is the width of variance) [121].

marks the onset of freezing of the spin component longitudinal to the field [40]:

$$\frac{H_{AT}(T)}{\Delta J} \propto \left(1 - \frac{T}{T_f}\right)^{3/2} \quad (2.115)$$

The instability line of the Sherrington-Kirkpatrick solution for the spin-glass state extends all the way from T_f down to 0, as depicted in Fig. 2.28(a) [91]. The experimental consequence is that below the stability line irreversibilities in the magnetic properties should appear, which, as mentioned previously, are the decisive characteristic of a frozen spin-glass state [273].

For non-Ising vector spin-glasses with transverse spin components, additional order parameters need to be considered. Gabay and Toulouse [121] extended the Sherrington-Kirkpatrick solution to Heisenberg spin-glasses, which resulted in another

phase boundary, also known as the GT line [273]:

$$\frac{H_{GT}(T)}{\Delta J} \propto \left(1 - \frac{T}{T_f}\right)^{1/2} \quad (2.116)$$

The GT line describes the freezing of the transverse spin component. The resulting phase diagram is shown in Fig. 2.28(b). In addition to the spin-glass, para- and ferromagnetic phases seen in the case of the Ising spins (Fig. 2.27(a)), two new regions are observed - M1 and M2. These are mixed states, where spin-glass and ferromagnetism coexist [273].

2.4 Superconductivity

Materials can be classified in terms of how well they conduct electricity. The idea that freely moving conduction electrons make a metal a good conductor was first developed by Drude in 1905 [20]. While the Drude model did not take into account wave-like properties of electrons, the formula for the conductivity of metals remains correct:

$$\sigma = \frac{ne^2\tau}{m} \quad (2.117)$$

where m is the effective mass of the conduction electrons, e is the electron charge, and τ is the average lifetime for free motion of an electron between collisions with impurities or other electrons [20]. Since resistivity ρ is the reciprocal of conductivity σ , ρ can be expressed as:

$$\rho = \frac{m}{ne^2\tau} \quad (2.118)$$

Resistivity depends on temperature mainly *via* different scattering processes, which alter the mean life-time τ . In a typical metal, there are three main scattering processes: scattering by impurities, by electron-electron interactions, and by electron-phonon collisions [20]. While the resistivity of a typical conductor decreases as a function of temperature, the minimum value is limited by impurities and other defects: even at temperatures close to the absolute zero, conductors show some resistance. According to Matthiessen's rule [248], the overall resistivity can be written as:

$$\rho = \rho_0 + \rho_{ph}(T) + \rho_{el}(T) + \rho_{sd} \quad (2.119)$$

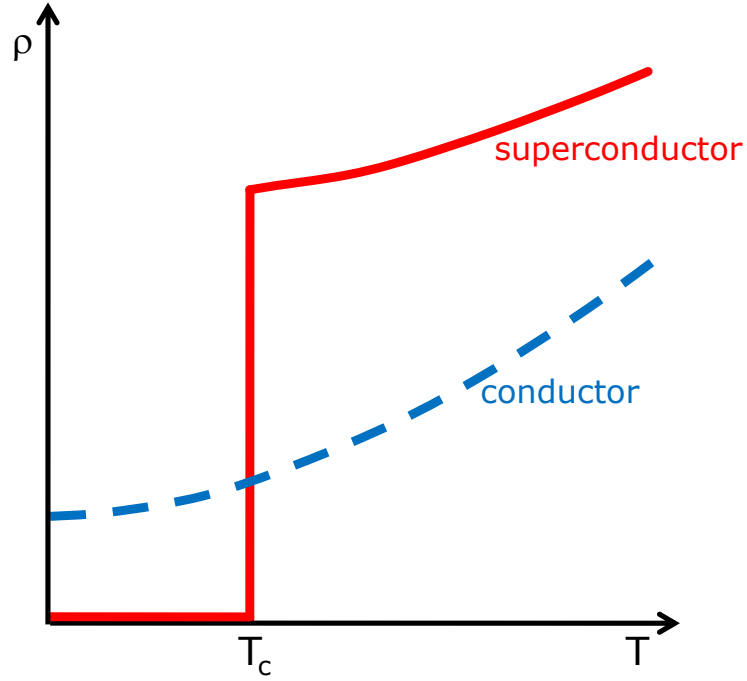


Figure 2.29: Resistivity of a typical conductor (dashed line) and a superconductor (solid line) [231].

The temperature-independent residual resistivity ρ_0 is caused mainly by electron-impurity and electron-defect scattering. All other terms are temperature-dependent: ρ_{sd} is caused by spin disorder, $\rho_{ph}(T)$ ($\propto T$ at high T and $\propto T^5$ at low T) describes lattice scattering, and ρ_{el} ($\propto T^2$) represents electron scattering. A typical resistivity plot for a conductor and a superconductor is shown in Fig. 2.29. The resistivity above T_c was chosen to be considerably higher for a superconductor in order to showcase an important trend: regular conductors do not become superconductors while many poor conductors are good superconductors [231]. High resistivity above T_c is caused by strong electron-phonon interactions, resulting in a high electron scattering rate. The same interaction is responsible for electron pairing in the superconducting state. In superconducting materials, the electrical resistivity disappears completely below the critical temperature T_c , allowing an electric current with no power source to flow indefinitely within a loop of superconducting wire (no change will be observed in times less than $10^{10^{10}}$ years [372]). For comparison, the age of the universe is 10^9 years [80].

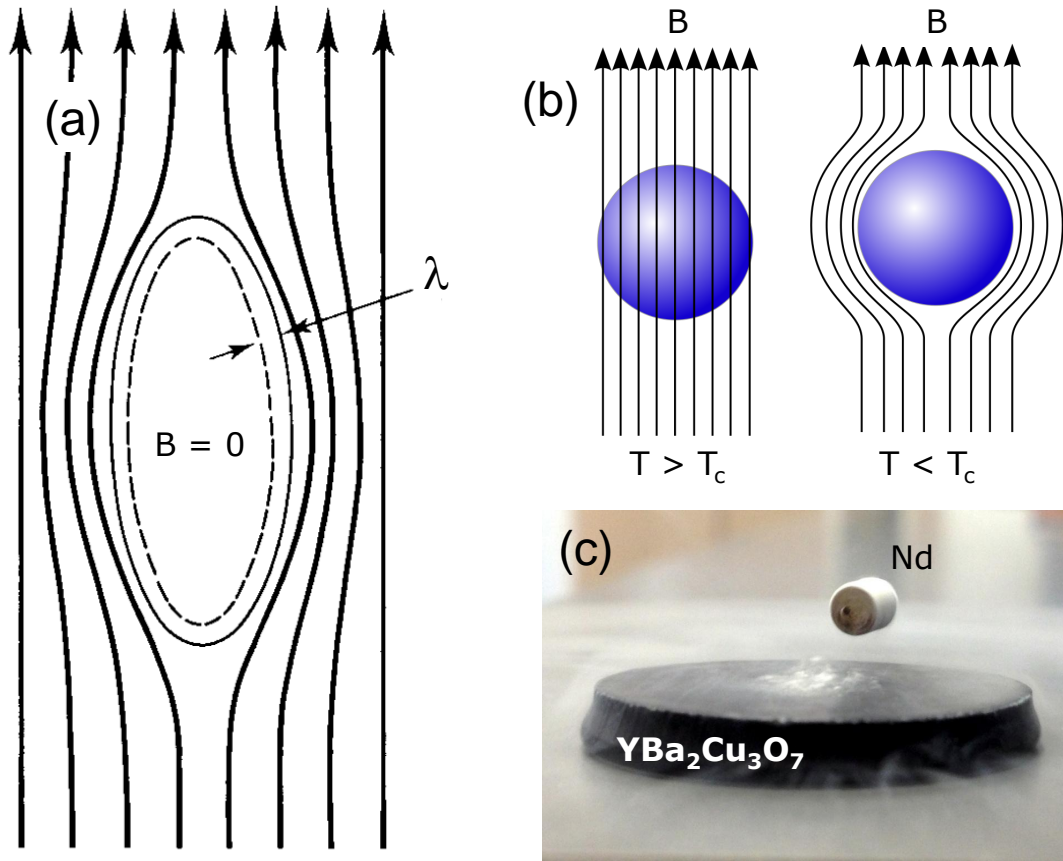


Figure 2.30: (a) Schematic diagram of the exclusion of magnetic flux from interior of a superconductor [372]. (b) Distribution of magnetic field lines around the superconductor below and above the critical temperature T_c . (c) A Nd-based magnet levitating above a $\text{YBa}_2\text{Cu}_3\text{O}_7$ pellet, cooled with liquid N.

The phenomenon was first observed by H. Kamerlingh Onnes in 1911 while he was testing the validity of Drude model at low temperatures using Hg (since Hg could be purified better than Pt, Au, or Cu). The complete disappearance of resistivity below 4 K was unexpected and its observation would not have been possible if it had not been for the significant breakthroughs in cryogenic research made by J. Dewar, G. Calude and H. Kamerlingh Onnes.

Because of the technical difficulties with cooling superconductors below their transition temperatures, it took twenty-two years to discover the next hallmark property of superconductors – perfect diamagnetism, first observed by Meissner and Ochsenfeld in 1933 [254]. As the sample is cooled below the critical temperature,

it becomes a perfect diamagnet with $\chi = -1/4\pi$ (Fig. 2.30(b)). Since the critical temperature of $\text{YBa}_2\text{Cu}_3\text{O}_7$ ($T_c = 93$ K [372]) is above the boiling point of liquid nitrogen (77 K), it is possible to observe the Meissner effect by placing a Nd magnet on top of a N-cooled $\text{YBa}_2\text{Cu}_3\text{O}_7$ pellet, as shown in Fig. 2.30(c).

As shown in Fig. 2.30(a), the magnetic field has a finite penetration depth λ (typically on the order of 500 \AA), which means that perfect diamagnetism can only be observed in bulk samples. The penetration depth λ , along with superconducting order parameter Φ and coherence length ξ [372] were first introduced as part of the phenomenological Ginzburg-Landau theory, proposed in 1950 [136]. The GL approach provides a reasonable explanation of several macroscopic properties of superconductors without any assumptions from the microscopic point of view. The London equations, which describe microscopic electric and magnetic fields, estimate the penetration depth as:

$$\lambda_L(0) = \sqrt{\frac{m^*}{\mu_0 n e^2}} \quad (2.120)$$

where m^* is the electron's effective mass and n is the total density of conduction electrons. Another characteristic length – coherence length ξ – was defined by Pippard [300] and later included in the Ginzburg-Landau theory, can be calculated as:

$$\xi(0) = \frac{0.18 \hbar k_F}{k_B T_c m^*} \quad (2.121)$$

The Ginzburg-Landau theory also defines a dimensionless, temperature-independent parameter κ , known as the Ginzburg-Landau parameter:

$$\kappa = \frac{\lambda_L(0)}{\xi(0)} \quad (2.122)$$

In 1957, it was shown by Abrikosov [7] that the Ginzburg-Landau parameter κ is related to the surface energy between the normal and superconducting phases. This energy is positive for $\kappa < 1/\sqrt{2}$ (Type I superconductor) and negative for $\kappa > 1/\sqrt{2}$ (Type II superconductor) [372]. The GL parameter is frequently used to classify superconductors into Type I and II. All elemental superconductors are Type I, exhibiting low critical temperatures, with the highest T_c of 9.2 K for Nb [20]. While the majority of composite superconductors are classified as Type II, only a few Type I compounds are known: LaRhSi₃ [17], YbSb₂ [408, 418], Ag₅Pb₂O₆ [413], ZrB₁₂ [376], Rh₂Ga₉ and Ir₂Ga₉ [393]. The physical properties of newly discovered Type II superconductors ScGa₃ and LuGa₃ are discussed in Chapter 9.

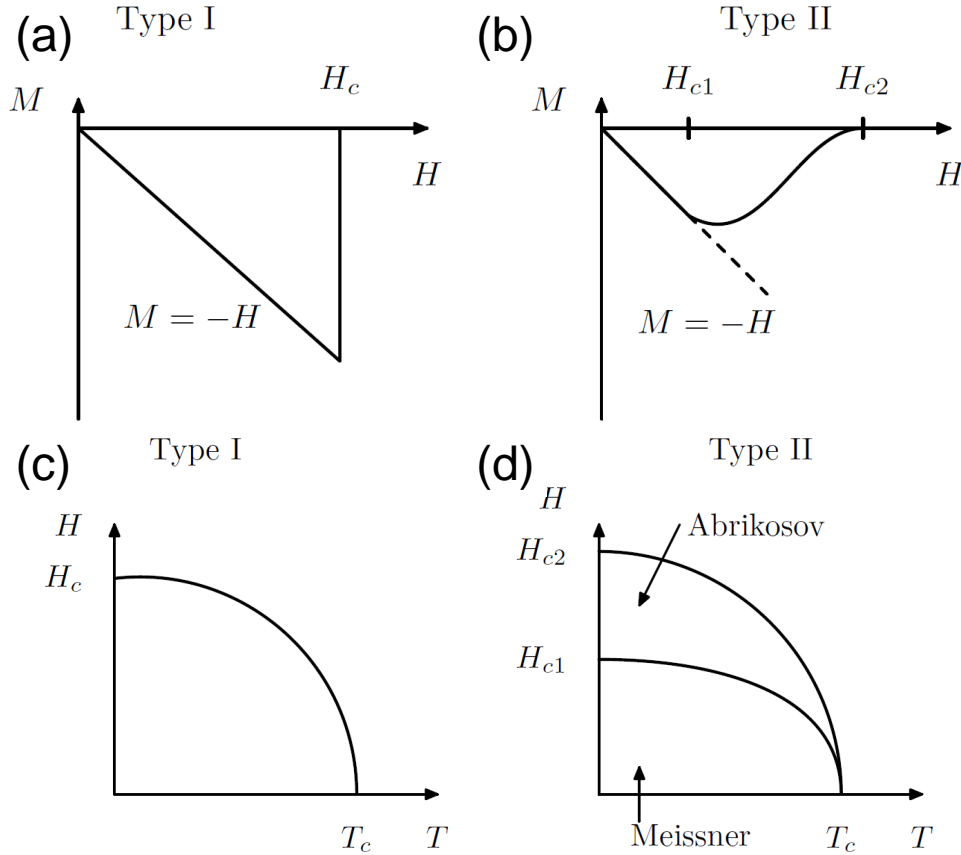


Figure 2.31: Typical field-dependent magnetization $M(H)$ curves of (a) Type I and (b) Type II superconductors. Temperature dependence of critical field(s) for a (c) Type I and (d) Type II superconductor [20].

The entrance into the diamagnetic state is different for Type I and Type II superconductors, as shown in Fig. 2.31(a) and (b). Moreover, the reversible nature of the Meissner effect implies that superconductivity can be destroyed if a high enough magnetic field H_c is applied [372]. For each temperature, there is a well-defined critical field H_c , at which superconductivity disappears. While the transition at zero field is of second order, the transition in the presence of field is of first order because there is a discontinuous change in the thermodynamic state of the system and the associated latent heat [372]. This is evident from the increased magnitude of the specific heat jump at T_c observed in Type I superconductors, with an example shown in Fig. 9.4(a) and (b) for ScGa_3 and LuGa_3 . For materials with $\kappa > 1/\sqrt{2}$, Abrikosov showed that instead of a discontinuous breakdown of superconductivity in a first-order phase transition at H_c , there was a continuous increase in flux penetration starting at lower critical field H_{c1} and reaching a maximum value at the upper critical field H_{c2} [7]. For $H_{c1} < H < H_{c2}$, the magnetic field lines penetrate inside the superconductor forming a vortex structure that consists of small normal state domains, surrounded by the superconducting phase. This state is known as a mixed or Abrikosov state, disappearing gradually as the field is increased to H_{c2} (Fig. 2.31(d)).

Fig. 2.31(c) and (d) shows this universal curve of the temperature dependence of H_c *vs.* T for both Type I and Type II superconductors. Empirically, it was found that the evolution of the critical temperature with field can be approximated by a Werthamer-Helfand-Hohenberg (WHH) parabolic law [372]:

$$H_c(T) = H_c(0) \left[1 - \left(\frac{T}{T_c} \right)^2 \right] \quad (2.123)$$

The effect of the external field on the sample depends on sample's shape. For example, for a long thin cylinder or sheet, the field everywhere on the surface of the sample H_a is the same as the applied field (Fig. 2.32(a)). This, however, is not

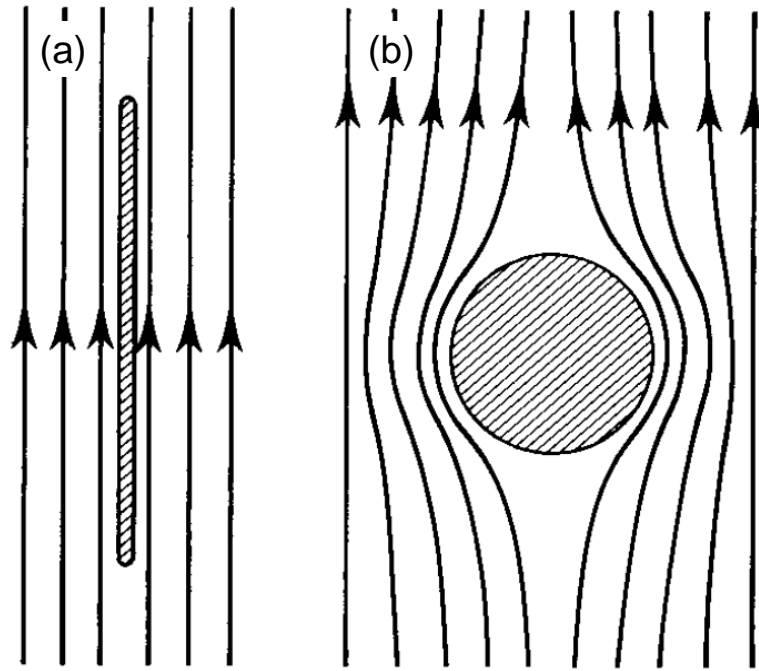


Figure 2.32: The distribution of magnetic field lines around a sample for a long, thin cylinder ($\eta = 0$) (a) and a sphere ($\eta = 1/3$) (b) [372].

true for a sphere, shown in Fig. 2.32(b). To account for various sample geometries, a demagnetizing factor η was introduced [372]. The demagnetizing factor η ranges from zero (for a long, thin cylinder) to unity for an infinite flat slab in a perpendicular field:

$$1 - \eta < \frac{H_a}{H_c} < 1 \quad (2.124)$$

For typical samples, a value of $\eta = 1/3$ (sphere) or $\eta = 1/2$ (cylinder) is generally used.

The next breakthrough in the theoretical understanding of superconductors was the development of the Bardeen-Cooper-Schrieffer (BSC) theory, published in 1957 [32]. It was shown that the phonon-mediated electron-electron interactions create bound electron pairs, also known as Cooper pairs, which comprise the supercon-

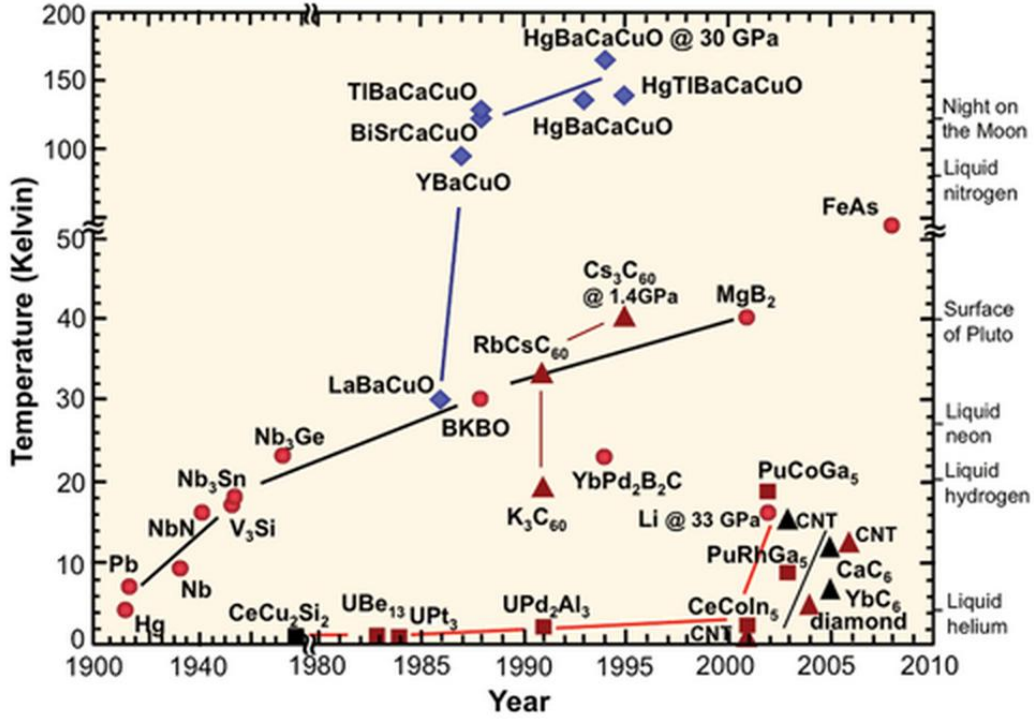


Figure 2.33: Progress in development of superconducting materials [286].

ducting charge carriers [372]. The BCS theory was the first microscopic theory that explained almost all of the unusual physical properties of superconductors known at that time, including the Meissner effect, zero resistivity, critical field and temperature, jump in the specific heat, and superconducting gap. The superconducting gap Δ was defined in terms of the minimum energy E_g , needed to break-up a Cooper pair:

$$E_g = 2\Delta(T) \quad (2.125)$$

$$\frac{2\Delta(0)}{k_B T_c} = 3.53 \quad (2.126)$$

The above ratio, extracted from the specific heat data, has been experimentally verified in a number of conventional superconductors. Another successful pre-

diction of the BCS theory is the jump in electronic specific heat at T_c :

$$\left. \frac{C_{es} - C_{en}}{\gamma T} \right|_{T_c} = 1.43 \quad (2.127)$$

where C_{es} and C_{en} are the electronic specific heat in the superconducting and normal states, respectively, and γ is the Sommerfeld coefficient. This ratio is frequently used in order to determine whether or not a superconductor is a conventional one, *i. e.* if it can be understood in the theoretical framework of BCS. BCS theory prompted Josephson's prediction of a zero voltage supercurrent flowing between two superconducting electrodes, separated by a weak link [180]. This hypothesis was soon confirmed experimentally [18], resulting in a variety of applications, one of which is SQUID magnetometry, described in Section 3.3.

Another milestone was the discovery of the high T_c family of superconductors in 1986 by J. D. Bednorz and K. A. Müller, who observed superconductivity in $\text{La}_{2-x}\text{Ba}_x\text{CuO}_4$ at 35 K [36]. While this T_c was still not high enough for broad practical applications, the discovery still attracted a lot of interest since a superconducting state was observed in an insulator. According to McMillan's theory, the maximum critical temperature T_c , derived from the BCS theory, could not exceed the limit of 40 K [251]. This was accepted until a compound with T_c of 93 K was discovered by M. K. Wu and C. W. Chu in 1987 [403]. This material not only contradicted McMillan's theory but also made more applications possible, as the superconducting state was achievable with liquid N, eliminating the need for expensive and technologically challenging liquid He cooling. Since the mechanism of superconductivity could not be explained within the BCS framework, the cuprates were categorized as unconventional superconductors.

Further search for high T_c compounds persisted with even more enthusiasm

as the invalidation of McMillan's theory opened the possibility for even higher T_c superconductors. The upper limit of experimentally detected T_c values has risen in incremental steps, as new families of superconductors were discovered, as shown in Fig. 2.33. The record for critical temperature was set by $\text{HgBa}_2\text{Ca}_2\text{Cu}_3\text{O}_{8+\delta}$ with T_c up to 165 K under pressure [72]. The understanding of superconductivity mechanism in cuprates is still lacking, with a general consensus that the superconductivity is associated with spin fluctuations. Another family of superconductors discovered in 2006 [187] are known as pnictides, they exhibit lower critical temperatures compared to cuprates but are still intriguing as the pair-breaking effect resulting from magnetic Fe ions was thought to be harmful to superconductivity. Additionally, their behavior cannot be explained within the framework of BCS, indicating that other pairing mechanisms rather than the electron-phonon coupling must be at play.

Experimental and Theoretical Techniques

An important part of sample synthesis and characterization relies heavily on a number of experimental and theoretical techniques, discussed in the following chapter. The search for new materials is followed by synthesis design, which is often one of the most challenging endeavors of the entire process. Physical characterization of structural, magnetic, thermal, and transport properties is often the initial step toward fully understanding a given compound. While those measurements can provide considerable information, additional techniques such as x-ray photoemission spectroscopy, neutron diffraction, and muon spin relaxation can lead to more in-depth characterization. For the final step, similar to many other disciplines, a comparison of experimental and theoretical results is necessary.

3.1 Sample Preparation

In a single crystal, the constituent atoms are arranged in an orderly manner that extends in all three spatial dimensions. Because of this periodicity and order, which give way to reduced strain, a smaller impurity concentration, reduced porosity and grain boundaries as well as smaller surface to bulk ratio, as compared to polycrystalline samples, single crystals allow to better probe the intrinsic properties of a given material [116]. Additionally, for reactive samples, single crystals can be significantly less air-sensitive, as compared with polycrystalline ones, due to the formation of a passivating surface layer [178]. By aligning a single crystal in a certain direction, with respect to the magnetic field, it is also possible to extract anisotropic information. The latter would be lost if the measurement is done on polycrystalline matter, where the random orientation of microscopic grains averages out any such properties. Moreover, some macroscopic and microscopic probes can only be utilized with single crystal material, examples include de Haas-van Alphen effect, as well as many neutron and x-ray scattering experiments [116]. While large crystals are certainly more desirable, crystals with dimensions of several mm on a side are more than sufficient.

Binary or ternary phase diagrams are the starting point of any growth recipe design. An example of a Sc-Ga composition dependent melting point phase diagram is shown in Fig. 3.1. The liquid region, shown in blue, is separated from the solid and mixed phases by the liquidus line. The compounds are represented by gray vertical lines, indicating five existing binary phases of Sc and Ga. Two of them – ScGa_3 and Sc_5Ga_3 – melt congruently, *i. e.* they can be obtained by mixing Sc and Ga in the same ratios as those specified by compound's stoichiometry, heating it above the melting temperature and then slowly cooling. The other three compounds are incongruent melters, which means that if the sample growth starts with the same elemental ratio as the targeted compound, it will result in a mixture of liquid and solid,

both with different compositions from the starting one. For majority of incongruent melters, the best preparation method is the liquid flux growth; where the flux can either be an extra quantity of one of the constituting elements (self flux) or an element that is not part of the desired compound. While the self flux method is generally more favorable, given it does not introduce extra elements into the reaction, for some compounds this is not feasible, either due to high melting temperature or vapor pressure [116]. When selecting an element as a flux, care must be taken so that the constituents of the targeted compound do not form any bonds with the flux within the given composition and temperature range [62]. Low melting metals such as Sn, Bi, Sb, Ga and In are commonly used, but binary phase diagrams of the flux with each of the reactants must be consulted. It has been noted, that for congruent melters, introduction of a new element as a flux is not as risky, given that the congruent melting compound is likely to precipitate [116].

Growth from high-temperature molten fluxes is the most common technique for growing small single crystals. While other options such as floating zone, Bridgman or Czochralski methods are possible and are widely used by the semiconductor industry, they are generally more successful for congruently melting compounds and require substantially more raw material as well as growth time [116]. The growth temperatures are also typically higher for this techniques, since the melt has to be heated above the melting temperature of the desired compound, which is frequently inaccessible in traditional furnaces and sample containers. On the contrary, liquid flux method allows materials to be grown well below their melting points, producing less thermal strain and fewer defects [116]. The flux also acts like a purifier, trapping impurities that would otherwise appear in the crystals [116]. After a homogeneous molten solution has been obtained, the process of cooling starts. A slow cooling rate, accessible *via* a programmable furnace, favors large crystal formation. The drawback of the spontaneous nucleation, which governs this type of crystal growth, is the

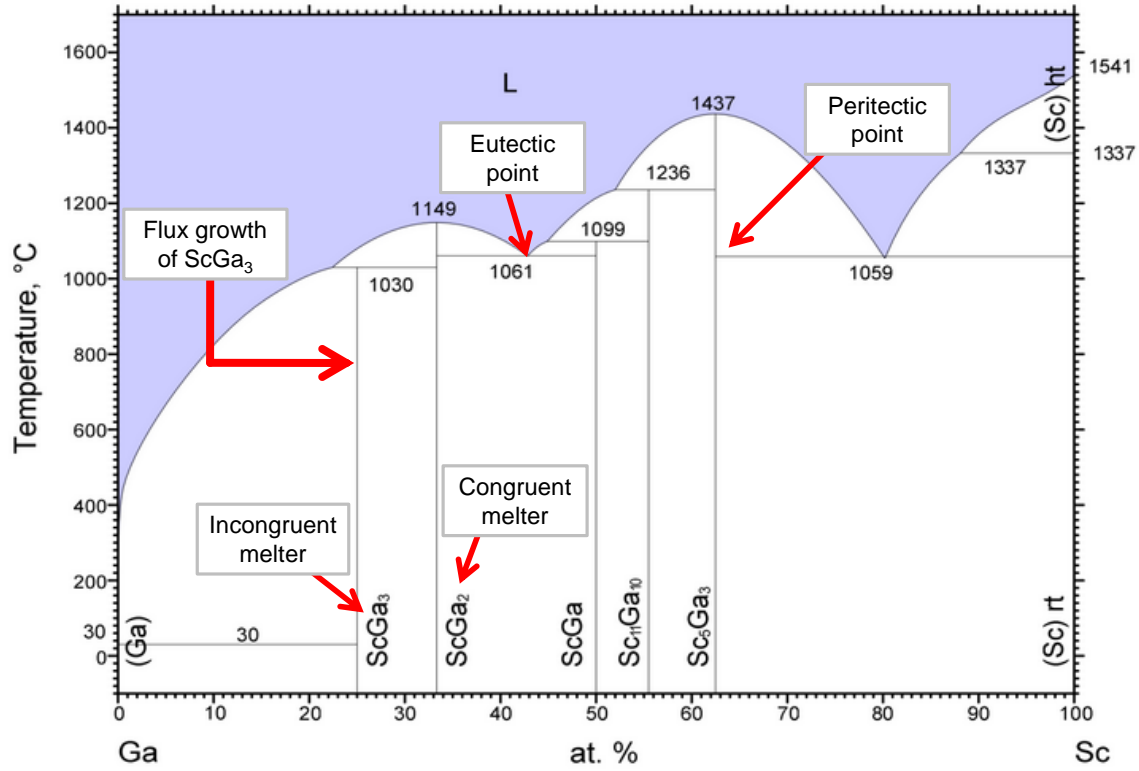


Figure 3.1: Phase diagram of ScGa_3 [389] with a few features specified on the plot. The growth recipe for the ScGa_3 compound is marked by a red line [357].

possibility of flux inclusions within a crystal, which can be addressed by using an oscillating temperature profile [203].

Problems also common to other methods include container issues, as secondary, unexpected reactions could occur between the sample and the container [116]. The choice of container for a particular growth mostly depends on the chemicals that will be used in a growth, with the most common crucibles being those made out of alumina (Al_2O_3) with volumes of 2 (Fig. 3.2) or 5 ml [60–62, 113, 116, 188]. The reacting elements are placed in the bottom crucible (growth crucible) with the low melting elements placed on top of the high melting ones. The growth crucible is covered by another inverted crucible (catch crucible), that is either filled with quartz wool (Fig. 3.2) or includes an alumina strainer (Fig. 3.2). Additional quartz wool (or quartz

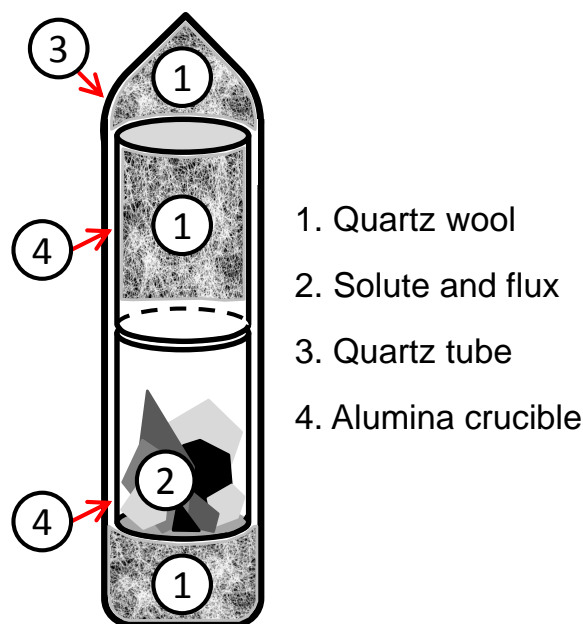


Figure 3.2: Packing scenario for a flux growth: constituents are combined in an alumina crucible, sealed in quartz ampoule.

shards) are placed below and above the crucibles in order to minimize the pressure exerted on the tube, and, given higher thermal expansion coefficient of alumina, as compared with quartz, to prevent outward pressure by the crucible upon heating [62].

To prevent the sample from reacting with air, the crucibles are sealed in an amorphous quartz ampoule under inert Ar atmosphere. This is done by first necking the tube and then sealing it off with a hydrogen-oxygen torch. The maximum temperature of such growth is 1200°C , as quartz starts to soften at higher temperatures. The resulting ampoule is placed in a furnace and a controlled method of heating and cooling is possible *via* a furnace equipped with a programmable temperature controller. Upon the completion of the growth, extra liquid is decanted by placing the inverted ampoule in a centrifuge, separating grown crystals from the flux. During the spin, the quartz wool or the alumina strainer separate the crystals from the flux, which flows to the bottom of the catch crucible where it solidifies. If the flux solidifies

around the crystals, it could later be removed mechanically or chemically, by etching the sample in a water-acid solution. The chemical etching process is complicated by finding a suitable etchant, one that would attack the flux more quickly than the crystals [62]. A detailed summary of etchants for various metals is given in Ref. [394].

High vapor pressure can be contained by double-sealing the quartz tube within a larger tube or by using a metal (Ta, Ni, Nb or Al) instead of a quartz ampoule. When using a metal ampoule, the alumina strainer can be replaced by a metal one – a second cap in which small holes have been drilled, placed in the middle of the sealed tube Fig. 3.2(d). The growth is sealed by welding a metal cap on top of the metal tube in partial Ar atmosphere using an arc melter, shown in Fig. 3.5(a).

An example of a self flux growth is the synthesis of ScGa_3 and LuGa_3 [357], shown in Fig. 3.1. Chunks of Sc or Lu (Hefa Rare Earth 99.999%) with Ga (Alfa Aesar 99.9999%) were combined in a ratio of 1:9 using packing method, shown in Fig. 3.2(a). The following temperature profile was used:

$$\text{R. T.} \xrightarrow{2 \text{ h}} 930^\circ\text{C} \text{ (2 h)} \xrightarrow{48 \text{ h}} 760^\circ\text{C} \rightarrow \text{spin} \quad (3.1)$$

Metallic cubic crystals with well-formed facets up to $2 \times 2 \times 2 \text{ mm}^3$ in size were obtained. In order to eliminate possible stress and strain in as-grown crystals, cubes of both ScGa_3 and LuGa_3 were wrapped in Ta foil (since Ta acts as oxygen getter) and annealed at 800°C for a week in a quartz ampoule, partially filled with Ar.

While growth of binary compounds can be somewhat straightforward at times, this is not always the case. Moreover, the process becomes even more complicated when the number of reactants is increased. The number of ternary phase diagrams is much lower and only a limited number of temperature cuts is generally available [389]. In some cases, even though a recipe is optimal for one member of the series, the other members cannot be grown in the same way. Although the growth of one phase over

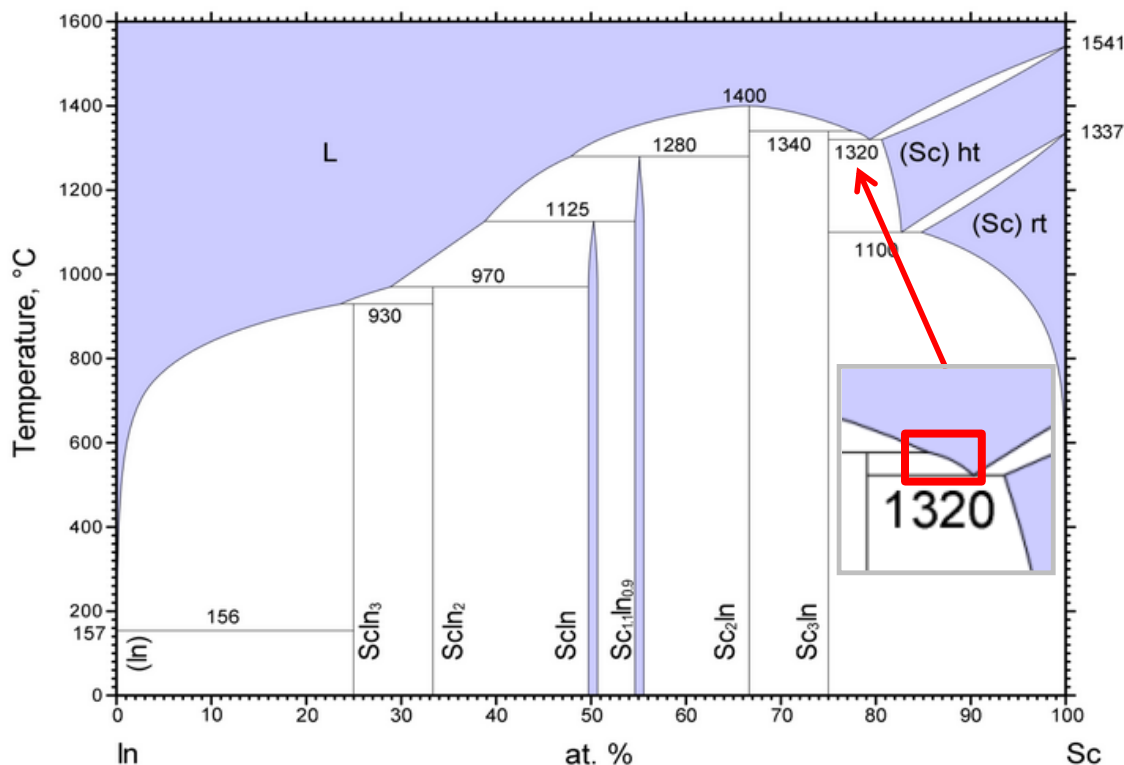


Figure 3.3: Single crystal growth of Sc_3In is complicated by high melting temperatures and short liquidus line [389].

another is governed by their respective stabilities, such data are often not available and are hard to model reliably, calling for a trial and error approach. While the accidental growth of undesired secondary phases may appear to be troublesome, it is often a source of new and interesting materials [62].

Whenever single crystal samples are not available, polycrystalline samples can be prepared either by arc melting or solid state reaction. The latter is more common for oxides or chalcogenides while the former is generally applied to metalloids. Arc melting involves weighing out the components in stoichiometric ratios and melting them with an electric arc in an inert atmosphere, using the arc melter shown in Fig. 3.5(a). For elements with low vapor pressure, this method yields small mass losses ($< 1\%$), preserving the correct stoichiometry. Frequently, small crystallites form

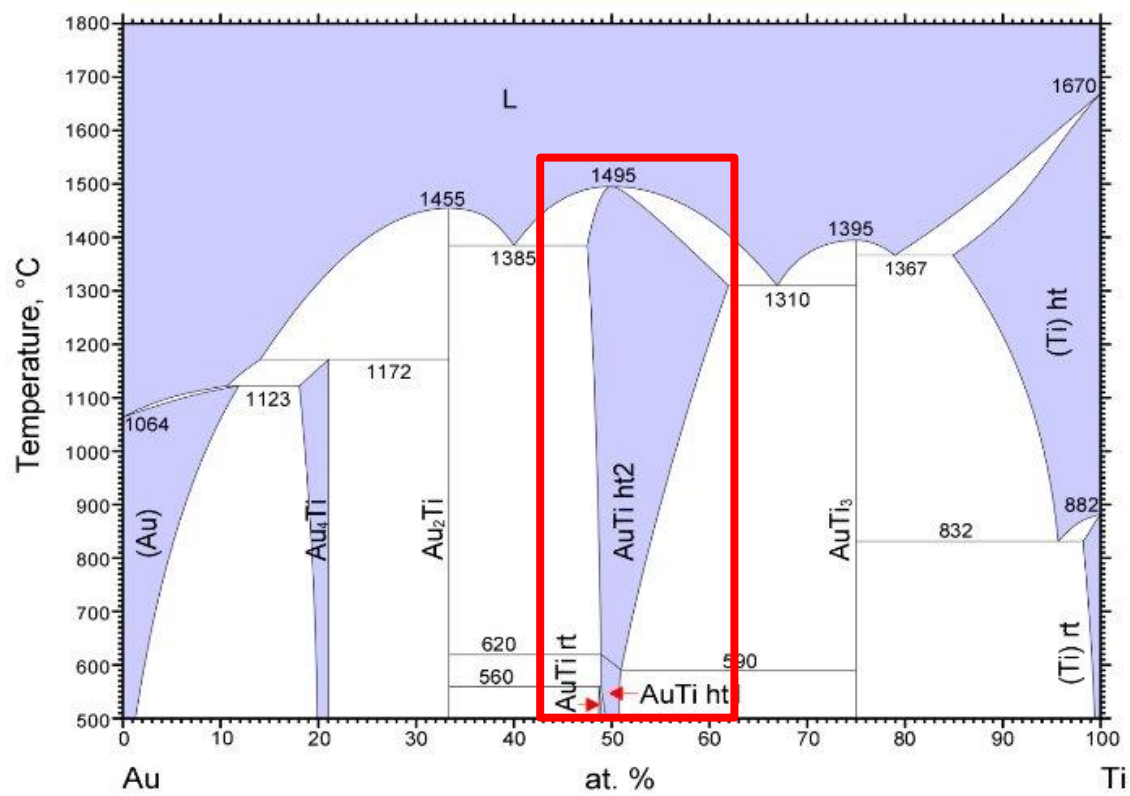


Figure 3.4: Single crystal growth of TiAu is complicated by a large width of formation and high melting temperature [389].

on the surface of arc-melted buttons, big enough to be used for single crystal x-ray diffraction experiments.

In the case of Sc_3In , obtaining single crystals is not possible due to high melting temperatures and short liquidus line (Fig. 3.3), calling for arc-melting. It has already been established [246] that the hexagonal Sc_3In (space group $\text{P6}_3/\text{mmc}$) forms non-stoichiometrically around the atomic ratio $\text{Sc}:\text{In} = 3:1$. In our studies, presented in Chapter 4, it was determined that the optimal composition, which yielded the highest Curie temperature T_C and paramagnetic moment μ_{PM}^{exp} , was $\text{Sc}:\text{In} = 3.1:1$. Therefore, polycrystalline samples of Lu-doped $\text{Sc}_{3.1}\text{In}$ (Chapter 4) and Er-doped $\text{Sc}_{3.1}\text{In}$ (Chapter 5) were prepared by arc-melting Sc (Cerac 99.99%) with In (Alfa Aesar, 99.9995%) and Er (Cerac 99.99%) or Lu (Ames Laboratory, 99.999%). The mass losses for both studies were no more than 0.3 %. The arc-melted buttons were subsequently wrapped in Ta foil and annealed under inert atmosphere in a quartz ampoule for over two weeks using following temperature profile:

$$\text{R. T.} \xrightarrow{\text{step}} 950^\circ\text{C} (96 \text{ h}) \xrightarrow{\text{step}} 850^\circ\text{C} (96 \text{ h}) \xrightarrow{\text{step}} 750^\circ\text{C} (96 \text{ h}) \xrightarrow{96 \text{ h}} \text{R.T.} \quad (3.2)$$

Arc-melting was also implemented for the case of TiAu , where high melting temperatures and large width of formation (Fig. 3.4), did not allow for single crystal synthesis. Annealing was performed but did not improve physical properties.

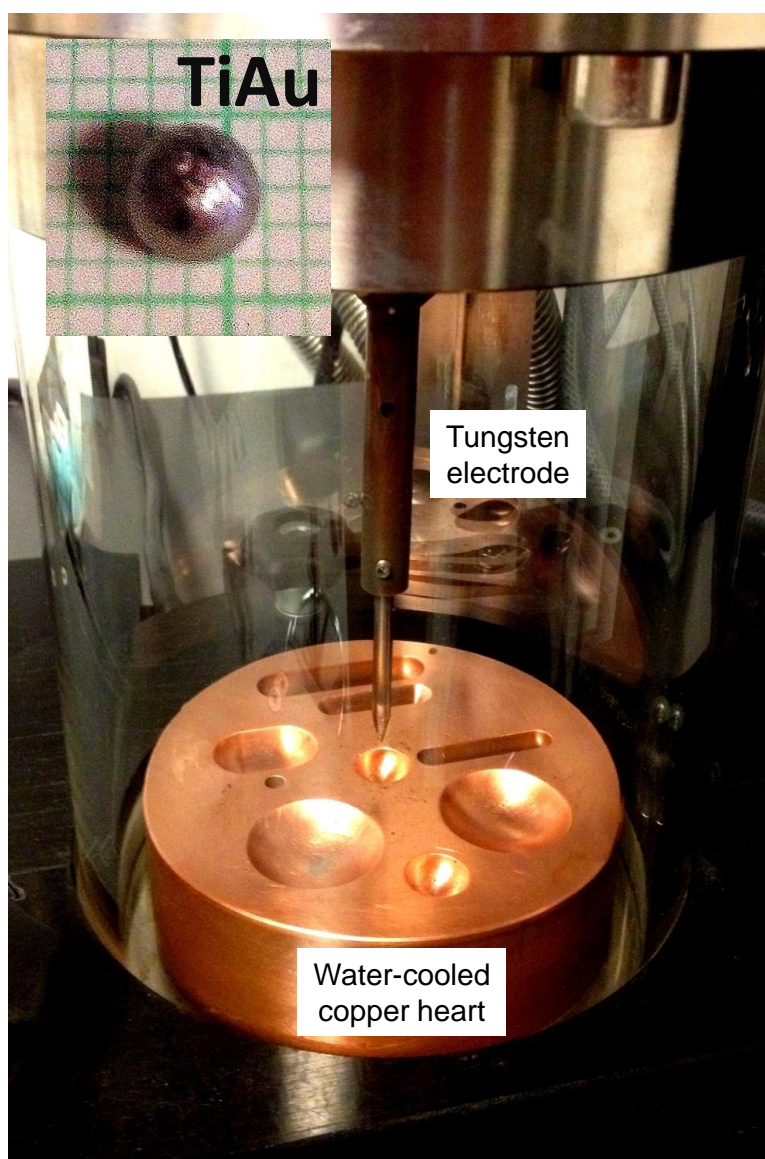


Figure 3.5: The arc melter, along with a TiAu sample prepared using it (inset).

3.2 Crystallography and X-ray Diffraction

Solids can be divided into two broad categories with respect to their structure: crystalline and noncrystalline [342]. Crystalline materials can be further separated into those occurring in a single crystal form (the orientation of the crystallographic axes is the same throughout the sample) and those found to be polycrystalline (the crystallographic axes of individual grains are oriented independently of each other) [342]. In an ideal single crystal, atoms are arranged in strictly periodic arrays, extending in all three dimensions, with a well-defined position of each of the atoms that can be easily determined. The surroundings of any two equivalent atoms are identical, no matter how far apart they are separated, producing what is known as long-range crystallographic order [342].

When describing a crystal, it is common to ignore the actual atoms and ions and focus on the lattice, a three dimensional array of points [86]. The unit cell is defined as the constituting basis for the crystal lattice, determined by vectors $(\vec{a}, \vec{b}, \vec{c})$ and the angles between them $\alpha = (\vec{b}, \vec{c})$, $\beta = (\vec{a}, \vec{c})$, $\gamma = (\vec{a}, \vec{b})$, as shown in Fig. 3.6. There are seven types of units cells (and, consequently, lattice systems), which have different edge lengths and internal angle measures.

Within a unit cell, atoms can occupy different positions: on the corners (simple), inside the body (body-centered), on the face (face-centered) or on the base (base-centered). However, not all of the combinations of the crystal systems and lattice centerings are necessary to describe all possible lattices, as several of these are equivalent to each other. The reduced number is fourteen, as shown in Fig. 3.6.

The lattice can also be thought of as a series of regularly arranged, parallel rows or planes. A family of planes, members of which are equidistant from one another, is characterized by three integers (h, k, l) , known as the Miller indices [86].

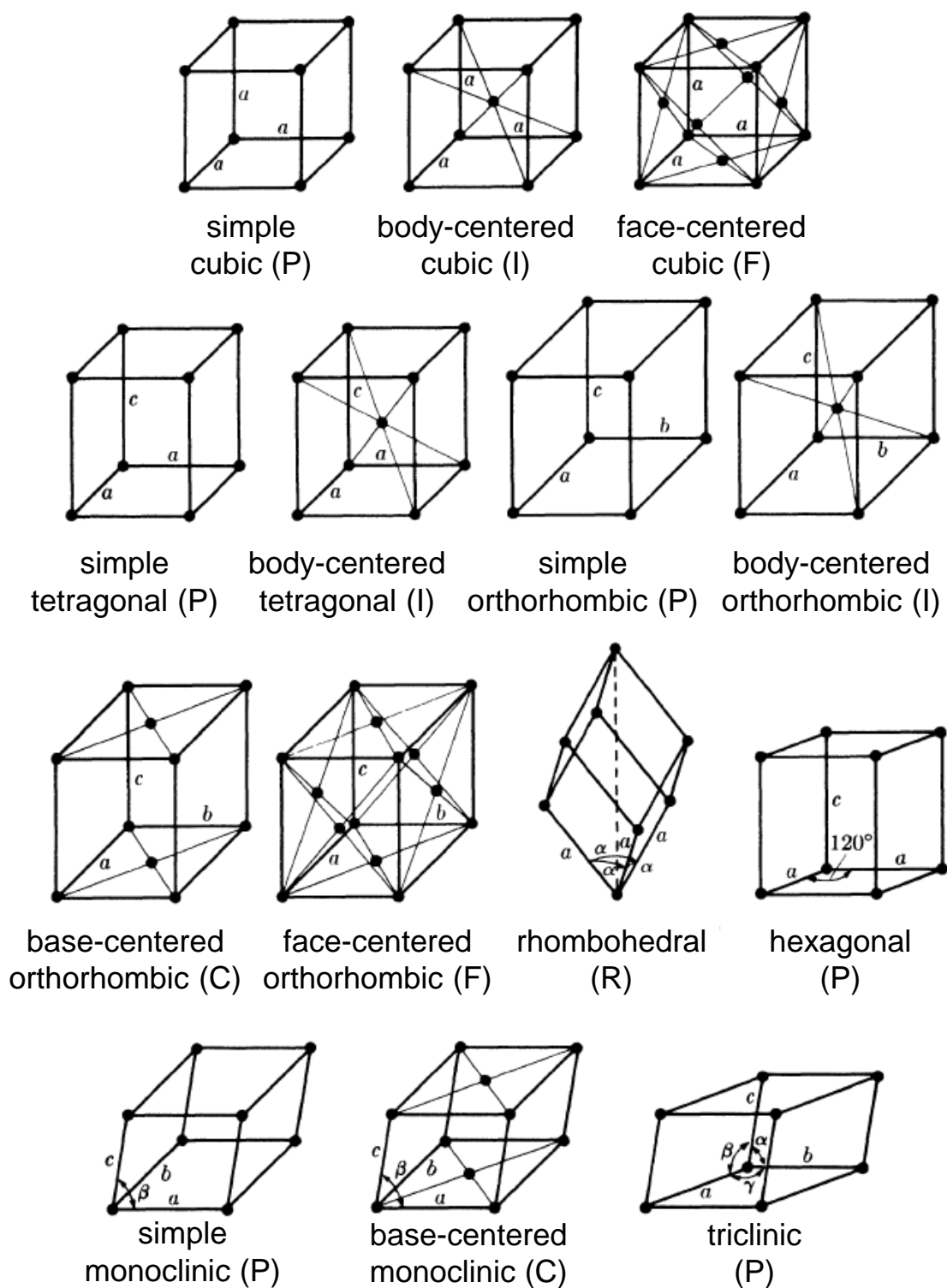


Figure 3.6: The fourteen Bravais lattices [86].

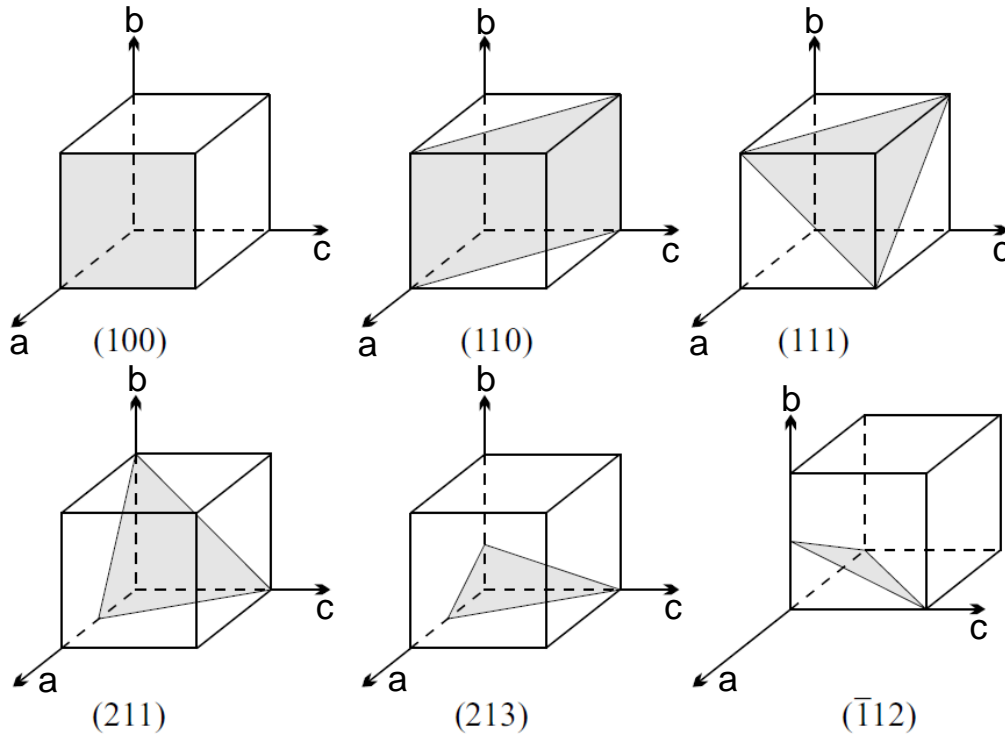


Figure 3.7: Planes in a cubic lattice and their Miller indices [144].

These are defined as the reciprocals of the fractional intercepts which the plane makes with the crystallographic axes. For example, if the Miller indices of a plane are (h, k, l) , then the plane makes intercepts of $1/h$, $1/k$ and $1/l$ with the axes, and, if the axial lengths are a , b and c , the actual intercepts would be a/h , b/k and c/l (Fig. 3.7).

One of the best methods used to determine the crystal structure of a given material is x-ray diffraction. It relies on constructive and destructive interference of monochromatic x-rays and a crystalline sample, governed by the Bragg's law:

$$n\lambda = 2d \sin \theta \quad (3.3)$$

where n is the order of diffraction, d is the spacing of crystallographic planes, λ is the incident wavelength, and θ is the incident angle [86].

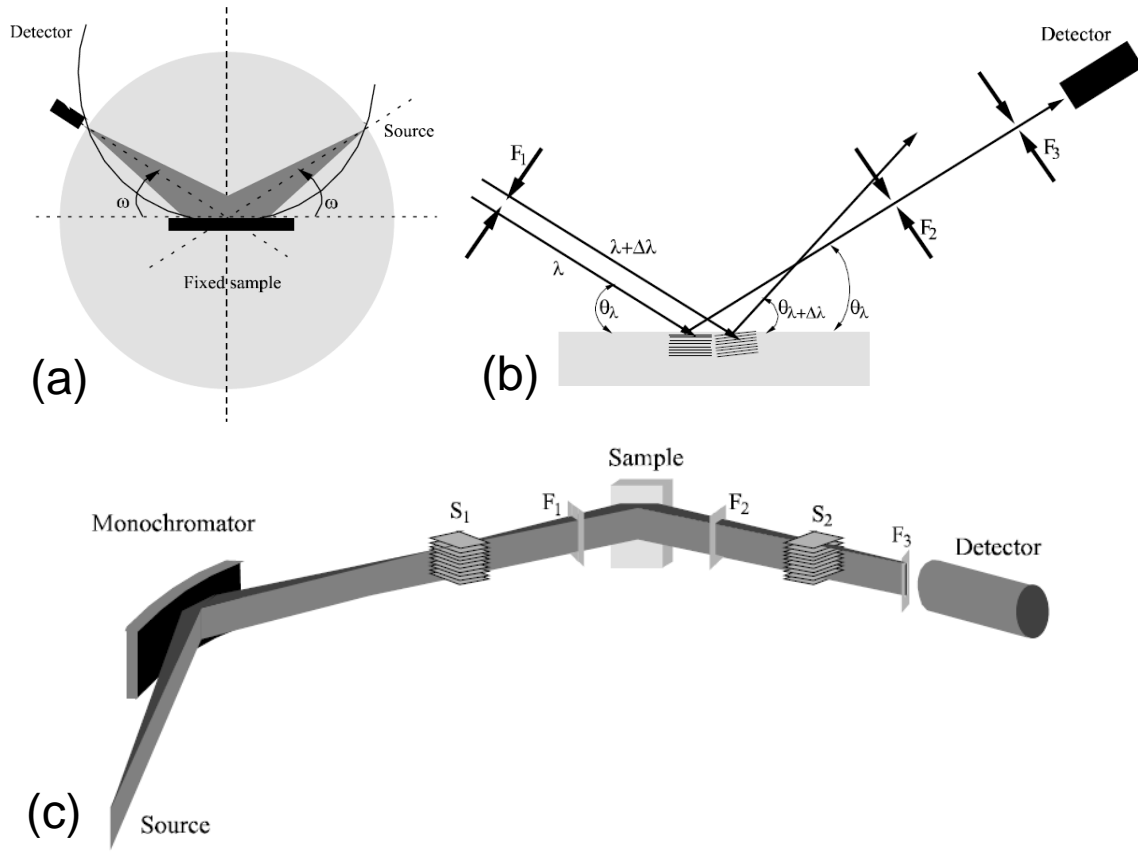


Figure 3.8: (a) The schematic for the Bragg-Brentano diffractometer configuration. (b) Adjustable slits that control the intensity of incident and diffracted beams. (c) The path of the x-ray beam in a diffractometer, equipped with a monochromator [144].

In an x-ray diffraction experiment, the layers of atoms in a crystal can be thought of as a three-dimensional collection of slits, which produce a pattern that changes with the incident angle. Since diffraction occurs when the wavelength of the radiation is comparable to the characteristic spacing within the object causing the diffraction, x-rays, with wavelength λ typically between 0.02 \AA and 100 \AA , are ideally suited to probe lattice spacing [86].

The x-rays, produced in the cathode tube are collimated and directed onto the sample's surface. The data are taken using Rigaku D/Max diffractometer with $\text{CuK}\alpha$ radiation ($\lambda = 1.5406 \text{ \AA}$) and a graphite monochromator, as depicted in Fig. 3.8. As both the x-ray source and the detector are moved to different angles, corresponding

intensity is recorded. Samples are typically scanned at room temperature for 2θ ranging from 5° to 90° , with 0.03° step intervals and 3 second collection time for each step. In order to improve the particle statistics, the sample stage is set to rotate at $60^\circ/\text{s}$.

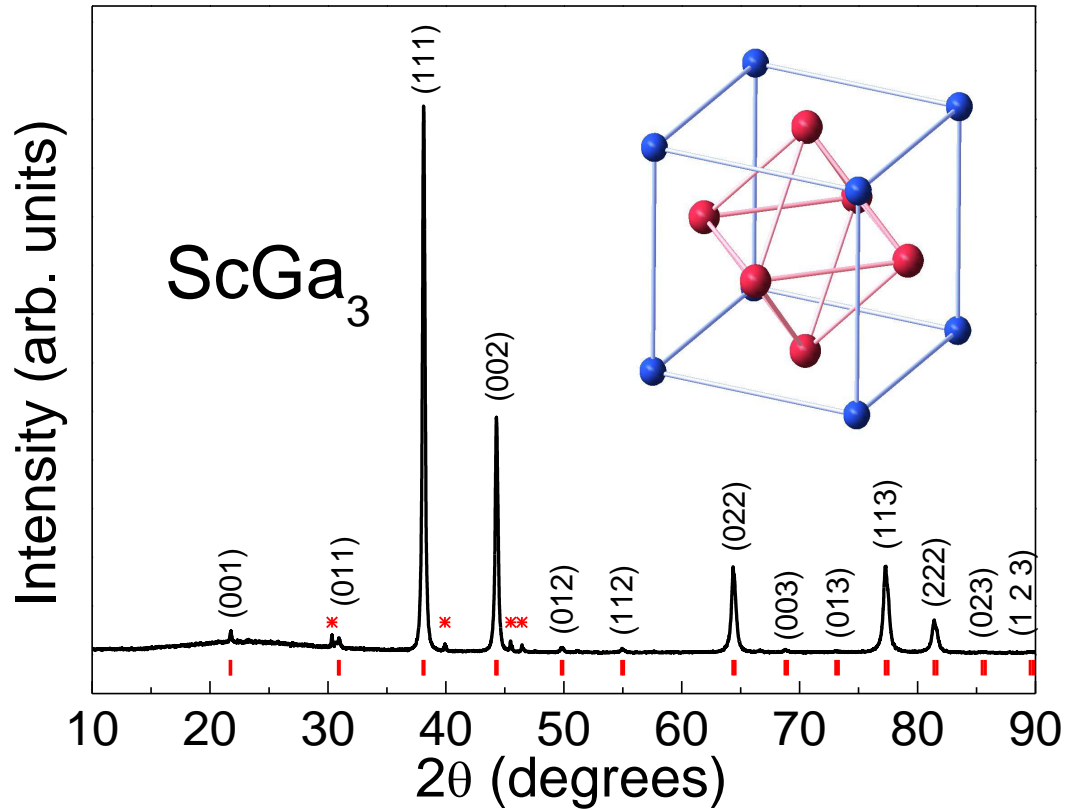


Figure 3.9: An example of a powder diffraction pattern for ScGa_3 with Miller indices for all peaks [357]. Asterisks represent flux, present on the surface of single crystals. Inset: the $Pm\bar{3}m$ crystal structure of ScGa_3 [389].

A sample used for powder x-ray diffraction is prepared by grinding either polycrystalline or single crystals into fine powders. A sample made in such a way will contain crystallites that are randomly oriented in all possible directions, yielding a complete diffraction pattern, an example is shown in Fig. 3.9. For every set of planes, there is a small percentage of crystallites that are properly oriented to diffract, yielding a diffraction peak with respective Miller indices. The resulting pattern is then

compared with diffraction patterns expected for various compounds (ICDD-PDF 2012 database), using the MDI Jade 9 software package. Reference to the Miller indices, extracted from the x-ray diffraction pattern, is used to identify the phase or phases, present in a sample. Structural refinements are performed using *General Structure Analysis System* (*GSAS*) software package, allowing for the resolution of relative amounts of phases (for those with concentration higher than 5% by weight), and estimate lattice parameters as well as atomic positions.

The hardness of some polycrystalline samples renders powder x-ray diffraction experiments impossible. Another way of collecting room temperature diffraction data is to scatter the x-rays off the cross section (about 3 mm in diameter) of cut and polished specimens. For samples with diameter of about 5 mm, this was done using a Rigaku D/Max diffractometer with $\text{CuK}\alpha$ radiation. For smaller sample size, a more sensitive alignment is necessary, achievable *via* a custom 4-circle Huber diffractometer with graphite monochromator and analyzer in non-dispersive geometry, coupled to a Rigaku rotating anode source producing $\text{CuK}\alpha$ radiation (FSU, Siegrist Lab). For these data, lattice parameter information was extracted using *Winprep* software package [347].

Higher resolution diffraction data were collected on the BT-1 powder diffractometer at the NIST Center for Neutron Research. Collimators of 15', 20' and 7' were used before and after the Cu (311) monochromator ($\lambda = 1.5401 \text{ \AA}$) and after the sample, respectively, and data were collected in steps of 0.05° in the 2θ range of 3° to 168° . The resulting patterns were analyzed using *GSAS* software packages.

In order to obtain single crystal x-ray data (UT Dallas, Chan Lab), pieces of cut crystals were fixed to thin glass fibers with epoxy, then mounted on the goniometer head of an Enraf Nonius single crystal X-ray diffractometer equipped with a Nonius Kappa CCD detector and a Mo $K\alpha$ radiation source ($\lambda = 0.72073 \text{ \AA}$). All

intensity data were collected at room temperature. Structural models were obtained with direct methods using *SIR971* and models were refined with *SHELXL97.2*. Final models include extinction corrections and anisotropically modeled atomic displacement parameters.

3.3 Magnetization Measurements

Tunneling of Cooper pairs, predicted in 1962 by B. D. Josephson [180] is the underlying principle of what is now known as the Josephson junction – two superconductors, separated by an insulating barrier. Shortly after the effect was observed experimentally in 1963 by Anderson and Rowell [18], the Josephson junction found a wide range of applications as part of superconducting computing circuits with switching times on the order of picoseconds. An example of such a device is a SQUID (Superconducting Quantum Interference Device), which is the crucial component of the Quantum Design (QD) Magnetic Property Measurement System (MPMS), shown in Figs. 3.10 and 3.11. During DC magnetization measurements, a constant field is applied to the measurement region as the sample is moved through the four coils, shown in Fig. 3.12. According to Faraday’s law, this induces a current in the coils, which are inductively coupled to the SQUID sensor, allowing for probing of the magnetic properties of the sample. The conversion between flux and current is incredibly accurate, capable of resolving a change in the external magnetic field on the order of 10^{-15} T, which corresponds to the magnetization detection limit of 10^{-8} emu [104]. The coil configuration, frequently referred to as the second-derivative (or second-order) gradient, is effective in suppressing the noise in the detection circuit, caused by fluctuations in the large magnetic field of the superconducting magnet [340]. Such configuration is shown in Fig. 3.12, along with the resulting signal.

As-measured temperature-dependent magnetization data in units of emu are scaled by mass m (g), field H (Oe) and molecular weight MW (g/mol), in order to convert them to molar susceptibility with the units of emu/mol_{FU} :

$$\chi \left[\frac{\text{emu}}{\text{mol}} \right] = \frac{M[\text{emu}] \cdot MW[\text{g/mol}]}{H[\text{Oe}] \cdot m[\text{g}]} \quad (3.4)$$

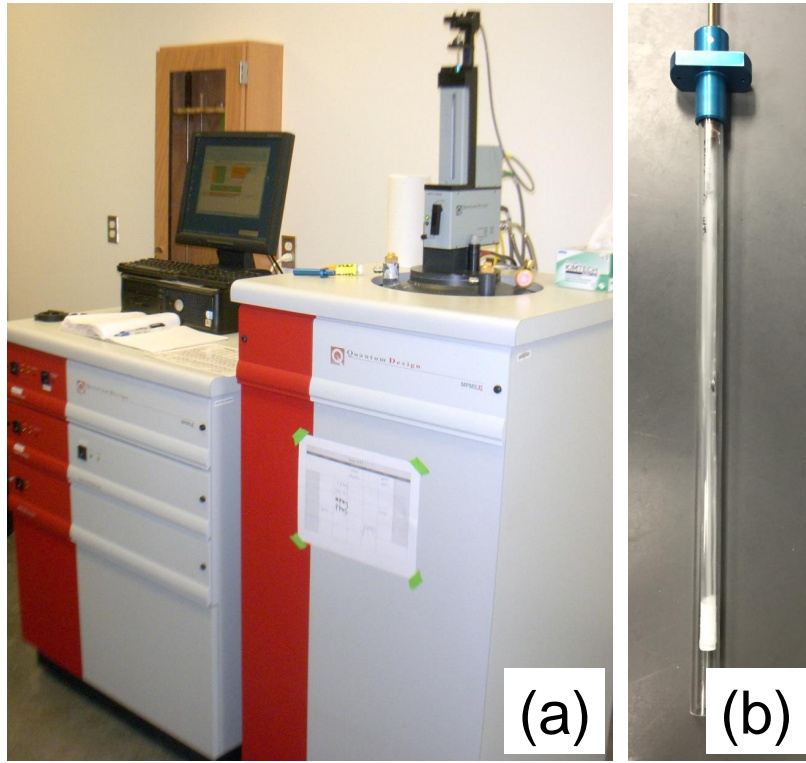


Figure 3.10: (a) QD MPMS instrument along with the (b) sample holder.

Similarly, the field-dependent data are scaled using the relation $1 \mu_B/\text{atom} = 5585 \text{ emu/mol}$, yielding:

$$M\left[\frac{\mu_B}{\text{atom}}\right] = \frac{M[\text{emu}] \cdot MW[\text{g/mol}]}{5585 \cdot m[\text{g}]} \quad (3.5)$$

Since for some samples hysteretic behavior can be observed, both zero-field cooled (ZFC) and field-cooled (FC) DC magnetization measurements are generally performed. The temperature range of MPMS in a standard configuration is 2 to 400 K. For higher temperatures, the magnetization data were collected using the Vibrating Sample Magnetometer option in a QD Physical Property Measurement System (PPMS) equipped with an oven (SUNY Stony Brook, Aronson Lab), with maximum temperature limit of 800 K. For temperatures under 400 K, the samples are mounted in a plastic straw, as shown in Fig. 3.12, while for higher temperatures,

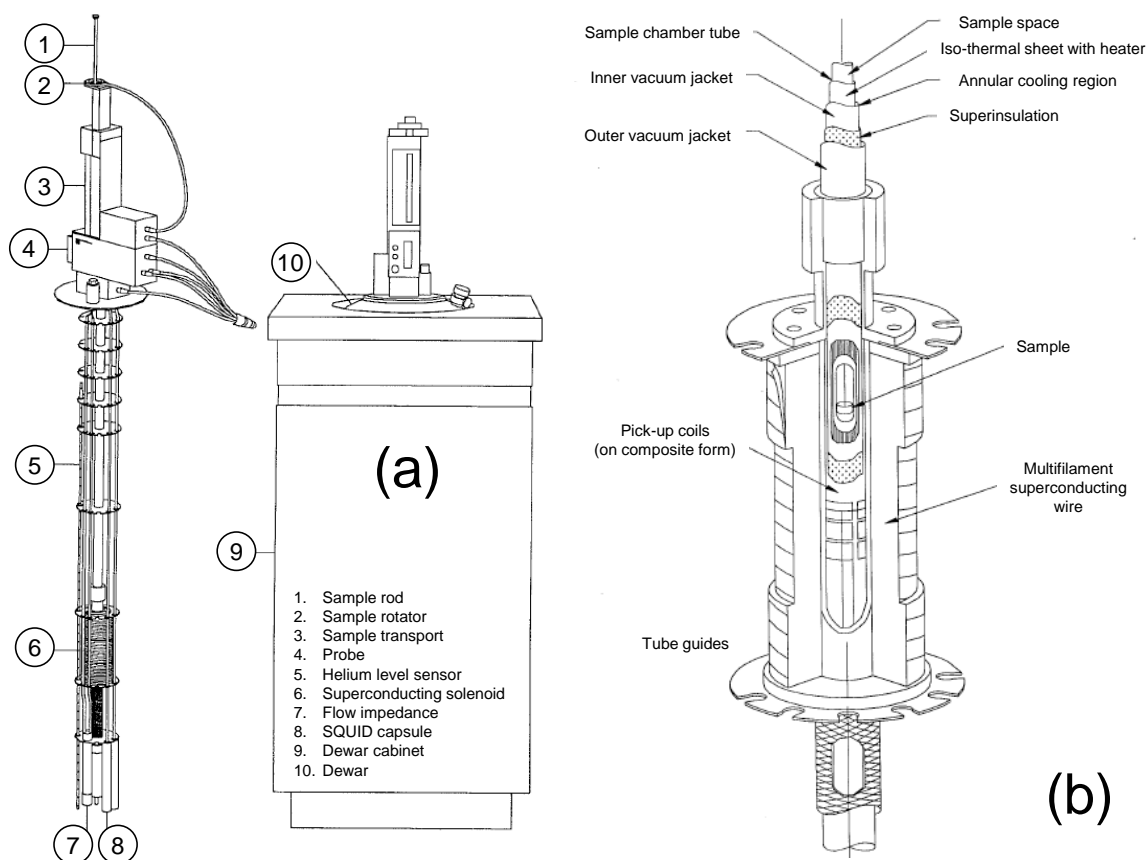


Figure 3.11: (a) Main components of the MPMS system along with (b) the MPMS magnet [340].

the samples are mounted in a brass holder or wrapped in aluminum foil. Whenever possible, temperature- and field-dependent magnetization measurements are recorded with the magnetic field H parallel or perpendicular to the crystallographic axes a , b or c in order to check for anisotropic properties.

While fields up to 7 T are readily available using the QD MPMS system, higher fields are provided by a 65 T short-pulse magnet at National High Magnetic Field Laboratory in Los Alamos. The pulsed-field magnetization experiments use a 1.5 mm bore, 1.5 mm long, 1500-turn compensated-coil susceptometer, constructed from 50 gauge high-purity copper wire [137]. When a sample is within the coil, the signal is $V \propto (dM/dt)$, where t is the time. Numerical integration is used to evaluate M . Rod-like samples are mounted within a 1.3 mm diameter ampoule that can be moved

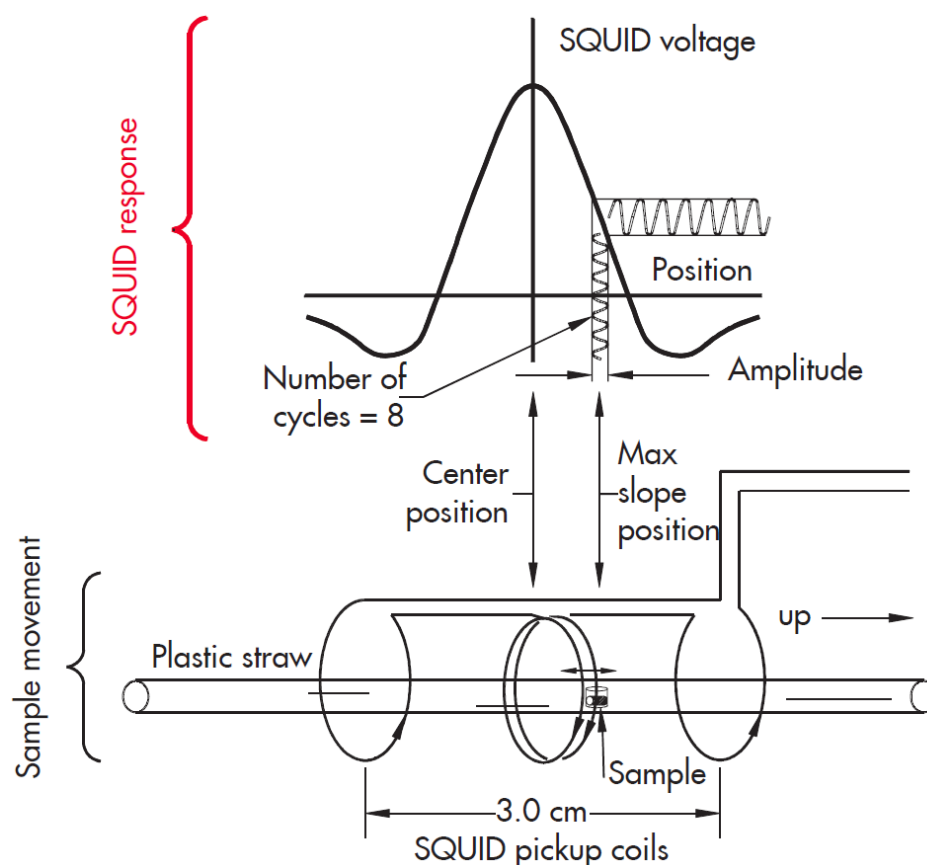


Figure 3.12: A schematic showing how magnetic properties of a sample are recorded using a second derivative gradient coil configuration [340].

in and out of the coil. Accurate values of M are obtained by subtracting empty-coil data from that measured under identical conditions with the sample present. The susceptometer is calibrated by scaling low-field M values to match those recorded with a sample of known mass measured in a commercial SQUID or vibrating-sample magnetometer. The accuracy of the $M(H)$ data is restricted by the mass measurement of the sample to around one percent. But in the regions of overlap with the low-field QD MPMS data the agreement is very good. The susceptometer is placed within a ^3He cryostat providing temperatures down to 0.4 K. Care is taken to avoid sample heating due to induced eddy currents. B is measured by integrating the voltage induced in a ten-turn coil calibrated by observing the de Haas-van Alphen oscillations of the belly orbits of the copper coils of the susceptometer [137].

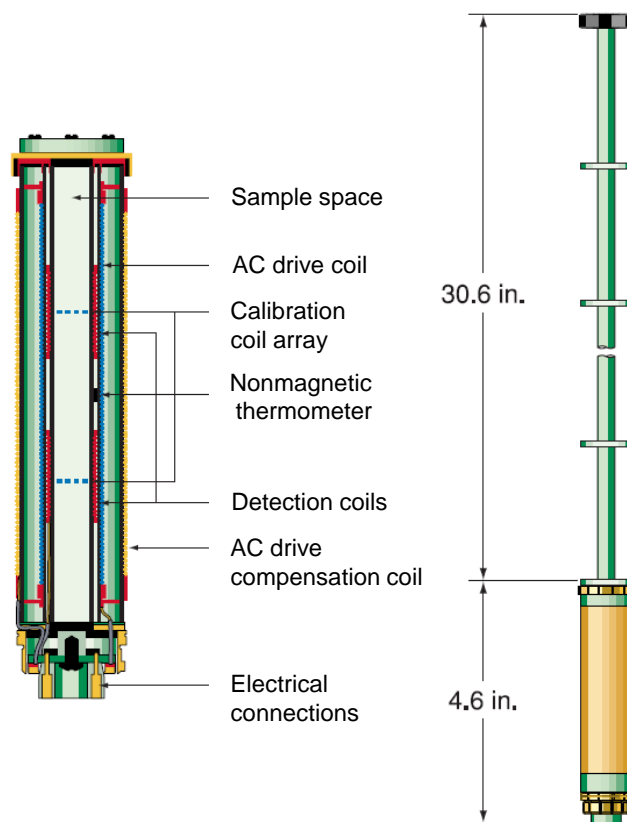


Figure 3.13: AC magnetic susceptibility coils configuration and sample insert [236].

During AC magnetic susceptibility measurements, an alternating field is applied to the measurement region either by itself or in addition to the constant magnetic field applied by the PPMS superconducting magnet. The schematic depicting the AC magnetic susceptibility insert along with the coils set is shown in Fig. 3.13. The PPMS does not utilize QD SQUID technology, instead the signal is analyzed with a digital signal processor. Typically, AC susceptibility measurements are carried out for frequencies f between 10 and 10^4 Hz, in a temperature range from 2 K to 50 K. The real and imaginary components of the susceptibility are recorded, as the imaginary components are in phase with the driving signal while the real components are 90° out of phase [236]. During each measurement, several waveform blocks can be measured and averaged to reduce random noise in the signal [236].

For temperature below those accessible by the QD PPMS, measurements of AC magnetic susceptibility are performed in a ^4He Dewar down to ~ 1.17 K (UCSD, Maple Lab). For measurements in the temperature range $T \leq 4.2$ K, the temperature is controlled by immersing the AC susceptibility coils in a bath of ^4He and carefully reducing the vapor pressure above the bath using a Stokes pump. For data measured at $T > 4.2$ K, the AC magnetic susceptibility coils are positioned in the thermal gradient above the ^4He bath by manually adjusting the vertical position of the probe. An AC current is driven on the primary coils with a frequency of 15.9 Hz using a Linear Research LR700 AC resistance bridge, which produces an AC magnetic field with magnitude of ~ 0.3 Oe. This bridge is also used to measure the in- and out-of-phase components of the signal, induced on the secondary pickup coils. The secondary coils are balanced by counter-winding the wire to cancel background signals, induced by the oscillating AC magnetic field. A small offset in the measured signal due to minor imbalances in the home-built AC susceptibility coils is subtracted from the data. The data are then scaled so that their arbitrary units are proportional to emu/mol.

3.4 Specific Heat Measurements

The QD heat capacity option of the PPMS (Fig. 3.14) measures the heat capacity by adding and removing a certain amount of heat from the system while monitoring the change in temperature and maintaining a constant pressure:

$$C_p = \left(\frac{dQ}{dT} \right)_p \quad (3.6)$$

The heat capacity puck, shown in Fig. 3.15, consists of a small microcalorimeter platform which is suspended by eight thin wires that serve as the electrical leads for the embedded heater and thermometer as well as a structural and thermal connection to the platform. The sample is mounted on the platform by applying a thin layer of cryogenic grease, generally Apiezon H or N, which provides the required thermal contact with the platform. To ensure good coupling between the two, the samples should be as flat as possible and smaller than the size of the platform. The sample mass is limited by the increased relaxation time for larger samples, and a heat capacity signal for smaller samples comparable to that of the background, restricting typical sample mass to around 10 mg. The puck temperature is recorded by the puck thermometer, while the outside thermal shield helps maintain stable and uniform temperature. High pressure (on the order of 0.01 μ bar) ensures that no heat is lost as part of the exchange gas.

As is the case with the MPMS, the lower temperature limit of PPMS is 2 K. This, however, can be extended down to 0.4 K by using the QD ^3He PPMS insert (Fig. 3.14(b)). While the upper temperature limit for PPMS is 400 K, the relaxation technique, employed in the specific heat measurements, limits the upper bound for specific heat measurements to 100 K. The relaxation times are on the order of minutes at 300 K, compared with fractions of a second at 2 K, resulting in prohibitively long

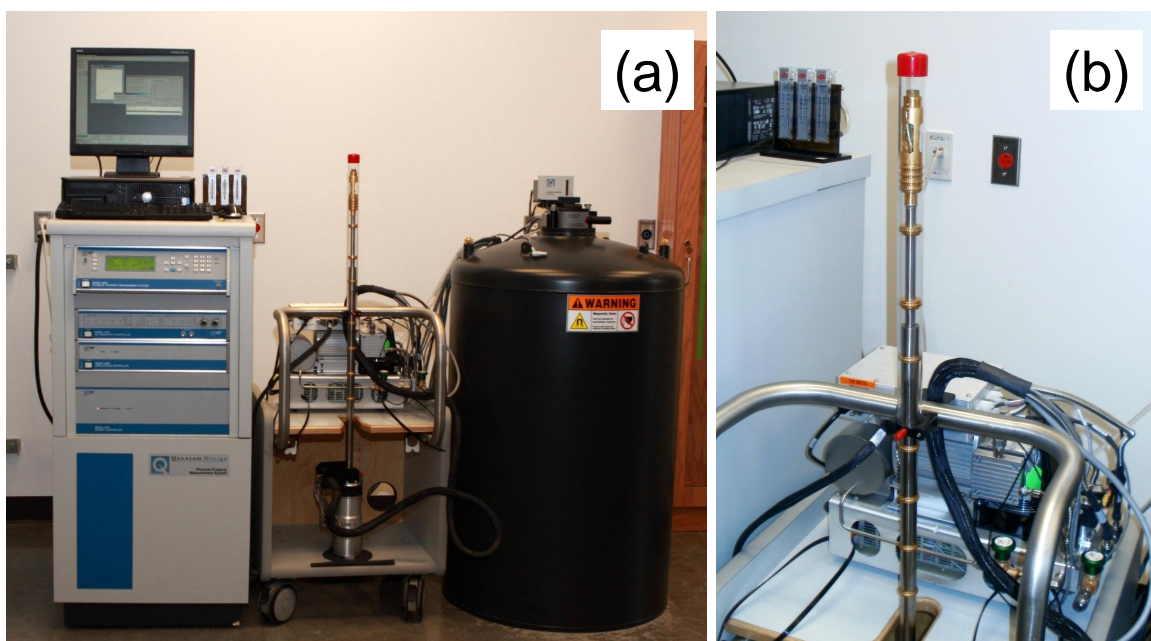


Figure 3.14: (a) QD PPMS instrument along with the (b) ^3He insert.

data collection cycles as the relaxation time is averaged over 10 values per data point. Moreover, the resolution is considerably worse for higher temperatures [236].

Prior to measuring heat capacity of the sample, an addenda measurement is recorded for a greased, empty puck in order to separate the heat capacity contribution of the sample from that of the entire puck. The measurement of each data point consists of multiples stages. After an initial temperature has been stabilized, a predetermined amount of heat is applied at a constant power for a fixed time. After the power is terminated, the temperature of the platform relaxes toward the puck temperature, corresponding to a cooling period [236]. Temperature data taken on both warming and cooling are then analyzed first using the simple model and then the 2τ model. The simple model assumes good coupling between the sample and the platform, ensuring the same temperature for both:

$$C_{\text{total}}\left(\frac{dT}{dt}\right) = -K_w(T - T_b) + P(t) \quad (3.7)$$

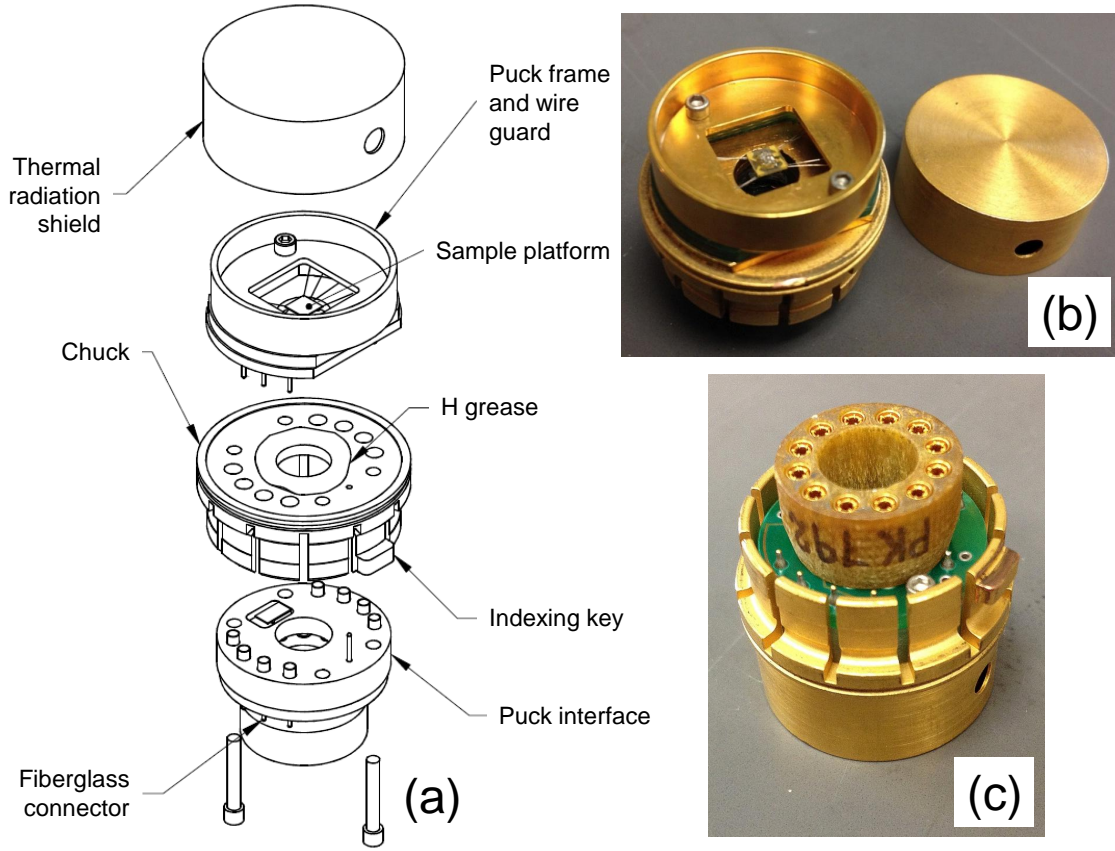


Figure 3.15: (a) Exploded view of the specific heat puck [236] along with (b) top and (c) bottom perspectives.

where C_{total} is the total heat capacity of both the sample and the platform, K_w is the thermal conductance of the supporting wires, T_b is the temperature of the thermal bath (puck frame) and $P(t)$ is the power supplied by the heater. Except for the addenda measurements, a 2τ model is also evaluated. For the 2τ model, it is assumed that the thermal contact between the sample and the platform is poor, hence two time constants τ_1 and τ_2 are employed. The heat flow between the platform and the sample as well as between the platform and the puck are estimated as follows [236]:

$$C_{\text{platform}} \left(\frac{dT_p}{dt} \right) = P(t) - K_w(T_p(t) - T_b) + K_b(T_s(t) - T_p(t)) \quad (3.8)$$

$$C_{\text{3Sample}} \left(\frac{dT_s}{dt} \right) = -K_g (T_s(t) - T_p(t)) \quad (3.9)$$

where C_{platform} and C_{3Sample} are the heat capacities of the platform and sample, respectively, K_g is the thermal conductance between the two due to the grease. The temperatures $T_p(t)$ and $T_s(t)$ correspond to the platform and sample, respectively.

By fitting the actual measurement with the above relations, the heat capacity parameters are extracted from whichever fit yields better least-squares fit. If the fit to the 2τ model does not converge, the simple model is assumed, indicating perfect coupling between the sample and the platform. The fitting process can be complicated by either poor mounting or small sample signal, relative to that of the platform, yielding an unrealistic 100% coupling value.

3.5 Resistivity Measurements

The electrical resistivity of metals is dominated by collisions of the conduction electrons with lattice phonons at room temperature and with impurity atoms and defects at temperatures closer to the absolute zero (see Section 2.4). From the electron theory of metals, this resistivity can be described as a sum of several contributions, according to Eq. 2.119. The residual resistivity ratio (RRR) is commonly listed to reflect the level of purity:

$$RRR = \frac{\rho(300 \text{ K})}{\rho(0 \text{ K})} \quad (3.10)$$

where $\rho(0 \text{ K})$ is the resistivity value at the lowest available temperature. For exceptionally pure materials, the RRR value can be as high as 10^6 , while for some alloys it can be as low as 1.1 [200].

Typically, the samples used for resistivity measurements are rather small, which makes their overall resistance comparable to that of contacts and leads, attached to the sample. In order to separate the two, it is common to use the four-probe method, also known as Kelvin sensing. In a four-probe resistivity measurement, the current I is supplied by the outside leads and the voltage drop V across the sample is measured by the inner leads, as shown in Fig. 3.16(a). This method is very accurate because there is almost no current in the loop used to measure voltage, which means that the recorded voltage drop corresponds only to the sample. The resistance R is then calculated from the Ohm's law:

$$R = \frac{V}{I} \quad (3.11)$$

Since resistance R depends on the sample geometry, the intrinsic property

such as resistivity ρ is more appropriate when comparing various systems. Based on the dimensions of the sample, the resistivity ρ can be calculated from the resistance R :

$$\rho = R \frac{a \cdot b}{L} \quad (3.12)$$

where a and b are the dimensions of the cross-section of the sample and L is the distance between two inner leads, as shown in Fig. 3.16(a).

The maximum excitation current value I is adjustable and should be chosen

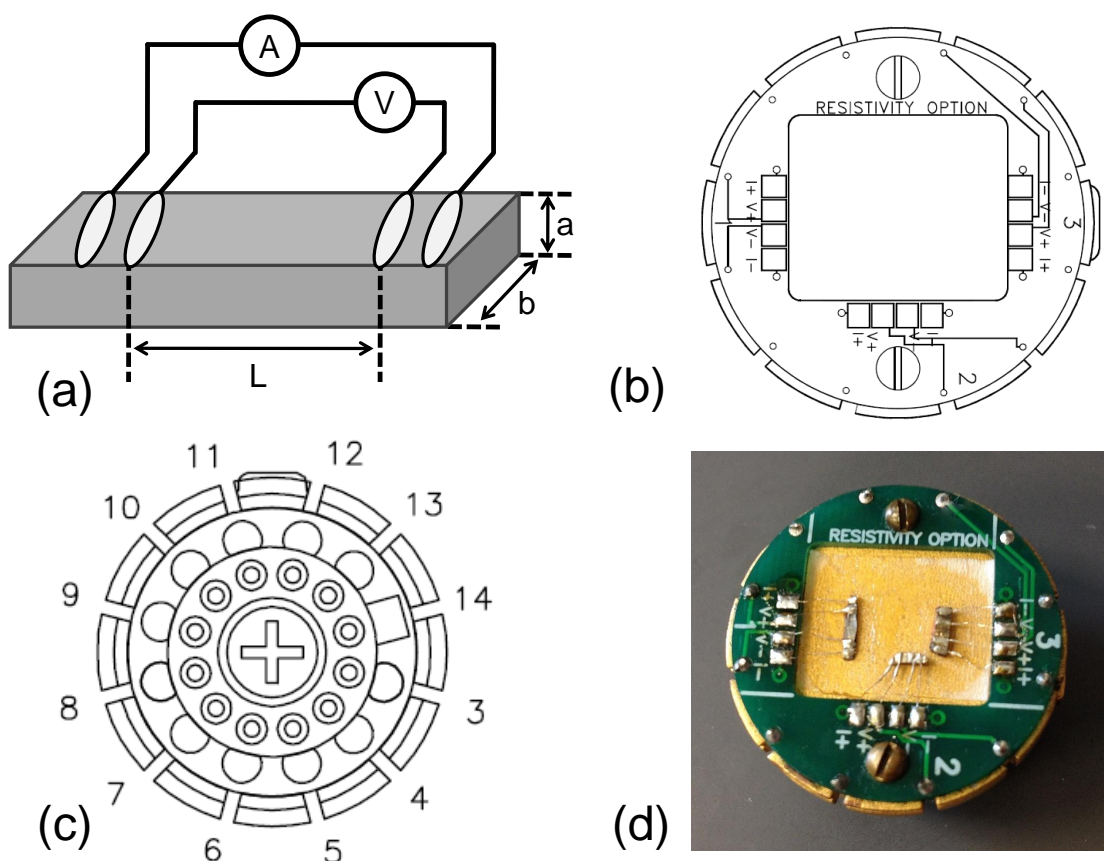


Figure 3.16: (a) Four-probe resistivity measurement. (b) Interface of the resistivity puck. (c) The bottom view of the resistivity puck features 12 pin connections, identical to those seen in the specific heat puck in Fig. 3.15 [236]. (d) A set of three samples, prepared for a resistivity measurement.

carefully; while it needs to be sufficiently high to yield a good signal, it must not exceed $5000 \mu\text{A}$, as higher values can overheat or even damage the sample [236]. Each resistivity puck is capable of measuring up to three samples simultaneously. The interface, shown in Fig. 3.16(b), contains three groups of contacts, each of which includes one positive and one negative terminal for both current and voltage. The 12 pins at the bottom of the resistivity puck (Fig. 3.16(b)) are again split into three groups, one group for each of the samples (or channels). An example of a prepared resistivity puck is shown in Fig. 3.16(d). Platinum wires are attached to the polished surface of the samples using Epo-Tek H20E silver epoxy and soldered to the four puck terminals. Samples must be electrically isolated from and thermally in contact with the puck which is achieved by placing a piece of KimWipe, soaked in Apiezon N grease, between the sample and the puck. Whenever possible, the resistivity measurements are done on single crystals, with the current direction parallel to one of the crystallographic axes. The temperature range is limited by the range of PPMS to values between 2 and 400 K, which, as previously mentioned, can be extended down to 0.4 K by using the QD ^3He PPMS insert.

For some samples, DC resistivity data have high noise level which can be resolved by using the AC transport option. The same standard four-probe method is employed and an applied AC current along with the resulting AC voltage are recorded as a function of temperature or field. By changing the frequency and excitation current, lower noise levels are possible; the values are sample-dependent with an available frequency range between 1 Hz to 1 kHz and current values from $10 \mu\text{A}$ to 2 A [236]. While AC transport tends to result in lower noise data, it is optimized for relatively low resistances, as compared to the DC method. Additionally, only two channels can be used to measure samples at a time.

Pressure-dependent electrical resistivity measurements (UCSD, Maple Lab)

were carried out using a standard four-wire technique with platinum wires affixed to the surface of the sample using a two-part silver epoxy to ensure a small contact resistance. The sample was contained within a Teflon capsule, which was then placed within a steel (MP35N) cylinder and compressed between tungsten-carbide pistons within a beryllium-copper clamp. Within the Teflon capsule, equal parts by volume of isoamyl alcohol and n-pentane served as the pressure transmitting medium while a small piece of high purity tin was used as the manometer. The load was applied to the clamp at room temperature (well above the melting point of the pressure transmitting medium) thus ensuring nearly-hydrostatic conditions [174]. The superconducting transition temperature of the tin manometer was measured using embedded induction coils within the pressure clamp at low temperature [338]. The clamp was cooled in a Dewar using liquid helium as the primary cryogen; temperatures below 4.2 K were achieved by pumping on the Dewar and reducing the pressure of the helium vapor above the bath.

3.6 X-ray Photoemission Spectroscopy

Even though the majority of the structural compound information can be extracted from x-ray diffraction experiments, as described in the previous section, a minimum component concentration (typically around 5%) is necessary in order for the material to register in the diffraction pattern. To resolve lower concentrations, x-ray photoemission spectroscopy can be utilized. This powerful surface-sensitive quantitative technique is capable of registering the elemental composition as low as 0.1% by weight [73]. The principle of x-ray photoemission spectroscopy is based on the photoelectric effect (Fig. 3.17(a)): a beam of incident photons strikes the surface of the material and if photon's energy $h\nu$ is higher than the electron's binding energy E_B , a core electron leaves the surface. The resulting electron will have kinetic energy E_K that can be expressed as:

$$E_K = h\nu - E_B - \phi \quad (3.13)$$

where the work function ϕ can be compensated for. The resulting kinetic energy E_K is a function of the binding energy E_B , which is element-specific. This is used to identify particular elements, corresponding to the resonance peaks in an x-ray photoemission spectroscopy spectrum. The x-ray photoemission spectroscopy spectra are quantified in terms of peak intensities (or areas) and peak positions. It is important to note that while the incident x-ray can penetrate the sample deeply, the escaping depth of ejected electrons is limited by inelastic collisions within the solid to under 10 nm (or about three times the inelastic mean free path) [235]. Therefore, x-ray photoemission spectroscopy has severe limitations for studying bulk material as the surface composition can be substantially different from that inside the bulk. In order to cleanse the surface of contaminants an Ar sputtering gun is used. One of the

problems, encountered during the spectra analysis is the background signal, which is non-trivial in nature. This contribution results from the electrons located below the resolution level and can be fitted using one of the preset function of the Casa XPS suite, an example is shown in Fig. 3.17(d) [235].

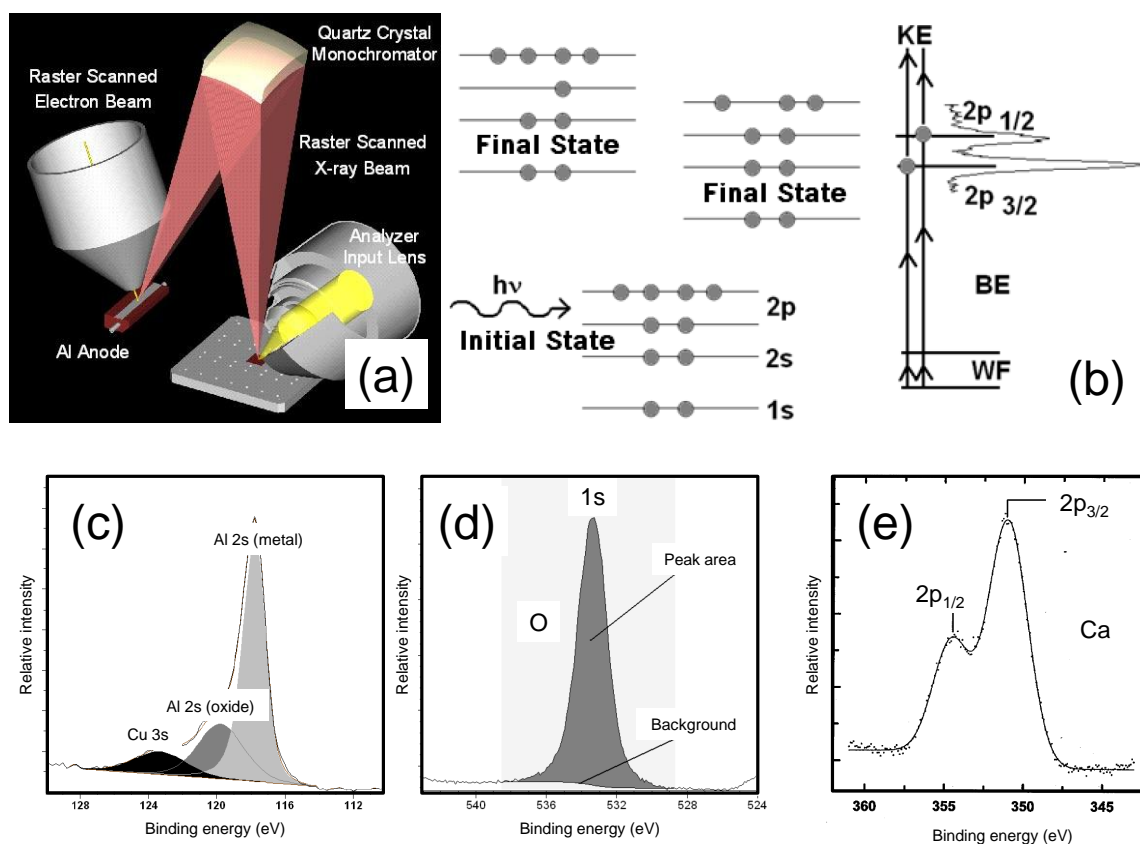


Figure 3.17: (a) Experimental layout of XPS Phi Quantera. (b) The mechanism of a peak doublet formation. (c) Deconvolution of a peak with elements whose binding energies are very similar. (d) Background subtraction fit. (e) A peak doublet of Ca [235].

The spectral peaks are named according to the orbital and spin quantum numbers (l and s) of the core levels from which they arise. For all orbitals where $l > 0$, spin-orbit splitting, shown in Fig. 3.17(b), is observed, resulting in two peaks

($j = l \pm 1/2$). The intensity ratio is proportional to j :

$$\frac{I_1}{I_2} = \frac{2j_1 + 1}{2j_2 + 1} \quad (3.14)$$

where $j_1 = l + 1/2$ and $j_2 = l - 1/2$. An example of such splitting is shown in Fig. 3.17(b), where the peaks' relative intensities have a ratio of 1:2. Due to element-dependent scattering intensity, when comparing intensities between various elements, the relative sensitivities must be taken into account [73]:

$$C_x = \frac{\frac{I_x}{S_x}}{\sum_i \frac{I_i}{S_i}} \quad (3.15)$$

where C_x , I_x , and S_x are the elemental concentration, intensity, and sensitivity, respectively while the ratio of I_i and S_i is summed over all constituent elements. In general, the concentration estimates C_x , obtained from a carefully analyzed spectrum using Eq. 3.15, will have error bars under 10%. While the x-ray photoemission spectroscopy technique is sensitive to all elements except for He and H, for some groups of elements, a systematic overlap of the spectral lines is possible. Deconvolution of peaks using a combination of Gaussian and/or Lorentzian line-shapes, shown in Fig. 3.17(c), is possible with Casa XPS software. Another solution is to analyze multiple transitions, arising from the same element [73].

The peak positions are used to differentiate between various oxidation states and to analyze chemical bonds: in elemental samples photoelectron core level peaks occur at the same binding energy while in compounds the peak positions shift due to ionic or covalent bonding. After initial alignment with the C1s peak ($E_B = 284.8$ eV [279]), the oxidation state of all elements in the spectrum can be estimated from tabulated values [279].

As mentioned earlier, due to limited depth resolution, samples used for x-ray photoemission spectroscopy must be homogeneous. Since the measurements are done in a high vacuum environment, air-sensitive samples do not present any issues. Moreover, this is a non-destructive technique, except for when prolonged sputtering is done (this feature is sometimes used for depth profiling [73]). Care must be taken when dealing with non-conductive samples as the ejected electrons create a charge on the sample's surface that accumulates over time and creates a barrier for future photoelectrons, shifting the resulting spectrum. Typically this is not a problem for conductive samples, which are grounded to the platen but might be problematic for semiconducting and insulating samples. This can be addressed by either using a charge neutralizer, which delivers a flux of low energy electrons to the surface, or by shifting the spectrum accordingly [235].

3.7 Hardness Measurements

As early as 300 BC, the hardness of a given material has been determined by its resistance to scratching or indentation by another material. To quantify geological samples, the well-known Mohs's scale was created in the beginning of the 19th century, ranging from 1 to 10, with 10 being the hardness of a diamond and 1 that of talc [134]. While this scale has proved to be useful for preliminary identification of minerals by geologists in the field, the standards are arbitrary – for example, the difference in hardness between 9 and 10 is much greater than that between 1 and 2. Moreover, the scale is not very quantitative since non-integer hardness values that fall within the same range are not easily comparable.

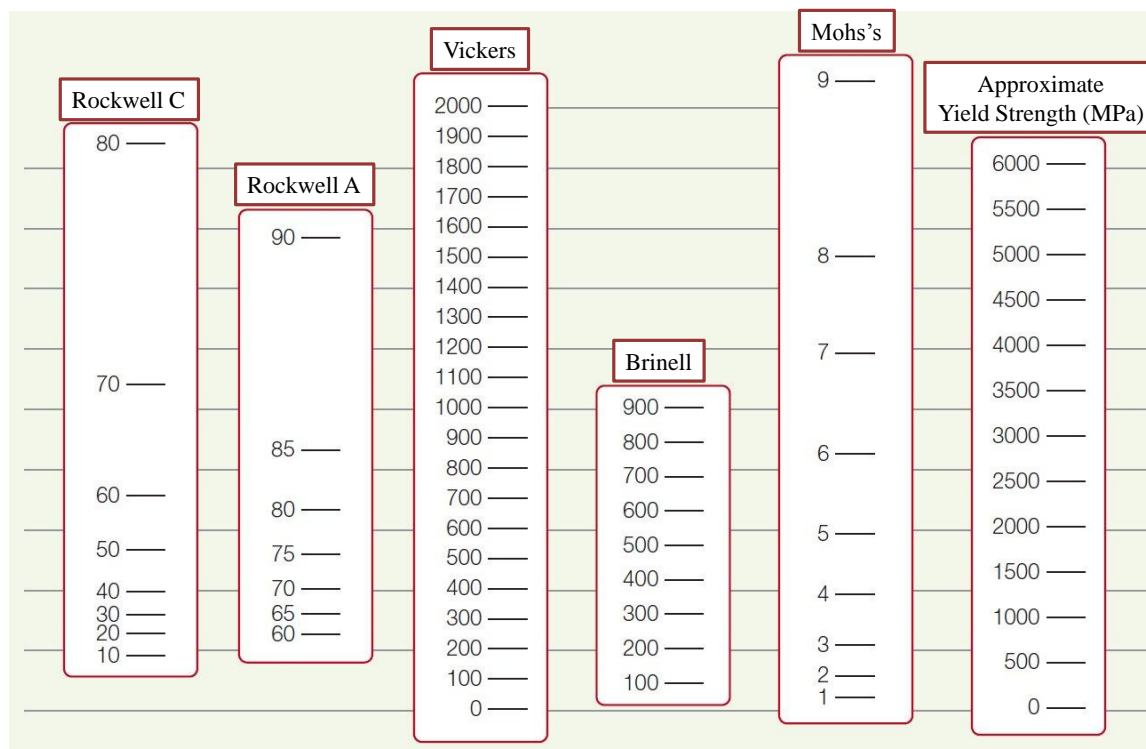


Figure 3.18: Scales for various hardness measurement methods compared to each other and the yield strength [26].

Currently, the four main methods of estimating hardness are conceptually the same: the depth or area of an indentation along with the force applied on the indenter for a certain time period is translated into a range of scales [134]. The difference lies in the hardness measurement is in the geometry of the indenter – a sphere (Brinell and Rockwell, Fig. 3.19(a)), a trigonal pyramid (Berkovich, Fig. 3.19(b)), a square pyramid (Vickers, Fig. 3.19(c)), or an elongated four-sided pyramid (Knoop, Fig. 3.19(d)) [134]. Depending on the material, the size of the irreversible indentation created in the specimen's surface will range from macro (millimeters), to micro (microns), and even to nano (nanometers). It is important to note that conversion between various scales cannot be exact due to the different loads, shapes of the indenters, as well as elastic properties and material homogeneity that affect

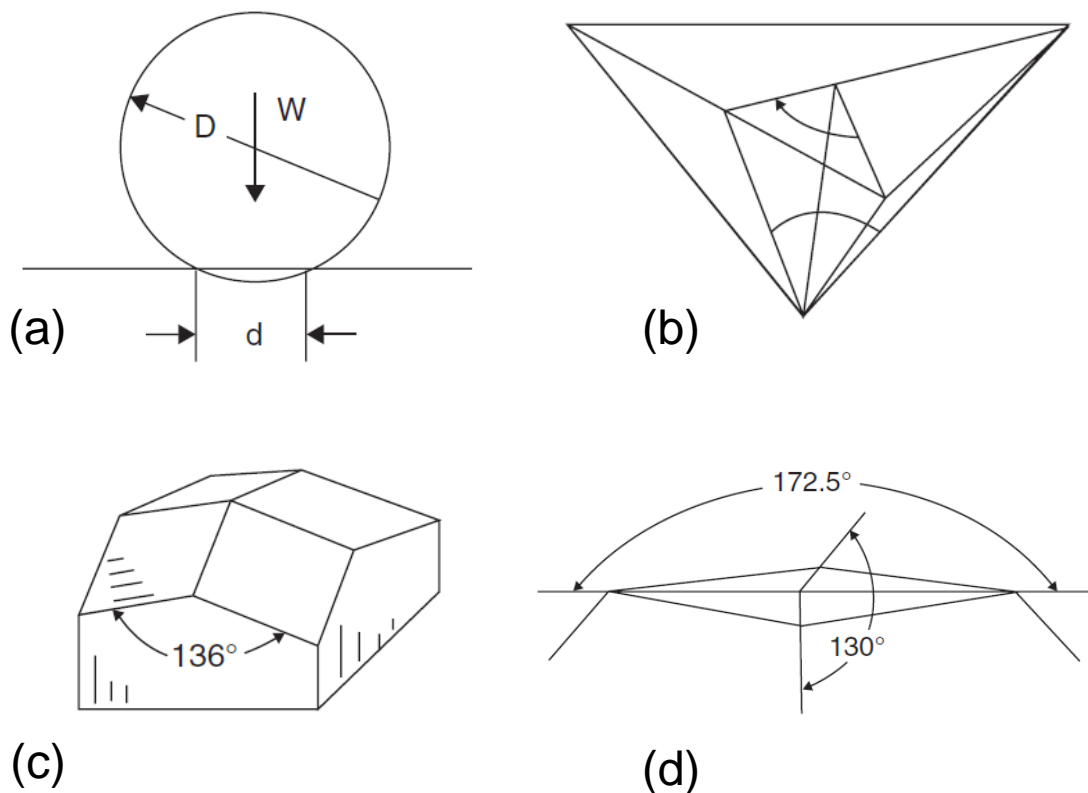


Figure 3.19: Shapes of various hardness indenters: (a) spherical, (b) trigonal pyramid, (c) square pyramid, and (d) elongated pyramid [134].

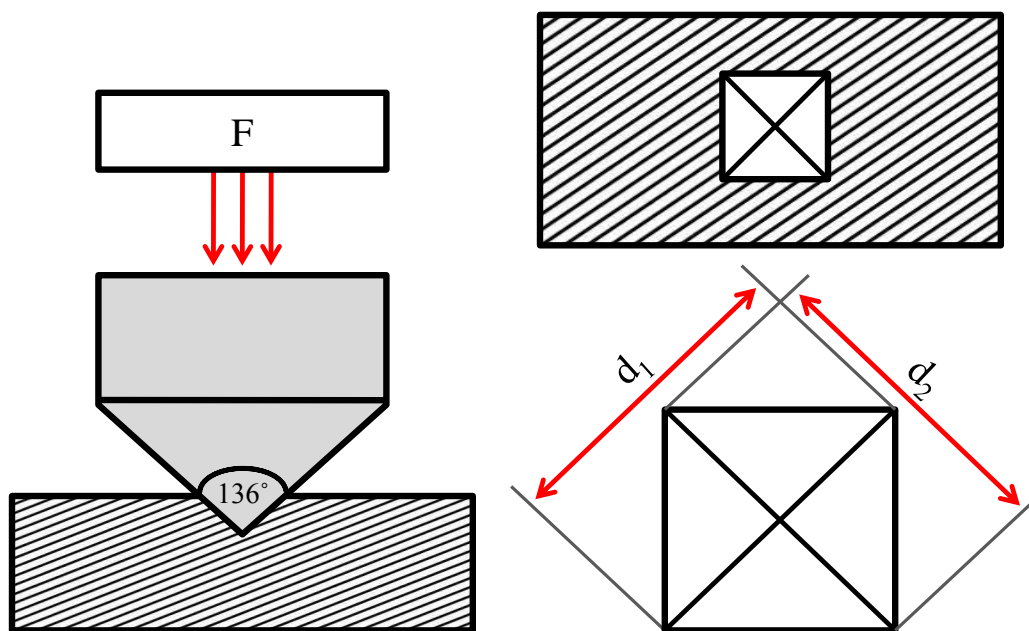


Figure 3.20: Geometry of the indenter for the Vickers hardness test.

the hardness of the material [134]. However, various approximate relations have been developed and are shown in Fig. 3.18 [26].

Due to their geometry, pyramid-shaped indenters generally yield more precise estimates, with the Vickers method being the most commonly used for ductile materials such as metals. The shape of a Vickers diamond indenter is shown in Fig. 3.20, and it consists of a square-base pyramid whose opposite faces are 136° apart. A load between 1 and 100 kgf is normally applied for 10 – 15 seconds after which the diagonals of the indentation d_1 and d_2 are measured. The Vickers hardness HV is then estimated using the following formula [134]:

$$HV = \frac{2F \sin\left(\frac{136^\circ}{2}\right)}{d^2} = 1.854 \frac{F}{d^2} \quad (3.16)$$

where d is the average of d_1 and d_2 and F is the applied force. Conversions of force from kgf to N ($1 \text{ kgf} = 9.81 \text{ N}$) and area from mm^2 to m^2 ($1 \text{ mm}^2 = 10^{-6} \text{ m}^2$) are used to convert from Vickers hardness (HV) to Pa: $1 \text{ Pa} = 9.807 \cdot 10^6 \text{ kgf/mm}^2$.

The microhardness Vickers test is very similar to the regular Vickers test, except that it is done on the microscopic scale with more precise instrumentation. Naturally, a smaller force (less than 1 kgf) is applied. Particular attention needs to be paid to the surface preparation since rough materials can produce erroneous hardness values, especially for smaller loads and sample dimensions. However the resulting error bars are significantly smaller than those obtained with macroscopic resolution. Hardness was measured using a Tukon 2100 microhardness tester, equipped with a Vickers diamond pyramid indenter. The tests were performed on polished sample surfaces of about 3 mm in diameter. Multiple tests were conducted for all samples, using a 300 g load, with a duration of 10 s.

3.8 Muon Spin Relaxation, Rotation, and Resonance

Muon spin relaxation, rotation, and resonance (μ SR) refers to a collection of methods that make use of a short-lived subatomic particle called a muon in order to probe the structural and dynamical processes on an atomic scale. A key difference of the μ SR technique, as compared with those involving x-rays or neutrons, is that scattering is not involved [43]. Muons are implanted into a sample and reside there for the rest of their lives, acting as microscopic magnetometers. The muons consequently decay into positrons which are then detected, carrying the information about the muons they came from [43]. With a mass of about 200 times greater than that of an electron and 9 times less than that of a proton, a muon can be thought of as a heavier electron (μ^-) or a lighter proton (μ^+) [276]. Even though both μ^+ and μ^- can be used for μ SR experiments, positive muons are generally preferred since their lifetime in a material is considerably longer [276]. Additionally, μ^+ is attracted to the electron cloud, which is more interesting from a condensed matter prospective. If a positive muon captures an electron it is referred to as muonium, in this way the electron acts as a very sensitive probe that passes on what it senses to the muon *via* hyperfine splitting [276].

In the upper layers of the atmosphere, muons are created by the interaction of cosmic rays with gas molecules, resulting in a few muons per minute at the sea level. In a lab environment, a higher flux of muons is needed, which can be produced from pions, which are in turn created from collisions of high-energy protons (> 500 MeV) with a carbon or beryllium target, as depicted in Fig. 3.21(a) [276] :

$$p + p \rightarrow \pi^+ + p + n \quad (3.17)$$

The pion π^+ then decays into a muon μ^+ and a muon-neutrino ν_μ :

$$\pi^+ \rightarrow \mu^+ + \nu_\mu \quad (3.18)$$

After muons are stopped within the sample, they will decay after time t with probability proportional to e^{-t/τ_μ} , where $\tau_\mu = 2.2 \mu\text{s}$ is the lifetime of the muon [43]. The decay of a muon is a three body process, creating a positron e^+ and two neutrinos ν_e and $\bar{\nu}_\mu$:

$$\mu^+ \rightarrow e^+ + \nu_e + \bar{\nu}_\mu \quad (3.19)$$

Between the three produced particles, the positron e^+ is the only one that can be detected reliably. Because muon decay involves weak interaction, it displays an unusual feature of not conserving parity, resulting in the direction of the emitted positron being identical to that of the muon spin right before it decayed [43].

The major advantage of muons is that their large magnetic moment (3.18 times larger than that of a proton) makes them an extremely sensitive microscopic probe of magnetic and electronic properties of matter. In systems with very small and/or dilute moments, μSR is frequently the only method available for clear detection of such phenomena, capable of sensing internal fields on the order of 0.1 G. Another advantage of μSR is the ability to differentiate between magnetic and non-magnetic regions within the same sample. These result in different signal amplitudes that are proportional to the volume of a given phase for the sample. The resulting magnetic volume fraction provides quantitative information on coexisting phases, inaccessible *via* any other measurement.

The TRIUMF facility uses a cyclotron to accelerate protons to approximately

three quarters of the speed of light. The implantation depths in solids are typically between fraction a nanometer. The type of material is not important, allowing for testing of gas, liquid or solid samples as well as single crystals, polycrystalline samples or thin films. For solid samples, typical thickness is around 0.1 cm; however, an area of about 3.5 cm^2 is required, as shown in Fig. 3.22. The samples are either mounted on a silver tape (M20) or silver plate using grease (M15) and the holder is oriented perpendicular to the direction of incoming muons. Air-sensitive samples are presented *via* a constant He gas flow within the sample space. A large variety of environments is available – dilution fridge temperatures, magnetic fields up to 8 T, electric fields, high pressure, light illumination, and application of RF pulses.

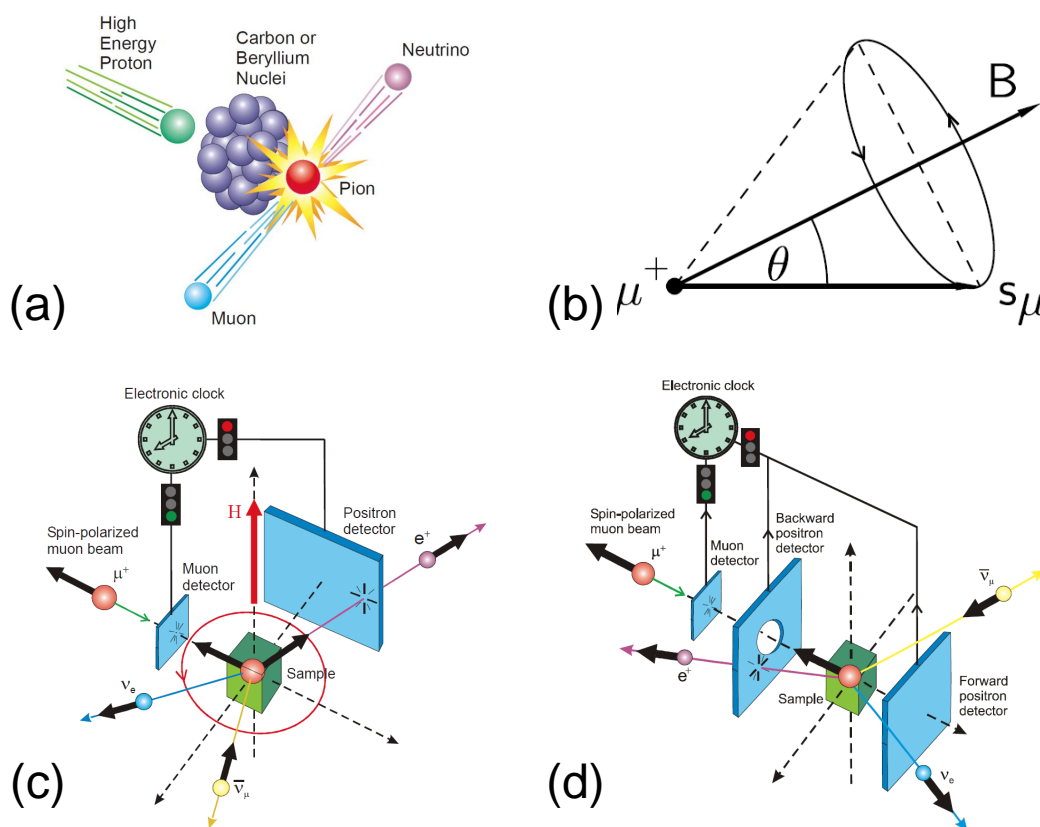


Figure 3.21: (a) The mechanism of muon production. (b) Muon-spin precession in a magnetic field B applied at an angle θ [43]. (c) The transverse field μ SR setup. (d) The zero-field μ SR setup.

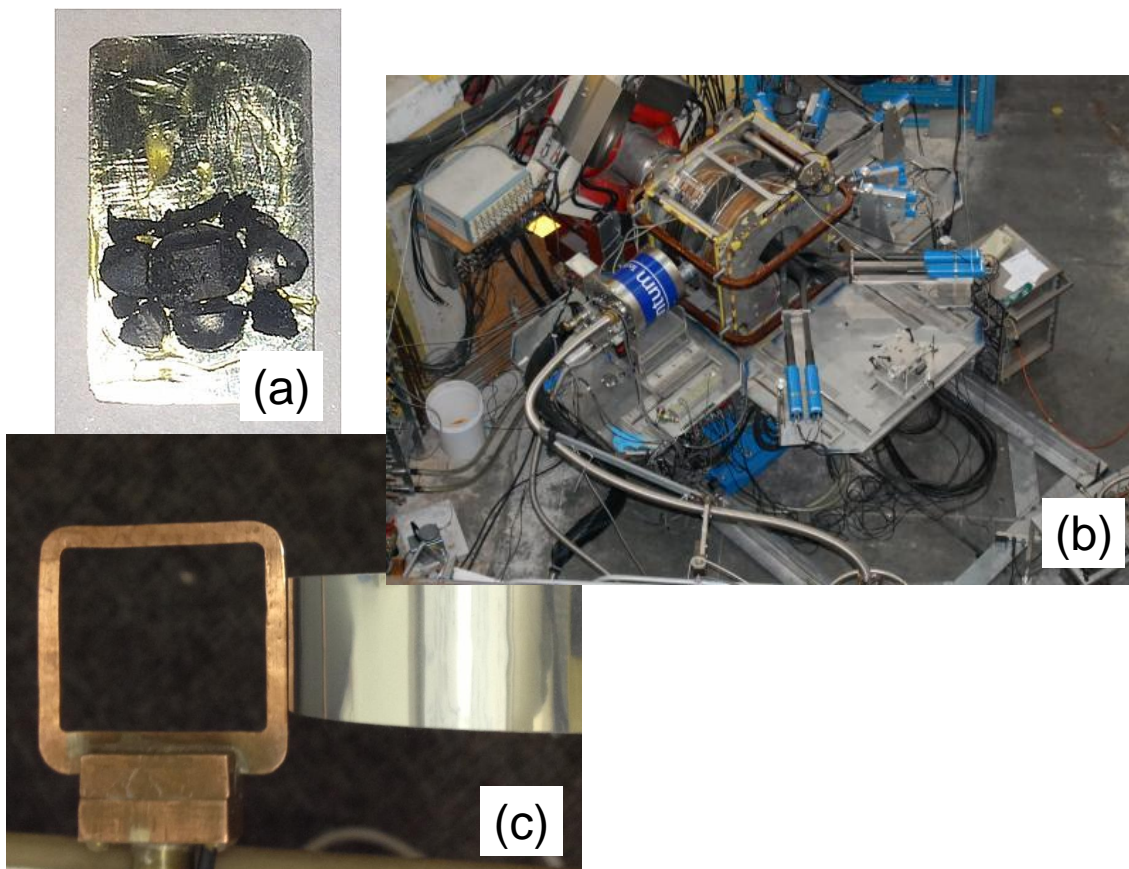


Figure 3.22: (a) Samples mounted on a silver plate for the M15 beamline. The area necessary for μ SR experiments is equivalent to the area of a penny. (b) The top view of the M20 experiment at TRIUMF. The main components include three orthogonal pairs of Helmholtz coils, a cryostat and various detectors. (c) The silver tape and holder used for the M20 beamline.

If the initial muon spin direction and the local magnetic field are at an angle θ with respect to each other, the muon spin will start to precess around the end of a cone of semi-angle θ about the magnetic field, as shown in Fig. 3.21(b) [43]. The asymmetry function of the decaying positron can be represented as:

$$G(t) = \cos^2 \theta + \sin^2 \theta \cos(\gamma_\mu B t) \quad (3.20)$$

where $\gamma_\mu = ge/2m_\mu$ is the gyromagnetic ratio for the muon. If the direction of the local magnetic field is random, the above expression should be averaged over all three

directions:

$$G(t) = \frac{1}{3} + \frac{2}{3} \cos(\gamma_\mu B t) \quad (3.21)$$

$$G(t) = \frac{1}{3} + \frac{2}{3} e^{-\Delta^2 t^2 / 2} (1 - \Delta^2 t^2) \quad (3.22)$$

where Δ/γ_μ is the width of a Gaussian distribution, which is centered around zero and used to estimate the strength of local magnetic field [43]. The result is known as the Kubo-Toyabe relaxation function [154]. For dilute magnetic systems, such as diluted alloys of Au with Fe and Cu with Mn [383], a Lorentzian distribution is more appropriate, yielding:

$$G(t) = \frac{1}{3} + \frac{2}{3} e^{-at} (1 - at) \quad (3.23)$$

where the parameter $a = \sqrt{\pi/2} C_x \Delta$ represents the average value of static and dynamic random fields at each muon site and depends on concentration C_x [383].

Two main techniques are generally implemented for μ SR studies – transverse field muon spin rotation (TF- μ SR) and longitudinal field muon spin relaxation (LF- μ SR). The former involves the application of an external field, perpendicular to the initial direction of the muon spin polarization, as shown in Fig. 3.21(b). The frequency of the precession of the muon spin is proportional to the size of the field at the muon site. This configuration is typically used to measure the magnetic field distribution of the vortex lattice or the Knight shift in metallic systems [276]. For the LF- μ SR scenario, the external magnetic field is applied parallel to the initial direction of the muon spin polarization. Therefore, the evolution of muon polarization along its original direction is recorded. For weak internal magnetism, a zero-field muon

spin relaxation (ZF- μ SR) is performed in absence of an external magnetic field [276]. This very sensitive method can therefore register magnetic fields as small as 10^{-5} T, that are either ordered or random, static or fluctuating with time [43]. In this sense, ZF- μ SR has a tremendous advantage over other resonance techniques [276]. Another type of μ SR measurements is referred to as muon spin resonance – a static magnetic field is applied parallel to the initial muon spin. The resonance occurs when the RF frequency matches an energy level splitting of one of the muon states present in the system [276]. The main limitation of the μ SR technique is the requirement of knowing the precise stopping site of the muon in the material – while in some systems this can be easily determined, in others the location is not known since there is a set of possible interstitial sites which the muon can occupy [43].

The study of magnetism is the most common application of μ SR, with examples including magnetically ordered, spin-glass, and frustrated compounds, materials displaying magnetoresistance, heavy fermions, quasicrystals, molecular magnets, and clusters [13, 14, 101, 146, 191, 191, 308, 380, 383]. In superconductors, μ SR technique is frequently applied to study phase separation, vortex phases, characteristic length scales, and pairing properties [14, 43, 198, 229, 381]. A number of μ SR experiments have also been applied to study conducting polymers, quantum diffusion, ion mobility, chemical mobility, and various biological systems.

3.9 Tunnel Diode Oscillation Measurements

Oscillators have been used widely to investigate condensed matter systems due to the great precision and high sensitivity with which frequency can be measured [93,345]. The tunnel diode oscillator is an LC tank circuit, powered by a tunnel diode [74]. The low noise level ($\Delta F/F_0 \approx 10^{-9}$) along with the low drift of the oscillator allows data to be obtained with a very small temperature spacing interval [66]. Additionally, the sensitivity of a properly constructed circuit is able to measure changes in the magnetic moment on the order of 10^{-12} emu [386,387], which is much more sensitive than the resolution limit of commercially available systems, such as an MPMS (10^{-8} emu, Section 3.3). The tunnel diode oscillator resistivity measurements do not require leads [75], eliminating sample stress, the possibility of sample damage, and overheating, making it more advantageous than a traditional four-probe method. This technique has been applied to numerous systems to investigate magnetoresistance [12,345], de Haas-van Alphen [28,75,303] and Shubnikov-de Haas [28,303] effects, to determine dielectric constants [93], surface impedance [93], conductivity [75] and resistivity [75], thermal expansion [93], as well as penetration depth and critical fields of superconductors [28,66,74,75,126].

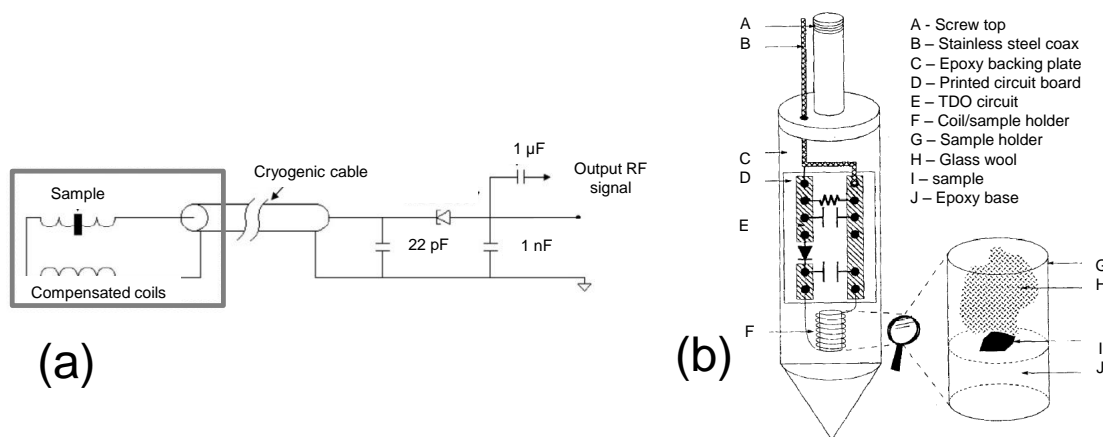


Figure 3.23: (a) Schematic representation of the tunnel diode oscillator circuit [99]. (b) Low temperature stage platform diagram along with an expanded view of the sample tube [28].

The general layout of the measurement system is shown in Fig. 3.23(a) and (b) [28, 74, 75, 93, 99, 345]. Depending on the type of measurement being done, the sample will either be placed between the capacitor plates (dielectric constant measurements) or in the inductor tank circuit (susceptibility, penetration depth, or resistivity measurements) [75]. The resonant frequency f , which is typically in the megahertz range, can be expressed in terms of inductance L and capacitance C :

$$f = \frac{1}{2\pi\sqrt{LC}} \quad (3.24)$$

While the tunnel diode oscillator technique is widely used, the interaction of the sample with the tank circuit is not yet fully understood – only approximations or empirical equations can relate the raw data to the properties of a sample [75]. The inductance of the tank circuit is shifted by a small amount ΔL when a magnetic sample is inserted into a tank coil [287]. This results in a shift of resonant frequency $\Delta f = f - f_0$, where f_0 is the resonant frequency of an empty coil. This shift is proportional to both the real and imaginary components of the conductivity, which allows to investigate both dielectric and magnetic properties of the material [12, 386, 387]. A relation between the frequency shift Δf and the susceptibility can be written in terms of the volumes of the sample (V_s) and the coil (V_c):

$$\frac{\Delta f}{f_0} = -\frac{\Delta L}{2L} \approx -\frac{1}{2} \frac{V_s}{V_c} 4\pi\chi \quad (3.25)$$

For insulators, the measured susceptibility χ from Eq. 3.25 coincides with the static dM/dH . However, the screening due to the surface effects results in an additional susceptibility contribution for metals [28]. For the latter, the frequency can only penetrate the sample by a finite depth, referred to as the skin depth δ . In superconductors, this contribution is associated with the London penetration depth

λ . Since change in inductance ΔL is proportional to change in impedance ΔZ which in turn is proportional to resistivity ρ , the latter can be related to the frequency shift Δf using the skin depth δ [12, 303]:

$$\frac{\Delta f}{\Delta f_0} \approx -\frac{G\Delta\delta}{\delta} \quad \text{with} \quad \delta = \sqrt{\frac{\rho}{\pi\mu_0 f}} \quad (3.26)$$

where G is the geometrical factor that depends on the sample and coil geometries and μ_0 is the magnetic permeability of free space. Even for values of δ greater than the sample, the effective diamagnetism will shift the frequency, allowing for good resistivity measurements [201, 219].

It has been reported that itinerant and local moment systems induce a substantially different frequency response, providing a new way of differentiating between them [386]. Itinerant ferromagnet ZrZn_2 does not show a sharp peak in the resonator frequency at T_C (Fig. 3.24(a)), as compared with a sharp peak in local moment ferromagnets CeVSb_3 and CeAgSb_2 (Fig. 3.24(b)) [386]. Additionally, under the influence of an applied magnetic field, the position of the peak shifts to higher values

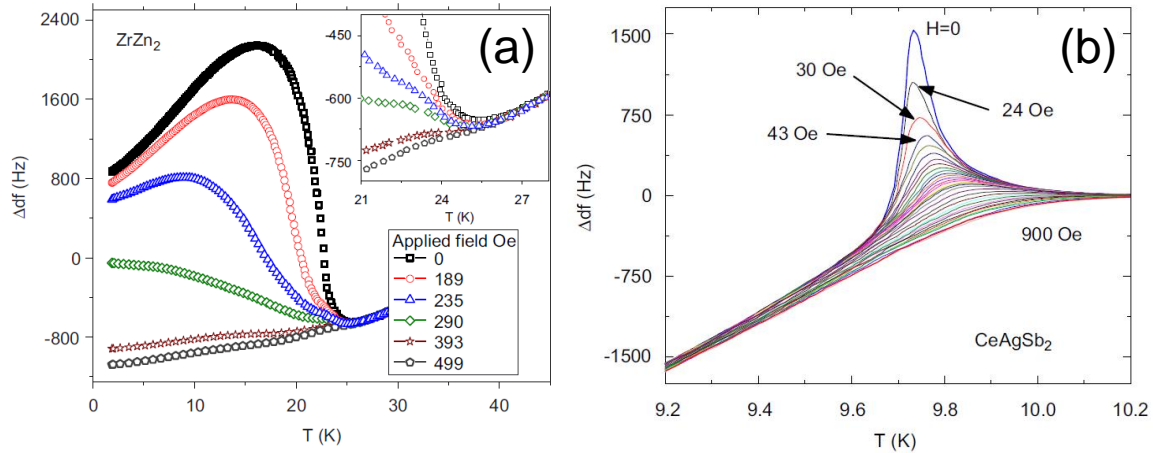


Figure 3.24: (a) A broad peak is observed close to T_C in an itinerant ferromagnet ZrZn_2 [386]. (b) A sharp cusp is visible around T_C in a local moment ferromagnet CeAgSb_2 [386].

for the local moment systems (Fig. 3.24(b)) and to lower values for itinerant ones (Fig. 3.24(a)).

As for the antiferromagnetic case, a local moment compound SmAgSb_2 was found to exhibit only a gradual decrease of susceptibility below the Néel temperature T_N , likely associated with the loss of spin-scattering which changes the penetration depth of the AC excitation field [386]. Itinerant antiferromagnets have not yet been analyzed. Therefore, the possibility of using tunnel diode oscillator as a tool to differentiate between itinerant and local antiferromagnets is investigated in Chapter 6 *via* tunnel diode oscillator measurements on the itinerant antiferromagnet TiAu .

3.10 Neutron Scattering

While comprehensive crystallographic information can be obtained *via* x-ray diffraction for the majority of compounds, those containing light atoms (O or H) cannot scatter x-ray efficiently. Electrons surrounding the nucleus scatter x-rays, hence heavy atoms with many electrons attenuate the x-ray beam better. Moreover, neutrons can penetrate matter far better than charged particles (Fig. 3.25). The value of the mass of the neutron results in the de Broglie wavelength of thermal neutrons being on the order of interatomic distances in solids and liquids (1 Å) [344]. The resulting interference effects yield structural information. The scattering of the neutron by a nucleus can be described in terms of a cross section σ – effective area presented by the nucleus to the passing neutron. The strength of the interaction between the neutron and the nucleus is known as scattering length b . The two quantities are related in the following manner [304]:

$$\sigma = 4\pi b^2 \tag{3.27}$$

Unlike x-rays, neutrons interact with atoms in a manner that does not seem correlated (Fig. 3.25). In fact, the neutron’s interaction with a nucleus varies from one isotope to another – a property that is frequently used in isotope labeling. The energy of thermal neutrons is on the same order as that of many excitations in condensed matter. Therefore, the change in the neutron’s energy during scattering is a large fraction of its initial energy [344]. The magnetic moment of a neutron interacts with unpaired electrons within an atom, thus elastic scattering from this type of interaction can be used to investigate the arrangement of electron spins and the density distribution of unpaired electrons [304]. On the other hand, inelastic scattering gives the energies of magnetic excitations, and permits the study of time-dependent spin

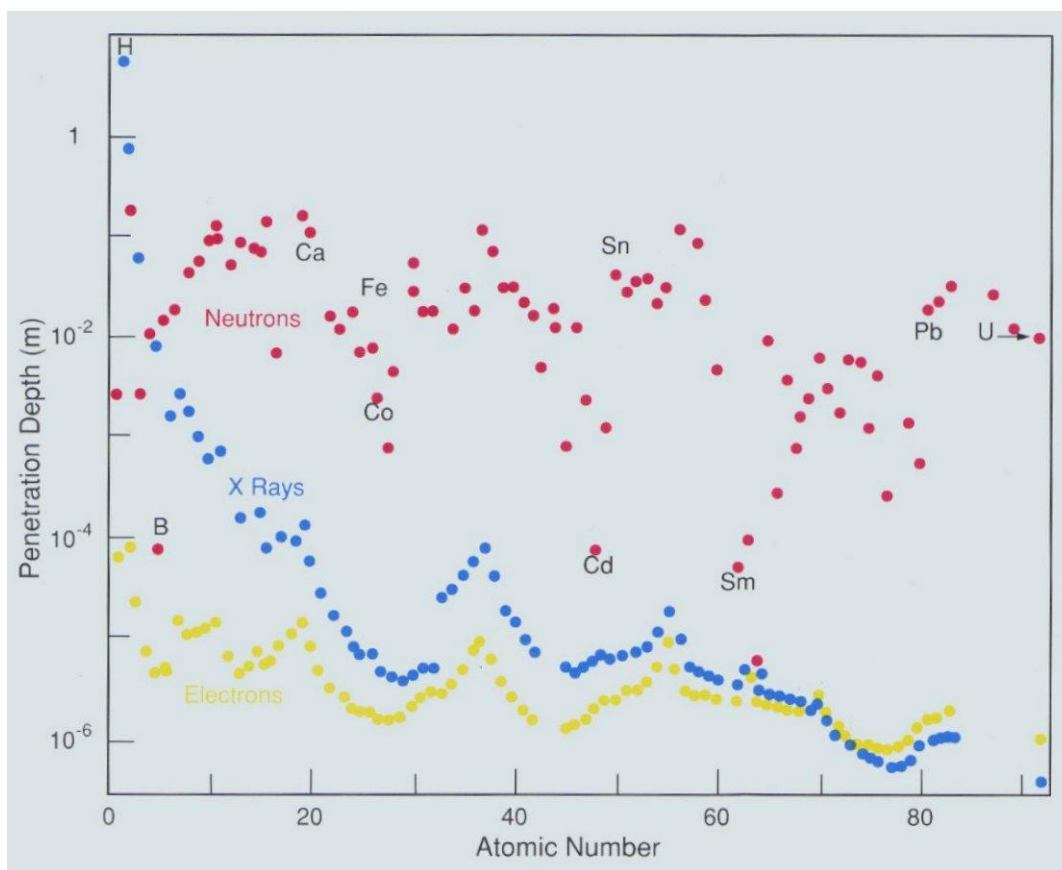


Figure 3.25: Penetration depth as a function of atomic number for neutron (red), x-rays (blue), and electrons (yellow). The penetration depth is taken as the depth at which the intensity has been reduced to about 37 % of its original value [304].

correlations within the scattering system [344].

When neutrons are scattered by matter, both the momentum and the energy of the neutrons and the matter are changed. Since the total momentum and energy are conserved, the momentum transfer is given by:

$$Q = k - k' \quad (3.28)$$

Q is known as the scattering vector and k is the wave vector ($hk = 2\pi mv$). The above expression is displayed pictorially in Fig. 3.27. The magnitude and direction of Q is determined by the magnitudes of the wave vectors for both incident and scattered

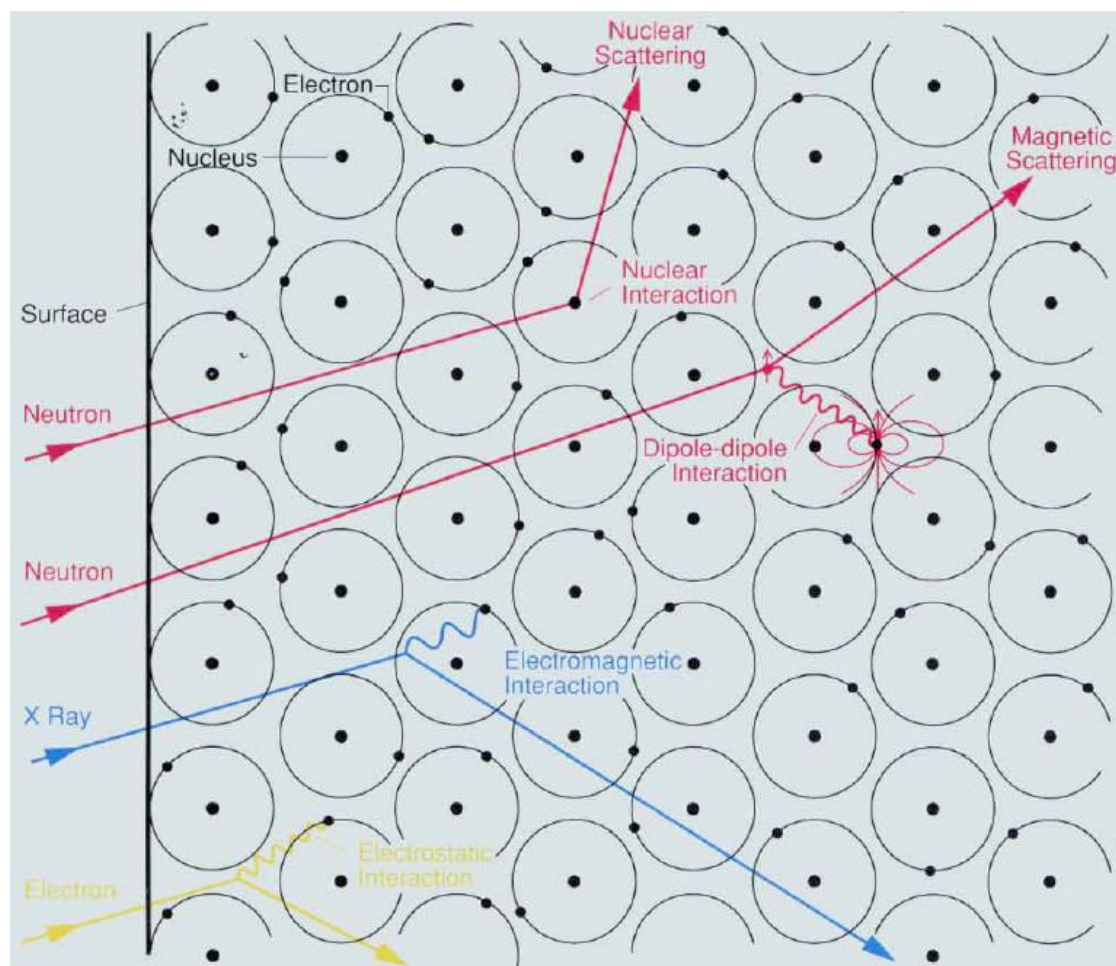


Figure 3.26: Types of interactions depending on the incoming beam type – neutrons (red), x-rays (blue), and electrons (yellow) [304].

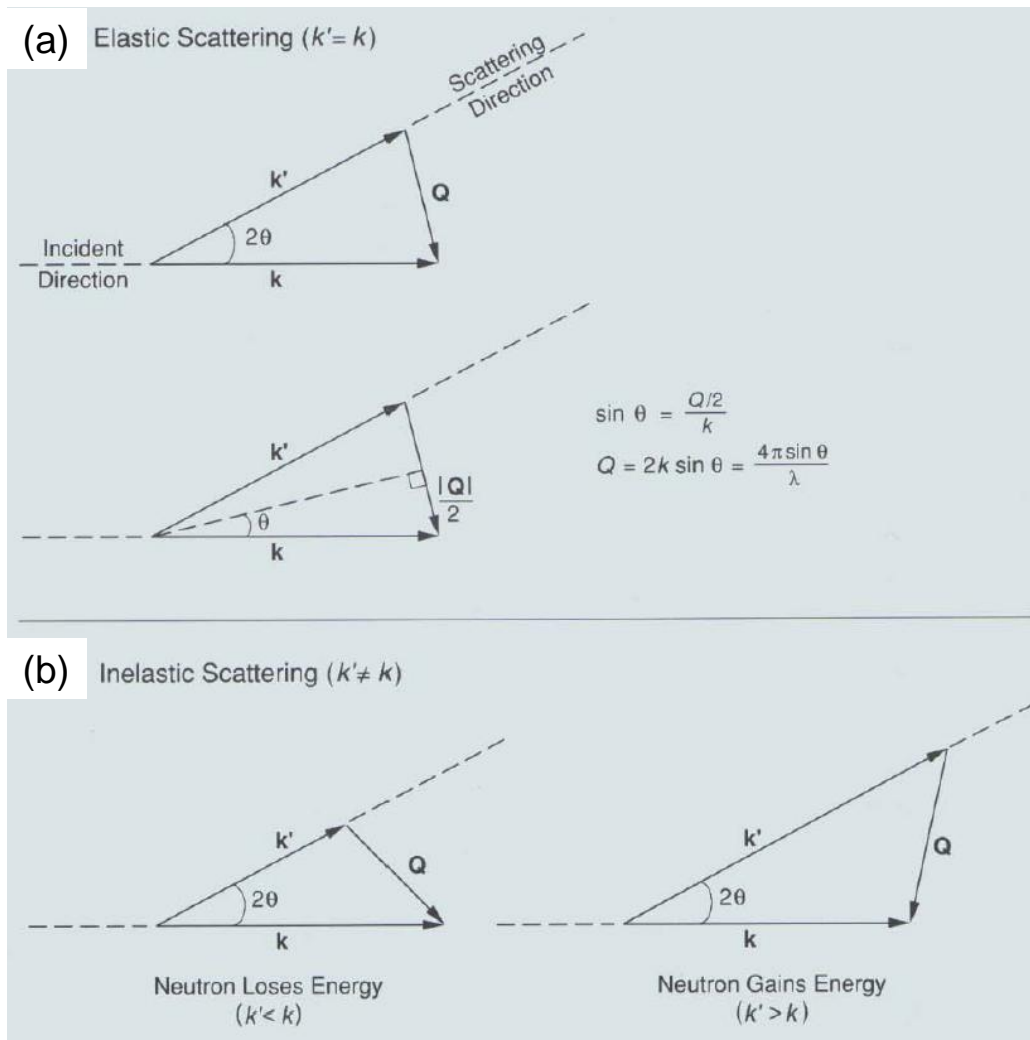


Figure 3.27: (a) Elastic ($k' = k$) and (b) inelastic ($k' > k$ or $k' < k$) scattering events [304]. In both cases, the neutron is scattered through the angle 2θ with a scattering vector is Q .

beams as well as the scattering angle 2θ . For elastic scattering:

$$Q = \frac{4\pi \sin \theta}{\lambda} \quad (3.29)$$

It as shown by Van Hove that the scattering intensity $I(Q, \eta)$ is proportional to the Fourier transform of a function that gives the probability of finding two atoms a certain distance apart [304]. This result can be manipulated to reveal scattering effects of two types – coherent *vs.* incoherent scattering. The former corresponds to

a scattering scenario in which the neutron wave interacts with the whole sample as a unit so that the scattering waves from different nuclei interfere with each other. This scattering provides structural information. Elastic coherent scattering can be used to investigate the equilibrium structure while the inelastic coherent scattering provides information about the collective motion of the atoms.

During incoherent scattering, the neutron wave interacts independently with each nucleus so that the scattered waves from each nucleus don't interfere (the intensities just add up). This type of scattering can arise from neutrons' interaction with the same atom but at different times or positions, providing information about atomic diffusion [304].

For our neutron diffraction measurements the sample was sealed with helium exchange gas and mounted in a closed cycle refrigerator with a base temperature of 2.6 K. To search for magnetic scattering the high intensity/coarse resolution BT-7 spectrometer was employed in two-axis mode, with a fixed initial neutron energy of 14.7 meV ($\lambda = 2.369$ Å) and collimator (full-width-half-maximum) configuration open – PG(002) monochromator – 80' – sample – 80' radial-collimator – position-sensitive detector [232]. To characterize the sample and search for possible structural changes associated with the magnetic phase transition the BT-1 high resolution powder diffractometer was used. Collimators of 15', 20' and 7' were used before and after the Cu (311) monochromator ($\lambda = 1.5401$ Å) and after the sample, respectively, and data were collected in steps of 0.05° in the 2θ range of 3° to 168° .

3.11 Band Structure Calculations

A number of physical properties of a solid depend on the collective behavior of electrons comprising it. While electrons of an isolated atom form discrete set of energy levels, multiple atoms brought together form an energy continuum, known as an energy band. The existence and size of energy gaps, *i. e.* the energy range where no electron states can exist, distinguishes semiconductors from metals and insulators [415]. The bands and band gaps near the Fermi level affect electronic properties the most, and thus are frequently given special names, *i. e.* the conduction and the valence bands .

Density functional theory is a modeling method used to investigate the electronic structure of many-body systems. The calculation begins by introducing a Hamiltonian that describes a perfect crystal. This Hamiltonian includes five terms that characterize the motion of ions and electrons, repulsion between the electrons, interaction between ions, and attraction between ions and electrons. Solving this Hamiltonian would require to evaluate 10^{23} equations, which is not currently possible. Therefore, a number of approximations is utilized by various band structure calculations methods.

The Born-Oppenheimer approximation [47] uses the fact that the ions of the lattice are much heavier than the electrons, which allows to separate the motion of electrons from that of the ions. This reduces the initial Hamiltonian to just three terms that describe the motion of electrons, repulsion between electrons, and attraction between electrons and ions. While the complexity of the Hamiltonian is reduced greatly, additional approximations are necessary to find the solution. The mean-field approximation assumes that every electron experiences that same average potential. The next approximation simplifies the solution of the Schrödinger's equation, postulating two theorems which result in a Kohn-Sham Hamiltonian [208]. This allows to calculate all physical properties of a system if the electron density is known.

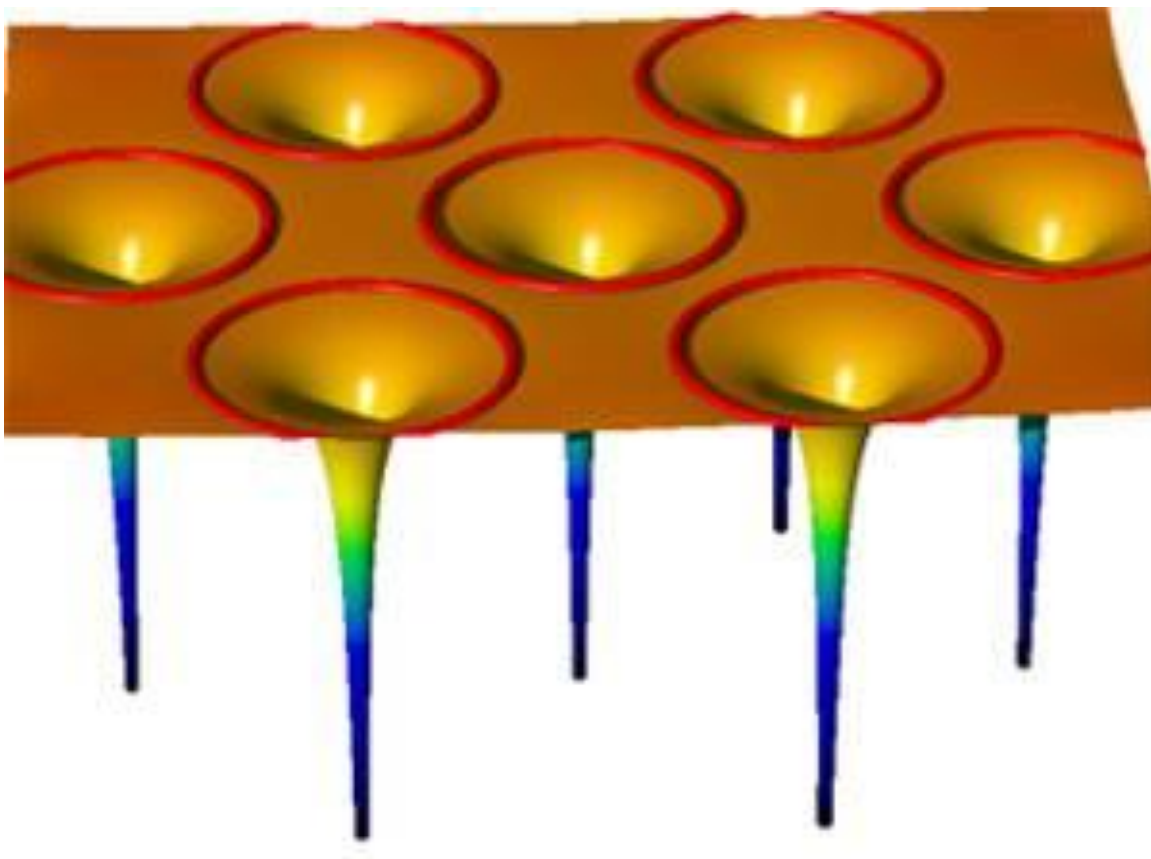


Figure 3.28: Pictorial representation of a muffin-tin potential [2].

Depending on the basis that is used to diagonalize the Kohn-Sham equation, several band structural calculation methods are typically implemented. For most metals, the augmented-plane wave method developed by Slater in 1953 [336], is used. It relies on the fact that the effective crystal potential is constant in most of the open spaces between the cores. The potential is referred to as the muffin-tin potential, consisting of that of a free ion at the core and strictly constant outside the core (Fig. 3.28).

Our band structure calculations were performed using the Full-Potential Linearized Augmented Plane-Wave method implemented in the *WIEN2K* package [41, 296]. The PBE-GGA was used as the exchange potential, the default generalized gradient approximation for the exchange correlation potential in *WIEN2K* [296].

The lattice parameters and atomic positions were determined from x-ray and neutron (whenever possible) diffraction experiments. More details regarding compound-specific band structure calculations are provided in respective sections: TiAu (Sections 6.3 and 7.3), ScGa₃ and LuGa₃ (Section 9.3).

From the value of the density of states at the Fermi surface $N(E_F)$, several quantities can be estimated. For example, the value of γ can be calculated as:

$$\gamma = \frac{2\pi^2}{3} N(E_F) k_B^2 \quad (3.30)$$

where k_B^2 is the Boltzmann's constant.

Typically, the temperature-independent susceptibility contribution is dominated by the Pauli susceptibility, as described in Section 2.1.4. Using Eq. 2.56, the value of the temperature-independent contribution χ_0 can be found as:

$$\chi_0 = 2\mu_0\mu_B^2 N(E_F) \quad (3.31)$$

where μ_B is the Bohr magneton, $\mu_0 = 1$, and the factor of two is included to account for both sub-bands.

Doping-induced Quantum Critical Point in (Sc_{1-x}Lu_x)_{3.1}In

A quantum critical point occurs upon chemical doping of the weak itinerant ferromagnet Sc_{3.1}In. Remarkable for a system with no local moments, the quantum critical point is accompanied by non-Fermi liquid behavior, manifested in the logarithmic divergence of the specific heat both in the ferro- *and* the paramagnetic states, as well as linear temperature dependence of the low temperature resistivity. With doping, critical scaling is observed close to the quantum critical point, as the critical exponents δ , γ and β have weak composition dependence, with δ nearly twice, and β almost half of their respective mean-field values. The unusually large paramagnetic moment $\mu_{PM} \sim 1.3\mu_B/F.U.$ is nearly composition-independent. Evidence for strong spin fluctuations, accompanying the quantum critical point at $x_c = 0.035 \pm 0.005$, may be ascribed to the reduced dimensionality of Sc_{3.1}In, associated with the nearly one-dimensional Sc-In chains.

4.1 Motivation and Background

Quantum critical points are ubiquitous features in the phase diagrams of strongly correlated electron systems, ranging from high temperature oxide superconductors [45, 291, 314] and low-dimensional compounds [90, 132, 158], to itinerant magnets [183, 341, 352, 409] and heavy fermions [55, 96, 261, 322, 348, 375]. Often, non-Fermi liquid behavior [76, 83, 131, 256, 377], and critical scaling [205] accompany the quantum critical point, and such novel phenomena have been extensively studied in heavy fermions, and in particular in antiferromagnetically ordered systems. However, fewer ferromagnetic quantum critical points are known and much less is currently understood about itinerant electron magnets and their quantum critical behavior, particularly due to the limited number of existent itinerant magnets. These observations make itinerant *ferromagnets* particularly appealing, given the comparatively smaller number of known ferromagnetic than antiferromagnetic quantum critical points. The quantum critical points recently observed in two substantively different systems, the itinerant ferromagnet ZrZn_2 [341] and the heavy fermion ferromagnet URu_2Si_2 [57], are two such ferromagnetic quantum critical point systems. non-Fermi liquid behavior is associated with the quantum phase transition induced by doping in the latter compound, but not the former, reemphasizing the imperious need for a unified picture of quantum criticality and non-Fermi liquid behavior in itinerant ferromagnet systems. This study of the doping-induced non-Fermi liquid state close to the quantum critical point in the itinerant ferromagnet $\text{Sc}_{3.1}\text{In}$ provides a first connection between the two previously known ferromagnetic quantum critical point systems, a precursor of such a unified theory.

Lu doping in $\text{Sc}_{3.1}\text{In}$ represents the first report of non-Fermi liquid behavior associated with a quantum phase transition in this itinerant ferromagnet. The critical composition x_c in $(\text{Sc}_{1-x}\text{Lu}_x)_{3.1}\text{In}$ is very small, close to 0.035. The critical scaling

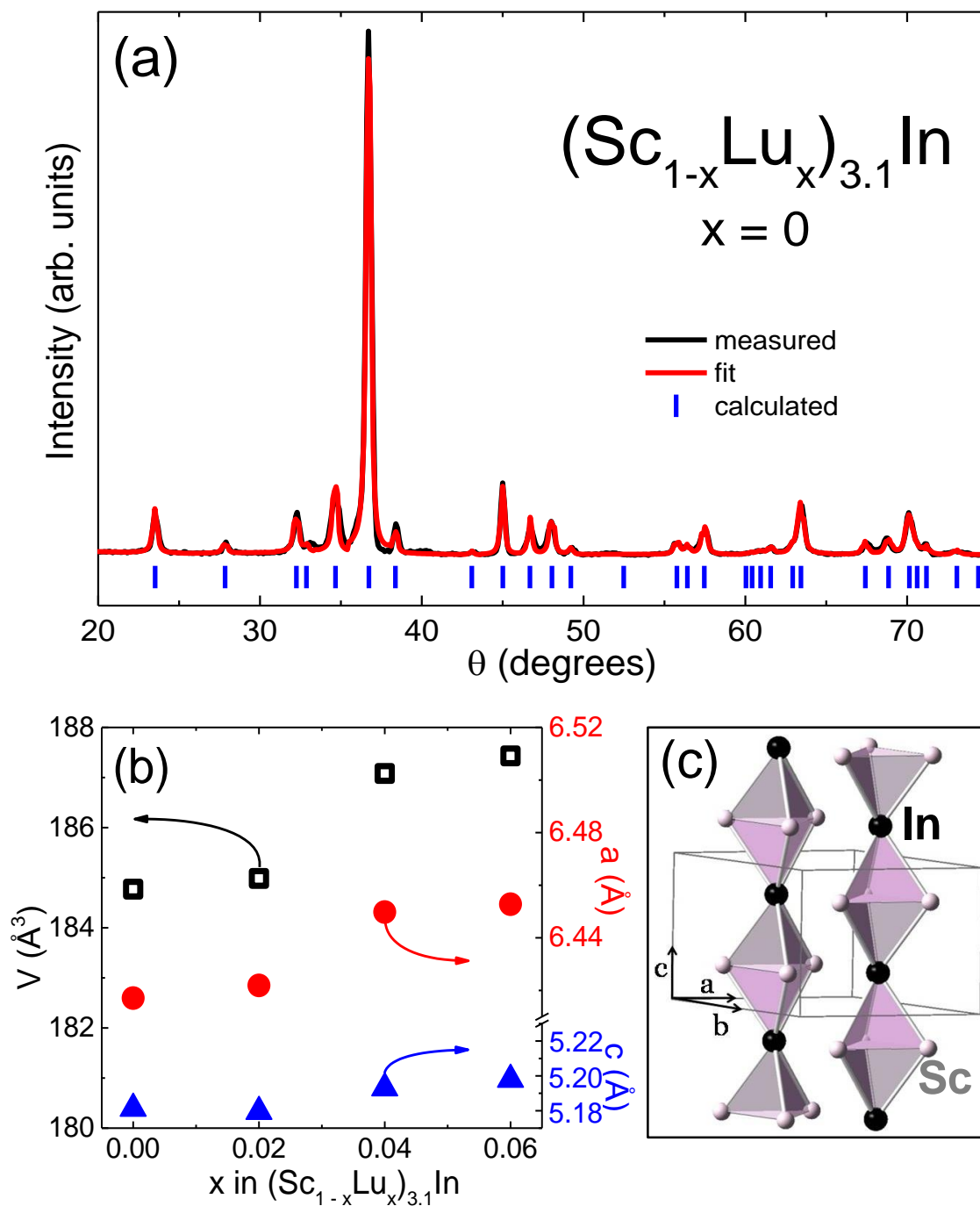


Figure 4.1: Measured X-ray diffraction pattern for $(\text{Sc}_{1-x}\text{Lu}_x)_{3.1}\text{In}$ (black line) where $x = 0$, with calculated peak positions marked by vertical lines, based on space group $P6_3/mmc$ and lattice parameters $a = 6.42 \text{ \AA}$ and $c = 5.18 \text{ \AA}$. The crystal structure of $\text{Sc}_{3.1}\text{In}$ (left inset) exhibits quasi-1D chains of Sc-In. Right inset: evolution of lattice parameters a and c and the unit cell volume V with composition x .

close to the quantum critical point is remarkable by comparison to ZrZn_2 or URu_2Si_2 : while $\text{Sc}_{3.1}\text{In}$ is similar to the former compound as the only other known ferromagnetic with no magnetic elements, its critical scaling is not mean-field-like, akin to that in the latter system. The reduced crystallographic dimensionality of $\text{Sc}_{3.1}\text{In}$, associated with quasi-1D Sc-In chains (Fig. 4.1(c)), provides one plausible justification for the similarities with the two-dimensional URu_2Si_2 , by contrast to the three-dimensional ZrZn_2 . In URu_2Si_2 the Kondo effect is inherently coupled with the quantum critical behavior, but $\text{Sc}_{3.1}\text{In}$ has no local moments, rendering its magnetism and the quantum critical point even more striking. What makes $\text{Sc}_{3.1}\text{In}$ even more unique is the non-Fermi liquid behavior, a trait so far not seen in itinerant ferromagnets without magnetic elements. It is therefore paramount to probe the existence of the quantum critical point in this itinerant ferromagnet system, and properly characterize the non-Fermi liquid behavior, as a precursor for a unified picture of quantum criticality in itinerant ferromagnets. The development of such a unified theory necessitates more itinerant ferromagnet systems, which starts with a thorough understanding of the few compounds that are already known.

Itinerant ferromagnets lack the complexity associated with the interplay between the local and itinerant character of the electrons observed in heavy fermions [9, 348]. Of the two known itinerant ferromagnets with no magnetic elements, ZrZn_2 and Sc_3In , the latter presents the advantage, from the quantum criticality perspective, of a much lower magnetic ordering temperature $T_C \leq 7.5$ K [124, 139, 168, 244, 367] in Sc_3In . This would likely facilitate the suppression of magnetic order towards a quantum critical point, but has proven difficult by the application of pressure [139] or magnetic field [168]. Here we show that the quantum critical point in $\text{Sc}_{3.1}\text{In}$ can indeed be reached by Lu doping, where the dopant ion is comparable in size ($r[\text{Lu}^{3+}] = 0.861$ Å) with the host ion Sc that it substitutes for ($r[\text{Sc}^{3+}] = 0.745$ Å) [329]. This way, the effects of chemical substitution can be deconvoluted from

those of chemical pressure, which is important given that pressure was shown to enhance the ordering temperature [139]. The systematic analysis of the magnetization isotherms $M(H)$, temperature-dependent magnetization $M(T)$ at low fields, and $H = 0$ specific heat data, for $0 \leq x \leq 0.10$ indicate that the magnetic ground state is suppressed in $(\text{Sc}_{1-x}\text{Lu}_x)_{3.1}\text{In}$ towards a quantum critical point close to $x_c \approx 0.035$. Remarkably, the logarithmic divergence of the specific heat and the low-temperature resistivity linear in T close to x_c evidence non-Fermi liquid behavior in both the ferromagnetic and the paramagnetic state. Additionally, the reduced crystallographic dimensionality, associated with quasi-1D Sc-In chains, may be linked to the non-Fermi liquid behavior and the non-mean-field critical scaling, similar to that in the more 2D ferromagnet, albeit with substantively different critical exponents.

4.2 Physical Properties

The hexagonal $\text{Sc}_{3.1}\text{In}$ compound has a Ni_3Sn -type structure, with space group $\text{P6}_3/\text{mmc}$ and lattice parameters $a = 6.42 \text{ \AA}$ and $c = 5.18 \text{ \AA}$ [82]. The reported crystal structure for Sc_3In is shown in Fig. 4.1(c). Highlighted are the Sc-In bipyramids which form nearly one dimensional chains along the hexagonal c axis. In addition to the nearly one-dimensional crystal structure, band structure calculations [177] also suggest possible reduced electronic dimensionality. These observations will be discussed in the context of the dimensionality of other itinerant ferromagnet systems close to quantum criticality.

Both annealed and non-annealed samples exhibit extreme hardness, comparable to that of high carbon steels [355], which made it very difficult to perform powder x-ray diffraction measurements. However, it was feasible to x-ray a polished surface of the arc-melted buttons, as described in Section 3.2. An example of a diffraction

pattern is shown in Fig. 4.1(a) for $(\text{Sc}_{1-x}\text{Lu}_x)_{3.1}\text{In}$ with $x = 0$. All observed peaks can be indexed with the space group $\text{P6}_3/\text{mmc}$. As shown in Fig. 4.1(b), both a (right axis, circles) and c (right axis, triangles) lattice parameters, along with the unit cell volume V (left axis, squares) for $(\text{Sc}_{1-x}\text{Lu}_x)_{3.1}\text{In}$ for $0 \leq x \leq 0.10$, increase nearly linearly with x .

4.2.1 Temperature-Dependent Magnetization Measurements

For weak itinerant ferromagnets, the low-field susceptibility is expected to follow a T^{-1} behavior [262]:

$$\frac{\chi_0}{\chi(T)} = 1 - \alpha + \lambda(T), \quad (4.1)$$

where the coefficient λ encompasses the dependence on the local amplitude of spin fluctuations and is linear in temperature $\lambda \sim T/T_C^*$, and $\alpha = I\rho(E_F)$, where I is the coupling constant and $\rho(E_F)$ is the density of states at the Fermi level. When $T^* \gg T_C^*$, $\alpha \sim (T/T^*)^2$ usually has only a weak T^2 dependence. However, the magnetic susceptibility $\chi(T)$ in $\text{Sc}_{3.1}\text{In}$ follows a modified Curie-Weiss-*like* law:

$$\chi(T) = \frac{C}{T^*} + \frac{C}{(T - T_C^*)}, \quad (4.2)$$

as illustrated in Fig. 4.2(a). Such a temperature dependence can possibly be understood when considering strong spin fluctuations, associated with the low-dimensional Fermi surface of Sc_3In [177]: if $T^* > T_C^*$ (but *not* $\gg T_C^*$), then the temperature dependence of α is not negligible compared to that of λ . In weak IFMs, the Curie-Weiss-*like* temperature T_C^* , determined from linear fits of the inverse susceptibility after the temperature independent term C/T^* was subtracted, coincides with the

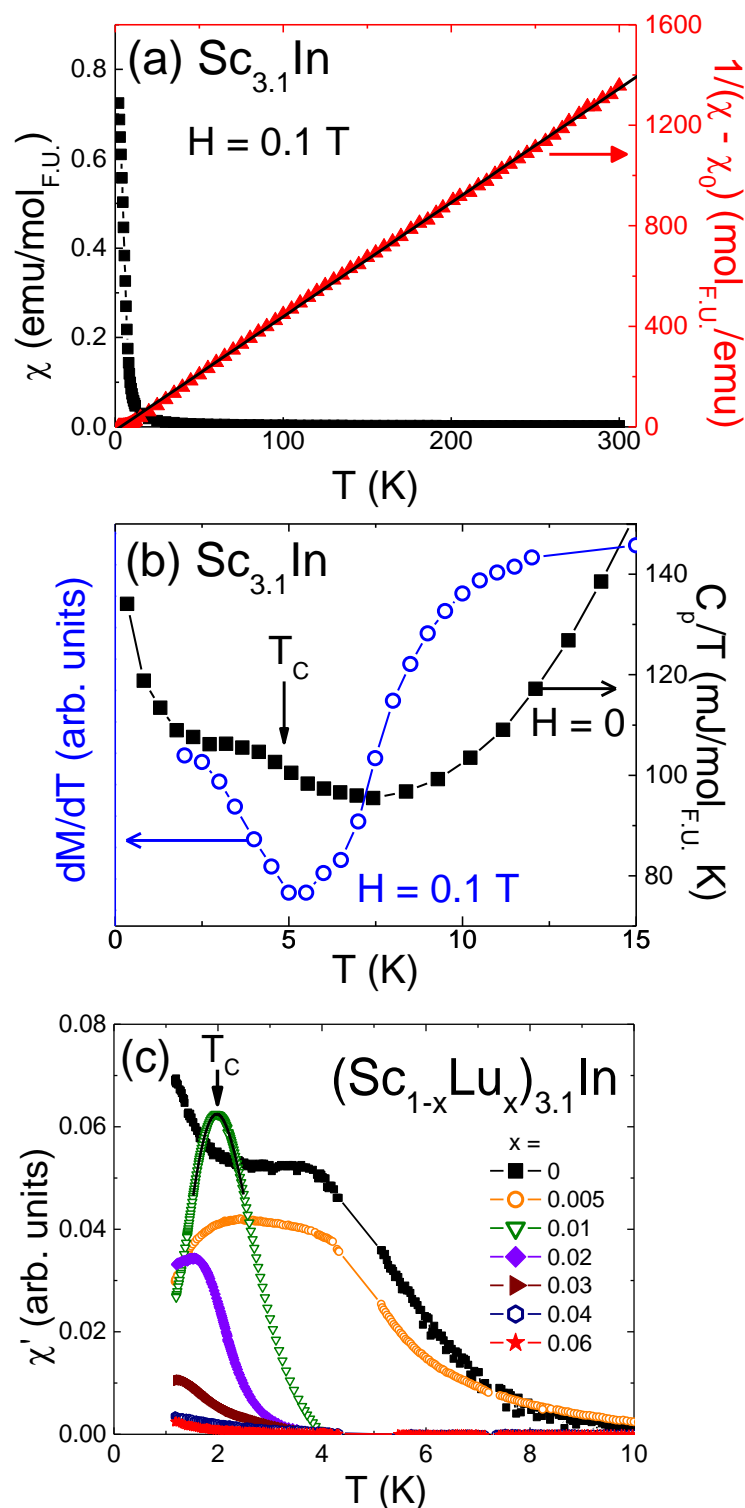


Figure 4.2: (a) Sc_{3.1}In susceptibility (left) and inverse susceptibility $1/(\chi - \chi_0)$ (right) for $H = 0.1$ T, where $\chi_0 = C/T^*$ (see text). (b) The magnetization derivative dM/dT (left) and specific heat C_p/T (right) for Sc_{3.1}In with the vertical arrow marking the Curie temperature T_C . (c) (Sc_{1-x}Lu_x)_{3.1}In AC susceptibility $\chi'(T)$. The Curie temperature T_C is estimated from the peak position (solid line), indicated by the vertical arrow.

Curie temperature T_C . As shown below, this is not the case in $(\text{Sc}_{1-x}\text{Lu}_x)_{3.1}\text{In}$, even though T_C and T_C^* are both continuously suppressed to 0 K with x .

A local minimum in the derivative dM/dT (Fig. 4.2(b), left axis) corresponds to the Curie temperature T_C in $\text{Sc}_{3.1}\text{In}$. Moreover, the specific heat data for $x = 0$, plotted as C_p/T (right axis, Fig. 4.2(b)), also displays a broad maximum at T_C . This is remarkable, given that such transitions are often difficult to identify in the field-independent properties of itinerant ferromagnets, even in single crystalline samples [57]. In $\text{Sc}_{3.1}\text{In}$, the susceptibility derivatives and specific heat data provide evidence that the ferromagnetic ordering occurs below $T_C \sim 4.5$ K, as also demonstrated by the field-dependent data shown below. The different measurements consistently indicate that T_C is significantly lower than the older estimates from Arrott isotherms alone [124, 139, 367], when Sc_3In was erroneously assumed to be a mean-field ferromagnet.

In $(\text{Sc}_{1-x}\text{Lu}_x)_{3.1}\text{In}$, T_C is continuously suppressed by Lu doping above $x = 0.02$ to values below those accessible by the QD MPMS system. Further data below $T = 2$ K was collected from ^4He AC susceptibility measurements shown in Fig. 4.2(c). Lack of data around the 4.2 K ^4He transition precludes a T_C estimate for $x = 0$ and $x = 0.005$, when the transition falls close to this temperature interval. However, for all other compositions up to $x = 0.04$, the peak corresponding to T_C (illustrated by the solid line fit in Fig. 4.2(c)) is continuously reduced to temperatures below $T = 1.17$ K, as shown in Fig. 4.2(c). This agrees with the critical composition $x_c = 0.035 \pm 0.005$, as determined from the analysis below.

4.2.2 Arrott and Arrott-Noakes Analysis

Strong spin fluctuations in $\text{Sc}_{3.1}\text{In}$ result in deviations from linearity in the inverse susceptibility around T_C^* which precludes the accurate determination of the Curie temperature T_C from the $\chi(T)$ data. Alternatively, Arrott isotherms M^2 vs. H/M [22]

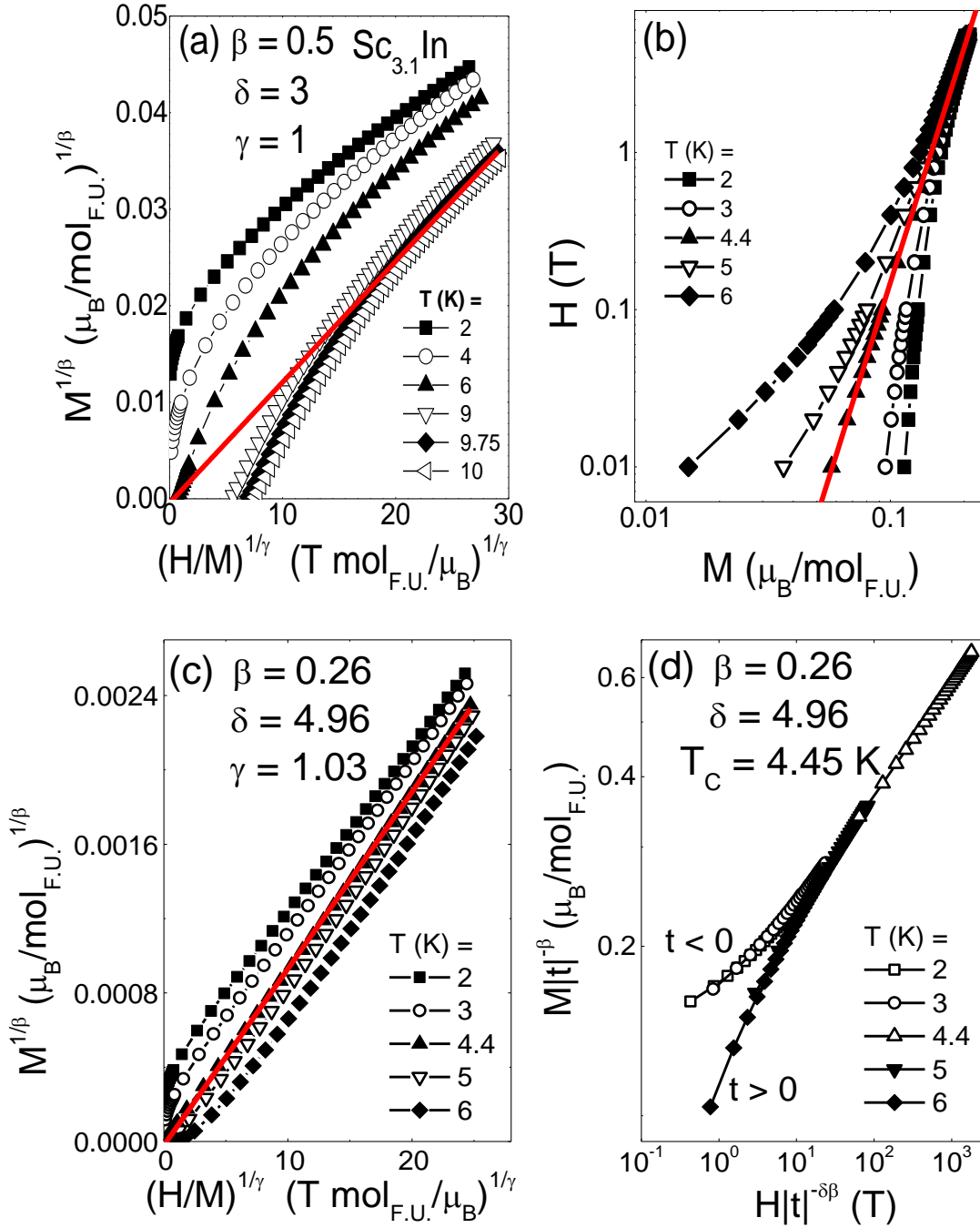


Figure 4.3: $M^{1/\beta}$ vs. $(H/M)^{1/\gamma}$ isotherms for $\text{Sc}_{3.1}\text{In}$ with (a) mean field exponents $\beta = \beta_{\text{MF}} = 0.5$ and $\gamma = \gamma_{\text{MF}} = 1$, $T_C = 9.75$ K (solid line) and (c) non-mean-field exponents $\beta = 0.26$ and $\gamma = 1.03$, $T_C = 4.45$ K (solid line). (b) Log-log plot of $\text{Sc}_{3.1}\text{In}$ $M(H)$ isotherms, with the straight line representing the fit for the critical isotherm. (d) Arrott-Noakes scaling plots $M|t|^{-\beta}$ vs. $H|t|^{-\delta\beta}$. The scaled $M(H)$ data collapses onto two diverging branches, one below T_C ($t < 0$, open symbols) and one above T_C ($t > 0$, full symbols).

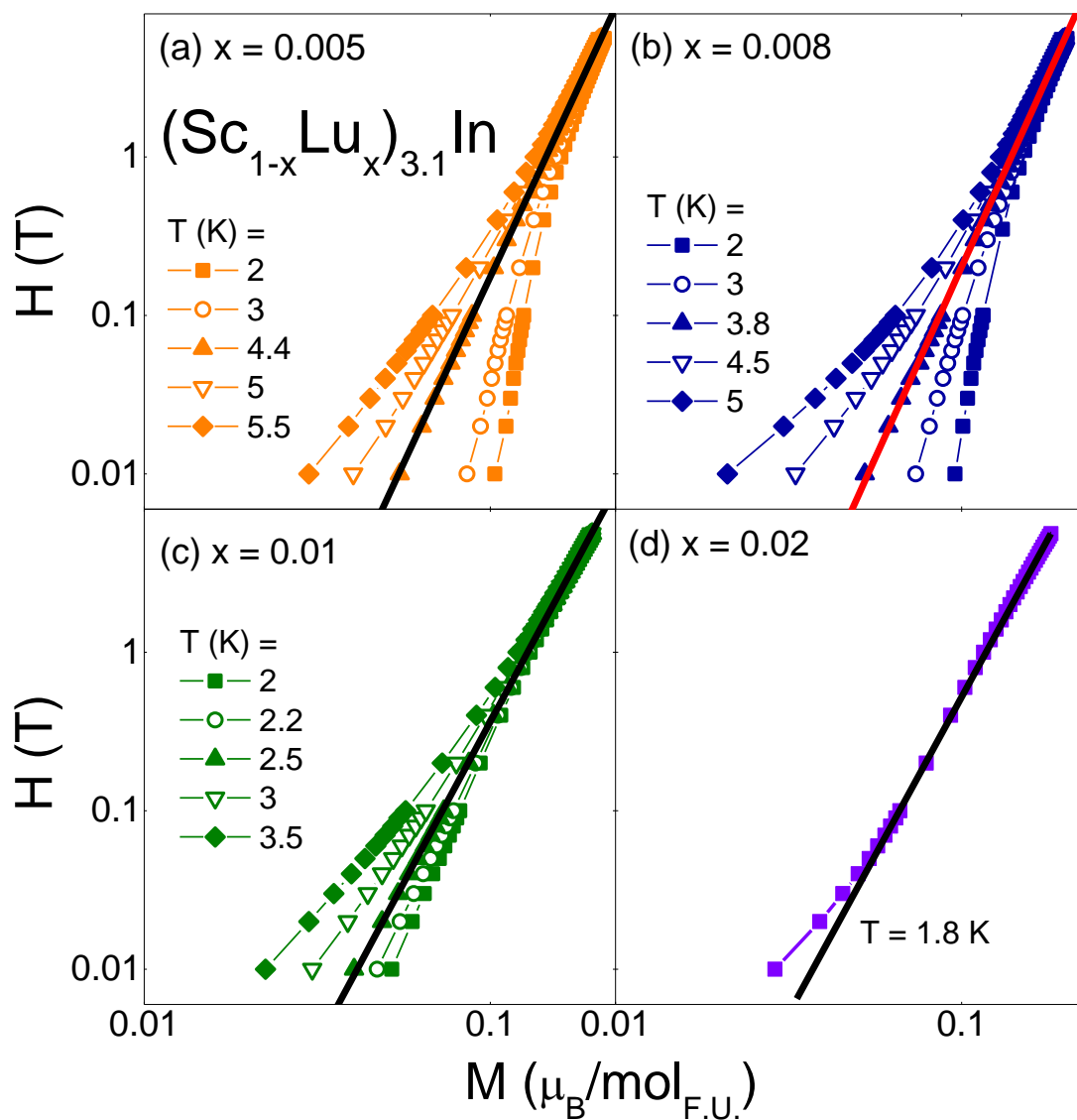


Figure 4.4: Log-log $(\text{Sc}_{1-x}\text{Lu}_x)_{3.1}\text{In}$ $M(H)$ isotherms for (a) $x = 0.005$, (b) $x = 0.008$ and (c) $x = 0.01$ with linear fits (solid lines) at the critical ($T = T_C$) isotherm. (d) Log-log $M(H)$ curve for $x = 0.02$ and $T = 1.8$ K, with a linear fit above $H = 0.05$ T.

had previously been employed to determine T_C in Sc_3In . Existing reports give this value to be less than 7.5 K [124, 139, 168, 244, 367]. If the Arrott plot technique were used for $\text{Sc}_{3.1}\text{In}$ (Fig. 4.3(a)), it would appear that ferromagnetic order occurred close to 9.75 K. This implies that the Sc-In ratio used for the current study is closest to the optimal one [244], compared to all previous reports. However, the Arrott isotherms deviate strongly from linearity at high H values [124, 139, 367]. This is a compelling indication that the mean-field theory cannot accurately describe the weak ferromagnetism in $\text{Sc}_{3.1}\text{In}$, in contrast with, for example, ZrZn_2 [341]. The more generalized Arrott and Noakes method [24] was successfully employed to characterize the critical scaling in the heavy fermion ferromagnet URu_2Si_2 doped by Re [57]. In the current work, this generalized critical scaling is applied to a different type of quantum critical point, in the weak itinerant ferromagnet $\text{Sc}_{3.1}\text{In}$ which has no local moment elements. It would appear that the non-Fermi liquid behavior results from the non-mean field character of the magnetism in these itinerant ferromagnets.

The Arrott-Noakes scaling represents a generalization of the mean-field scaling of the magnetization M , magnetic field H and the reduced temperature $t = (T/T_C - 1)$, as summarized in Section 2.2.3. In the case of $(\text{Sc}_{1-x}\text{Lu}_x)_{3.1}\text{In}$, the Curie temperature T_C and exponent δ are first determined from log-log $M(H)$ plots for each composition, as shown in Fig. 4.3(b) for $x = 0$ and in Fig. 4.4(a-c) for $x = 0.005, 0.008$, and $x = 0.01$. At T_C , critical scaling requires that the isotherm be linear, with a slope equal to the critical exponent δ . The $T = 1.8$ K isotherm for $x = 0.02$ is nearly linear all the way down to $H = 0$ T (Fig. 4.4(d)), indicating that T_C for $x = 0.02$ is finite and smaller than 1.8 K. For all other ferromagnetic compositions (Fig. 4.4(a-c)), non-linear isotherms occur within 20% of T_C . Therefore, in the absence of $M(H)$ measurements below 1.8 K, the nearly linear log-log $M(H; 1.8 \text{ K})$ isotherm for $x = 0.02$ is a good indication that the T_C value estimate for this composition is within 20% of T_C , which yields $T_C(x = 0.02) = 1.5 \pm 0.3$ K.

This value agrees well with the AC susceptibility estimate, where $T_C = 1.62$ K.

Next, the critical exponents β and γ are determined from the expected linear dependence of $M^{1/\beta}$ vs. $(H/M)^{1/\gamma}$. A subset of the resulting isotherms is shown in Figs. 4.3(c) ($x = 0$) and 4.1(a-c) ($x = 0.005, 0.008$ and 0.01). The extrapolations of the linearized isotherms in the ferromagnetic state yield the spontaneous magnetization M_0 from the vertical axes intercepts. As expected, M_0 scales with $|t|^\beta$, as shown in Fig. 4.6(a) for $(\text{Sc}_{1-x}\text{Lu}_x)_{3.1}\text{In}$ where $0 \leq x \leq 0.02$. In contrast with $\text{URu}_{2-x}\text{Re}_x\text{Si}_2$ [57], M_0 for $(\text{Sc}_{1-x}\text{Lu}_x)_{3.1}\text{In}$ (Fig. 4.6(a)) grows faster in the ordered state, as the critical exponent β for the former, $\beta = 0.26 \pm 0.05$, is less than half of the respective value in the latter system [57]. However, the β values in $(\text{Sc}_{1-x}\text{Lu}_x)_{3.1}\text{In}$ are unusually small, which implies that the ordered moment in this weak itinerant ferromagnet is more readily destabilized by fluctuations close to T_C . This might indicate a fragile magnetism in a nearly 1D electron system [177], which doping and the attendant disorder immediately suppress to 0 K.

The Arrott-Noakes critical exponents δ (triangles), γ (squares) and β (circles), scaled by their mean-field (MF) values, are presented in Fig. 4.6(b) as a function of composition. Most strikingly, δ is nearly twice as large as its mean-field value δ_{MF} , while β is nearly half of β_{MF} , leaving γ nearly identical to its mean-field value γ_{MF} . δ is a measure of the curvature of $M(H)$ at T_C , with larger values signaling faster saturation. A comparison between $(\text{Sc}_{1-x}\text{Lu}_x)_{3.1}\text{In}$ and $\text{URu}_{2-x}\text{Re}_x\text{Si}_2$ [57] shows that larger δ values for the former compound are also associated with a larger relative magnetization $M(5.5 \text{ T}; 1.8 \text{ K}) \approx 0.2 \mu_B$. This value at $t = 0.6$ is nearly 15% of the paramagnetic moment $\mu_{PM} \approx 1.3 \mu_B$ for the composition $x = 0$ with maximum T_C . The corresponding value for $\text{URu}_{2-x}\text{Re}_x\text{Si}_2$ is $M(5.5 \text{ T}; 1.8 \text{ K})/\mu_{PM} \approx (0.4 \mu_B)/(3.8 \mu_B) \approx 10\%$ (for which $T_{C,max} = 27 \text{ K}$ is obtained for $x = 0.6$), nearly one third less at a comparable relative temperature t (Fig. 1, bottom panel, in Ref.

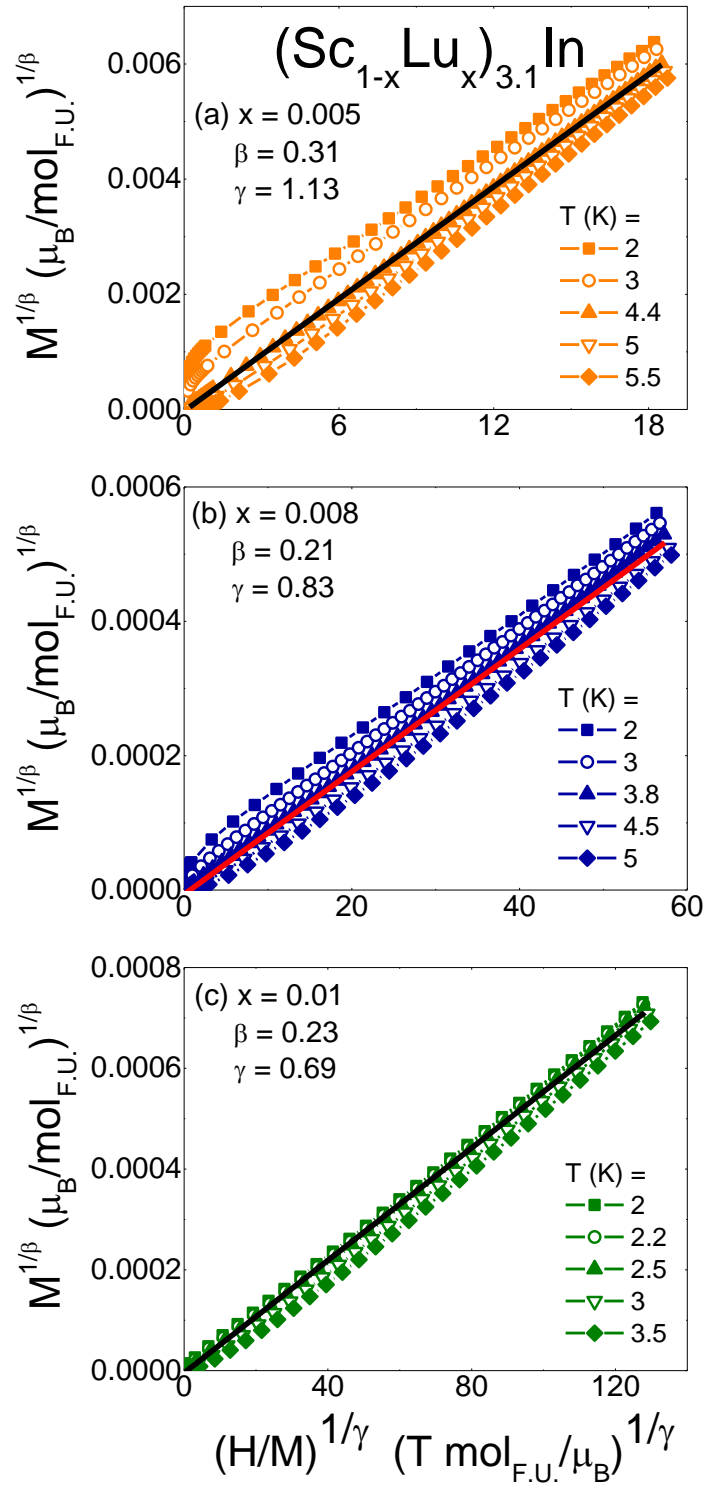


Figure 4.5: $(\text{Sc}_{1-x}\text{Lu}_x)_{3.1}\text{In}$ Arrott-Noakes $M^{1/\beta}$ vs. $(H/M)^{1/\gamma}$ isotherms for (a) $x = 0.005$, (b) $x = 0.008$, and (c) $x = 0.01$ with linear fits (solid lines) at T_C .

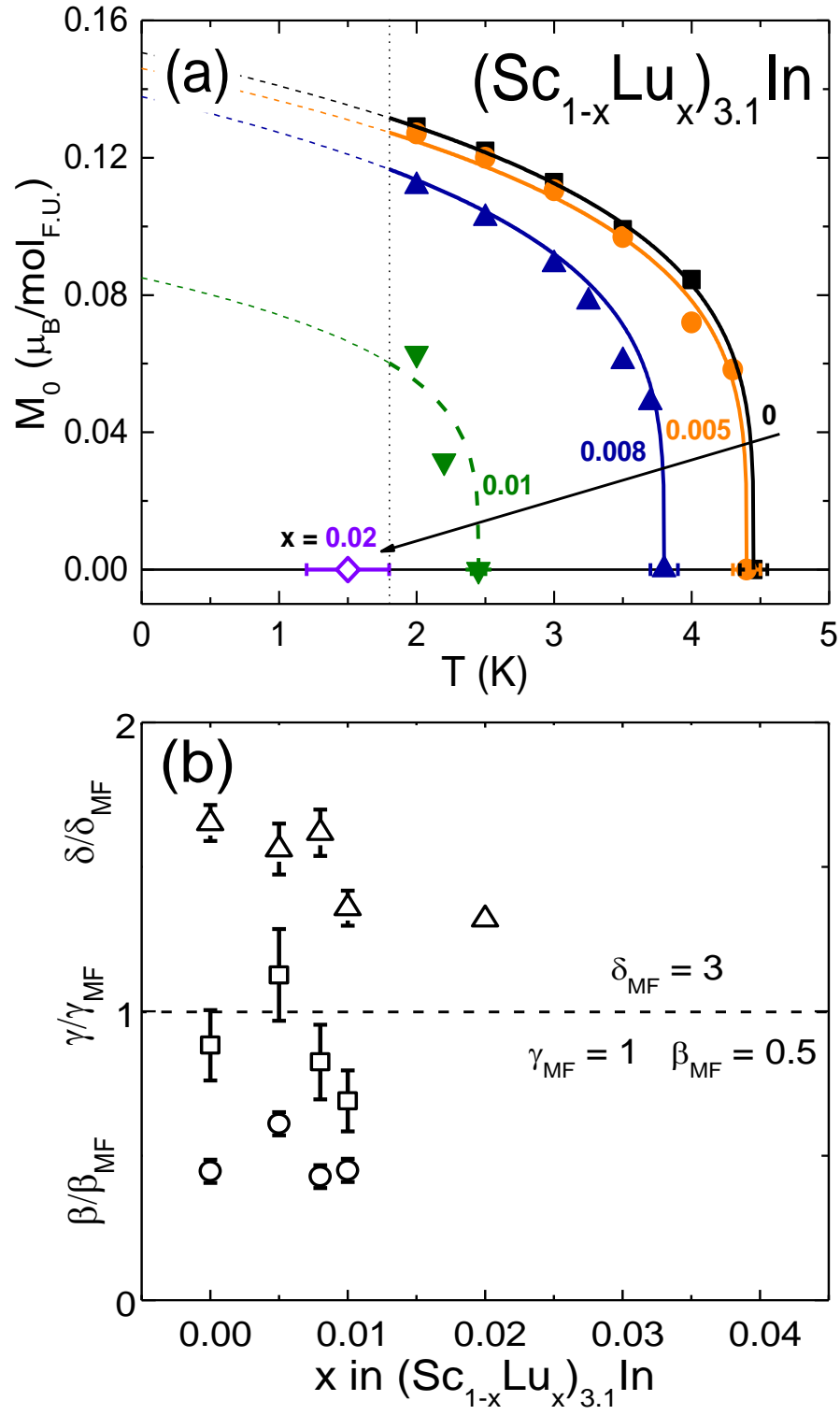


Figure 4.6: (a) Spontaneous magnetization $M_0(T)$ for $(\text{Sc}_{1-x}\text{Lu}_x)_{3.1}\text{In}$ where $0 \leq x \leq 0.02$. (b) The critical exponents scaled by their mean-field values $\delta/\delta_{\text{MF}}$ (triangles), $\gamma/\gamma_{\text{MF}}$ (squares) and β/β_{MF} (circles) as a function of composition x .

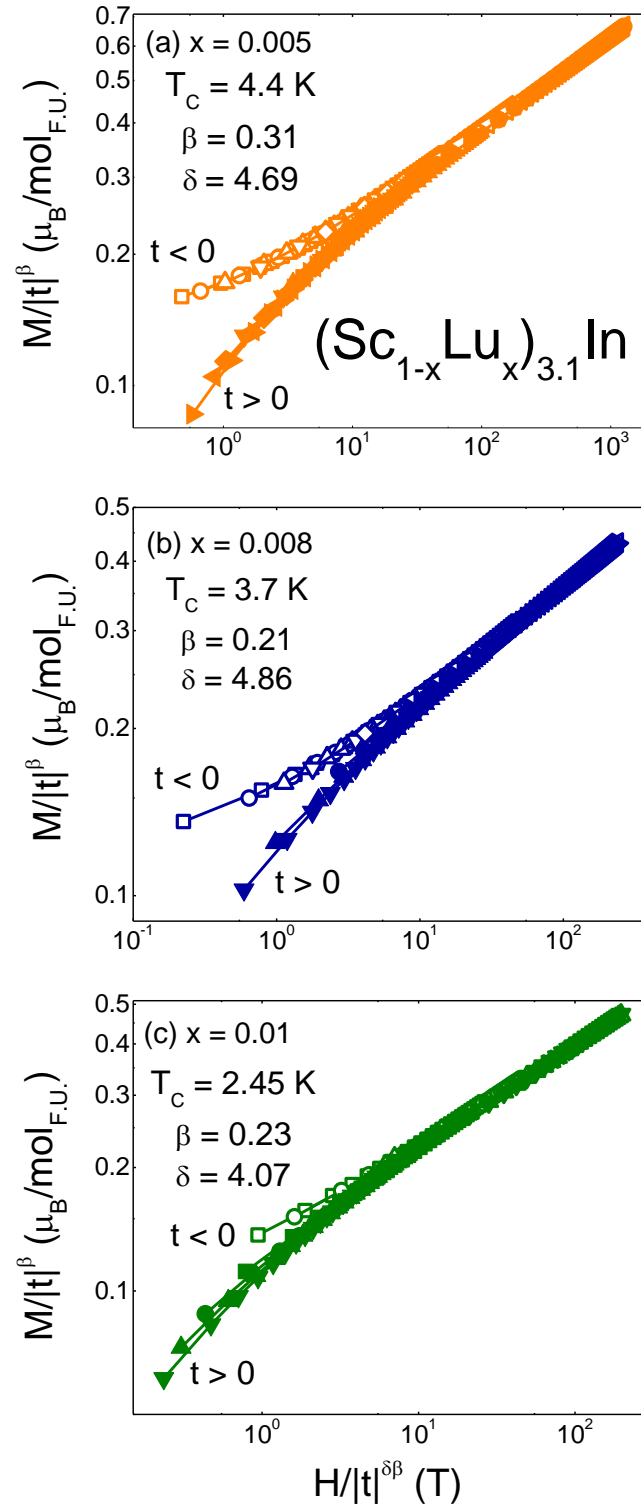


Figure 4.7: Scaling plots $M|t|^{-\beta}$ vs. $H|t|^{-\delta\beta}$ for (a) $x = 0.005$, (b) $x = 0.08$ and (c) $x = 0.01$ in $(\text{Sc}_{1-x}\text{Lu}_x)_{3.1}\text{In}$.

[24]).

The scaling collapse of $M|t|^{-\beta}$ vs. $H|t|^{-\delta\beta}$, shown in Figs. 4.3(d) and 4.1(a-c), exemplifies how the $M|t|^{-\beta}$ vs. $H|t|^{-\delta\beta}$ curves collapse onto two diverging branches, for $t < 0$ (open symbols) and $t > 0$ (full symbols). This collapse is similar to that observed for the heavy fermion $\text{URu}_{2-x}\text{Re}_x\text{Si}_2$ [57], which is remarkable, given the lack of formal local moments in the constituent elements of $(\text{Sc}_{1-x}\text{Lu}_x)_{3.1}\text{In}$.

4.2.3 Non-Fermi Liquid Behavior

An independent and compelling evidence for the quantum critical point in the doped $\text{Sc}_{3.1}\text{In}$ system is the non-Fermi liquid behavior below $x = 0.04$. One signature of non-Fermi liquid behavior is the logarithmic temperature dependence of the specific heat C_p/T (Fig. 4.8(a)), which occurs over a decade in temperature. The $T\ln T$ specific heat, shown in Fig. 4.8(a), may, in principle, have two possible origins: non-Fermi liquid behavior or Schottky anomaly. For a Schottky anomaly, a low- T peak in the specific heat would move up in temperature with increasing H . However, the decrease of the low temperature C_p/T with increasing H (inset, Fig. 4.8(a)) invalidates the Schottky anomaly scenario and not surprisingly, since this would be associated with low-lying energy states (not the case for a system with no formal local moments). The non-Fermi liquid scenario is therefore more plausible in $(\text{Sc}_{1-x}\text{Lu}_x)_{3.1}\text{In}$ for $0 \leq x \leq 0.04$. More interestingly, the non-Fermi liquid behavior coexists with the ferromagnetic state. This coexistence has been explained based on magnetic cluster formation as a result of competition between Ruderman-Kittel-Kasuya-Yosida (RKKY) coupling and Kondo effect [35, 280]. However, this is the *first* observation of non-Fermi liquid behavior within the ferromagnetic state in a weak itinerant ferromagnet without magnetic elements. The implication is that a new model would be required to describe the ground state in $\text{Sc}_{3.1}\text{In}$, or that the Griffiths-McCoy model [141]

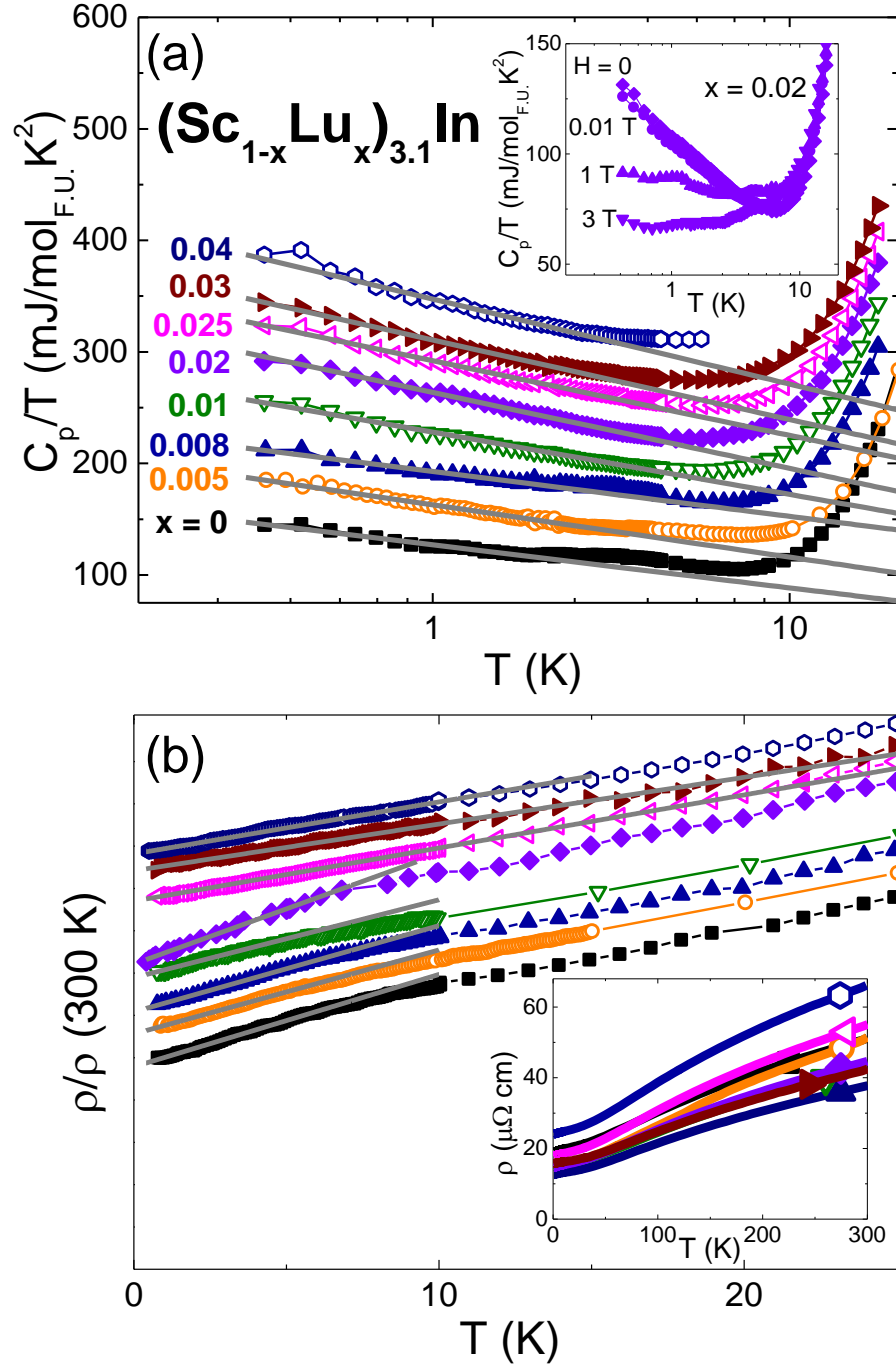


Figure 4.8: (a) Semi-log plot of the specific heat C_p/T (symbols) and the linear fits (lines) at low temperatures. The data for $x > 0$ are shifted vertically for clarity by 30 $\text{mJ/mol}_{\text{F.U.}} \text{K}^2$. Inset: Specific heat for $(\text{Sc}_{0.98}\text{Lu}_{0.02})_{3.1}\text{In}$ in various magnetic fields: $H = 0, 0.01, 1$ and 3 T. (b) Temperature-dependent resistivity for $(\text{Sc}_{1-x}\text{Lu}_x)_{3.1}\text{In}$ ($0 \leq x \leq 0.04$). The data are shifted vertically for clarity. Inset: the whole range of $\rho(T)$ from which RRR is determined.

may still be appropriate if evidence for Kondo effect emerged for this compound.

Besides the $T\ln T$ behavior in the specific heat, $(\text{Sc}_{1-x}\text{Lu}_x)_{3.1}\text{In}$ displays linear resistivity at the lowest temperatures $\rho(T) = \rho_0 + AT^n$ ($n = 1$), as shown in Fig. 4.8(b). A detailed study of the $(\text{Sc}_{1-x}\text{Lu}_x)_{3.1}\text{In}$ resistivity and non-Fermi liquid behavior as a function on both T and x is underway, revealing that the resistivity exponent remains $n = 1$ well beyond T_C , substantively different from the marginal Fermi liquid exponent $n = 5/3$ of ZrZn_2 [337]. Moreover, the specific heat data for ZrZn_2 is Fermi liquid-like [297], with no $T\ln T$ dependence like that reported here for $(\text{Sc}_{1-x}\text{Lu}_x)_{3.1}\text{In}$. As illustrate by the inset in Fig. 4.8b for $x = 0$, all polycrystalline $(\text{Sc}_{1-x}\text{Lu}_x)_{3.1}\text{In}$ samples have comparable $\rho(T)$ values for $0 \leq x \leq 0.10$. It should be remarked that the absolute residual resistivity values ρ_0 and the residual resistivity ratios $\text{RRR} = \rho(300 \text{ K})/\rho_0$ for $(\text{Sc}_{1-x}\text{Lu}_x)_{3.1}\text{In}$ are $\rho_0 \sim \mu\Omega\text{cm}$ and $\text{RRR} \sim 3 - 4$, values characteristic of good metals, comparable even with those of ZrZn_2 single crystals [337]. These are arguments suggesting minimal disorder effects on the quantum critical behavior of the doped $\text{Sc}_{3.1}\text{In}$. Even more important for the question of disorder, the resistivity change $\Delta\rho$ in the range of linearity (Fig. 4.8b) is also comparable to the residual resistivity values ρ_0 , whereas strong disorder effects would result in $\Delta\rho \ll \rho_0$. Therefore the resistivity exponent itself $n = 1$ and the $T\ln T$ specific heat in $(\text{Sc}_{1-x}\text{Lu}_x)_{3.1}\text{In}$ speak in favor of small disorder effects, by contrast with, for example, doped $\text{Ni}_x\text{Pd}_{1-x}$ [281]. In the latter compound, disorder was considered to change the temperature dependence of the specific heat from the expected non-Fermi liquid $T\ln T$ in the quantum critical region, to $T^{3/2}$ slightly away from the quantum critical point. Even for the pressure-induced quantum critical point in MnSi [297], the resistivity exponent is found to be $n = 3/2$, a value attributed to frozen-in disorder even in very high purity systems.

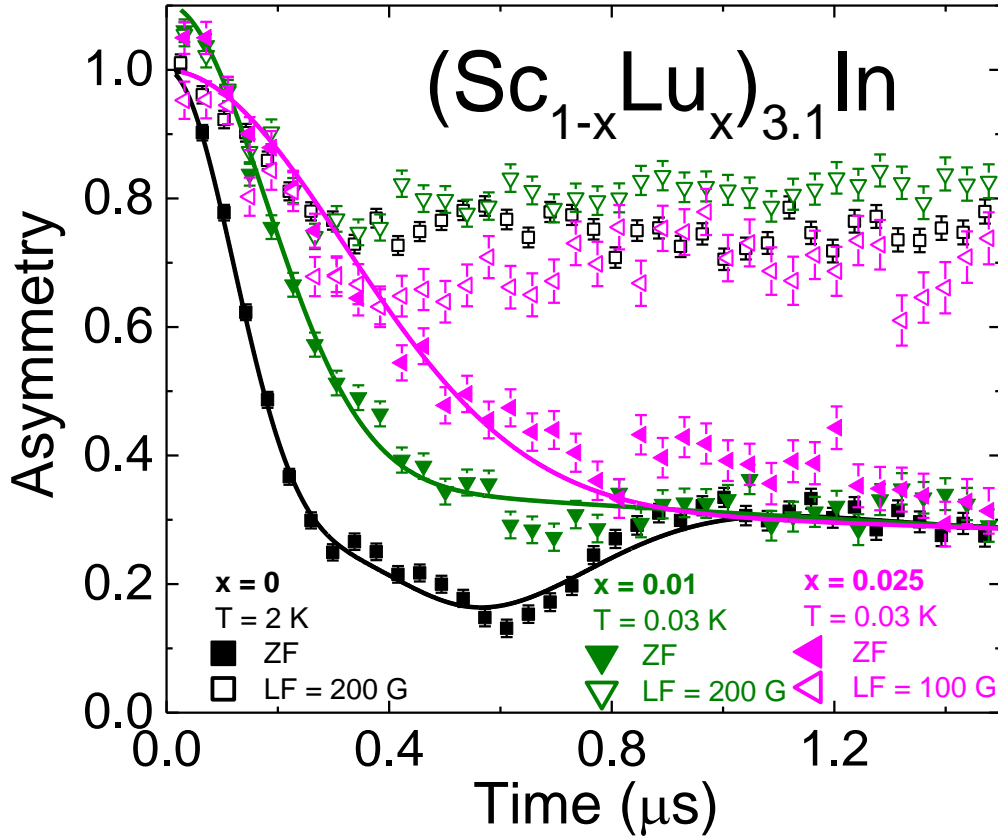


Figure 4.9: Time spectra of zero field and longitudinal field μSR of $(\text{Sc}_{1-x}\text{Lu}_x)_{3.1}\text{In}$ where $x = 0$ (squares), 0.01 (downward-facing triangles) and 0.025 (leftward-facing triangles). The background sample holder contribution in the two Lu-doped samples was subtracted. The solid lines represent fits to Eqs. 4.3 and 4.4.

4.2.4 Muon Spin Relaxation Measurements

The small saturation moments of itinerant systems preclude the accurate determination of the small ordered moment from neutron diffraction investigations, similar to the case of ZrZn_2 [6]. On the contrary, the muon spin relaxation (μSR) technique is extremely sensitive to local magnetic fields and has been used to investigate multiple itinerant systems [65,128,284,380,383]. Figure 4.9 shows the time spectra observed in zero field and longitudinal field at the lowest temperature. The fast relaxation in the early time region in zero field is eliminated by the decoupling effect in longitudinal field, which indicates that the observed relaxation is due to a static field, generated

by the static magnetic order in both the undoped and doped systems. For the zero field $\text{Sc}_{3.1}\text{In}$ spectrum, two precession frequencies at low temperatures can be seen, as shown in Fig. 4.10(a). The zero field time spectra were analyzed by assuming a functional form of:

$$G(t) = [A_1 \cos(2\pi\nu_1 t)e^{(-\Lambda_1^2 \frac{t^2}{2})} + A_2 \cos(2\pi\nu_2 t)e^{(-\Lambda_2^2 \frac{t^2}{2})} + (A_{1Z} + A_{2Z})e^{(-\frac{t}{T_1})}]V_M + \frac{(1 - V_M)[G_{KT}(t, \Delta_{KT1}) + G_{KT}(t, \Delta_{KT2})]}{2} \quad (4.3)$$

where $G_{KT}(t)$ is the Kubo-Toyabe function [154] for random nuclear dipolar fields, and A_{1Z} and A_{2Z} are assumed to be a half of A_1 and A_2 , respectively, as expected for polycrystalline specimens. A very good fit was obtained by assuming $A_1 = A_2$, presumably due to two magnetically-nonequivalent muon sites populated with equal probabilities. For the longitudinal relaxation rate $1/T_1$, two values for the two different sites could not be resolved. So, one value of T_1 was used in the fit. The temperature dependence of the two frequencies ν_1 and ν_2 is shown in Fig. 4.10(a). The volume fraction V_M of the magnetically ordered region, shown in Fig. 4.10(b), was determined from the amplitudes of the precession signals. The volume fraction V_M decreases gradually with increasing temperature, indicating co-existence of volumes (or regions) with and without static magnetic order. Although the precession signal disappears around $T = 5.5$ K, a small V_M remains above this temperature up to $T \approx 8$ K. This is due to a non-precessing but relaxing signal with a small amplitude, caused by static random fields from the electron system remaining in a small volume fraction.

The Lu-doped samples show relaxing signal without precession at low temperatures, indicating a more random internal field, as compared with the undoped

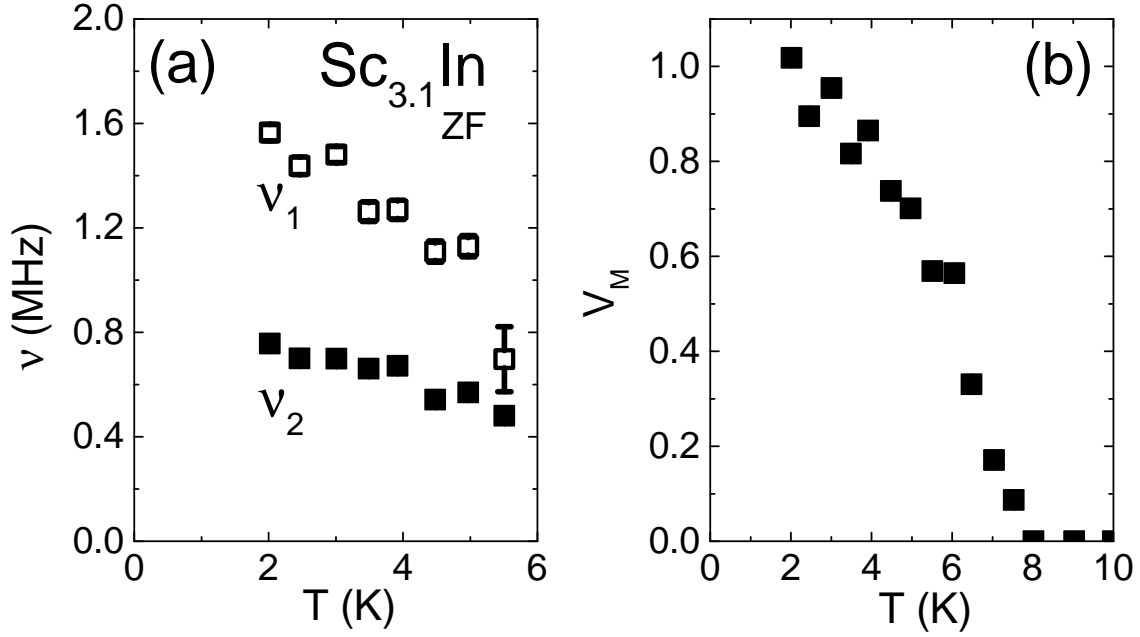


Figure 4.10: (a) The muon spin precession frequencies ν_1 (full squares) and ν_2 (open squares), and (b) the volume fraction V_M of the magnetically ordered regions, obtained from zero field μSR of $\text{Sc}_{3.1}\text{In}$

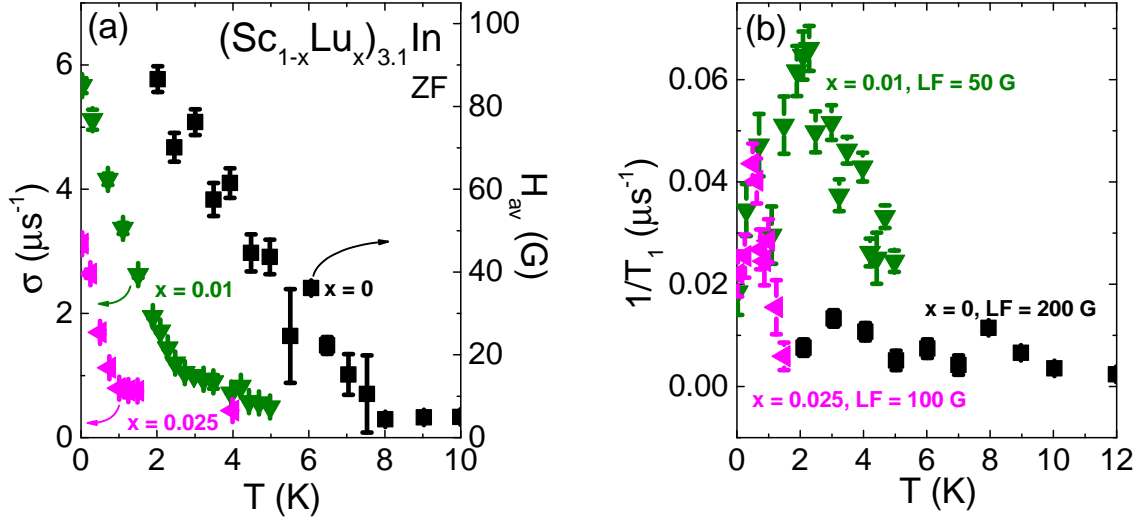


Figure 4.11: (a) Muon spin relaxation rate σ for $x = 0.01$ (downward-facing triangles) and $x = 0.025$ (leftward-facing triangles) for $(\text{Sc}_{1-x}\text{Lu}_x)_{3.1}\text{In}$ (left axis) along with the average static internal field H_{av} for $x = 0$ (right axis), obtained from the fits of zero field μSR measurements. The vertical axes are scaled with γ_μ , the gyromagnetic ratio of a positive muon. (b) The longitudinal relaxation rate $1/T_1$, obtained from the longitudinal field μSR measurements.

Sc_{3.1}In. In order to reproduce the observed line shape, the zero field time spectra of the Lu-doped samples have been analyzed by assuming the following functional form:

$$G(t) = A_1(1 - p\sigma^2)e^{-\frac{1}{2}\sigma^2 t^2} + \frac{A_1}{2}e^{(-\frac{t}{T_1})} + A_{bg} \quad (4.4)$$

where the first term represents the transverse relaxation, the second term is the longitudinal $1/T_1$ component, and the third term is a background signal from the sample holder. From independent measurements in weak transverse field at low temperatures, the values of the non-relaxing background signal from a silver sample holder A_{bg} were estimated to be 0.36 and 0.55 for $x = 0.01$ and 0.025 samples, respectively. These values are consistent with the known background level from the cryostat and sample holder, and a rather small sample size. It is, however, not possible to eliminate the possibility that signal from a small paramagnetic volume in the specimen, persisting to $T = 0$ K, is included in the background signal. Due to difficulty in separating the effects of slow relaxation and partial volume fraction, the amplitude A_1 was fixed to be temperature-independent, allowing to extract the relaxation rate σ . A phenomenological "dip" parameter p ($p = 1$) for the Kubo-Toyabe function was introduced, while smaller p values would fit line shapes with a shallower dip, which are often observed in real materials, including the present case of Lu-doped systems. Although the fit is not perfect, as shown by the lines in Fig. 4.9, the functional form of Eq. 4.4 was used to compare the relaxation rates in different specimens without introducing additional free parameters. Fig. 4.11(a) shows the temperature dependence of σ in the two Lu-doped specimens. To compare the relaxation rates σ with the static field measured in undoped Sc_{3.1}In, the spatially averaged value of the static local field was determined as:

$$H_{av} = V_M \frac{A_1\nu_1 + A_2\nu_2}{A_1 + A_2} + \frac{(1 - V_M)(\Delta_{KT1} + \Delta_{KT2})}{2\gamma_\mu} \quad (4.5)$$

where γ_μ represents the gyromagnetic ratio of a positive muon and Δ_{KT} are the widths of the Kubo-Toyabe function for nuclear dipolar fields. We plot H_{av} in Fig. 4.11(a) with the relaxation rate (left axis) and the average field (right axis), scaled with γ_μ . Since the static internal field is expected to be proportional to the local static spin polarization, Fig. 4.11(a) demonstrates the development of the spatially-averaged magnetic order parameter which can be compared to the spontaneous magnetization M_0 , shown in Fig. 4.6(a).

Measurements of the spin-lattice relaxation rate $1/T_1$ were performed in an applied longitudinal field. Figure 4.11(b) shows the temperature dependence of $1/T_1$ for $(\text{Sc}_{1-x}\text{Lu}_x)_{3.1}\text{In}$ with $x = 0, 0.01, 0.025$. There is no divergent behavior in $\text{Sc}_{3.1}\text{In}$, while the Lu-doped samples exhibit a peak in $1/T_1$ at the ordering temperature. In either case, the absolute values of $1/T_1$ are less than $0.1/\mu\text{s}$, which implies that the relaxation rate measured in zero field (Fig. 4.11(a)) is predominantly due to a static field, even at temperatures very close to the ordering temperature. In Fig. 4.11(a), a finite relaxation rate/average field persists up to high temperatures for all the three systems. This is attributed to the nuclear dipolar field, as Sc has a very large nuclear moment.

The absence of dynamic critical behavior and the gradual change of the volume fraction V_M , observed in undoped $\text{Sc}_{3.1}\text{In}$, indicates a first-order transition at the magnetic order. It is interesting to note that a weak "second order" feature is observed for Lu-doped samples. However, further experimental data are needed given the fact that the order parameter (Fig. 4.11(a)) exhibits a non-linear dependence on the Curie temperature T_C , suggesting a remaining effect of first-order quantum evolution. Additionally, the difficulty in separating the effects of moment sizes and volume fraction at very small relaxation rates, as well as the uncertainty in estimating background level, prevent reliable determination of V_M for the Lu-doped samples.

4.3 Discussion

The paramagnetic moment μ_{PM} (diamonds, Fig. 4.12(a)), determined from the Curie-Weiss-*like* law, is nearly composition-independent $\mu_{PM} \sim 1.3\mu_B/F.U.$ Moreover, the Weiss-*like* temperature T_C^* decreases nearly linearly with x for $x \leq 0.10$, after an initial jump between $x = 0$ and 0.005 (squares, Fig. 4.12(a)). Considering that Curie-Weiss-*like* behavior in the itinerant scenario arises from the temperature-dependence of the amplitude of spin fluctuations [262], this sudden increase in the corresponding T_C^* signals enhanced spin fluctuations due to the disorder brought on by Lu doping. Between $x = 0.02$ and $x = 0.04$, T_C^* changes sign in a continuous manner, suggesting the presence of a (second order) doping-induced quantum critical point in this composition range near $x_c = 0.035 \pm 0.005$. Moreover, T_C determined either from $\chi'(T)$ or $M(H)$ data (Figs. 4.2(c)-4.1) moves down continuously in temperature below 1.17 K for the doping amounts above 0.03, indicating that the quantum critical point is close to this composition.

The determination of the critical composition x_c at the quantum critical point requires consistency between the $M(T)$ and $\chi'(T)$ data, the critical scaling analysis of the $M(H)$ measurements as well as the μ SR results. Indeed, the critical composition $x_c = 0.035 \pm 0.005$ is determined from (i) the T_C (circles and triangles) and T_C^* (squares) values (Fig. 4.12(b)) approaching 0 K at the quantum critical point and (ii) the critical scaling rendering the Arrott-Noakes plots $M^{1/\beta}$ vs. $(H/M)^{1/\gamma}$ as parallel isotherms, equally spaced in t (Figs. 4.3(c) and 4.1(a-c)). Moreover, the μ SR results confirm the development of static magnetic order with a nearly full volume fraction at low temperatures, and diminishing moment size as a function of decreasing ordering temperature. Moreover, the continuous variation of T_C^* and T_C with x and the μ SR evidence for a second order phase transition in the Lu doped samples are also evidence for the quantum phase transition induced by Lu doping.

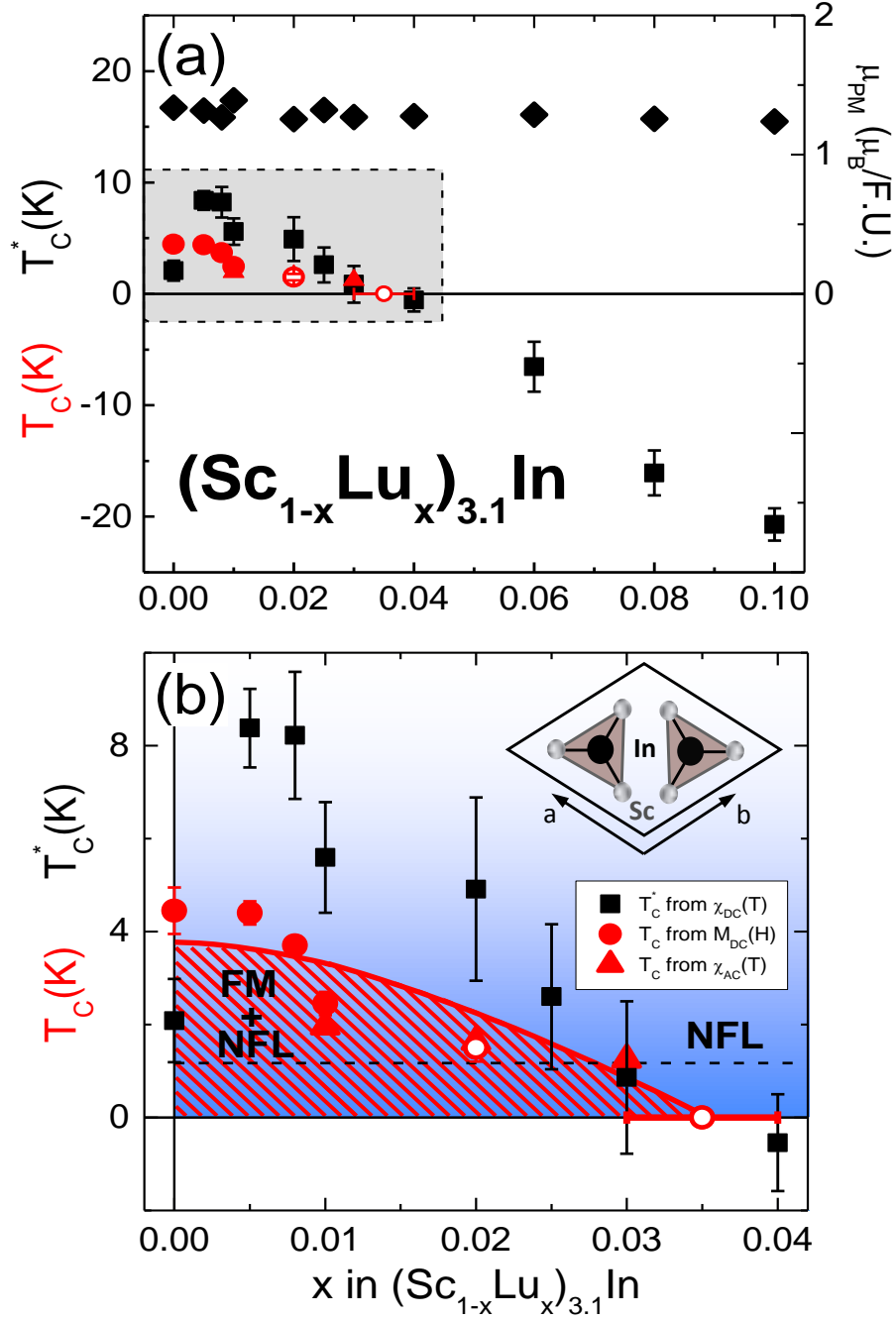


Figure 4.12: (a) $T-x$ phase diagram for $(\text{Sc}_{1-x}\text{Lu}_x)_{3.1}\text{In}$ for $0 \leq x \leq 0.10$, with the Weiss-like temperature T_C^* (squares, left axis), the Curie temperature T_C (circles, left axis) and paramagnetic moment μ_{PM} (diamonds, right axis). (b) Enlarged $T-x$ phase diagram for $x \leq 0.04$ [shaded area in (a)], with the ab plane projection of the $\text{Sc}_{3.1}\text{In}$ unit cell shown in the inset. The horizontal line at $T = 1.17$ K denotes the minimum experimental temperature, with the open symbols representing T_C estimates extrapolated from accessible measurements.

Doping in $\text{Sc}_{3.1}\text{In}$ reveals intriguing traits associated with quantum criticality in general, and with weak itinerant ferromagnet systems in particular: the paramagnetic moment μ_{PM} is surprisingly large in $(\text{Sc}_{1-x}\text{Lu}_x)_{3.1}\text{In}$, and nearly independent of x , even as the system goes through the quantum phase transition at $x_c = 0.035 \pm 0.005$. Not surprisingly then, the critical exponent β is unchanged through the ferromagnetic state, although its value $\beta = 0.26 \pm 0.05$ is smaller than that in any other known quantum critical system. The minute critical composition and small β value, together with the jump in T_C^* as $x > 0$ (Fig. 4.12(b), squares) point to a weak itinerant ferromagnet ground state, easily perturbed by doping. This may seem unusual in light of the stark differences between $\text{Sc}_{3.1}\text{In}$ and the related itinerant ferromagnet system ZrZn_2 [341], with mean-field specific heat and marginal Fermi liquid resistivity behavior, or the similarities with the extraordinary critical scaling in the heavy fermion ferromagnet $\text{URu}_{2-x}\text{Re}_x\text{Si}_2$ [57], close to these systems' respective doping-induced quantum critical points. However, these observations may be reconciled from crystallographic and electronic properties considerations: as a nearly 1D structure is formed by bipyramidal Sc-In chains (Fig. 4.1(c)), the reduced dimensionality in $\text{Sc}_{3.1}\text{In}$ renders it more similar to the layered (2D) URu_2Si_2 compound than the cubic (3D) ZrZn_2 . It appears that the non-Fermi liquid behavior in the ferromagnetic state may also be correlated with the non-mean-field scaling, and, more importantly, that this correlation is independent of the presence of hybridized f -electrons. Consequently, the universality of the quantum critical behavior common to the former two compounds may be ascribed to spin fluctuations, associated with reduced crystallographic dimensionality. More itinerant ferromagnet systems are needed to probe this universality. Equally important is the synthesis of single crystals of $\text{Sc}_{3.1}\text{In}$, which would enable further characterization of the implications of dimensionality on the quantum critical point, as well as to probe the potential non-Fermi liquid behavior at the quantum critical point and in the ferromagnetic state.

Doping-induced Cluster-glass Behavior in (Sc_{1-x}Er_x)_{3.1}In

As it was mentioned previously, Sc_{3.1}In is a weak itinerant ferromagnet with no magnetic constituents. While doping with non-magnetic Lu, discussed in Chapter 4, resulted in a quantum critical point, the interplay of local and itinerant moments in this system has not been investigated. In the following Chapter, this scenario is investigated by doping Sc_{3.1}In with Er³⁺ local moment ions, to form (Sc_{1-x}Er_x)_{3.1}In. As x increases, the Weiss-like temperature θ stays positive and nearly triples up to $x = 0.10$. Moreover, Er doping of as little as $x = 0.02$ induces a cluster-glass state, which persists up to $x = 0.10$, as evidenced by DC and AC susceptibility measurements, and confirmed by the Vogel-Fulcher analysis.

5.1 Motivation and Background

While it has been shown that, in some magnetic systems, the nature of the magnetic moment can be changed from local to itinerant *via* pressure [69] or doping [79, 331], distinguishing between the two types of moments within a given system has proven to be difficult [386, 387]. A possible solution is to use an itinerant electron ferromagnet compound in which all constituents are non-magnetic, and then titrate in local moment-bearing ions. Currently, only two compounds, ZrZn_2 [245] and Sc_3In [246], are known to exhibit itinerant ferromagnetism despite the fact that their components do not possess any magnetic moment. An addition of local moment to the itinerant matrix was attempted *via* Gd^{3+} substitution in $\text{Zr}_{1-x}\text{Gd}_x\text{Zn}_2$ [25]. Surprisingly, it appeared that the instability of the itinerant magnetism in ZrZn_2 [246] prevented the enhancement of the overall magnetization upon doping [25]. Moreover, the Curie temperature T_C and the Weiss-like temperature θ decreased with increasing x in $\text{Zr}_{1-x}\text{Gd}_x\text{Zn}_2$, resulting in the suppression of the ferromagnetic state at $x_c = 0.025$ [25]. Perhaps not as surprising, non-magnetic element doping also resulted in the suppression of the Curie temperature T_C [341]. The similarity between the magnetic and non-magnetic doping effects is quite striking but could possibly be explained by the instability of ferromagnetism in ZrZn_2 , as predicted by the band structure with a narrow peak at the Fermi surface [246, 402]. For Sc_3In , the peak in the density of states at the Fermi level was found to be broader than that of ZrZn_2 [88]. Attempts to drastically alter the overall magnetization *via* pressure [124, 140] and magnetic field [167] were unsuccessful. However, Lu^{3+} doping resulted in remarkable non-Fermi liquid behavior, and revealed the existence of a quantum critical point at $x_c \approx 0.03$ [355], as described in Chapter 4.

The addition of local moment ions in itinerant magnets should provide an insight into the interplay between the two types of magnetism: the itinerant moment

is expected to have a weak variation with the composition, but the overall magnetic moment should increase with increasing amounts of local moment. However, the itinerant magnetic moments was suppressed to zero upon Gd doping of ZrZn_2 [25]. Therefore it is crucial to elucidate how the local and itinerant moments interact. To this end, the effects of Er doping into $\text{Sc}_{3.1}\text{In}$ are presented below. In order to minimize the chemical pressure effects caused by doping, Er^{3+} ($r[\text{Er}^{3+}] = 0.890 \text{ \AA}$) [329] was chosen, since this magnetic rare earth was closest in size to the host Sc ion ($r[\text{Sc}^{3+}] = 0.745 \text{ \AA}$) [329] that it substituted for. Er doping as small as $x = 0.02$ in $(\text{Sc}_{1-x}\text{Er}_x)_{3.1}\text{In}$ induced a cluster-glass state [358]. The corresponding freezing temperature T_f increased with increasing x up to $x \approx 0.10$, a composition which appears to correspond to the solubility limit of Er in $\text{Sc}_{3.1}\text{In}$.

5.2 Physical Properties

It has been established that the mechanism of the cluster-glass behavior relies heavily on the existence of frustration and disorder [273]. Antiferromagnetic coupling [225, 282, 353] lends itself more readily to geometric frustration than ferromagnetic coupling, explaining the limited number of metallic, ferromagnetically coupled cluster-glass systems, as described in Section 2.3.1. Several cases are known, where a cluster-glass states arises from a ferromagnetic ground state in metal oxides [162, 250, 310, 416], however the metallic examples are limited to Pd-Mn [190] and Ce-Ni-Cu [237] alloys, U_2IrSi_3 [224], U_2CoSi_3 [360], and PrRhSn_3 [15]. While the cluster-glass state in both U_2IrSi_3 and U_2CoSi_3 has been attributed to crystallographic disorder [224, 360], dynamic fluctuations of crystal-field levels have been suggested as the underlying mechanism for the magnetic frustration in PrRhSn_3 [15], based on the fact that neither site disorder nor geometric frustration is present in this compound. The current study shows that the addition of Er^{3+} local moments in the ferromagnet $\text{Sc}_{3.1}\text{In}$ induces a

cluster-glass state in $(\text{Sc}_{1-x}\text{Er}_x)_{3.1}\text{In}$ ($0 < x \leq 0.10$), while the Weiss-like temperature θ , a measure of the local-to-itinerant moment coupling, remains positive. The Er-induced site disorder, along with frustration in the bipyramidal Sc/Er-In chains (Fig. 5.1(b)) is the underlying source of the glassy behavior.

The $P6_3/mmc$ structure and purity of the $(\text{Sc}_{1-x}\text{Er}_x)_{3.1}\text{In}$ samples for $0 \leq x \leq 0.10$ was confirmed by x-ray diffraction measurements. The lattice parameters were determined using GSAS refinement, as described in Section 3.2. In the case of undoped $\text{Sc}_{3.1}\text{In}$ (Fig. 5.1(a)), the lattice parameters $a = 6.42 \text{ \AA}$ and $c = 5.18 \text{ \AA}$ agree with the previously reported values [82]. The composition dependence of the lattice parameters a (triangles) and c (circles), together with the change in the unit cell volume V (squares), is shown in Fig. 5.1(b) for $(\text{Sc}_{1-x}\text{Er}_x)_{3.1}\text{In}$ ($0 \leq x \leq 0.10$). A systematic increase in the lattice parameters a and c , and the unit cell volume V is observed with increasing Er concentration. Secondary phase peaks become visible in the x-ray data for $x > 0.10$, suggesting that this is the solubility limit for Er in this hexagonal structure.

The DC magnetic susceptibility presented in Fig. 5.2(a) shows irreversibility between zero field cooled (full symbols) and field cooled (open symbols) data at low temperatures. This irreversibility, together with the increase of the field cooled magnetization upon cooling, is likely associated with either a cluster-glass state or a long-range ferromagnetic order. AC susceptibility data presented below points to the cluster-glass scenario.

At high temperatures, the temperature-dependent susceptibility should be analyzed in the context of the interplay between local and itinerant moment magnetism. For local moments, the susceptibility $\chi_L(T)$ is described by the Curie-Weiss

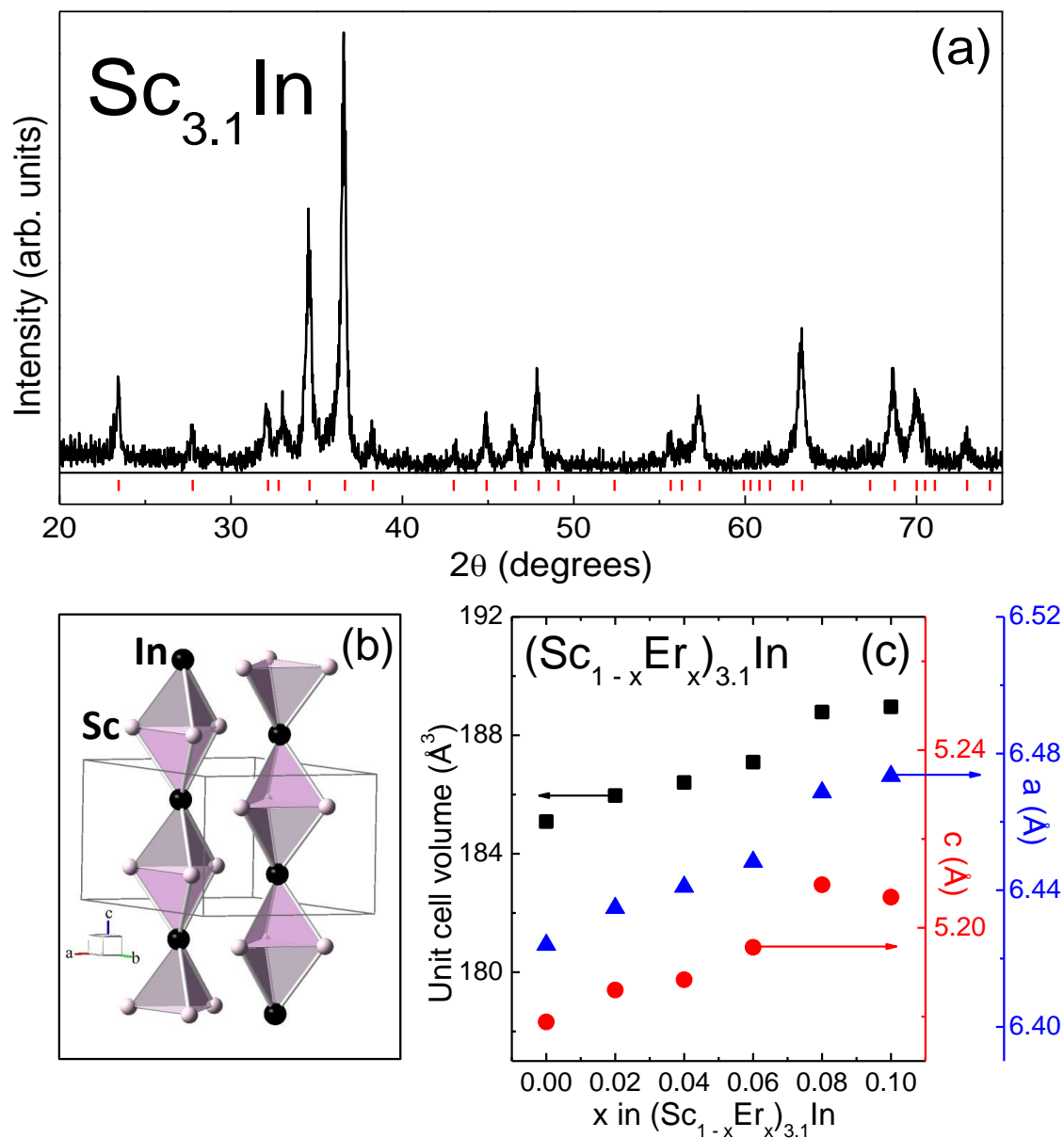


Figure 5.1: (a) X-ray diffraction pattern for $\text{Sc}_{3.1}\text{In}$, obtained from an arc-melted polycrystalline specimen (see text). Vertical marks correspond to the $\text{P6}_3/\text{mmc}$ phase. (b) Nearly one-dimensional bipyramidal Sc-In chains. (c) Evolution of the lattice parameters a (triangles), c (circles) and the unit cell volume V (squares) with composition x .

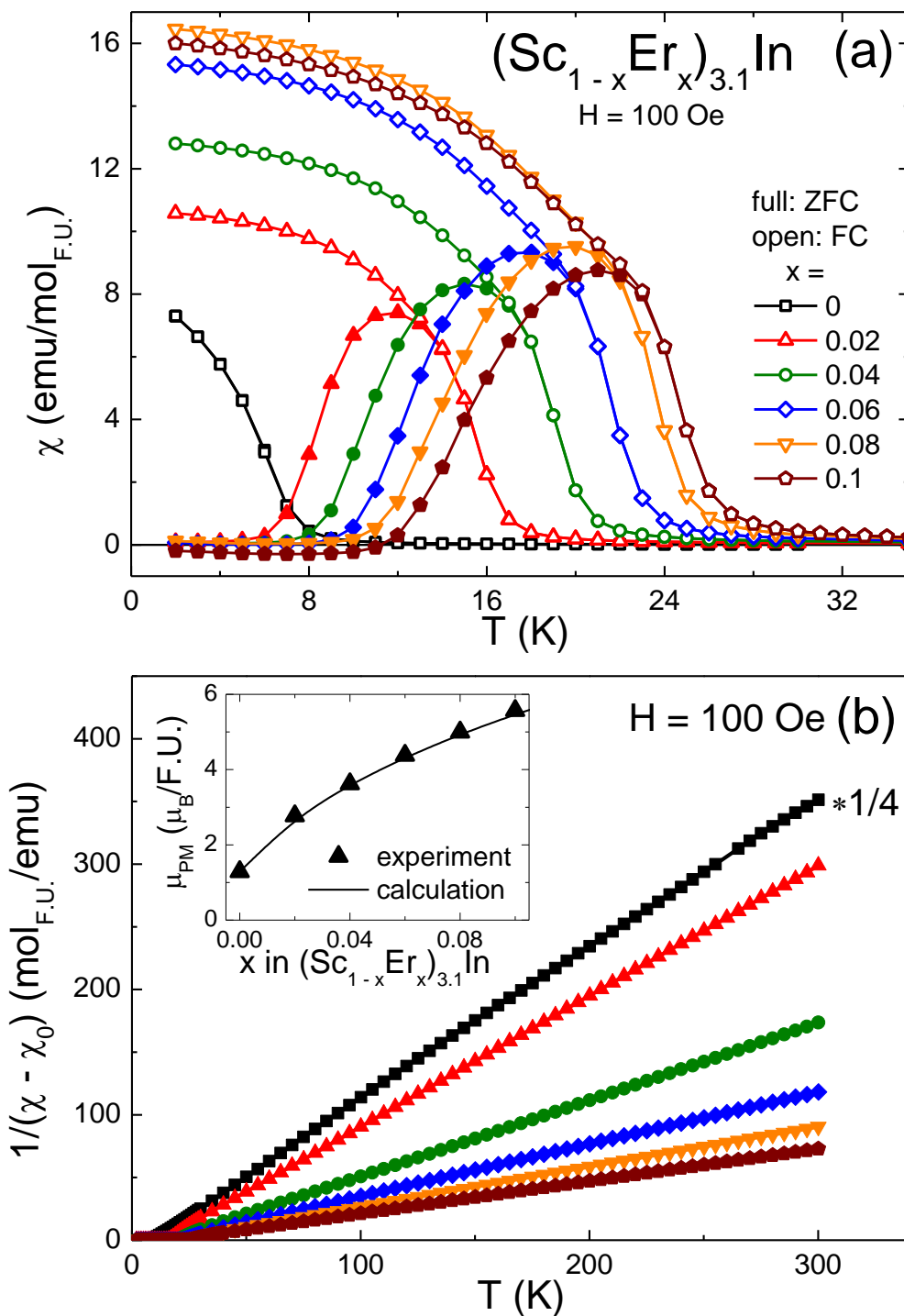


Figure 5.2: (a) zero field cooled (full) and field cooled (open) DC susceptibility for $(\text{Sc}_{1-x}\text{Er}_x)_{3.1}\text{In}$ ($0 \leq x \leq 0.10$). (b) Inverse susceptibility for $(\text{Sc}_{1-x}\text{Er}_x)_{3.1}\text{In}$ where $0 \leq x \leq 0.10$. The $x = 0$ data is scaled by a factor of 1/4. Inset: composition dependence of measured (triangles) and calculated (line) paramagnetic moments μ_{PM}^{exp} and μ_{PM}^{calc} .

law [261]:

$$\chi_L(T) = \chi_{0,L} + \frac{C_L}{T - \theta_W} \quad (5.1)$$

where χ_0 is the temperature-independent magnetic susceptibility, C_L is the local moment Curie constant, and θ_W is the Weiss temperature. The itinerant moment susceptibility $\chi_I(T)$ also varies inversely proportional to the temperature [261], and, in the case of strong spin fluctuations, $\chi_I(T)$ can be written as [261, 355]:

$$\chi_I(T) = \chi_{0,I} + \frac{C_I}{T - T_C^*} \quad (5.2)$$

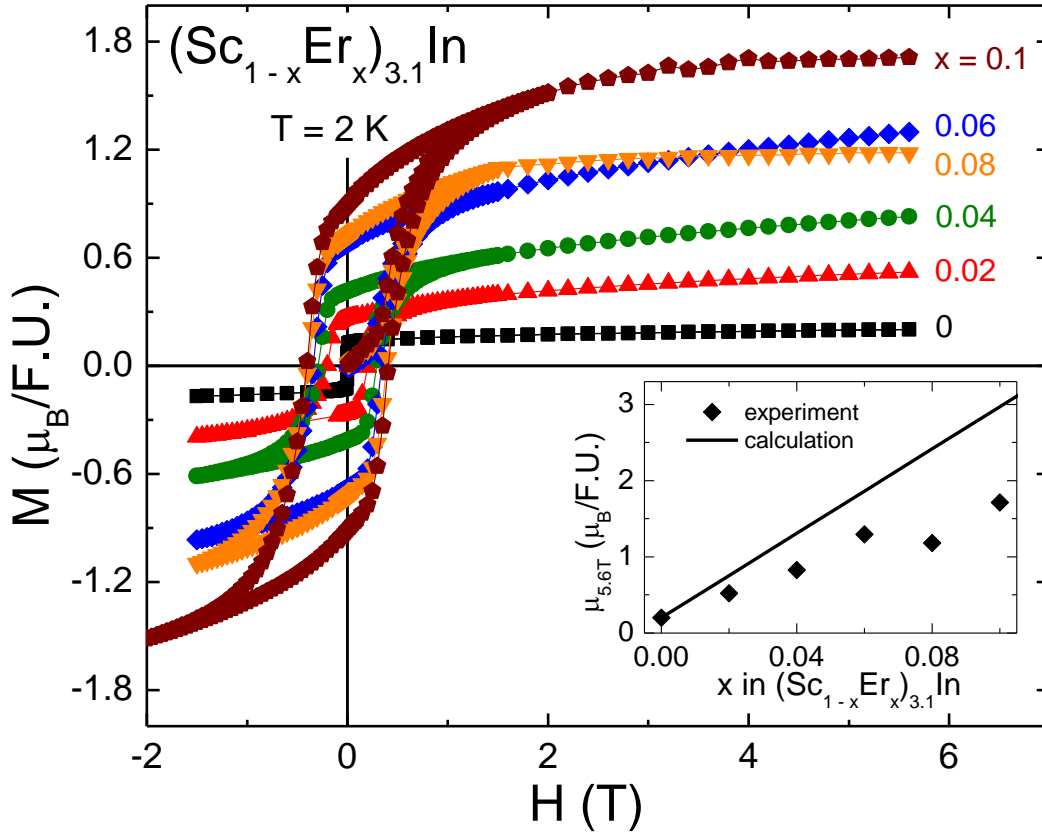


Figure 5.3: $T = 2$ K magnetization as a function of field for $(\text{Sc}_{1-x}\text{Er}_x)_{3.1}\text{In}$ with $0 \leq x \leq 0.10$. Inset: calculated saturated moment μ_{sat}^{calc} (line) and measured magnetic moment $\mu_{5.6T}$ (diamonds).

Here C_I is a Curie-*like* constant, proportional to the quadratic paramagnetic itinerant moment, and T_C^* is a Weiss-*like* temperature. For a system with mixed local and itinerant moment contributions, their linear superposition would result in a magnetic susceptibility of the form:

$$\chi(T) = \chi_0 + a \frac{C_L}{T - \theta_W} + b \frac{C_I}{T - T_C^*} \quad (5.3)$$

As seen in Fig. 5.2(b), the inverse high-temperature susceptibility $1/(\chi(T) - \chi_0)$ is linear in T for $x \leq 0.10$, which is consistent with Eq. 5.3 only if $\theta_W = T_C^* = \theta$, suggesting cooperative behavior of the local and itinerant moments in $(\text{Sc}_{1-x}\text{Er}_x)_{3.1}\text{In}$:

$$\Delta\chi(T) = \chi(T) - \chi_0 = \frac{x C_L + (1 - x) C_I}{T - \theta} = \frac{C_{tot}}{T - \theta} \quad (5.4)$$

The paramagnetic moment μ_{PM}^{exp} and the Weiss-like temperature θ can be determined from the linear fits of the inverse susceptibility at high temperatures, using Eq. 2.28. The θ values, listed in Table 5.1, remain positive and increase monotonously with x up to $x = 0.10$, in contrast with the Gd-doped ZrZn_2 where θ values decreased with Gd concentration [25]. Despite the fact that the $x = 0$ sample has no magnetic constituents, the value of its paramagnetic moment $\mu_{PM}^{exp}(x = 0) = \mu_I \approx 1.3 \mu_B/\text{F.U.}$ is remarkably large, consistent with previous reports [167, 246, 355]. As the amount x of Er is increased, the overall paramagnetic moment μ_{PM}^{exp} grows, as indicated by the decreasing slope of the inverse susceptibility in Fig. 5.2(b). The calculated paramagnetic moment μ_{PM}^{calc} can be estimated as a function of x :

$$\mu_{PM}^{calc} = \sqrt{(1 - x)\mu_I^2 + 3.1x\mu_L^2} \quad (5.5)$$

where $\mu_I = 1.3 \mu_B/\text{F.U.}$ is the itinerant contribution and $\mu_L = 9.59 \mu_B/\text{Er}^{3+}$ is the

local moment per Er^{3+} ion. Good agreement between μ_{PM}^{exp} and μ_{PM}^{calc} , revealed in the inset of Fig. 5.2(b), is an indication of cooperative behavior of the local and itinerant moments in this system.

5.3 Cluster-Glass Analysis

In order to verify the glassiness of $(\text{Sc}_{1-x}\text{Er}_x)_{3.1}\text{In}$, suggested by the DC magnetization data above, additional AC and DC magnetization, and specific heat measurements have been performed. The DC magnetization measurements have already revealed some signatures of cluster glass behavior, including zero field cooled-field cooled irreversibility, increasing χ_{FC} on cooling and $T_f(0) < T_{irr}$ (Fig. 5.2(b)). The AC susceptibility $\chi'(T)$ and specific heat data, together with the magnetization isotherms $M(H)$ at $T = 2$ K, presented below, reveal additional traits associated with the cluster glass behavior, enumerated in Sections 2.3.1.

A notable effect of Er doping in $\text{Sc}_{3.1}\text{In}$ is large hysteresis and finite coercivity in $(\text{Sc}_{1-x}\text{Er}_x)_{3.1}\text{In}$ ($0.02 \leq x \leq 0.10$, Fig. 5.3), while in the pure itinerant system ($x = 0$, squares, Fig. 5.3) no hysteresis is observed at $T = 2$ K. It has been remarked [19] that the low-temperature magnetic moment in a cluster glass is often less than the one for the saturated single ion moment. The field-dependent magnetization data, shown in Fig. 5.3 can be used to determine $\mu_{5.6T}$ as the lower limit for the saturated magnetic moment for all compositions, which can then be compared to the calculated values. The calculated saturated moment is found as the superposition of the itinerant μ_{sat}^{calc} contribution from $\text{Sc}_{3.1}\text{In}$, and the local Er^{3+} contribution, scaled per formula unit:

$$\mu_{sat}^{calc}(x) = 3.1 x \mu(\text{Er}^{3+}) + (1 - x) \mu(\text{Sc}_{3.1}\text{In}) \quad (5.6)$$

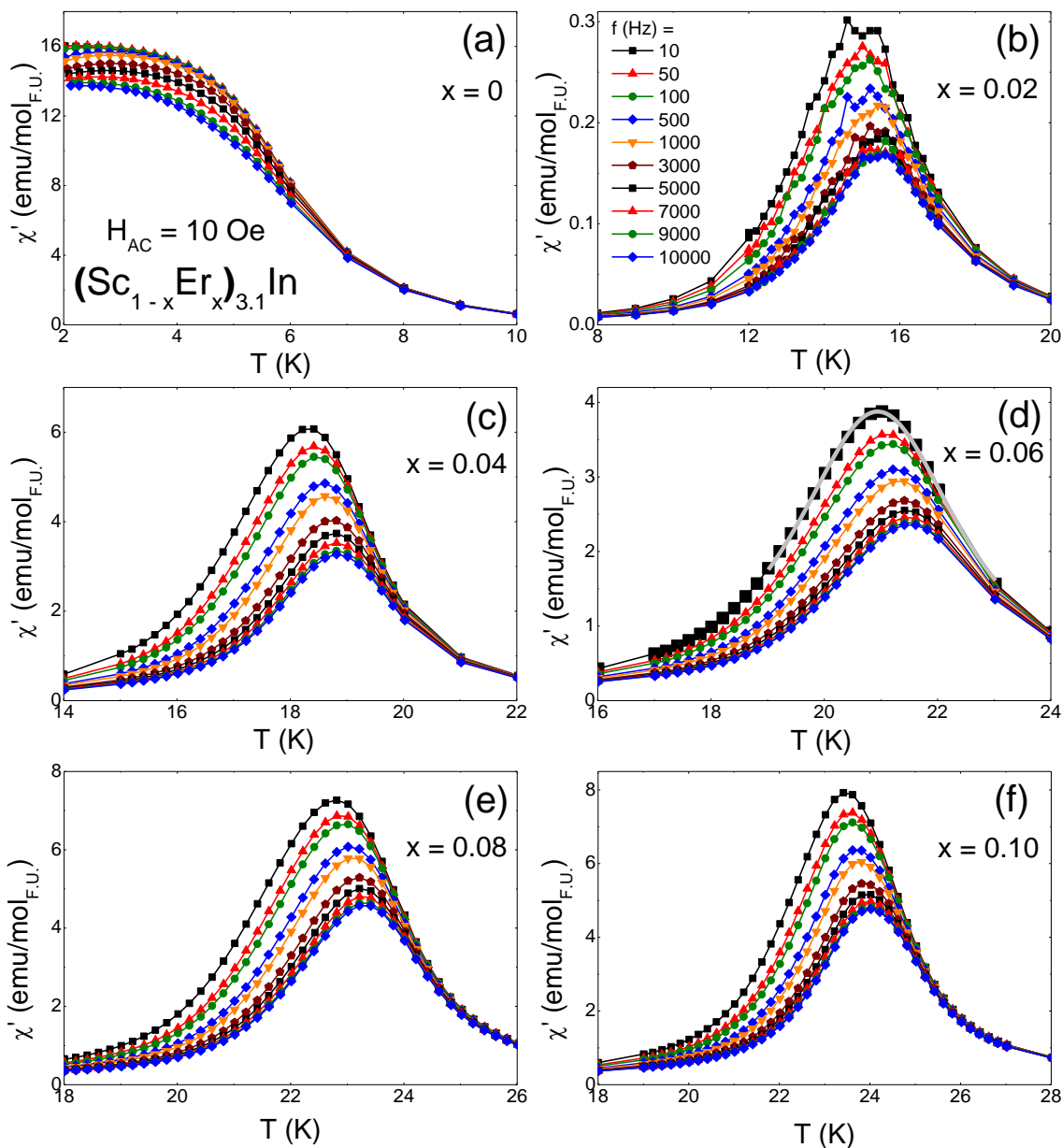


Figure 5.4: Frequency-dependence of the real component $\chi'(T)$ of the AC susceptibility data for $(\text{Sc}_{1-x}\text{Er}_x)_{3.1}\text{In}$ with $0 \leq x \leq 0.10$. An example of fit used to determine the freezing temperature $T_f(f)$ is shown in panel (d) for $f = 10$ Hz.

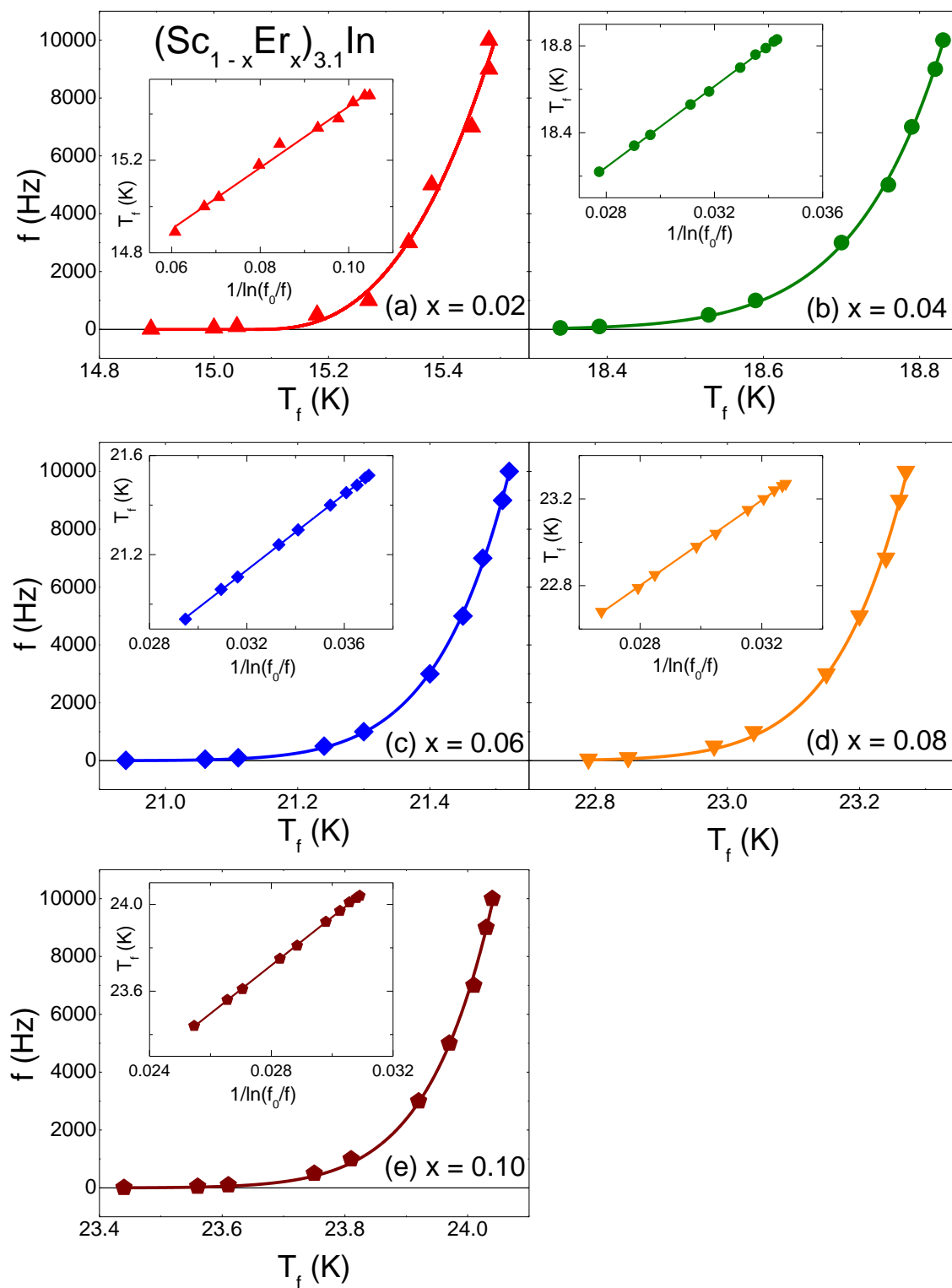


Figure 5.5: (a) - (e) Frequency f versus freezing temperature $T_f(f)$ for $0 \leq x \leq 0.10$ in $(\text{Sc}_{1-x}\text{Er}_x)_{3.1}\text{In}$. Insets: $T_f(f)$ vs. $1/\ln(f_0/f)$ along with the fits (solid lines) to the Vogel-Fulcher law (see text).

where $\mu(\text{Er}^{3+}) = gJ\mu_B = 9 \mu_B$, and $\mu(\text{Sc}_{3.1}\text{In}) = 0.20 \mu_B/\text{F.U.}$ is the magnetic moment of $\text{Sc}_{3.1}\text{In}$ at maximum field available for these measurements ($H = 5.6 \text{ T}$). For example, for $x = 0.10$, the largest measured magnetic moment, taken as the $M(H)$ value at 5.6 T (Fig. 5.3), is $\mu_{5.6T}(x = 0.10) = 1.71 \mu_B$. For $x > 0$ the calculated values of $\mu_{\text{sat}}^{\text{calc}}(x)$ are larger than the measured $\mu_{5.6T}$ ones, as seen in the inset of Fig. 5.3, consistent with the cluster glass state [19].

For $0.02 \leq x \leq 0.10$, $\chi'(T)$ (Fig. 5.4) reveals a broad, frequency-dependent peak, another indicator of glassy behavior [273] (Section 2.3). Conversely, no peak and no frequency-dependence can be detected for $x = 0$, indicating that doping is necessary to induce glassiness. Fits to the measured $\chi'(T)$ peaks, with an example shown in Fig. 5.4(d) (solid line), yield values of the freezing temperature $T_f(f)$, which are plotted in Fig. 5.5. A parameter δ can be determined from the change in the frequency f with the freezing temperature $T_f(f)$ [273]. This is a quantitative measure of peak shift in $\chi'(T)$ with frequency, and it is used to discriminate between spin-glass, cluster glass and superparamagnetic systems (Eq. 2.94).

For $0.02 \leq x \leq 0.10$ in $(\text{Sc}_{1-x}\text{Er}_x)_{3.1}\text{In}$, the δ values are around 0.01, higher than those reported for typical canonical spin-glasses ($\delta \approx 0.005$ for $\text{Cu}_{1-x}\text{Mn}_x$, Table 2.5) [40, 273], and lower than those for noninteracting ideal superparamagnetic systems ($\delta > 0.10$), [98] but comparable to those of known cluster-glass compounds (PrRhSn_3 and $\text{CeNi}_{1-x}\text{Cu}_x$) [15, 237]. This provides more evidence for a cluster-glass state induced by Er doping in $\text{Sc}_{3.1}\text{In}$ [273].

In a cluster glass, the relaxation time τ is a measure of the proximity to the spin-glass limit [40]. The power-law fits to Eq. 2.97, shown in Fig. 5.5(a-e) for $(\text{Sc}_{1-x}\text{Er}_x)_{3.1}\text{In}$ for $0.02 \leq x \leq 0.10$, are used to determine the parameters $z\nu$ and τ_0 . Common values of the characteristic relaxation time τ_0 in glassy systems are $\sim 10^{-12}$ s, comparable to that obtained for $(\text{Sc}_{1-x}\text{Er}_x)_{3.1}\text{In}$. Empirically, the $z\nu$ values for

glassy systems have been observed to fall within the range $2 \leq z\nu \leq 14$ [371]. This is also true in the case of $(\text{Sc}_{1-x}\text{Er}_x)_{3.1}\text{In}$, as the $z\nu$ values, listed in Table 5.1, are close to 10 for most $x \leq 0.10$ samples, and smaller (but still > 2) only for $x = 0.02$.

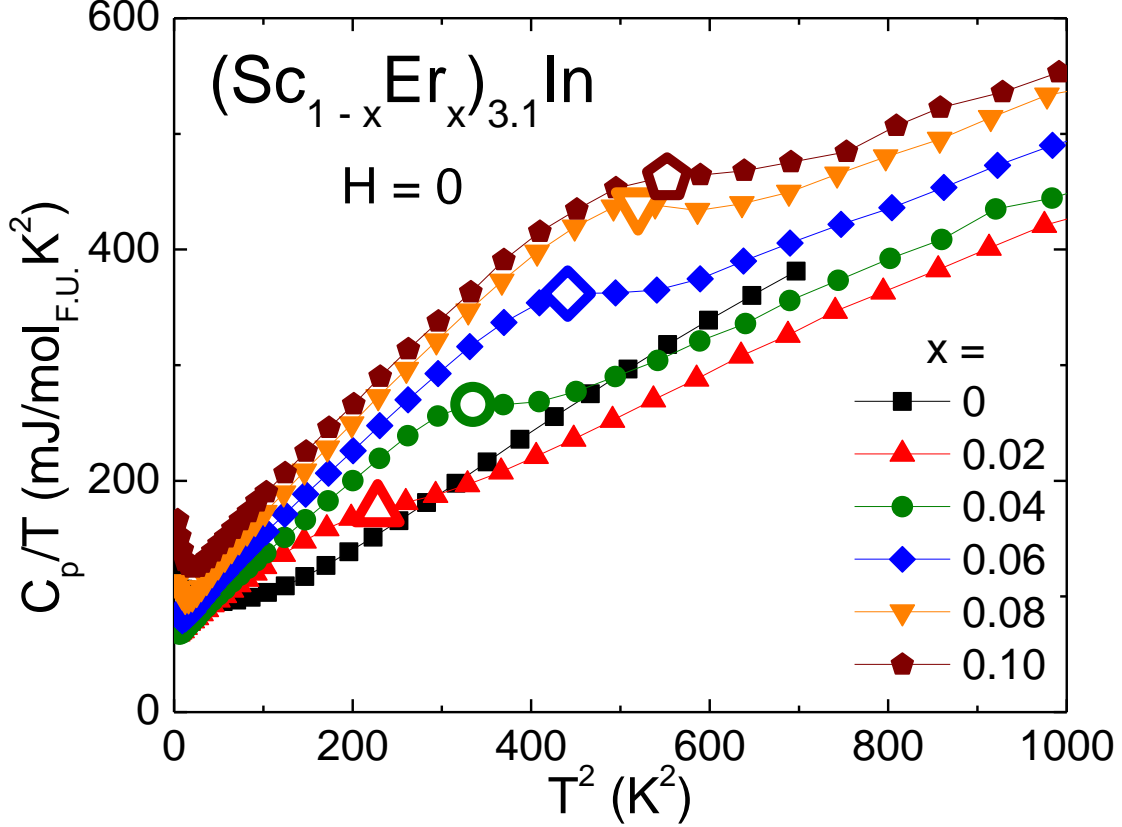


Figure 5.6: C_p/T vs. T^2 for $(\text{Sc}_{1-x}\text{Er}_x)_{3.1}\text{In}$ ($0 \leq x \leq 0.10$), with open symbols corresponding to the freezing temperature $T_f(0)$, as determined from $\chi'(T)$.

Using the values of the relaxation time τ_0 determined above, the characteristic frequency f_0 is calculated as $f_0 = 1/(2\pi\tau_0)$. The relationship between the freezing temperature $T_f(f)$ and the characteristic frequency f_0 is given by the empirical Vogel-Fulcher law (Eq. 2.96) [119, 273, 343, 371] which takes into consideration the strength of intercluster interactions [15, 414]. It is possible to fit the data with the Eq. 2.96 rewritten as:

$$T_f(f) = \frac{E_a}{k_B} \frac{1}{\ln(f_0/f)} + T_0 \quad (5.7)$$

The parameters E_a and T_0 , derived respectively from the slope and intercept of the Vogel-Fulcher fits of $T_f(f)$ *vs.* $1/\ln(f_0/f)$ (shown in the insets of Fig. 5.5(a-e)), are summarized in Table 5.1. The nonzero values of T_0 [15, 414] confirm that the clusters are strongly correlated, while $T_0 \leq 0$ would correspond to a collection of non-interacting spins, *i.e.* a spin-glass compound.

The specific heat data for $(\text{Sc}_{1-x}\text{Er}_x)_{3.1}\text{In}$ ($0.02 \leq x \leq 0.10$), plotted as C_p/T *vs.* T^2 in Fig. 5.6 displays a broad peak near the freezing temperature $T_f(0)$, marked by the large open symbols. A broad maximum at the temperature exceeding the freezing temperature $T_f(0)$ is usually observed in cluster-glass systems, as mentioned above. No such peak is visible for $x = 0$, although at low T the upturn in C_p/T is thought to be associated with non-Fermi liquid behavior [355]. Even for $x > 0$, C_p/T *vs.* T^2 (Fig. 5.6) displays a low- T upturn, whose origin maybe be attributed to either a Schottky anomaly or non-Fermi liquid behavior. This remains to be clarified in a future study.

The composition dependence of the freezing temperature $T_f(0)$ and the irreversibility temperature T_{irr} is shown as squares in Fig. 5.7. By contrast to the effects of Gd doping in ZrZn_2 [25], where the Weiss-like temperature θ was suppressed with increasing amounts of local moment, Er doping of $\text{Sc}_{3.1}\text{In}$ resulted in an increase of θ .

The paramagnetic moment μ_{PM}^{exp} and the saturated moment estimate $\mu_{5.6T}$ can be used to determine the magnetic carrier per atom q_c and q_s [309]. The q_c parameter describes the behavior of the system for temperatures above the transition temperature, and is determined from the paramagnetic moment μ_{PM}^{exp} , using Eq. 2.78 [309].

Similarly, q_s is obtained from the saturation magnetization at temperatures below the transition temperature as $q_s = \mu_{5.6T}/2$, where $\mu_{5.6T}$ is assumed to be close to the saturated moment given the small slope of the $M(H)$ isotherms in Fig. 5.3. If the

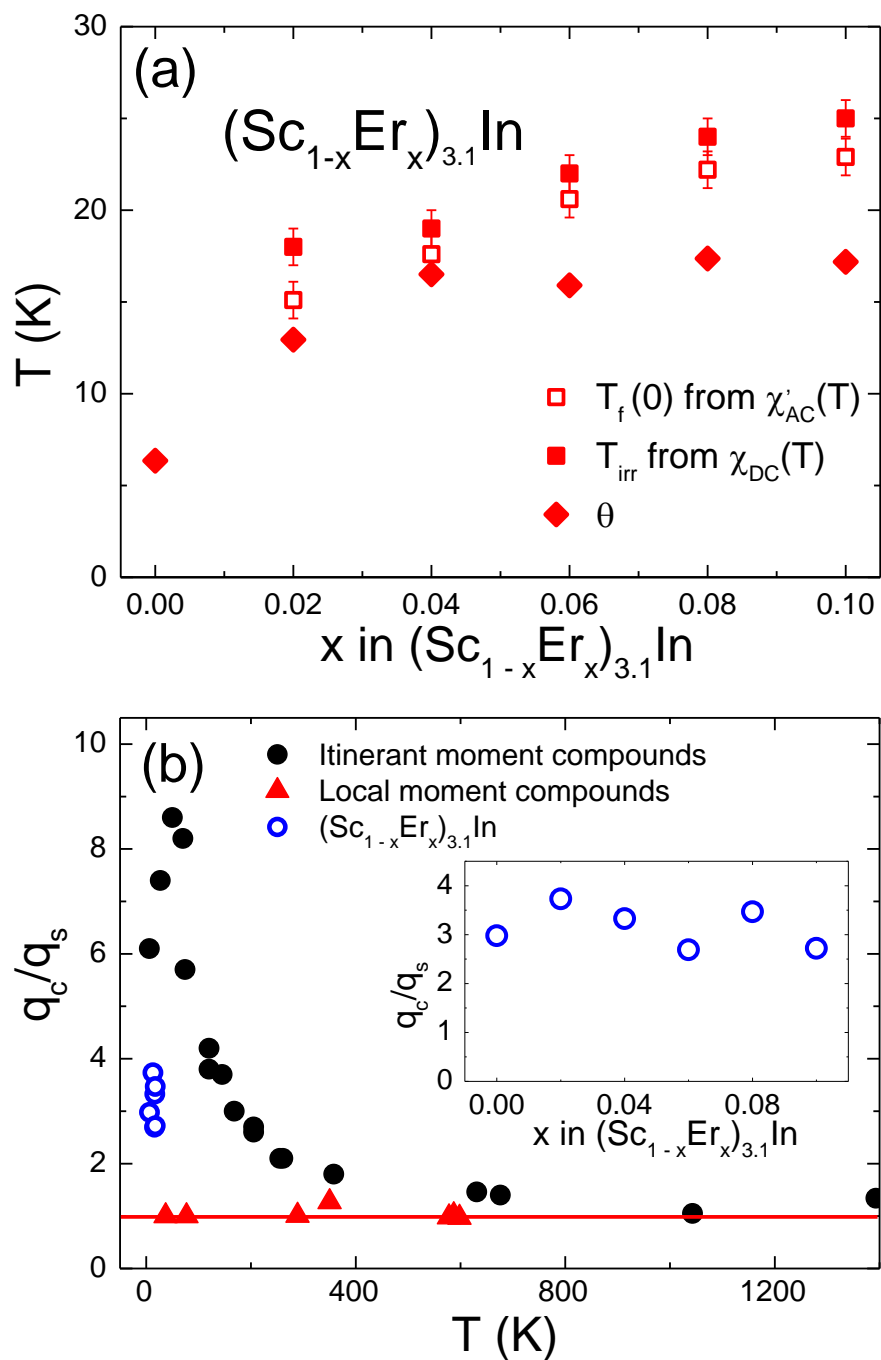


Figure 5.7: (a) The freezing temperature $T_f(0)$ (open squares), the irreversibility temperature T_{irr} (full squares) and the Weiss-like temperature θ (full diamonds) as a function of x in $(\text{Sc}_{1-x}\text{Er}_x)_{3.1}\text{In}$. (b) Rhodes-Wohlfarth plot for local-moment compounds (triangles), itinerant-moment compounds (full circles) and $(\text{Sc}_{1-x}\text{Er}_x)_{3.1}\text{In}$ ($0 \leq x \leq 0.10$) (open circles). The red line indicates the local limit for $q_c/q_s \approx 1$. Inset: the Rhodes-Wohlfarth ratio for $(\text{Sc}_{1-x}\text{Er}_x)_{3.1}\text{In}$ ($0 \leq x \leq 0.10$).

number of carriers below the transition temperature, q_s , is the same as the one above the transition temperature, q_c , the Rhodes-Wohlfarth ratio is $q_c/q_s \sim 1$, indicating a local-moment system. The other limiting case is that for $q_c/q_s > 1$, observed in delocalized or itinerant magnets ($q_c/q_s = 4$ for ZrZn_2 and 6.1 for Sc_3In [309]). The values of the Rhodes-Wohlfarth ratio for local (full triangles) and itinerant (full circles) moment compounds, together with those for $(\text{Sc}_{1-x}\text{Er}_x)_{3.1}\text{In}$ (open circles), are shown in Fig. 5.7(b). The coexistence of local and itinerant magnetic moments in Er-doped $\text{Sc}_{3.1}\text{In}$ yields Rhodes-Wohlfarth ratios between 2.7 and 3.7 (see Table 5.1, as evidenced in the inset of Fig. 5.7(b)). However, this ratio remains enhanced compared to the local moment limit for $x \leq 0.10$, suggesting that larger amounts of local moments would be necessary before the local moment magnetism became predominant.

Table 5.1: Cluster-glass parameters for $(\text{Sc}_{1-x}\text{Er}_x)_{3.1}\text{In}$ ($0 \leq x \leq 0.10$).

x	T_{irr} (K)	μ_{PM}^{exp} ($\mu_B/\text{F.U.}$)	θ (K)	δ	$T_f(0)$ (K)	$z\nu$	T_0 (K)	q_c/q_s
0	-	1.29 ± 0.05	6.4 ± 1	-	-	-	-	2.98
0.02	18 ± 1	2.77 ± 0.05	13.0 ± 1	0.014	15.1 ± 1	2.7 ± 2	14.1	3.73
0.04	19 ± 1	3.62 ± 0.05	16.5 ± 1	0.012	17.6 ± 1	11.0 ± 2	15.6	3.33
0.06	22 ± 1	4.38 ± 0.05	15.9 ± 1	0.010	20.6 ± 1	8.8 ± 2	18.7	2.69
0.08	24 ± 1	5.00 ± 0.05	17.4 ± 1	0.009	22.2 ± 1	10.1 ± 2	20.0	3.47
0.10	25 ± 1	5.57 ± 0.05	17.2 ± 1	0.009	22.9 ± 1	10.8 ± 2	20.6	2.72

5.4 Conclusions and Open Questions

A non-magnetic dopant such as Lu [355] yielded no glassy behavior in $(\text{Sc}_{1-x}\text{Lu}_x)_{3.1}\text{In}$, but rather a gradual suppression of the ferromagnetic state towards a quantum critical point. Conversely, Gd local moment doping of another itinerant ferromagnet with no magnetic moments, ZrZn_2 , also resulted in a gradual suppression of the ferromagnetic

state, with no evidence for the glassiness [25]. Er doping in $\text{Sc}_{3.1}\text{In}$ contrasts the findings for $\text{Zr}_{1-x}\text{Gd}_x\text{Zn}_2$, as the paramagnetic moment is enhanced with increasing x in the former, while the doping results in cluster-glass behavior in $(\text{Sc}_{1-x}\text{Er}_x)_{3.1}\text{In}$, with cooperative behavior of the local and itinerant moments suggested by the DC susceptibility χ .

The AC and DC magnetization measurements, along with specific heat data, show that $(\text{Sc}_{1-x}\text{Er}_x)_{3.1}\text{In}$ ($0.02 \leq x \leq 0.10$) exhibits cluster-glass behavior below the characteristic freezing temperature $15 \text{ K} \leq T_f(0) \leq 24 \text{ K}$, which is enhanced by the increasing doping amount x . The cluster-glass behavior is marked by the irreversibility of zero field cooled-field cooled DC magnetization data, a broad frequency-dependent peak in the AC susceptibility, a large value of δ parameter, the lack of saturation in the low temperature magnetization at high fields, and a weak anomaly in the specific heat data. Moreover, the Vogel-Fulcher analysis established that the clusters are strongly correlated.

Given that the emergence of cluster-glass state is only possible *via* frustration of the lattice, crystal-field-induced destabilization of magnetic moments, and site disorder, we propose site disorder and frustration to be at play here. The lattice of $\text{Sc}_{3.1}\text{In}$ exhibits reduced dimensionality [176] due to nearly one-dimensional bipyramidal Sc-In chains. The crystallographic frustration and site disorder, induced by Er doping on the bipyramidal sites, induces a cluster-glass state that originates from a metallic ferromagnetic ground state. It is imperious that the interplay between the local and itinerant moment in this system be elucidated, which can be achieved *via* muon spin relaxation measurements.

Novel Itinerant Antiferromagnet TiAu

As mentioned previous, the origin of magnetism in metals has been traditionally discussed within either itinerant or local pictures. Surprisingly, there are very few known examples of materials that are close to the itinerant limit, and their properties are not universally understood. In the case of the two such examples discovered several decades ago, the itinerant ferromagnets ZrZn_2 and Sc_3In , the understanding of their magnetic ground states draws on the existence of $3d$ electrons subject to strong spin fluctuations. Similarly, in Cr, an elemental itinerant antiferromagnet with a spin density wave ground state, its $3d$ -electron character has been deemed crucial to it being magnetic. Here we report the discovery of the first itinerant antiferromagnet metal with no magnetic constituents, TiAu. Antiferromagnetic order occurs below a Néel temperature $T_N \simeq 36$ K, about an order of magnitude smaller than in Cr, rendering the spin fluctuations in TiAu more important at low temperatures. This new itinerant antiferromagnet challenges the currently limited understanding of weak itinerant antiferromagnetism, while providing long sought-after insights into the effects of spin fluctuations in itinerant electron systems.

6.1 Motivation and Background

The local and itinerant moment are extreme limits of magnetic behavior, with poorly understood physics associated with in-between scenarios. While the local moment magnetism (or real-space localized magnetic moments and fluctuations) was readily understood early on within a Heisenberg model [156] using a Weiss molecular field, the itinerant moment behavior (corresponding to moments and fluctuations localized in the reciprocal space) can only partially be reproduced by current theoretical approaches (Section 2.1.8). Despite the success of the Stoner model [350] and the subsequent improvements when spin fluctuations were accounted for [264–266], a unified picture of magnetism (which to encompass both extreme scenarios, local and itinerant moment) remains elusive. A practical limitation is the small number of known itinerant moment magnetic systems. In one extreme case, that of magnetic metals without magnetic constituents, only two itinerant ferromagnets, Sc_3In [246] and ZrZn_2 [245], have been known for fifty years (see Section 2.1.8). Here we report the discovery of the first itinerant antiferromagnet metal with no magnetic constituents, TiAu . Given the small number of known itinerant magnets, the discovery of the novel itinerant antiferromagnet TiAu provides an opportunity for detailed studies which to advance the understanding of the physics of itinerant magnets in general, and of itinerant antiferromagnets in particular. Thermodynamic and transport measurements reveal the antiferromagnetic order at a Néel temperature $T_N \simeq 36$ K. The long range static order is further confirmed by neutron diffraction data, which, together with μSR experiments indicate small moment ordering in the whole sample volume. In addition to the overwhelming experimental evidence for the itinerant moment antiferromagnetic order in TiAu , density functional theory calculations confirm the spin density wave small moment ordering, with more detailed calculations using dynamical mean-field theory, left to a future in-depth theoretical study.

6.2 Physical Properties

6.2.1 Structural and Composition Analysis

Evidence for itinerant moment antiferromagnetic order. TiAu has been reported to form in three distinct crystal structures, cubic $Pm\bar{3}m$ [97], tetragonal $P4_1/nmm$ [323] and orthorhombic $Pmma$ [97], posing an inherent difficulty in synthesizing it as a single phase. It comes as no surprise then, that no reports of physical properties of TiAu exist. Here we report the magnetic and electronic properties of phase pure orthorhombic TiAu, and show that it is a new itinerant electron antiferromagnet.

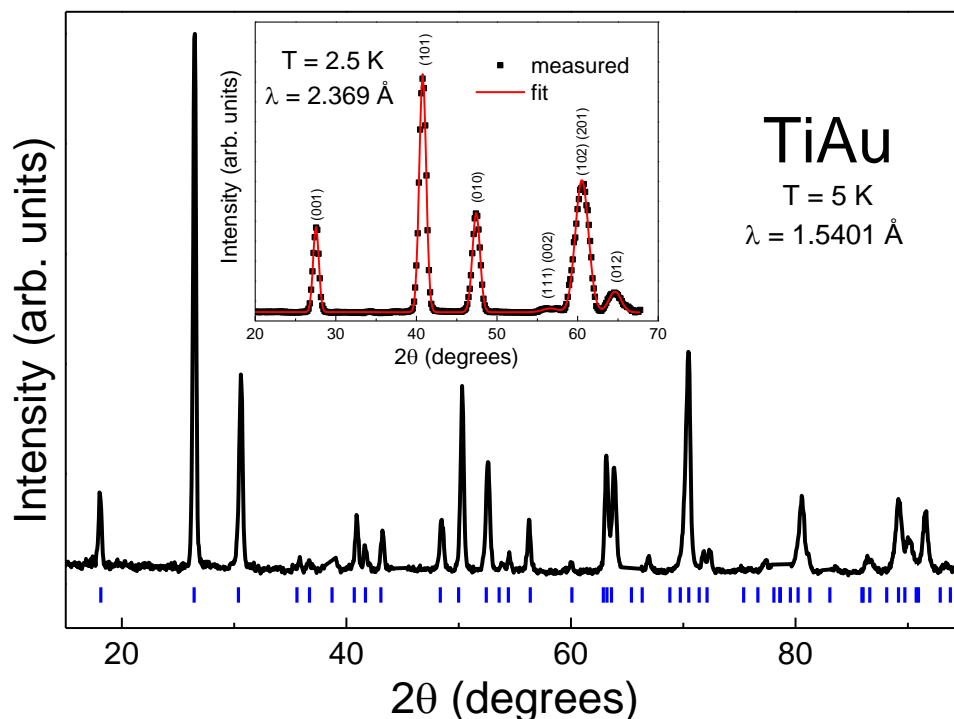


Figure 6.1: Neutron diffraction data: a high resolution diffraction pattern for $T = 5$ K is indexed with the orthorhombic $Pmma$ TiAu phase, denoted by blue vertical marks. The inset shows a portion of the high-intensity diffraction data (solid circles) taken on BT-7 at $T = 2.5$ K. Fig. 6.5(d) shows the observed counts (solid circles) for the magnetic peak, with the solid curves representing fits to Gaussian (instrumental) peaks.

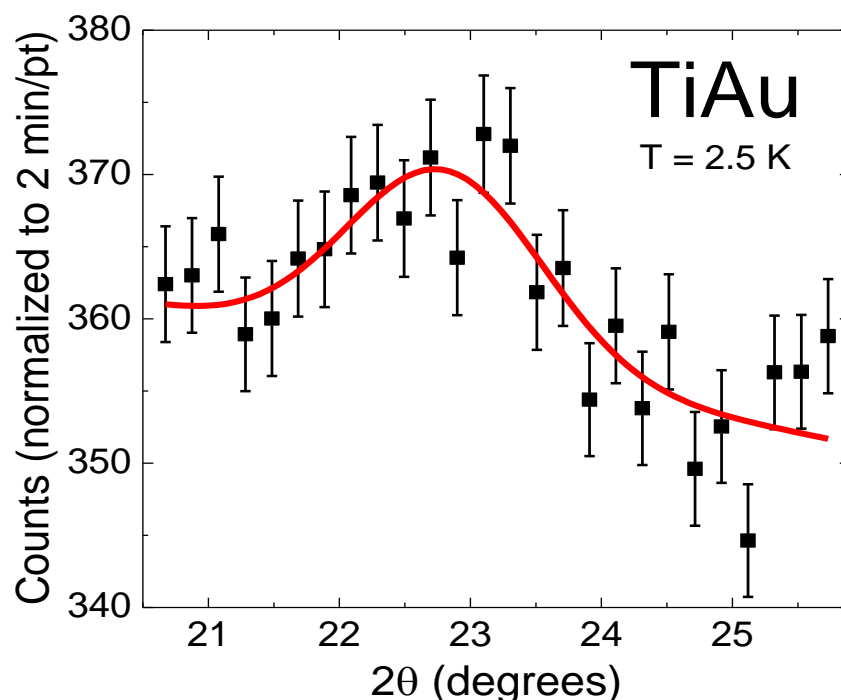


Figure 6.2: Magnetic peak data at $T = 2.5$ K: The symbols are measured data, with the Gaussian fit shown as a solid line.

Neutron diffraction data were collected on the BT-1 powder diffractometer and BT-7 thermal triple-axis spectrometer at the NIST Center for Neutron Research. BT-1 data were used for the crystallographic analysis at $T = 5$ K (black) as shown in Fig. 6.1, with all peaks identified as the orthorhombic $Pmma$ TiAu phase (vertical marks). Fig. 6.2 shows the observed counts (solid circles) for the magnetic peak. The solid curve is a fit to Gaussian (instrumental) peaks (solid curve). The results of structural refinements of the data below ($T = 5$ K) and above ($T = 60$ K) T_N as well as those obtained from room temperature x-ray diffraction are summarized in Table 6.1 and Table 6.2, respectively.

X-ray photoemission spectroscopy is a technique extremely sensitive in resolving the elemental composition [73] (see Section 3.6). O and C peaks can often be present in spectra [73], a consequence of sample preparation. The rest of the peaks in Fig. 6.3 correspond to Ti and Au, confirming the purity of the 1:1 $Pmma$ phase,

Table 6.1: Crystallographic information for *Pmma* TiAu extracted from neutron diffraction data.

	Neutron diffraction	
Temperature (K)	$T = 5$	$T = 60$
Lattice parameters		
a (Å)	4.622(1)	4.622(0)
b (Å)	2.914(5)	2.916(6)
c (Å)	4.897(0)	4.895(9)
Atomic positions		
Ti	(0.250(0), 0.000(0), 0.311(0))	(0.250(0), 0.000(0), 0.308(2))
Au	(0.250(0), 0.500(0), 0.817(6))	(0.250(0), 0.500(0), 0.817(6))

Table 6.2: Crystallographic information for *Pmma* TiAu extracted from x-ray diffraction analysis.

	X-ray diffraction
Temperature (K)	$T = 300$
Lattice parameters	
a (Å)	4.632(3)
b (Å)	2.948(9)
c (Å)	4.885(5)
Atomic positions	
Ti	(0.250(0), 0.000(0), 0.313(3))
Au	(0.250(0), 0.500(0), 0.820(2))

consistent with neutron (below) and x-ray (not shown) diffraction data. X-ray photoemission spectroscopy is also employed in determining the valence of elements in many compounds [100, 199, 238, 283]. Fig. 6.3(b) reveals that the binding energy of $4f_{7/2}$ Au is close to 85 eV, suggesting that Au is close to a Au^{1+} state [252]. The large energy absorption of Ti does not allow for high resolution measurements, limiting the number and quality of peaks that can be successfully analyzed. In TiAu, the binding energy for the most pronounced Ti $2p_{3/2}$ line is split into two peaks, one at ≈ 455 eV (for Ti^{2+} or Ti^{3+}) [279] and another one at ≈ 459 eV (Ti^{4+}) [279], as

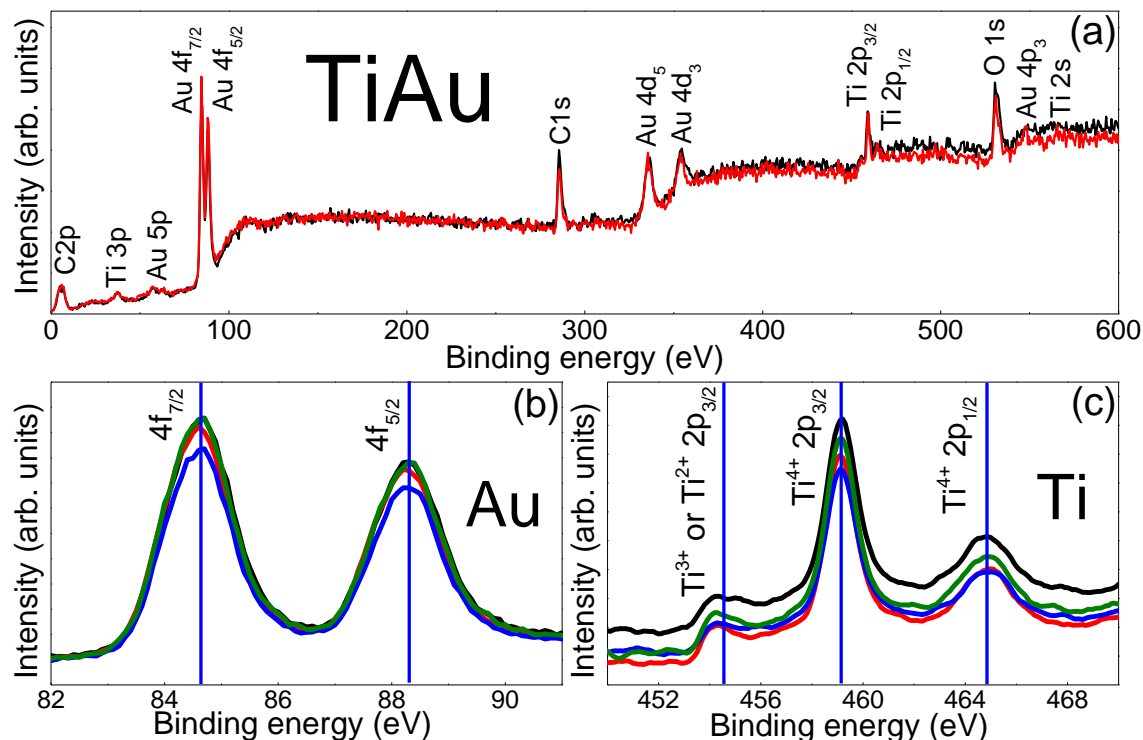


Figure 6.3: X-ray photoemission spectroscopy: (a) survey scan along with elemental scans for Au (b) and Ti (c).

shown in Fig. 6.3(c). A comparison of the areas under the respective curves suggests the valence of Ti to be 3.8 ± 0.12 . In this itinerant magnet, the x-ray photoemission spectroscopy results showing a small d electron contribution are consistent with the small itinerant moment ordering indicated by μ SR and neutron measurements, and rule out the presence of a local moment in TiAu.

6.2.2 Magnetization, resistivity, and specific heat

The first evidence for the antiferromagnetic ground state is the cusp around 36 K in the temperature-dependent magnetic susceptibility $M(T)/H$, shown in Fig. 6.4 (left axis). By analogy with local moment antiferromagnets, the TiAu zero field-cooled and field-cooled data are indistinguishable. The value of the temperature-independent Pauli susceptibility, calculated from the magnetic density of states $\chi_0 \approx 0.2 \cdot 10^{-3} \text{ emu mol}^{-1}$, agrees well with the experimental one $M_0/H \approx 0.3 \cdot 10^{-3} \text{ emu mol}^{-1}$. Upon warming above the Néel temperature, the inverse susceptibility $H/(M - M_0)$ (right axis, Fig. 6.4) is linear in temperature up to 800 K. Such linear T dependence of

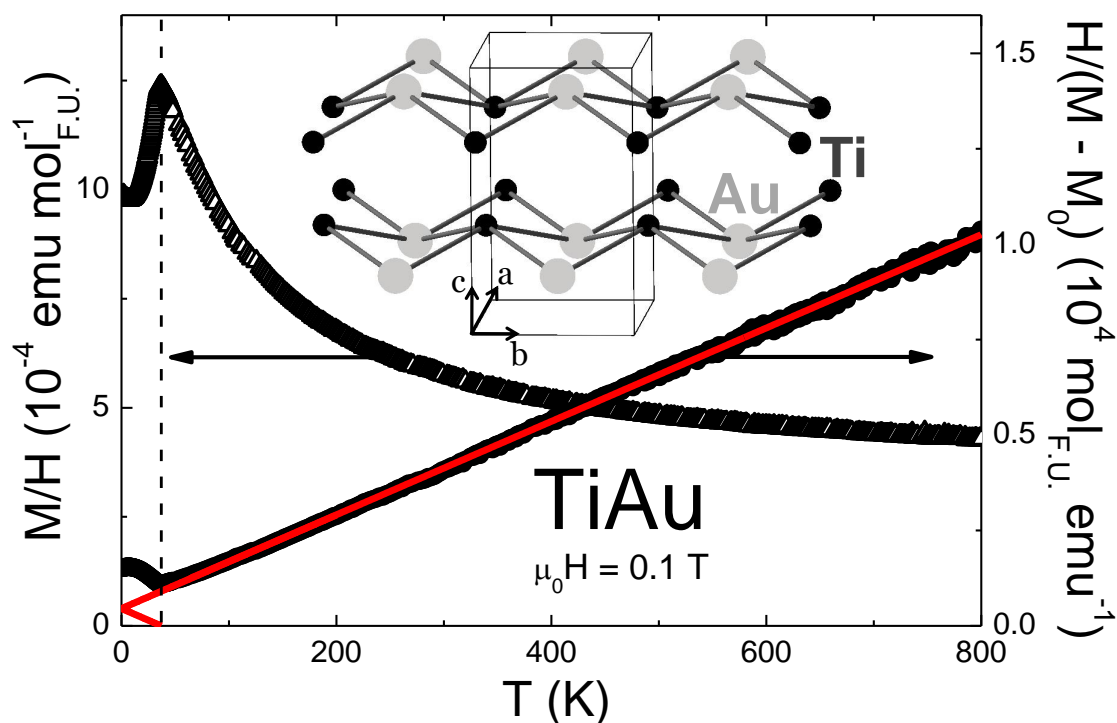


Figure 6.4: Temperature-dependent magnetization of TiAu. Left axis: zero-field cooled magnetic susceptibility as a function of temperature for $\mu_0 H = 0.1 \text{ T}$ applied field. Right axis: inverse susceptibility H/M along with a Curie-Weiss-like fit (solid line), with $\theta \approx -37 \text{ K}$. Inset: the crystal structure of TiAu with Ti (small) and Au (large) atoms.

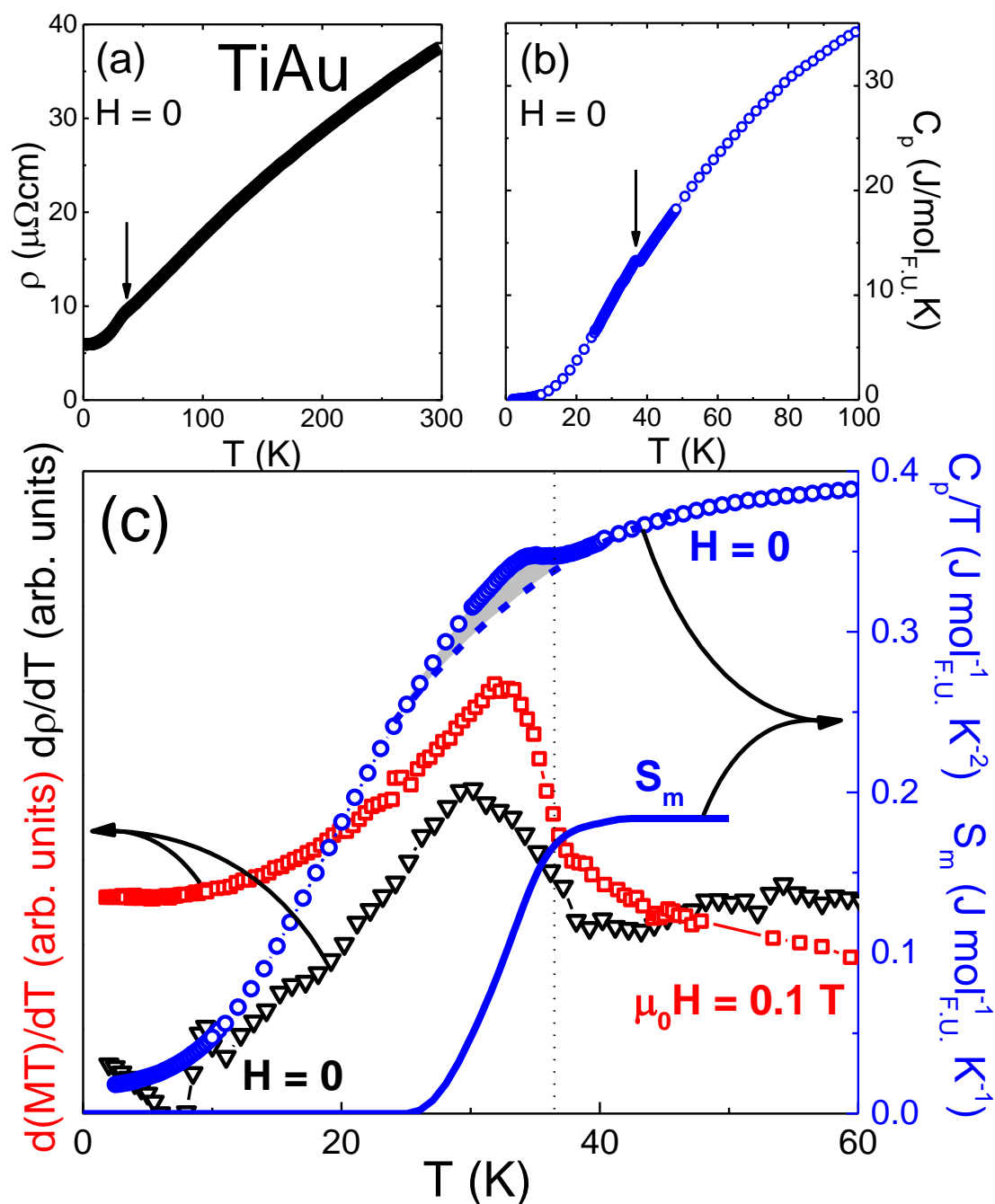


Figure 6.5: Specific heat and resistivity of TiAu. $H = 0$ temperature-dependent resistivity (a) and specific heat (b). (c) The ordering temperature T_N (vertical dotted line) for TiAu determined from peaks in the temperature derivatives of resistivity, $d\rho/dT$ (black triangles), and MT , $d(MT)/dT$ (red squares), and in C_p/T (blue circles). The entropy S_m (solid blue line, right axis) is calculated by subtracting a polynomial non-magnetic component (dashed line) from the measured specific heat data.

H/M has been long considered the hallmark of local moment magnetism, until it was observed in the weak itinerant ferromagnets without local moments, ZrZn_2 [245] and Sc_3In [246] (see Section 2.1.8). Puzzling at first, the origin of this behavior was reconciled in the case of itinerant ferromagnets, when spin fluctuation effects were considered by Moriya [264, 265]. The self-consistent renormalization theory unified the local and itinerant pictures of ferromagnetism, and postulated a new origin for the Curie-Weiss-*like* susceptibility in the latter, as the interactions of the spatially extended modes of spin fluctuations [151, 261]. TiAu however is an itinerant antiferromagnet, and no existing theory accounts for an itinerant antiferromagnetic ground state if neither Ti nor Au have conventional local moments. X-ray photoemission spectroscopy analysis suggests that Ti is close to the non-magnetic 4+ oxidation state. This is striking in light of the high magnetic volume fraction observed in the muon spin relaxation measurements presented below, which, together with the single phase x-ray photoemission spectroscopy and neutron patterns shown in Figs. 6.3 and 6.1, indicates that the observed magnetic behavior is indeed intrinsic. Therefore, $Pmma$ TiAu is *the first* itinerant antiferromagnet metal with no magnetic constituents, with the magnetic ground state strongly affected by spin fluctuations.

Remarkable for a weak itinerant (ferro- or antiferro-) magnet, the electrical resistivity (Fig. 6.5(a)) and specific heat data (Fig. 6.5(b)) also show signatures of the phase transition around 36 K. The $H = 0$ $\rho(T)$ data are typical of a good metal, decreasing nearly linearly from room temperature down to ~ 40 K. A drop of about 10 %, similar to the loss of spin-disorder scattering, occurs at T_N (Fig. 6.5(a)). Although often the gap opening associated with the spin density wave ordering results in a resistivity increase, a similar drop was observed in BaFe_2As_2 single crystals [395]. In the absence of local moment ordering, the decrease in the resistivity at T_N results from the balance of the loss of scattering due to Fermi surface nesting (see below) and the gap opening due to the spin density wave antiferromagnetic state. At the same

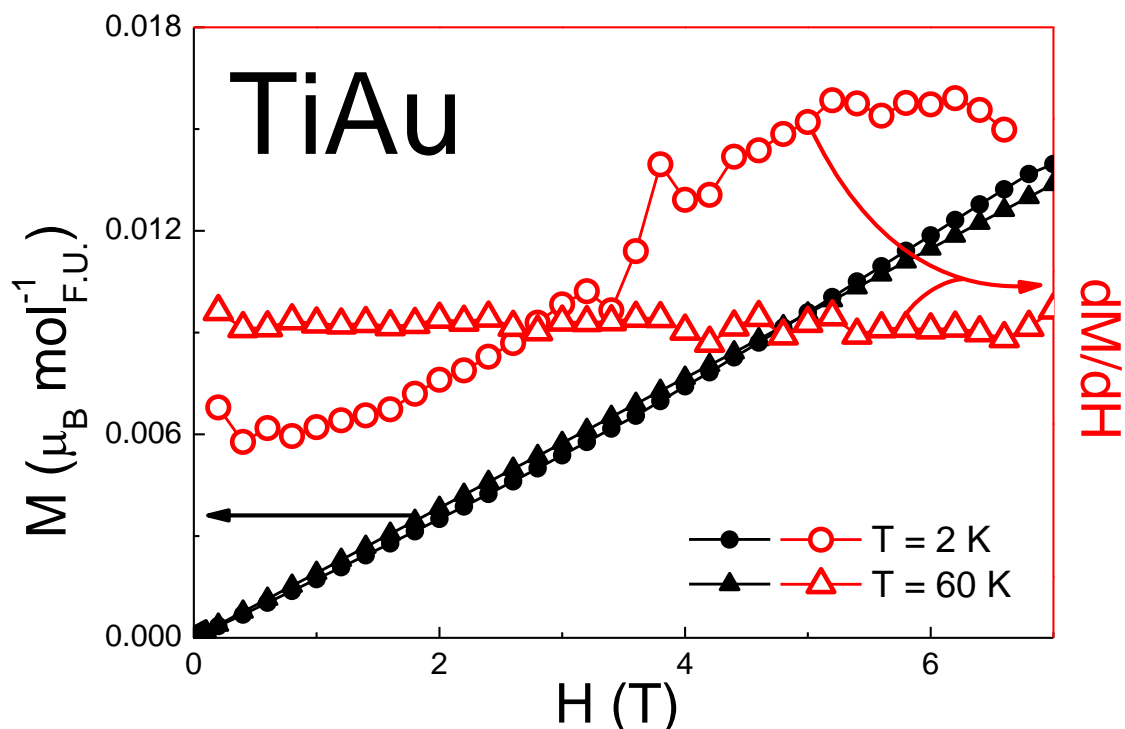


Figure 6.6: Field-dependent magnetization of TiAu. The magnetization isotherms $M(H)$ (solid, left axis) and the derivative dM/dH (open, right axis) for $T = 2 \text{ K}$ (circles) and 60 K (triangles). No saturation is achieved for magnetic fields up to 7 T . A metamagnetic transition is observed around 4 T in the $T = 2 \text{ K}$ isotherm, but not in the one above the magnetic order.

temperature in TiAu, a small peak becomes visible in the specific heat data C_p (Fig. 6.5(b)), such that T_N in this antiferromagnetic metal can be determined, as shown by Fisher [114,115], from peaks in C_p (most visible in C_p/T), $d(MT)/dT$ and $d\rho/dT$ (Fig. 6.5(c)). Distinguishing between local and itinerant moment magnetism is inherently difficult, especially in the nearly unexplored realm of itinerant antiferromagnets. It is therefore striking that in TiAu, abundant evidence points towards its itinerant magnetic moment character. The fact that the peak in C_p is not as strong as Fisher's prediction [114] is one such argument favoring the itinerant moment scenario in TiAu. Another argument is the small magnetic entropy S_m (gray area, Fig. 6.5(c)) associated

with the transition (solid blue line, Fig. 6.5(c)). Even though the S_m calculated after assuming a polynomial non-magnetic C_p around the transition (dashed line, Fig. 6.5(c)) is an underestimate, it amounts to only $0.2 \text{ J mol}^{-1} \text{ K}^{-1}$ or $\sim 3 \%$ of $R \ln 2$.

Despite the remarkably large paramagnetic moment $\mu_{PM} \simeq 0.8 \mu_B$, derived from the Curie-Weiss-*like* fit of the inverse susceptibility (Fig. 6.4(a), right axis), the field-dependent magnetization $M(H)$ does not saturate up to $\mu_0 H = 7 \text{ T}$, and the maximum measured magnetization is only $0.01 \mu_B$ (Fig. 6.6). A closer look at the low temperature $M(H)$ reveals a weak metamagnetic transition starting around $\mu_0 H = 3.6 \text{ T}$ for $T = 2 \text{ K}$ (circles, Fig. 6.6). This is most apparent in the derivative dM/dH (open symbols) rather than in the as-measured isotherms (full symbols), with the latter nearly indistinguishable well below ($T = 2 \text{ K}$) and above ($T = 60 \text{ K}$) the magnetic ordering temperature. It has been shown by Sandeman *et. al.* [318] that, within the Stoner theory, the presence of a sharp double peak structure in the electronic density of states sufficiently close to the Fermi level results in a metamagnetic transition. The argument requires that the paramagnetic Fermi level lie in between the two peaks of the density of states, and this is indeed revealed by the band structure calculation for TiAu, as is shown below. It results that, as the Fermi sea is polarized by the applied magnetic field H , the majority and minority spin Fermi levels feel the effect of the two density of states peaks at different values of induced magnetization. The density of states peak that is closest to the Fermi level will lead to a sharp increase (decrease) in the population of the majority (minority) spin band, resulting in a metamagnetic transition.

6.2.3 Muon Spin Relaxation and Neutron Diffraction Measurements

In the ordered state of prototypical ferromagnets or antiferromagnets at low temperatures, long-lived sinusoidal muon spin precession has been observed with more than several oscillation periods in zero field μ SR. Good examples for those can be found in antiferromagnetic Ca_2RuO_4 ($T_N = 110$ K) ([65], supplementary info A), La_2CuO_4 ($T_N = 240$ K) [319], BaFe_2As_2 ($T_N = 140$ K) [8], $(\text{CuBr})\text{LaNb}_2\text{O}_7$ ($T_N = 35$ K) [379], Ca_2CuO_3 ($T_N = 10$ K) [209], Sr_2CuO_3 ($T_N = 5$ K) [209], and helical magnet MnSi ($T_C = 29$ K) [369]. Bessel function line shapes with long lived oscillations were observed in the incommensurate spin density wave (IC-spin density wave) system $(\text{TMTSF})_2\text{PF}_6$ [380] and for the stripe magnetic order of $(\text{La, Ba})_2\text{CuO}_4$ [319]. Observation of homogeneous internal fields can certainly indicate long-range spatial spin order.

However, there are also many cases of known long-range ordered magnetic systems in which muon spin precession is either heavily damped or even absent. Examples for these cases include ferromagnetic systems $(\text{Sr, Ca})\text{RuO}_3$ [128, 380], $(\text{Sc, Lu})_3\text{In}$ [355], IC-spin density wave systems CeCu_2Si_2 (α - phase) [349, 382], $(\text{Sr}_{1.5}\text{Ca}_{0.5})\text{RuO}_4$ [65, 218], and $\text{Sr}_2(\text{Ru, Ti})\text{O}_4$ [50, 65], as well as low-dimensional and/or frustrated magnetic systems such as $\text{Sr}_2(\text{Ca, Pd})\text{O}_3$ [210], $\text{Cu}(\text{Cl, Br})\text{LaNb}_2\text{O}_7$ and $\text{CuClLa}(\text{Nb, Ta})_2\text{O}_7$ [383]. In general, the absence of oscillation or overdamped line shapes could result from several reasons including: (a) multiple muon sites, (b) inhomogeneous fields from magnetic domain boundaries and/or crystallographic grain boundaries, as well as (c) spatial variation of the ordered moment size in long-range ordered systems. An example for the case (c) is discussed in Ref. [210] for $\text{Sr}_2(\text{Cu, Pd})\text{O}_3$, where Pd atoms generate spatial inhomogeneity in the ordered moment size of the quasi one-dimensional $S = 1/2$ Cu spin chain, as illustrated in Fig. 6.7.

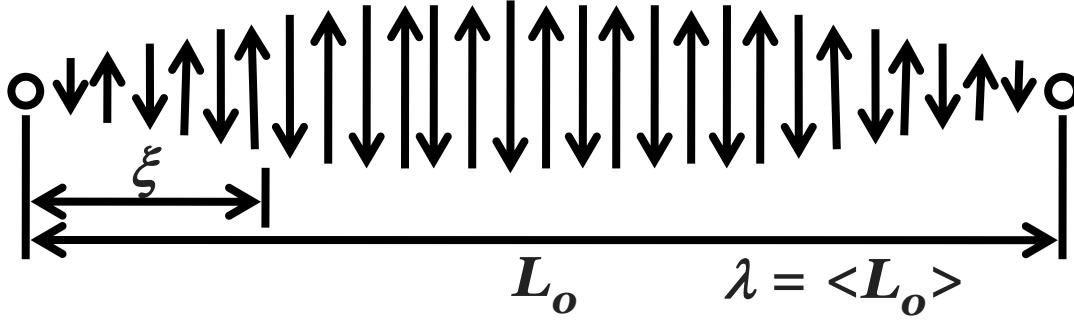


Figure 6.7: Spin chain: quasi one-dimensional $S = 1/2$ spin chain [210].

In TiAu, the initial fit of the muon spin relaxation data includes two simple exponential relaxing components, yielding the black curve shown in Fig. 6.8. The corresponding asymmetry function is of the following form:

$$A(t) = A(fe^{-\lambda_s t} + (1 - f)e^{-\lambda_f t}) \quad (6.1)$$

However, considering the polycrystalline nature of our sample, the isotropy of the overall local magnetic field dictates an average of 1/3 of all muons to have spin parallel to the local field, hence showing no relaxation arising from the random static magnetic field in the sample. In a system with randomly oriented, dense, and static magnetic moments, a Gaussian Kubo-Toyabe relaxation function [154] is usually expected:

$$A_{Gaussian\ KT}(t) = A\left(\frac{1}{3} + \frac{2}{3}(1 - \sigma^2 t^2)e^{-\frac{1}{2}\sigma^2 t^2}\right) \quad (6.2)$$

while in dilute spin systems a corresponding Lorentzian spin-glass (LSG) function, initially developed [383] for dilute alloy SGs CuMn and AuFe, is due to the Lorentzian

internal field distribution [209]:

$$A_{Lorentzian\ SG}(t) = A\left(\frac{1}{3} + \frac{2}{3}(1 - at)e^{-at}\right) \quad (6.3)$$

For the polycrystalline TiAu sample a LSG function (blue line, Fig. 6.8) is more appropriate and yields a distinctively better fit than the Gaussian Kobo-Toyabe function. This might give an impression that magnetic order of TiAu is associated with very dilute ordered moments. However, both in ferromagnetic systems (Ca,Sr)RuO₃ and IC-spin density wave systems (Sr_{1.5}Ca_{0.5})RuO₄, which have a decent density of ordered Ru moments, the LSG line shape was observed over a large doping range near the disappearance of the static magnetic order [65,128,380]. Furthermore, this line shape also fit well the 5 % Mn-doped CuMn SGs [383], in which more than one Mn moment exists in every 5 unit cells of the FCC Cu crystal structure. In the FCC structure, one atom belongs to 8 unit cells. Therefore, in 5 % CuMn, most of the Mn spins have their nearest neighbor Mn spin within these 8 unit cells. In this sense, the observation of the LSG line shape is not restricted to just dilute spin systems.

Table 6.3: Comparison of μ SR results for itinerant helimagnetic, ferromagnetic, spin density wave, spin glass, and charge density wave systems.

	Pressure (kbar)	Chemical composition	Relaxation rate ($T = 0$) Δ^1 (μs^{-1})	Precession frequency ν (MHz)	Ordered volume ($T = 0$) (%)
TiAu	0		1		100
MnSi	0			12	100
MnSi	13-15			11	20 - 80
SrRuO ₃	0		80	15, 30	100
(Sr, Ca)RuO ₃	0	Ca _{0.6-0.7}	20		40 - 60
(Sr, Ca) ₂ RuO ₄	0	Ca _{1.5} Sr _{0.5}	8		100
Cu(Mn)	0	1 % Mn	10		100
BaTi ₂ (As, Sb) ₂ O	0		0.1 - 0.2 (NDB) ²		

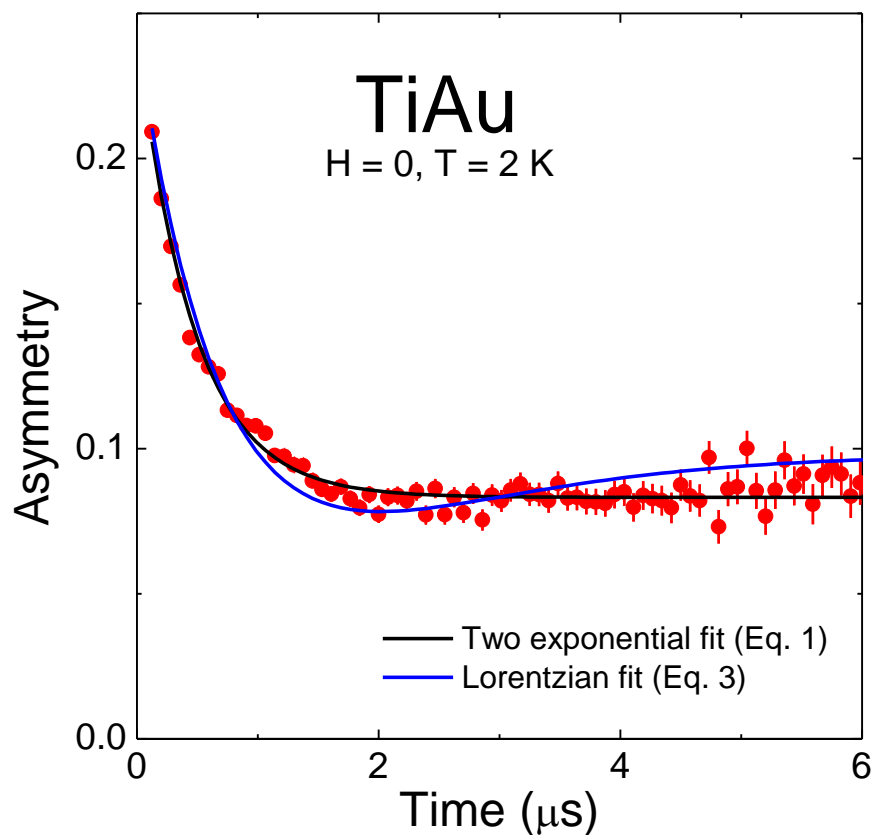


Figure 6.8: μ SR asymmetry analysis: Comparison of the fit with the LSF line shape (Eq. 6.3, blue line) and the two-exponential phenomenological line shape (Eq. 6.1, black line). The difference is subtle, and the choice between these two functions does not alter the essential part of the presented conclusions. The reasoning for using LSG function is described below.

As shown in Fig. 6.8, the two-exponential function (Eq. 6.1) gives a slightly better fit than the LSG function (Eq. 6.3). This is partly due to the fact that Eq. 6.3 has more freedom than the Eq. 6.1. For the estimate of the magnetic volume fraction f , it is important to use a theoretically derived LSG function which properly accounts for the "1/3" component in zero field. There is no theoretical field distribution which can generate the sum of two exponential function Eq. 6.1. In view of these two limitations of Eq. 6.1, we used the LSG function (Eq. 6.4 and Eq. 6.3) for the present analysis.

Even for systems which exhibit Bragg peaks in neutron diffraction due to

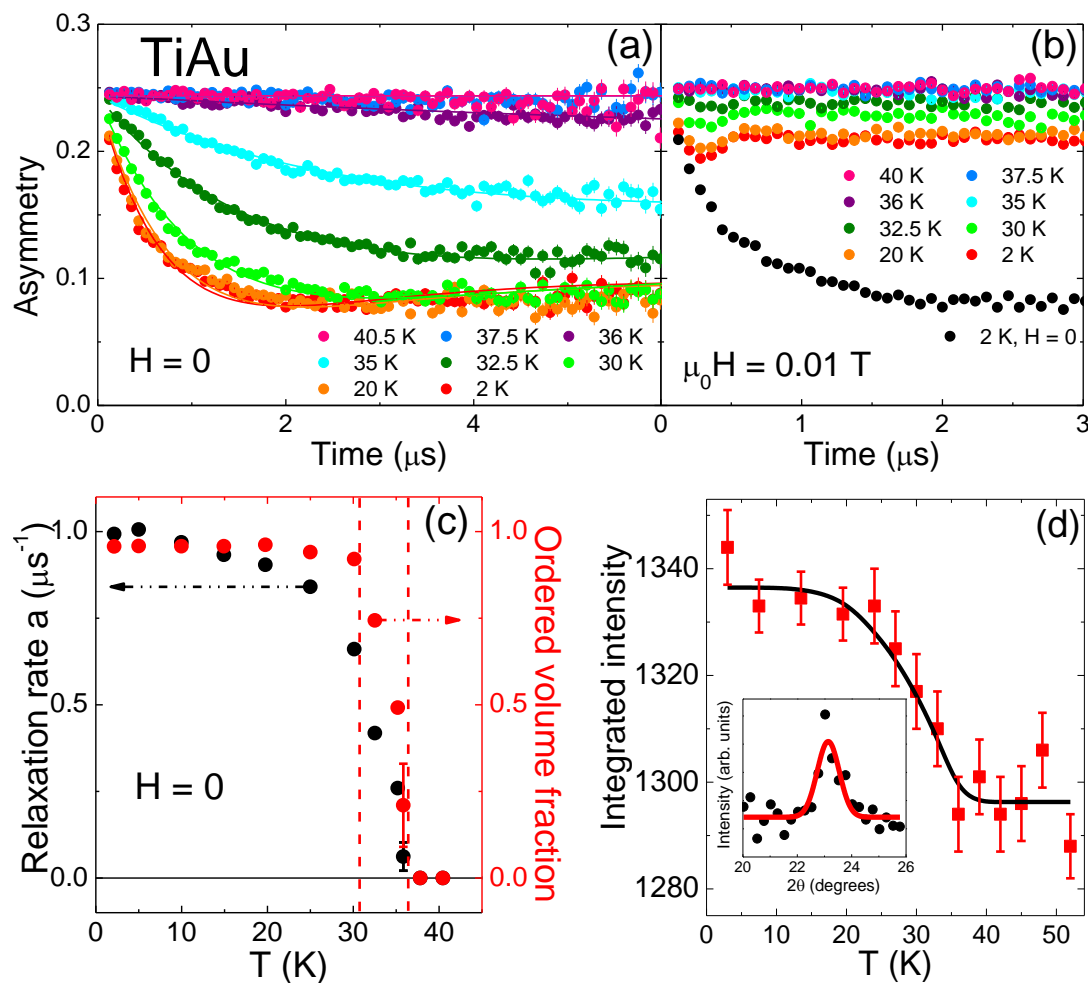


Figure 6.9: Muon spin relaxation and neutron diffraction. (a) Time dependence of the asymmetry, fit with Eq. 6.4 (solid lines). (b) A small applied longitudinal field $\mu_0 H = 0.01 \text{ T}$ eliminates the relaxation response. (c) Relaxation rate a (black circles, left) and volume fraction (red circles, right) as a function temperature. (d) Integrated intensity of the $(0, \pi/b, 0)$ TiAu magnetic Bragg peak as a function of temperature with mean-field fit ($T_N = 36(2)$, black curve). Inset: net counts normalized for 2 min. counting time between 2.5 K and 60 K, showing the $(0, \pi/b, 0)$ magnetic peak fit with a resolution-limited Gaussian (red line). Uncertainties are statistical in origin and represent one standard deviation.

Table 6.4: Comparison of μ SR results for itinerant helimagnetic, ferromagnetic, spin density wave, spin glass, and charge density wave systems.

	Ground state	Ordered moment (μ_B F.U. ⁻¹)	Transition temperature range (K)	Dynamical critical behavior	Reference
TiAu	AFM SDW		33 - 38	no	Present
MnSi	Helical	0.4	29	yes	[380]
MnSi	Helical	0.4	5, 10	no	[380]
SrRuO ₃	FM	0.7	160	yes	[128]
(Sr, Ca)RuO ₃	FM	0.1 - 0.2	25	weak	[128]
(Sr, Ca) ₂ RuO ₄	IC-SDW	0.2 - 0.3	8	yes	[65]
Cu(Mn)	SG	0.04 (4/Mn)	10	yes	[383]
BaTi ₂ (As, Sb) ₂ O	CDW ¹				[284]

long-range magnetic order, if there is spatial distribution in the ordered moment size, then the μ SR line shape can exhibit fast damping or absence of oscillations. This could explain the absence of oscillations in the zero field μ SR data [65] in the IC-spin density wave systems (Sr_{1.5}Ca_{0.5})RuO₄ [218] and Sr(Ti_{0.09}Ru_{0.91})O₄ [50]. Therefore, the observation of an antiferromagnetic Bragg peak in neutron scattering and the over-damped LSG line shape in μ SR can be reconciled within the picture of long-range (neutrons) static (μ SR) magnetic order. Positive muon is a local probe whose information is integrated over momentum space. The determination of long-range magnetic order can be done better by neutron scattering.

However, μ SR results reflect signals from all the muons in the total sample volume, with the information about the volume fraction of the magnetically ordered region. In μ SR studies, the local field at the muon site is generated mainly *via* dipolar interactions of surrounding magnetic moments. If an ordered moment of 1 μ_B is 1 Å away from a muon site, it will generate a local field of 1 T. When the distance is 3 Å, the local field becomes about 400 G. For the distance of 10 Å, the field becomes 10 G. The randomness of the internal magnetic field of 10 G will result in muon spin

relaxation rate of about $1 \mu\text{s}^{-1}$ in zero field. Therefore, the observation of relaxation in the ordered state in TiAu, with the relaxation rate of $1 \mu\text{s}^{-1}$ in the full volume fraction can rule out the existence of paramagnetic or non-magnetic domains larger than 10 - 15 Å in size with more than $\sim 5\%$ of the volume fraction.

Zero field μSR spectra with overdamped or absent oscillations have been often observed in various magnetic systems near the disappearance of magnetic order and/or at a quantum critical point. On the other hand, many of the above-mentioned examples involve built-in randomness due to chemical substitutions. TiAu is synthesized with nominal 1 : 1 stoichiometric composition. Further detailed studies of the origin of the observed LSG line shape and local field distributions in TiAu could lead to more insight on the generic behavior of homogeneity near a magnetic quantum critical point. With the currently available data, however, it is impossible to determine the origin of the LSG line shape. Thus, we rely on the neutron scattering information for discussions of the long-range magnetic order, and μSR for discussions of the volume fraction of magnetic order.

Muon spin relaxation (μSR) data shown in Fig. 6.9 unambiguously confirm the static magnetic order developing in the full volume fraction, with the transition temperature corresponding to the anomaly in the magnetic susceptibility, resistivity and specific heat shown in Fig. 6.5(c). For temperatures above 35 K, the total asymmetry undergoes a negligibly small relaxation, signaling lack of static magnetic order (Fig. 6.9(a)). In the time spectra observed in zero field, a fast decaying front end begins to develop around 35 K, and becomes more pronounced for lower temperatures. This early time decay results from the build up of static internal field, since a small longitudinal field, $\mu_0 H = 0.01$ T, eliminates this relaxation *via* the decoupling effect (Fig. 6.9(b)). The time spectra in zero field are fitted with the relaxation function,

expected for a Lorentzian distribution of local fields [383]:

$$G(t) = f \left(\frac{1}{3} + \frac{2}{3}(1 - at)e^{-at} \right) + (1 - f) \quad (6.4)$$

where f represents the volume fraction with static magnetic order. The temperature dependence of the relaxation rate a and the magnetic volume fraction f are shown in Fig. 6.9(c). A reasonably sharp transition occurs below $T_N = 36$ K to a state with 100 % ordered volume, preceded on cooling by a small temperature region around T_N characterized by the finite volume fraction f , which suggests co-existence of ordered and paramagnetic volumes in real space *via* phase separation.

A remarkable feature found in both zero field and longitudinal field time spectra is the absence of dynamic relaxation, expected for critical slowing down of spin fluctuations around T_N . Such an effect should have resulted in the $1/T_1$ relaxation of the asymmetry measured in $\mu_0 H = 0.01$ T, since this longitudinal field can eliminate the effect of static magnetism, while dynamic effects survive in a small longitudinal field. The observed relaxation rate $1/T_1$ in LF = 100 G was smaller than $0.02 \mu\text{s}^{-1}$. Using the well-known formula $1/T_1 \sim \Delta^2 \tau_c$, with the local field strength $\Delta = 1 \mu\text{s}^{-1}$, we then find that the correlation time τ_c of the local field fluctuations should be shorter than 20 ns. Critical slowing down of spin fluctuations slower than this should have resulted in an observable decay in the longitudinal field spectra near the spin freezing temperature ~ 36 K. Another piece of information comes from the absence of the decay of the "1/3" component in zero field and the decoupled time spectra in longitudinal field at low temperatures. These spectra indicate that the local field at low temperatures in the ordered state is quasi-static, with the time scale of 10 μs or more. See Ref. [383] for more details.

Together with the zero field relaxation function (Eq. 6.4) which solely in-

volves static effects, the present data indicate complete absence of dynamic critical behavior. Although occurring in a limited temperature region, the aforementioned phase separation indicates that the transition is likely first-order, without dynamic critical behavior. As shown in Table 6.4, similar absence of dynamic critical behavior associated with phase separation was observed in μ SR studies of the itinerant helimagnet MnSi in an applied pressure of 13 - 15 kbar [380], near the pressure-tuned quantum crossover to the paramagnetic phase. Such tendencies were also seen in the itinerant ferromagnet (Sr,Ca)RuO₃ close to the disappearance of static magnetic order around a Ca concentration of 0.7 [128]. The first-order transition may be a generic feature of weak magnetic order in itinerant-electron systems [37].

As Tables 6.3 and 6.4 show, the magnitude of the internal magnetic field in TiAu in the ordered state is remarkably small, compared to μ SR results in other itinerant electron systems, dilute alloy spin glasses (SGs) or the incommensurate spin density wave system (Sr_{1.5}Ca_{0.5})RuO₄ [65]. Although this indicates a very small ordered moment in TiAu, it is not possible to estimate the moment size since the hyperfine coupling constant could depend strongly on the assumption of the location of muon sites. The line shape of the zero field μ SR data in Eq. 6.4 is obtained for the case of dilute-alloy SGs where the local field at the muon site varies due to different distances to the moment site [383]. However, the same line shape was also observed in (Sr_{1.5}Ca_{0.5})RuO₄ in which incommensurate spin density wave order was recently confirmed by neutron scattering. Therefore, it is difficult to determine the spin structure of the TiAu system from the present μ SR data alone. In general, the observation of long-lived oscillations by μ SR can indicate homogenous long-range order, but the absence of oscillations does not rule out long-range magnetic correlations. This feature can be found in many cases of known antiferromagnetic and ferromagnetic systems, as reviewed in Table 6.4.

Neutron diffraction measurements above ($T = 60$ K) and below ($T = 2$ K) the ordering temperature reveal a resolution-limited magnetic peak (inset, Fig. 6.9(d)) in the low temperature data. The temperature dependence of this peak indicates magnetic ordering at $T_N = 36 \pm 2$ K. The magnitude of the ordered moment is estimated to be $0.15 \mu_B/\text{Ti}$, consistent with a small itinerant moment. The neutron data eliminate the possibility that the observed magnetism is due to dilute magnetic impurities. The μSR results show a magnetic phase fraction of 100 % eliminate the possibility of neutron signal coming from a minority phase of small volume. These arguments demonstrate that the magnetism of the present system is an intrinsic feature of TiAu.

6.2.4 Tunnel Diode Oscillator Measurements

It has been reported that itinerant and local moment systems induce a substantially different frequency shift, providing a new way of differentiating between them [386] (Section 3.9). Itinerant ferromagnet ZrZn_2 does not show a sharp peak in the resonator frequency at T_C as compared with a sharp peak in a local moment ferromagnet CeVSb_3 [386]. The lack of peak at the transition temperature was also reported for a local moment antiferromagnet SmAgSb_2 , in which only a gradual decrease of susceptibility below the Néel temperature T_N is observed due to the loss of spin-scattering which changes the penetration depth of the AC excitation field [386].

The itinerant magnet TiAu, composed of non-magnetic elements, displays antiferromagnetism below the Néel temperature $T_N \approx 36$ K [359]. The oscillator frequency shift Δf as a function of temperature T is shown in Fig. 6.10(b). The resonant frequency f_0 was 13.5 MHz and the total frequency shift was about 90 KHz. Since the TDO measurement probes both electric and magnetic susceptibility, it is complementary but not equivalent to the resistivity measurement, shown in Fig.

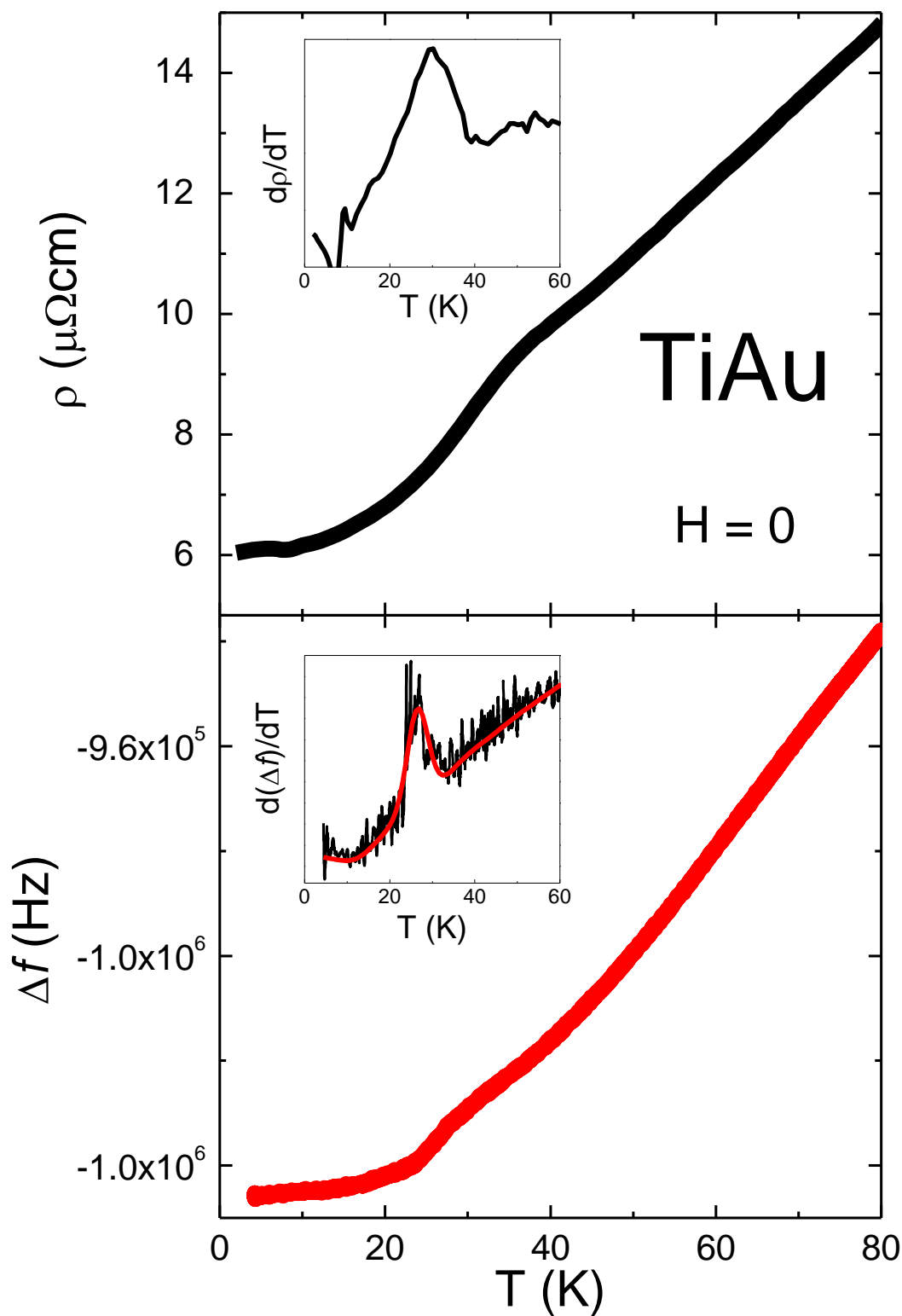


Figure 6.10: (a) Temperature-dependent DC resistivity of TiAu along with the derivative (inset). (b) Frequency shift Δf of the tunnel diode oscillator resonance as a function of temperature for TiAu. Inset: the derivative of the frequency shift with respect to temperature $d(\Delta f)/dT$ reveals a peak around 27 K.

6.10(a). The transition is less visible, compared to the DC resistivity curve. The temperature derivative, shown in the inset of Fig. 6.10(b) estimates the transition temperature to be around 27 K, similar to that determined from DC resistivity.

6.2.5 High Field Magnetization Measurements

Given that no saturation was observed in fields up to 7 T, the high-field experiments were carried out. The VSM data, shown in Fig. 6.11(a), agrees well with the low-field measurements. A small increase in $M(13 \text{ T})$ is observed for $5 < T < 26 \text{ K}$, followed by a decrease with increasing temperature. The high-field VSM magnetization data is exceptionally linear, reminiscent of some of the Kondo systems [118, 155, 315].

The calibrated $M(H)$ data up to $H = 60 \text{ T}$ is shown in Fig. 6.11(b). For temperatures below $T = 30 \text{ K}$, the value of magnetization at the maximum field is temperature-independent. For higher temperatures, the value of magnetization at high fields decreases. Additionally, the $M(H)$ data above $T = 30 \text{ K}$ confirm the remarkable linearity, observed in the pulsed field data.

While the the Rhodes-Wohlfarth ratio of magnetic carries [309] is generally used to differentiate between local and itinerant mechanisms in ferromagnetic materials (see Section 2.1.7), similar analysis has been applied to antiferromagnetic systems [31, 288, 301]. The q_s is obtained from the saturation magnetization at temperatures below the transition temperature, while q_n is determined from the paramagnetic moment μ_{pm} , which describes the behavior of the system for temperatures above the transition temperature [309]:

$$q_s = \frac{\mu_{sat}}{2} \quad \text{and} \quad q_n(q_n + 1) = \frac{\mu_{pm}^2}{4} \quad (6.5)$$

For the localized case, the values of the magnetic moment above and below

T_N are the same, yielding $q_n/q_s \approx 1$. The Rhodes-Wohlfarth ratio values are larger in the itinerant case, as exemplified by ferromagnets ZrZn_2 ($q_n/q_s = 4$) and Sc_3In ($q_n/q_s = 6$) [309]. The paramagnetic moment of TiAu has been extracted from the Curie-Weiss-like fit and is equal to $\mu_{pm} = 0.8 \mu_B/\text{F.U.}$ [359]. Since no saturation is observed, the lower bound estimate of q_s can be extracted from $\mu_s(64 \text{ T}) \approx 0.13\mu_B$. This yields $q_n/q_s = 0.14/0.065 = 2.2$, confirming the itinerant character of TiAu. Combined Rhodes-Wohlfarth is shown in Fig. 2.13.

Combined $M(H)$ data from pulsed and VSM methods are shown in Fig.

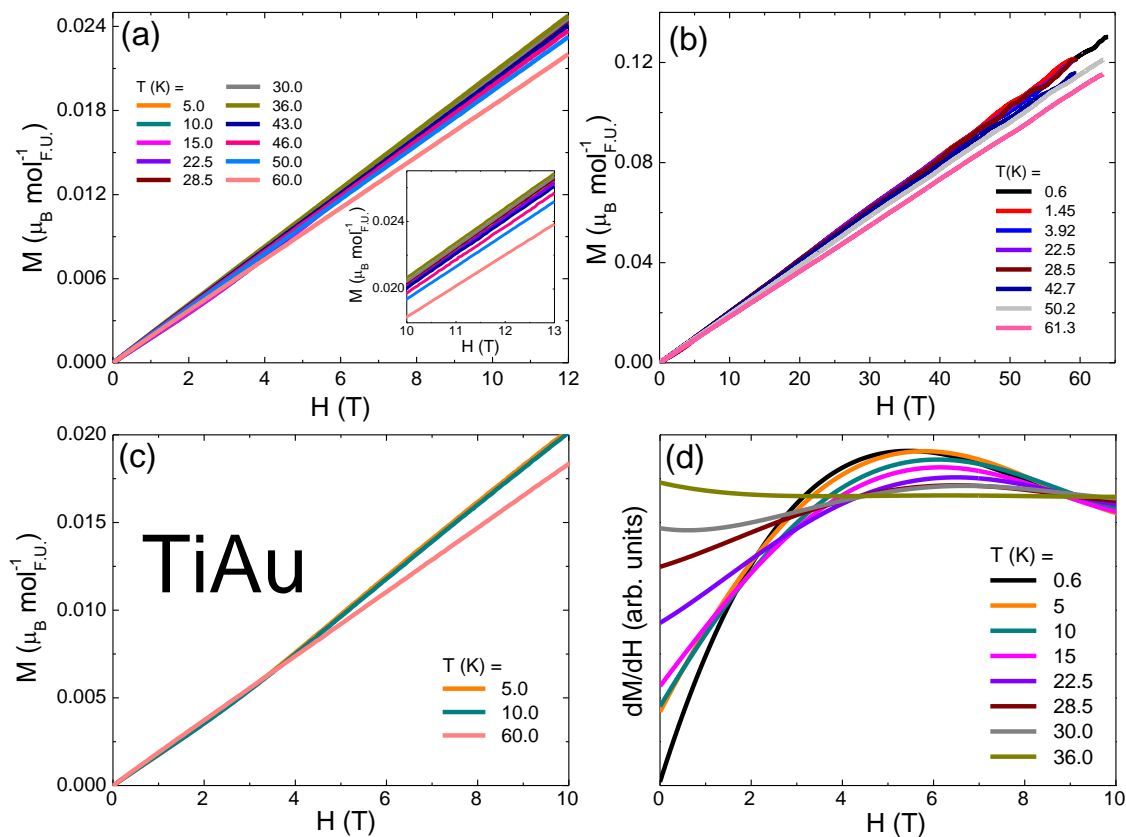


Figure 6.11: (a) Field-dependent magnetization data taken using the VSM option. Inset: high-field data exhibits a remarkably linear behavior. (b) Pulsed field magnetization data for TiAu at various temperatures. Combined high-field magnetization data: (c) the $M(10 \text{ T})$ decreases with increasing temperature while the derivative dM/dH , shown in (d), exhibits a feature around 5 T which is suppressed for $T > 36$ K.

6.11(a). The derivative dM/dH , shown in Fig. 6.11(d), indicates that most of the changes in $M(H)$ are due to a low-field increase in gradient at low temperatures that fades away as T is raised. This is clearly seen in dM/dH , which has a peak that moves to higher field with increasing T before fading away at around 30 K. This is consistent with a metamagnetic transition, suggested above.

6.2.6 High Pressure measurements

In weakly magnetic materials, low ordering temperatures are easily suppressed to zero by small perturbations that arise from change in composition, application of pressure or magnetic field [140]. In ferromagnets, this is attributed to the decrease of the density of states at the Fermi level, which reduces the Stoner product [401]. As for the antiferromagnetic case, similar mechanism has been suggested [117].

While ferromagnetism in ZrZn_2 is suppressed by $p_c \approx 9$ GPa [163, 339, 396], application of pressure in Sc_3In enhanced the magnetic properties [124, 140], contrary to what is predicted by the Wohlfarth's theory [400, 401]. On the other hand, doping experiments were successful in inducing a quantum critical point in both compounds [341, 359], indicating that a combination of both disorder and pressure are likely necessary to induce a quantum phase transition. Moreover, in ZrZn_2 , the order of the quantum phase transition changes from first to second upon doping.

In TiAu , application of pressure increases T_N , as shown in Fig. 6.12. Given that from band structure calculations, the pressure needed to suppress magnetic ordering is estimated to be about 70 GPa, it is possible that higher values of pressure will reduce T_N . Comparison with Sc_3In and ZrZn_2 along with the analysis of the possible quantum critical point are of interest. Thus, experiments with applied pressures of up to 30 GPa are currently underway.

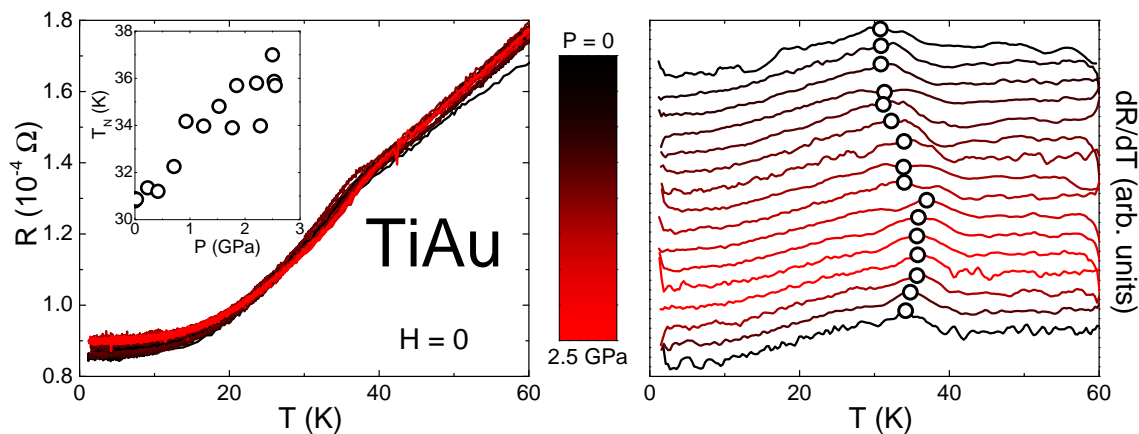


Figure 6.12: (a) Temperature-dependent resistance for various pressure values. Inset: the value of T_N , determined from dR/dT . (b) The transition is more visible in the derivative of resistance with respect to temperature dR/dT .

6.3 Band Structure Calculations

Band structure calculations were performed using full-potential linearized augmented plane wave method implemented in the *WIEN2K* package [41]. PBE-GGA was used as the exchange potential, as the default suggestion by *WIEN2K* [296]. A $10 \times 10 \times 10$ k-point grid was used, and shift away from high symmetry directions was allowed. The convergence criterion for force is 1 mRyd/a.u. (1 Ryd = 13.6 eV), with the residual force for the $Q = (0, 2b/3\pi, 0)$ state less than 3.5 mRyd/a.u. (or 90 meV/Å). For the density of states plot, the Gaussian broadening was used, with a broadening factor of 3 mRyd. In order to make the Fermi surface plot (shown in Fig. 6.13(c)) easier to read, a separated Fermi surface plot for the different bands is shown in Fig. 6.14.

Even though the experimental evidence demonstrates long range antiferromagnetic, small moment ordering in orthorhombic TiAu, a comparison between the experimental data with theoretical results from band structure calculations are of interest. These were performed using a full-potential density functional theory [239] while taking spin-orbit coupling into account. A number of possible magnetic configurations were considered: ferromagnetic (FM), antiferromagnetic spin density wave

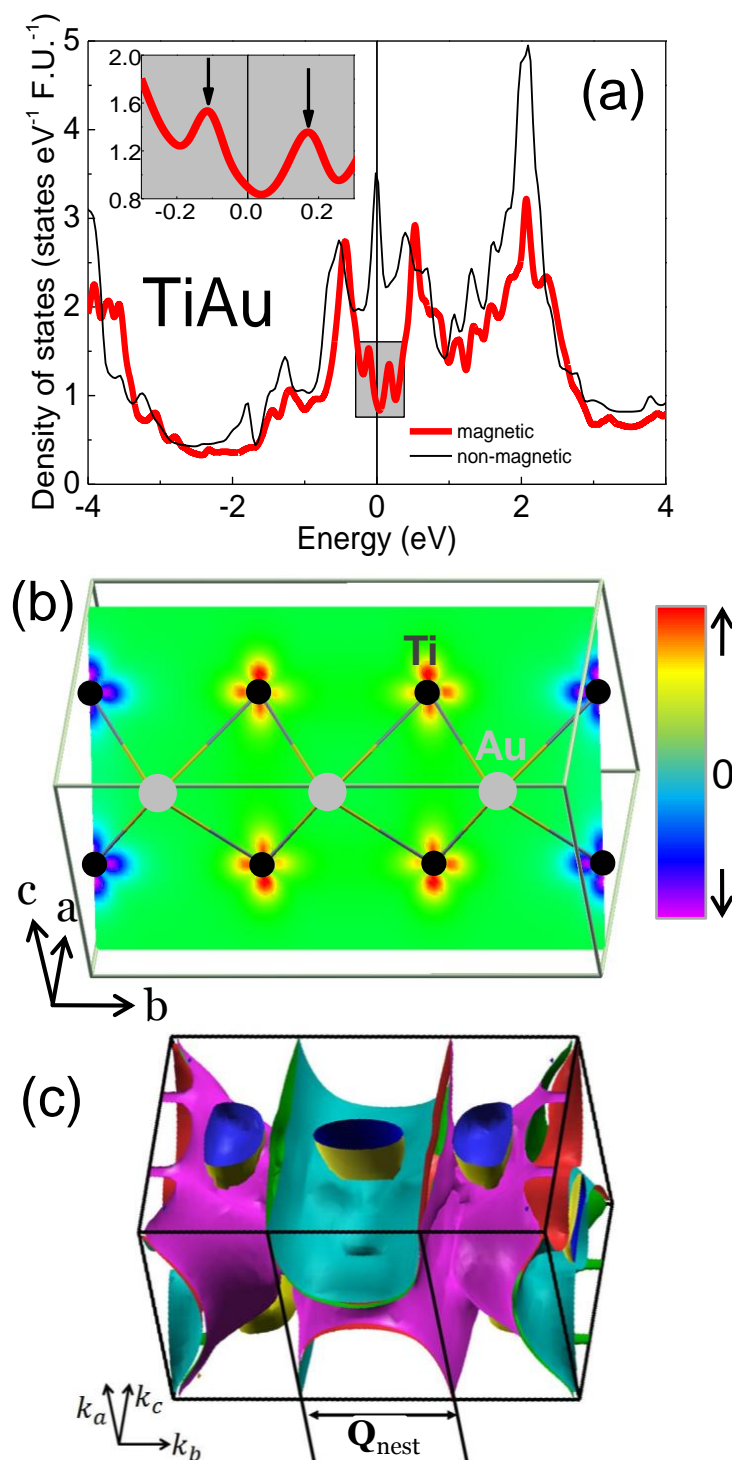


Figure 6.13: Band structure calculations for TiAu. (a) The non-magnetic density of states (thin black line) exhibits a peak close to the Fermi surface, similar to that seen in other itinerant magnets. For the AFM1 ground state, the finite total density of states (thick red line) at the Fermi energy is flanked by two peaks around 0.1 eV (inset), which explains the metamagnetic transition at low T (see text). (b) The electron spin density shows a modulation along the b axis, consistent with the $k = 2\pi/(3b)$ nesting shown in (c). Fermi surface with nesting vector $Q_{\text{calc}} = (0, 2\pi/3b, 0)$ is shown in (c). Separated Fermi surface plot is shown in Fig. 6.14.

with modulation vectors $Q_1 = (0, 2\pi/3b, 0)$ (AFM1) and $Q_2 = (0, \pi/b, 0)$ (AFM2). Their energies relative to the paramagnetic state were estimated to be $E_{\text{FM}} = -35$ meV/Ti, $E_{\text{AFM1}} = -47$ meV/Ti and $E_{\text{AFM2}} = -34$ meV/Ti, respectively. Given the systematic error bars of the exchange-correlation potential employed in the density functional theory, the calculated energy values point to an antiferromagnetic ground state with wavevector $Q_{\text{exp}} = (0, k, 0)$, with k between $2\pi/3b$ (AFM1) and π/b (AFM2), a value consistent with the neutron diffraction experiments. However the uncertainty in determining the exact wavevector from density functional theory does not affect the conclusions from the overwhelming experimental evidence for the itinerant antiferromagnetic order in TiAu. Furthermore, the calculation yields a small ordered magnetic moment μ_{calc} for all surveyed configurations, $0.52 \mu_B/\text{Ti}$

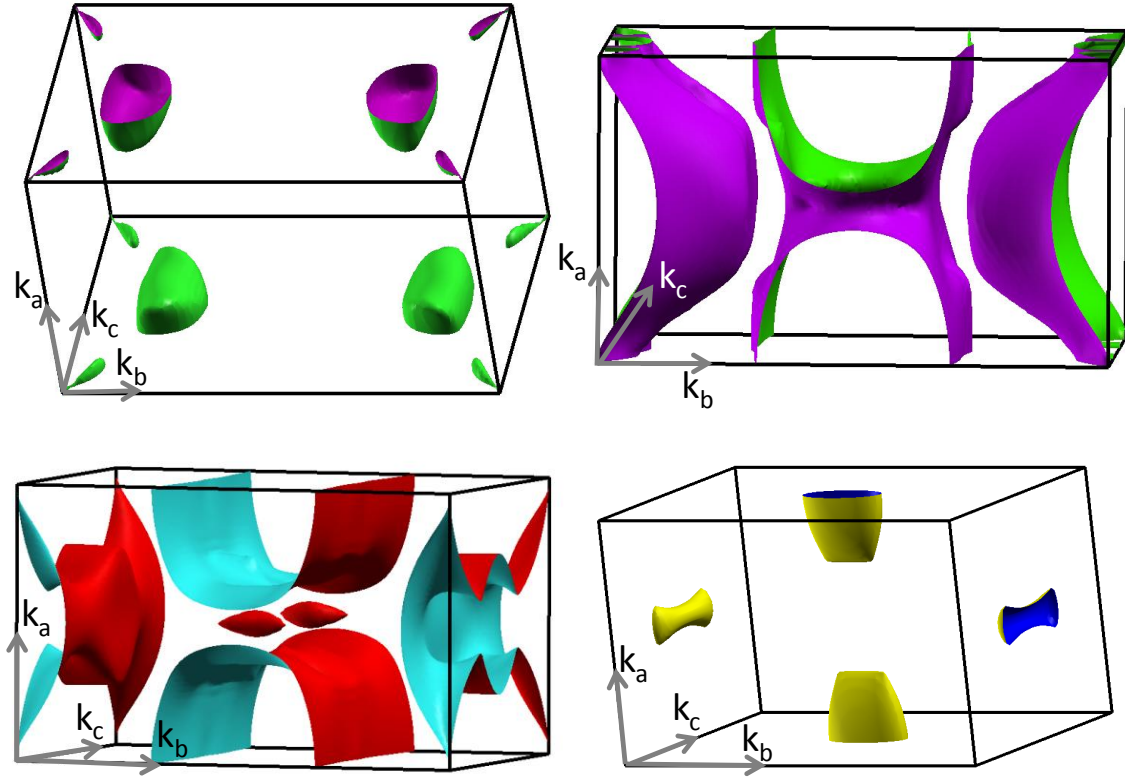


Figure 6.14: Separated Fermi surface for different bands. Color is used for the ease of viewing only.

$\leq \mu_{calc} \leq 0.74 \mu_B/\text{Ti}$, reflecting the itinerant nature of the ordered moment. This density functional theory overestimate compared to the experimental moment estimate of $0.15 \mu_B/\text{Ti}$ from neutron scattering is likely a result of strong spin fluctuations which cannot be accounted for by the density functional theory calculations. The same problem was also encountered in Fe pnictides, which are also itinerant d_{xy} density wave antiferromagnetic compounds [92, 234]. In the case of TiAu this may be remedied by future dynamical mean-field theory calculations, beyond the scope of this mainly experimental report of itinerant antiferromagnet in TiAu.

It is instructive to analyze the origin of magnetism in TiAu using the input from the band structure calculations. A picture that is often employed is that of the weak-coupling random phase approximation, resulting in the generalized Stoner criterion for the bare magnetic susceptibility $\chi^{(0)}$ at a reciprocal wavevector Q [214]:

$$I(Q)\chi^{(0)}(Q, \omega = 0) \geq 1 \quad (6.6)$$

Within this picture, the idealized itinerant limit can be understood as the case where $\chi(Q)$ is strongly peaked at a particular Q vector, resulting in a spin density wave ordering at that wavevector. In this case, the Q dependence of the interaction strength $I(Q)$ is unimportant. Traditionally, for instance in Cr [108], the peak in $\chi^{(0)}(Q)$ is understood as originating from Fermi surface nesting. Indeed, the calculated Fermi surface of the non-magnetic TiAu (Fig. 6.13(c)) exhibits large nearly nested regions in the k_b direction with the nesting wavevector $Q_{\text{nest}} = (0, k, 0)$ discussed above. In one spatial dimension, nesting is known to result in a logarithmic divergence of the susceptibility at $Q_{\text{nest}} = 2k_F$, $\chi^{(0)}(Q_{\text{nest}}) \sim -\rho(E_F) \log [\rho(E_F)T]$, resulting in the celebrated Peierls mechanism for charge density wave and spin density wave, with $\rho(E_F)$ representing the electronic density of states at the Fermi level. However in higher dimensions, it was pointed out that the divergence of $\chi^{(0)}$ is strongly

suppressed [410], and moreover, the ordering wavevector Q of the charge density wave (and by analogy, spin density wave) does not generally coincide with the nesting wavevector Q_{nest} [249], shown to be the case in *e.g.* rare earth tritellurides [249, 410]. The reason behind this is that the real part of the susceptibility $\chi(Q)$ contains the integration over all bands deep below the Fermi level, whereas nesting is the property of the Fermi surface itself and its effect is limited (except in the special case of perfect nesting, as in 1D).

It is a non-trivial task to calculate $\chi^{(0)}(Q)$ accurately from the density functional theory results, however the fact that all three magnetic configurations considered above have comparable energies indicates that $\chi^{(0)}(Q)$ is not a simple single-peaked function. This goes to show that, while magnetism in TiAu is close to the itinerant limit, its mechanism is more complicated than in Cr [108]. The difference between Cr and TiAu is further highlighted by the fact that the latter has a considerably larger drop in the relative magnetic susceptibility $\Delta M/M$ at T_N , where $\Delta M/M = [M_{T_N} - M_{T=0}]/M_{T_N}$. In TiAu, $\Delta M/M$ is $\sim 20\%$, nearly five times larger than in Cr [108]. In the latter, the small magnetization decrease at T_N had been attributed to the small spin susceptibility (and *not* the larger orbital component) being affected by the gap associated with the spin density wave transition. Conversely, the larger magnetization change in TiAu might indicate a sizable effect on the orbital magnetization, as the spin density wave transition is now associated with more 2D nesting than that in Cr.

6.4 Conclusion and Open Questions

In this Chapter it was shown that the orthorhombic TiAu is a new itinerant antiferromagnetic metal, the first of its kind, and analogous to the only two itinerant

ferromagnets with no magnetic elements, Sc_3In and ZrZn_2 . Ample experimental evidence for the itinerant character of the magnetic state in TiAu comes from the small magnetic moment in the ordered state compared to the paramagnetic moment, small magnetic entropy at T_N , it is readily apparent that strong spin fluctuations are at play in this novel magnetic system. The exact role of the spin fluctuations, their strength, as well as the details of the magnetic structure in the ordered state, remain to be fully elucidated with further experiments. Doping experiments presented in the following Chapter indicate that the magnetic order in doped TiAu is suppressed to 0 in a quantum critical regime with strong spin fluctuations. This provides a long sought after insight on quantum critical behavior of itinerant magnets in general and itinerant antiferromagnets in particular. Ultimately, the search for itinerant antiferromagnet materials appears to be a promising avenue for furthering our understanding of the complex magnetism, and providing the unifying picture for local and itinerant moment magnetism.

Doping-induce Quantum Critical Point in

$\text{Ti}_{1-x}\text{Sc}_x\text{Au}$

In previous Chapter, a novel antiferromagnet composed on non-magnetic constituents has been described. A number of measurements as well as theoretical analysis indicated a spin density wave ground state below $T_N \approx 36K$. It is particularly interesting to investigate the behavior of this system under various perturbations. Since application of high field and pressure did not result in the suppression of the ordering temperature, partial substitution of Ti by Sc was implemented. It was found that a small doping amount of about 13 % induces a quantum critical point in $\text{Ti}_{1-x}\text{Sc}_x\text{Au}$. Non-Fermi liquid behavior observed in both resistivity ($\rho \propto T$) and specific heat ($C_p/T \propto -\log T$) is consistent with a 2D antiferromagnetic quantum critical point. Moreover, divergent magnetic Grüneisen ratio clearly signals critical behavior. Enhanced value of the Sommerfeld coefficient indicates strong spin fluctuations, while diverging value of the resistivity coefficient has been attributed to enhanced electron-electron correlations around the quantum critical point [354].

7.1 Motivation and Background

Many interesting phenomena in condensed matter physics occur in the vicinity of quantum critical points, with notable examples including unconventional superconductivity [84, 175, 242, 320], non-Fermi liquid [34, 129, 226, 227] and heavy fermion behavior [129, 206, 207, 322], as well as the coexistence of superconductivity and magnetism [207, 242, 419]. The emergence of such exotic ground states is possible due to competing interactions in the zero temperature limit, where thermal fluctuations cease to exist [348]. While the notion of competing interactions is old, a complete understanding of the resultant quantum critical phenomena is still a subject of great interest [285]. Conveniently, the presence of a quantum critical point manifests itself in the physical properties well above absolute zero. In particular, deviations from the Fermi liquid behavior that frequently accompany quantum phase transitions have been the central topic of both experimental and theoretical studies of correlated electron systems in the past decade [227]. In a number of materials, it has been possible to reach a quantum critical point *via* the application of pressure [110, 142, 207, 384], doping [34, 175, 341, 355], or magnetic field [129, 294, 373]. Fine tuning capability is key in probing quantum critical points systematically, as the role of disorder is still unclear [391]. For instance, while the ferro- to paramagnetic quantum phase transition is theoretically of first order [38], doping-induced disorder changes the transition to second order [51].

While a plethora of antiferromagnetic quantum critical points has been observed in heavy fermion materials [129, 175, 206, 207, 322], this is not the case for the d electron systems for which the examples of antiferromagnetic quantum critical points are limited to Cr [172, 173, 223, 253, 368, 411] and $V_{2-y}O_3$ [30, 182]. In the latter, the quantum critical point is accompanied by an insulator-to-metal transition [182] and the antiferromagnetic order arises from local rather than itinerant moments. Cr, on

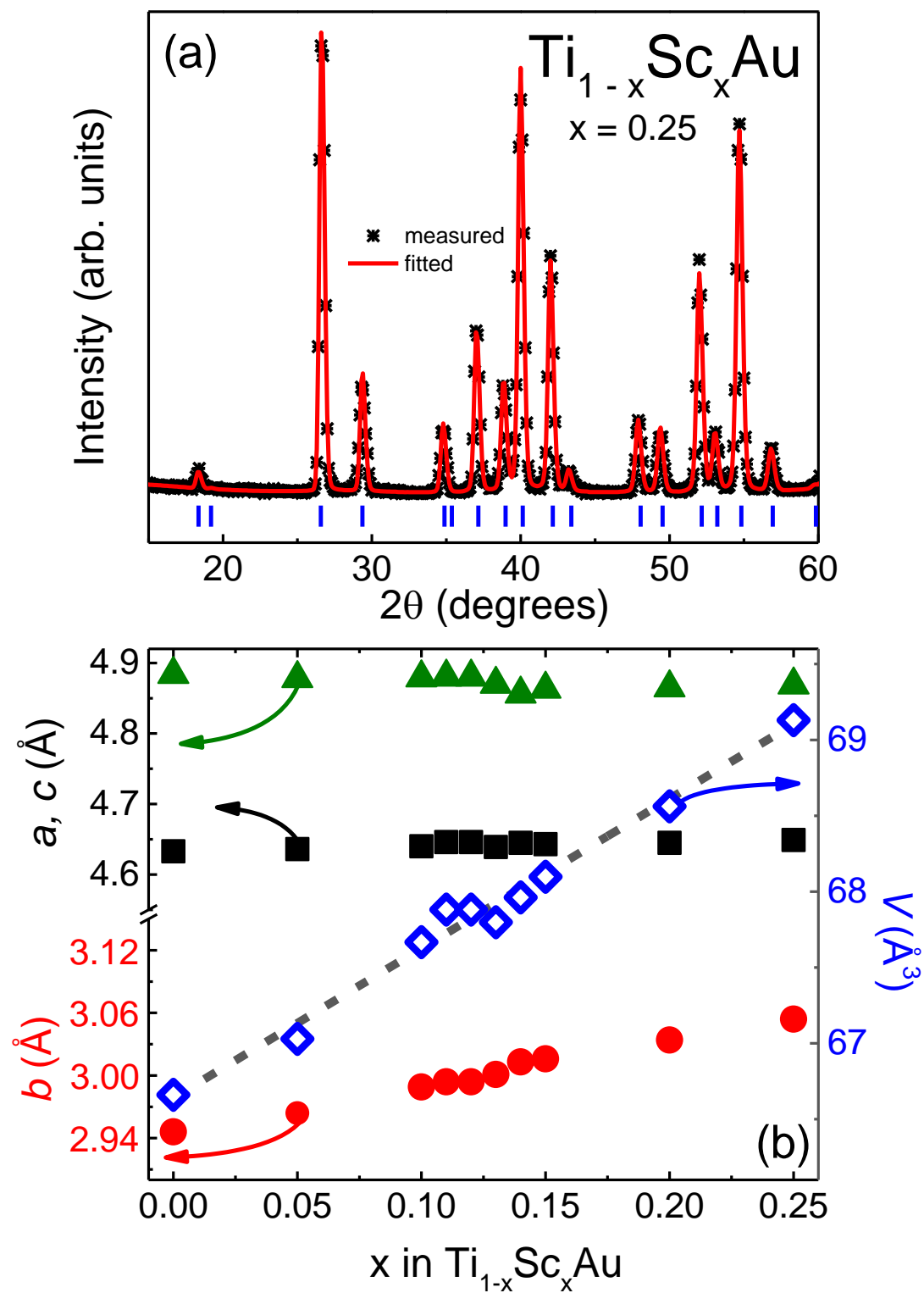


Figure 7.1: Evolution of lattice parameters a (triangles, left axis), b (circles, left axis), and c (squares, left axis) along with the unit cell volume V (diamonds, right axis) with doping x in $\text{Ti}_{1-x}\text{Sc}_x\text{Au}$ ($0 \leq x \leq 0.25$).

the other hand, is the archetypical 3D antiferromagnetic metal for which conduction electrons are lost as they order magnetically when the temperature is decreased below the Néel temperature T_N . While it was suggested that a 2D antiferromagnetic metal should exhibit a continuous second order quantum phase transition [4], experimentally this has not yet been realized, perhaps explaining why the detailed characteristics of metallic antiferromagnetic quantum phase transitions in 2D remain one of the pressing questions from both theoretical and experimental viewpoints [227]. Not surprisingly, the nature of spin fluctuations in antiferromagnetic metals is even less understood [181, 184, 269]. Here we present the *first* experimental realization of a 2D antiferromagnetic quantum critical point in a d electron system $\text{Ti}_{1-x}\text{Sc}_x\text{Au}$ metal, with a critical doping $x_c = 0.13 \pm 0.01$.

7.2 Physical Properties

Recently, we reported TiAu as the first itinerant antiferromagnetic metal with no magnetic constituents [359]. The antiferromagnetic spin density wave order for TiAu develops below 36 K, and is surprisingly robust to perturbation with pressure [356], with the Néel temperature enhanced by small increasing pressure [356], similar to what has been observed for the ferromagnet without magnetic elements Sc_3In [124, 140]. Moreover, according to band structure calculations [356], a pressure of nearly 80 GPa is predicted theoretically to suppress T_N to zero in TiAu. However, it has been established that Ti bands contribute the most to the density of states at the Fermi level [359], and so it appears that partial substitution of Ti may provide an avenue for reducing T_N . In order to minimize the effects of chemical pressure, host Ti atoms were partially replaced with Sc, a dopant of similar size ($r(\text{Ti}^{4+}) = 0.61 \text{ \AA}$ and $r(\text{Sc}^{3+}) = 0.75 \text{ \AA}$ [329]). Doping with a slightly larger Sc ion expands the lattice, as evidenced by the evolution of the volume V with doping x , shown in Fig.

7.1 (right axis). The monotonic change in all three lattice parameters a , b and c (full symbols) as well as the unit cell volume (open symbols) is shown in Fig. 7.1. It is important to note that, although the TiAu crystal structure is intrinsically 3D, we believe that the spin fluctuations have a 2D character, as evidenced by the behavior of specific heat and resistivity close to the quantum critical point summarized below. This dimensional discrepancy so far has only been observed in the heavy fermion $\text{CeCu}_{6-x}\text{Au}_x$ [125].

Similar to local moment magnets, a cusp in the magnetic susceptibility marks the transition from antiferromagnetic to paramagnetic state in TiAu [359]. With Sc doping (Fig. 7.2), T_N moves down in temperature, and is suppressed below 1.8 K for $x \geq 0.13$. At high temperatures ($T > T_N$), the $H = 0.01$ T magnetic susceptibility for $\text{Ti}_{1-x}\text{Sc}_x\text{Au}$ exhibits Curie-Weiss-like behavior for the whole composition range

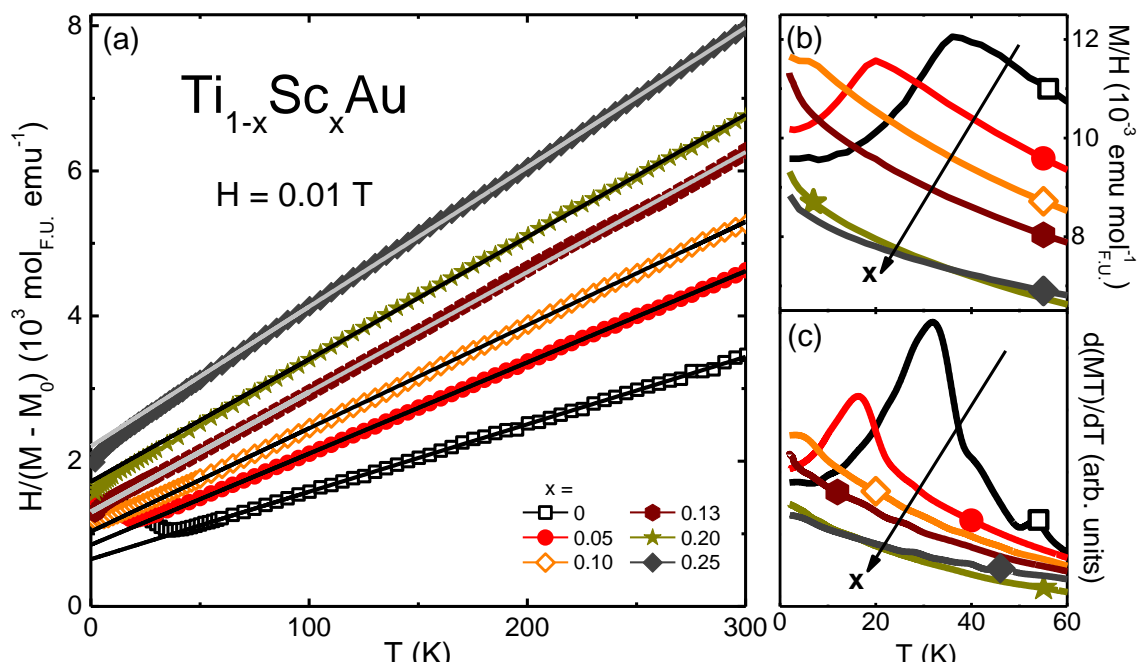


Figure 7.2: (a) Inverse susceptibility $H/(M - M_0)$ (symbols) along with respective Curie-Weiss fits (lines) for $\text{Ti}_{1-x}\text{Sc}_x\text{Au}$ with $0 \leq x \leq 0.25$. (b) Magnetic susceptibility M/H as a function of temperature T for $\text{Ti}_{1-x}\text{Sc}_x\text{Au}$ with $0 \leq x \leq 0.25$. (c) The Néel temperature T_N is determined from the peak in $d(MT)/dT$, which is reduced below $T = 2$ K for $x \geq 0.12$.

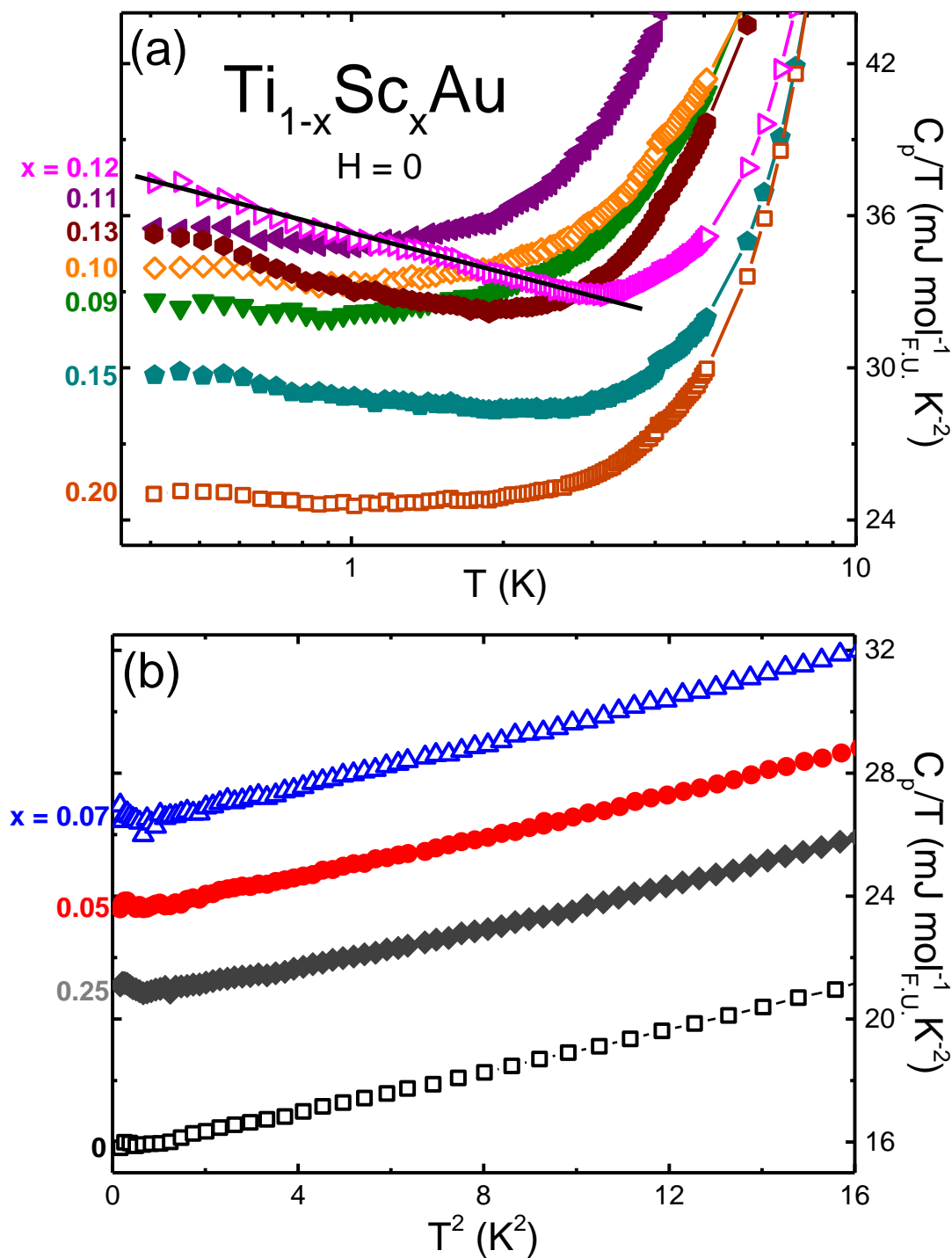


Figure 7.3: (a) non-Fermi liquid behavior is evident from $C_p/T \propto -\log T$ for $0.09 \leq x \leq 0.20$ in $\text{Ti}_{1-x}\text{Sc}_x\text{Au}$. (b) A Fermi liquid specific heat temperature dependence $C_p/T \propto T^2$ is recovered away from the quantum critical point for $0 \leq x \leq 0.07$ and $x = 0.25$ in $\text{Ti}_{1-x}\text{Sc}_x\text{Au}$.

$0 \leq x \leq 0.25$, similar to what has been observed in doped itinerant ferromagnets [341,355], but distinct from the behavior of the itinerant antiferromagnetic Cr [261]. This is in stark contrast with the self-consistent renormalization theory prediction, where the Curie-Weiss-*like* behavior is expected in both the 2D [169] and 3D [151] antiferromagnetic cases. In $\text{Ti}_{1-x}\text{Sc}_x\text{Au}$, the value of the paramagnetic moment μ_{PM} , determined from the linear fits of the inverse susceptibility (Fig. 7.2a) remains nearly constant even as the transition is suppressed by increasing x . The ordered moment μ_{ord} in TiAu [359] is $\sim 0.1 \mu_B/F.U.$, four times smaller than that of Cr [411]. It is thus very difficult to track the evolution of μ_{ord} with x in $\text{Ti}_{1-x}\text{Sc}_x\text{Au}$ by means of neutron diffraction as μ_{ord} is close to the instrumental resolution limit. An estimate of T_N for $\text{Ti}_{1-x}\text{Sc}_x\text{Au}$ ($0 \leq x \leq 0.25$) is obtained from the local maximum of the derivative $d(\chi T)/dT$ (Fig. 7.2c) [114,115]. The resultant suppression of the ordering temperature is nearly linear as a function of doping x , similar to what has been seen in $\text{Cr}_{1-x}\text{V}_x$ [411] and consistent with a second order 2D antiferromagnetic quantum critical point [4].

A theoretical description of the behavior close to a quantum critical point for d electron systems was established on the basis of the self-consistent renormalization theory of spin fluctuations for both ferromagnetic [261] and antiferromagnetic materials [267]. However, while these predictions are consistent with a number of experimental ferromagnetic quantum critical points [170,171,181,228,281,298,341,366], the antiferromagnetic comparison had only been possible for the 3D case [184], given the limited number of d electron antiferromagnetic quantum critical points [227]. According to Moriya's prediction for a 2D antiferromagnet, quantum fluctuations in the vicinity of the respective quantum critical point result in the breakdown of the Fermi liquid state, yielding $C_p/T \propto -\log T$ [268]. In $\text{Ti}_{1-x}\text{Sc}_x\text{Au}$, this divergence persists over nearly a decade in temperature for $x = 0.12$ (Fig. 7.3a), with non-Fermi liquid behavior signaled by the divergent $\gamma = C_p/T \propto \log T$ for $0.09 \leq x \leq 0.20$.

Away from the quantum critical point, the Fermi liquid-like specific heat behavior ($C_p/T \propto \gamma + \beta T^2$) is recovered for $0 \leq x \leq 0.05$ and $x > 0.5$, as shown in Fig. 7.3b. As a result, the Sommerfeld coefficient γ is maximum close to $x_c \approx 0.13$ as shown in Fig. 7.10c, left axis. Such behavior of the electronic specific heat coefficient was also reported for $\text{Cr}_{1-x}\text{V}_x$ [368]. Positive pressure induced by the slightly larger Sc ions substituting for Ti [329] is expected to decrease band overlap, increasing the density of states at the Fermi level, and, consequently, yielding larger γ and M_0/H values [150, 368]. However, while M_0/H increases gradually over the whole composition range (Fig 7.10(b), right axis), γ values exhibit a peak centered around x_c (Fig. 7.10c, left axis), most likely a signature of the critical fluctuations associated with the quantum critical point in itinerant magnets: $\gamma = \gamma_{band} + \gamma_{SF}$ [150]. According to the self-consistent renormalization theory for antiferromagnets [151], $T_N \propto (2I\chi_s - 1)^{2/3}$ and $\gamma_{SF} \propto (2I\chi_s - 1)^{1/2}$ (where I is the exchange interaction and χ_s is the staggered susceptibility), which indicates that γ_{SF} should scale with T_N as $\gamma_{SF} \propto T_N^{3/4}$. Indeed, Fig. 7.4b shows the linear relationship between γ and $T_N^{3/4}$, evidence for strong spin fluctuations in $\text{Ti}_{1-x}\text{Sc}_x\text{Au}$ [261].

The resistivity of TiAu [359] decreases below T_N , a feature that is typically observed in local moment systems and is due to loss of spin disorder scattering. By contrast, in both Cr and V_{2-y}O_3 antiferromagnets, the resistivity increases below T_N due to the partial gapping of the Fermi surface [30]. In $\text{Ti}_{1-x}\text{Sc}_x\text{Au}$, magnon scattering results in resistivity exponent values n ($\rho = \rho_0 + A_n T^n$) distinct from the Fermi liquid $n = 2$ value [261]. As shown in Fig. 7.10(e) (triangles, left axis), $n \geq 2$ is observed for $0 \leq x \leq 0.10$ samples, for which $T_N \geq 2$ K (Fig. 7.10a). As the quantum critical point is approached both from below ($x \leq 0.13$) and above ($x \geq 0.13$), n decreases to $n \approx 1$ at the quantum critical point, corroborating the non-Fermi liquid scenario close to the quantum critical point, as previously indicated by the specific heat data.

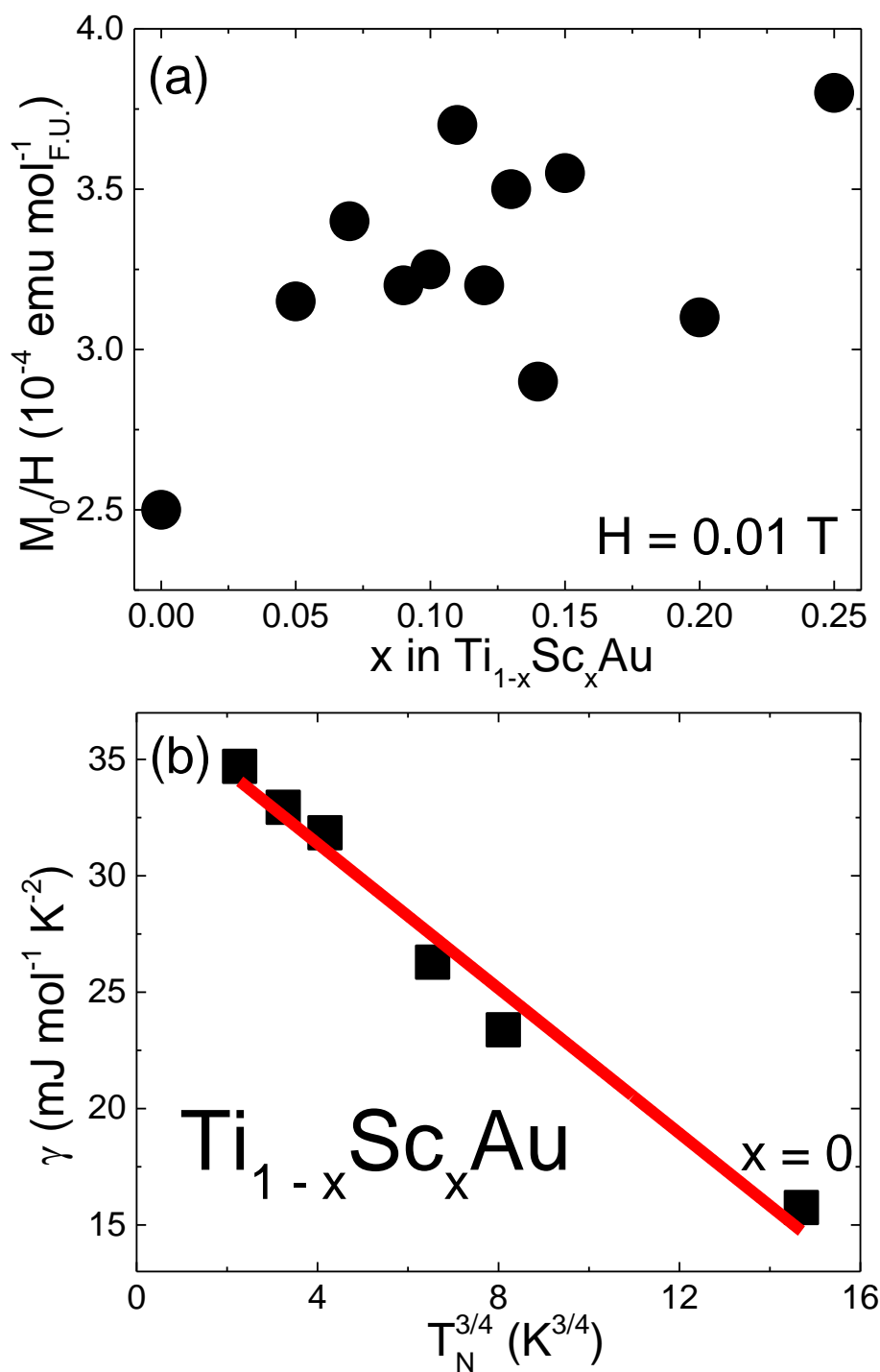


Figure 7.4: (a) Temperature-independent contribution to the susceptibility χ_0 as a function of doping x in $\text{Ti}_{1-x}\text{Sc}_x\text{Au}$. (b) Sommerfeld coefficient γ as a function of $T_N^{3/4}$ (symbols), line is a guide to the eye.

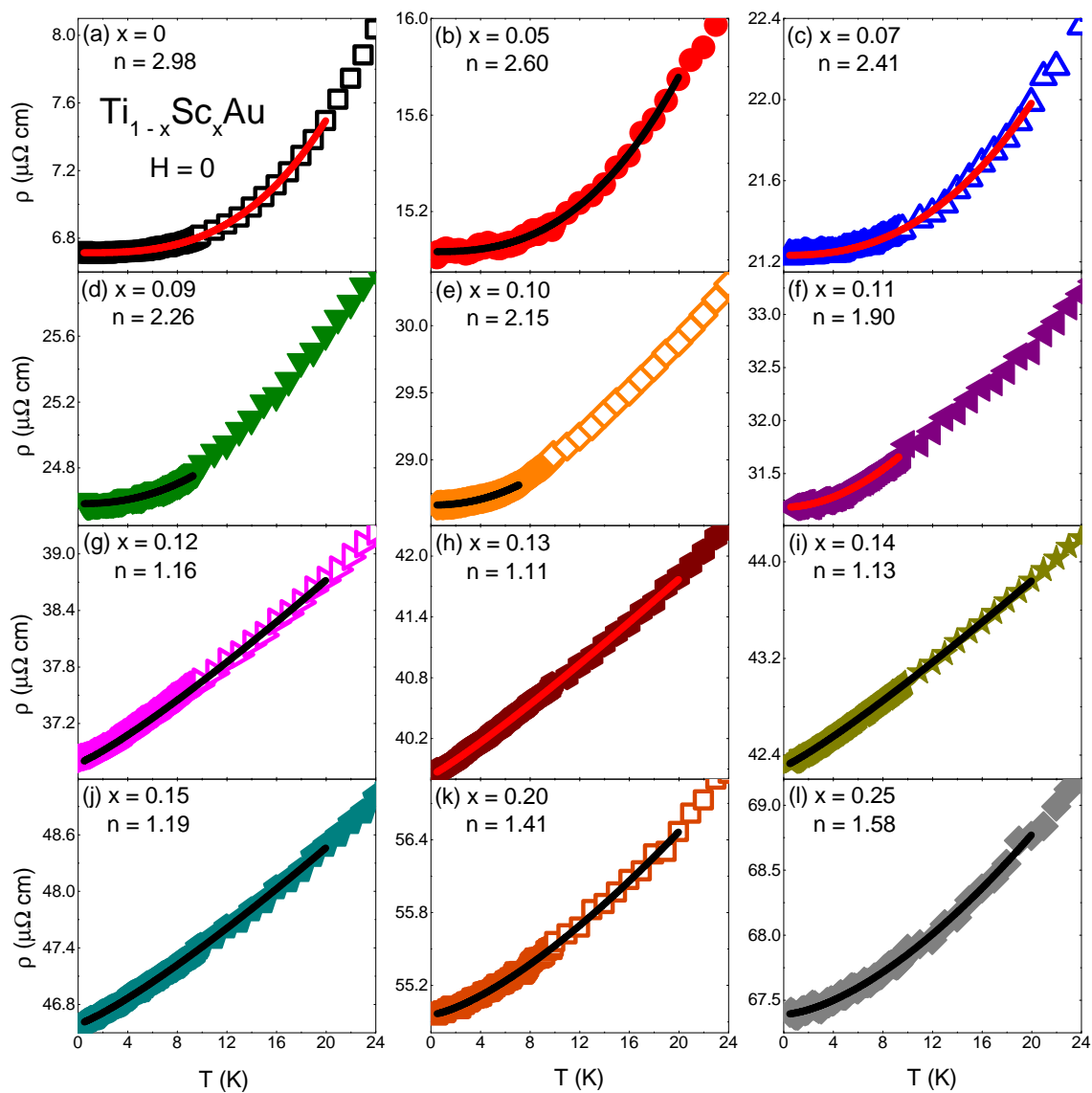


Figure 7.5: (a) - (l) Resistivity as a function of temperature T for $\text{Ti}_{1-x}\text{Sc}_x\text{Au}$ where $0 \leq x \leq 0.25$. Solid lines represent fit to $\rho = \rho_0 + A_n T^n$.

The T^n resistivity behavior is best reflected in the ρ vs. T^n plots shown in Fig. 7.6. Close to the quantum critical point ($x = 0.14$) ρ vs. T^n is linear over a decade in temperature (up to $T = 65$ K), with n near a local minimum $n \approx 1$. Close to a quantum critical point, exponent values n smaller than 1.5 have been attributed to reduced dimensionality [242], with $n = 1.5$ expected for a 3D antiferromagnetic quantum critical point [267]. This would suggest that, upon approaching the quantum critical point in $\text{Ti}_{1-x}\text{Sc}_x\text{Au}$, the critical fluctuations become more 2D rather than 3D [78, 313].

The resistivity coefficient A_n for both optimal n (full diamonds) and fixed $n = 2$ (open diamonds) is shown in Fig. 7.10(e) (left axis) as a function of x . Both sets of A_n values diverge as the quantum critical point is approached from the paramagnetic state. The expected divergence is given by $A_n \propto (\sigma - \sigma_c)^{0.5}$ [378], where σ is an extrinsic tuning parameter such as pressure, composition or magnetic field. In the case of $\text{Ti}_{1-x}\text{Sc}_x\text{Au}$, $A_n \propto (x - 0.13)^\alpha$ fit yields a slightly slower divergence with an exponent $\alpha = 0.46$ (Fig. 7.10(e), black line). Similar behavior of A_n has been observed near $x = x_c$ in a number of heavy fermion quantum critical points for antiferromagnets [33, 129, 142, 206, 207, 419] and ferromagnets [281], and has been interpreted as a signature of increased electron-electron correlations. Additional evidence for the stronger correlations close to the quantum critical point in $\text{Ti}_{1-x}\text{Sc}_x\text{Au}$ is provided by the Wilson ratio given by $R_W = 4\pi^2 k_B^2 \chi_0 / 9\mu_B^2 \gamma$ [399]. As seen in Fig. 7.10d, R_W increases from 1 close to the quantum critical point ($x_c \approx 0.13$) to 2 at high x ($x \approx 0.25$), as compared with the free-electron value of $R_W = 1$, has been suggested to arise due to the Stoner enhancement in itinerant magnets [130].

On the other hand, the $n \leq 2$ values have been previously employed to pinpoint the quantum critical point in both antiferromagnetic [207] and ferromagnetic [281] materials. For a 2D antiferromagnetic quantum critical point, the resis-

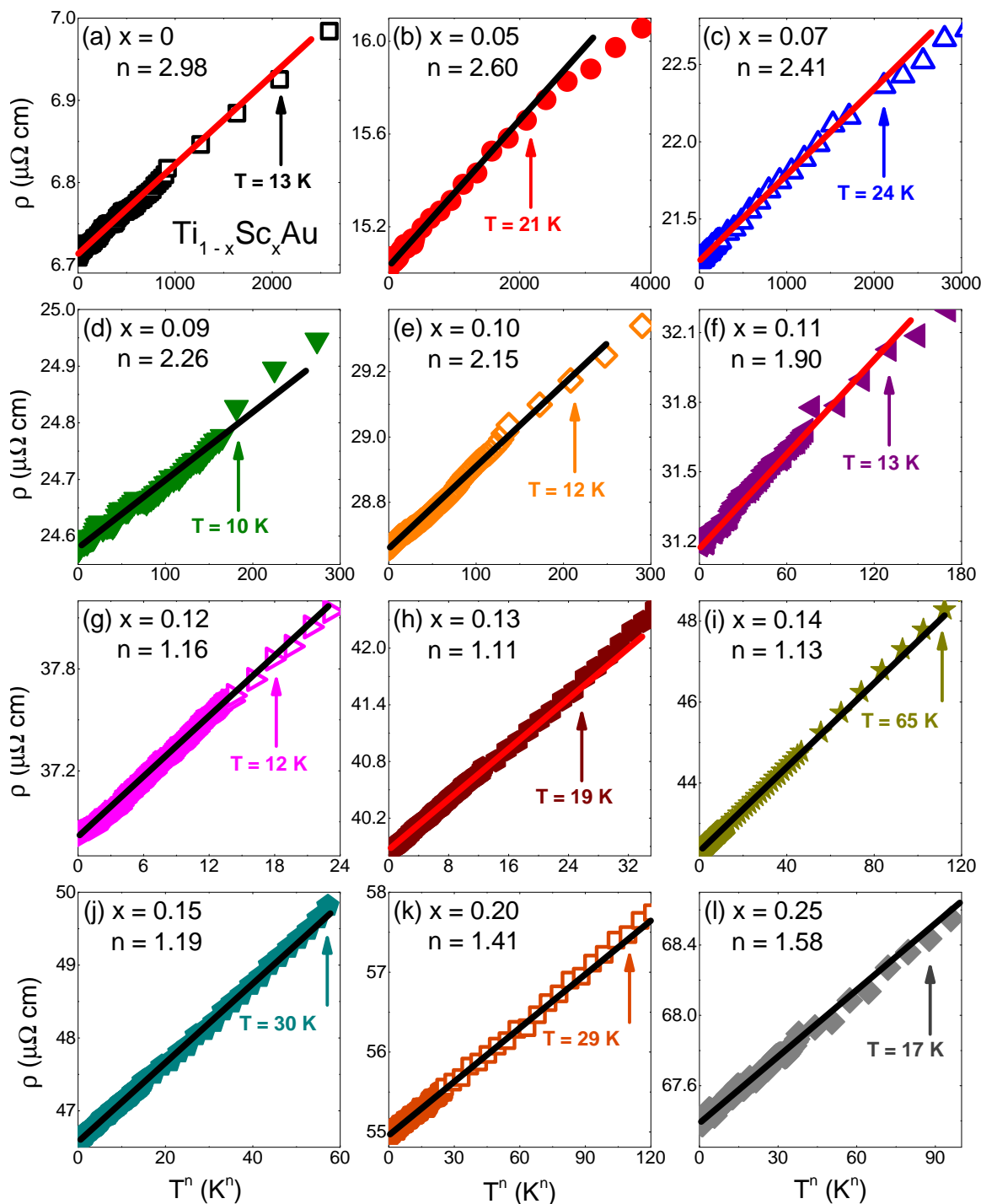


Figure 7.6: (a) - (l) Resistivity as a function of temperature T^n for $\text{Ti}_{1-x}\text{Sc}_x\text{Au}$ where $0 \leq x \leq 0.25$. The value of the exponent n achieves a minimum for $x = 0.13$, consistent with the breakdown of the Fermi liquid regime for which $n = 1$. On either side of the critical point, Fermi liquid resistivity is regained with n values close to 2.

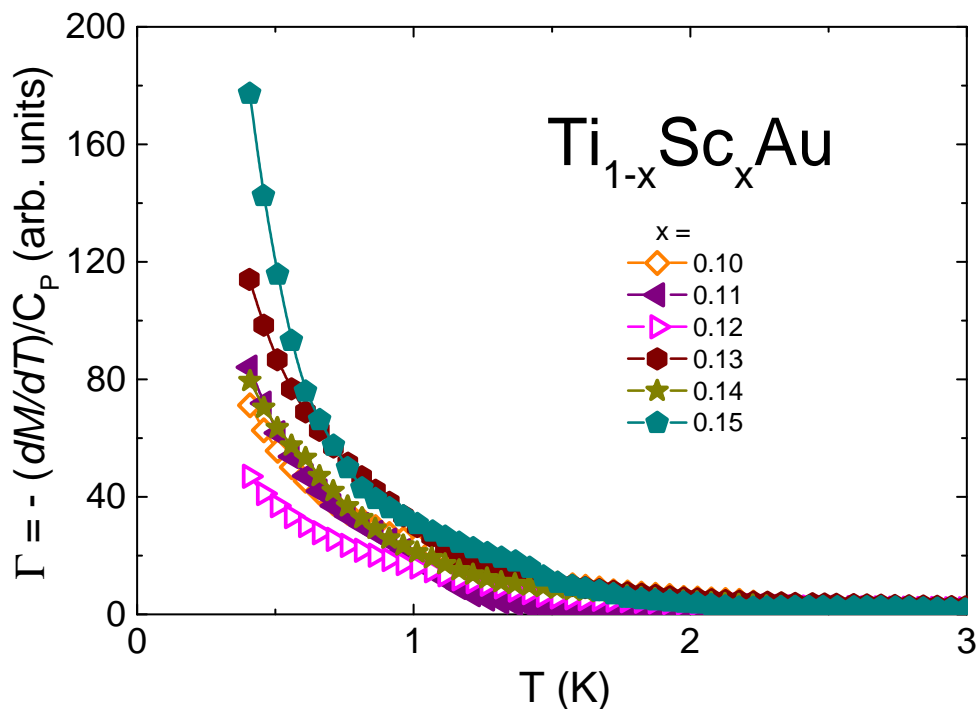


Figure 7.7: Magnetic Grüneisen ratio Γ_{mag} for $\text{Ti}_{1-x}\text{Sc}_x\text{Au}$ where $0 \leq x \leq 0.25$: the value of Γ_{mag} at lowest temperature diverges as $x \rightarrow x_c$.

tivity exponent $n = 1$ is expected [267, 268], marking the onset of the non-Fermi liquid behavior in $\text{Ti}_{1-x}\text{Sc}_x\text{Au}$ with $n \rightarrow 1$ as $x \rightarrow x_c$ from both sides (Fig. 7.10(e), right axis). Although the existence of the quantum critical point in $\text{Ti}_{1-x}\text{Sc}_x\text{Au}$ is confirmed unambiguously by the onset of the non-Fermi liquid behavior as the Néel temperature T_N is suppressed to zero, an insight on the nature of the quantum critical point can be gained from examining the Grüneisen ratio [143]. The magnetic Grüneisen ratio ($\Gamma_m = -(dM/dT)/C_p(T)$) is expected to diverge at any quantum critical point [420], however, this has only been observed in antiferromagnetic heavy fermions [131, 215–217, 374], unlike the ferromagnetic systems for which Γ_m remains finite as $T \rightarrow 0$ [166]. The evolution of the magnetic Grüneisen ratio Γ_m for $\text{Ti}_{1-x}\text{Sc}_x\text{Au}$ at low temperature is shown in Fig. 7.7. The divergence is evident from the $\Gamma_m(0)$ values (Fig. 7.10c, right axis) which exhibit a step close to $x_c = 0.13 \pm 0.01$. Furthermore, the temperature exponent of the Grüneisen ratio closest to the quantum

critical point provides a direct way to measure the product of the dynamical critical exponent z and the exponent of the correlation length ν since $\Gamma_{cr} \propto T^{-z\nu}$ [420]. In $\text{Ti}_{1-x}\text{Sc}_x\text{Au}$, a fit of the $\Gamma_{cr}(x = 0.13)$ yields $z\nu = 0.4$. Fractional Grüneisen exponents have been previously attributed to a localized quantum critical point, for which spatially local critical excitations emerge and coexist with the spatially extended critical spin fluctuations [217, 374]. This scenario is, however, inconsistent with a fully itinerant mechanism of magnetism in $\text{Ti}_{1-x}\text{Sc}_x\text{Au}$.

7.3 Band Structure Calculations

The suppression of the antiferromagnetic spin density wave in $\text{Ti}_{1-x}\text{Sc}_x\text{Au}$ is evidenced by a number of physical properties summarized above. Several phenomena contribute to this evolution: change in number of valence electrons, lattice expansion, atomic displacement, and effects of disorder. Addressing the latter is not possible within the DFT framework. Since the volume change for the entire doping range is less than 4%, we believe that the slight expansion of the crystal structure does not contribute to the quantum critical phenomenon. Therefore, only change in the valence electron number was taken into account – the VCA approximation was used for the $x = 0.20$ and $x = 0.40$ samples. While quantitative agreement between theory and experiment is often not possible, present theoretical analysis fits well within the qualitative picture of the effects of Sc doping on TiAu. Relative energies of surveyed magnetic configurations for $\text{Ti}_{1-x}\text{Sc}_x\text{Au}$ compounds with $x = 0, 0.2$ and 0.4 are summarized in Table 7.1. As discussed in Ref. [359], the $(0, 1/3, 0)$ spin density wave state is the ground state of the undoped TiAu. From Table 7.1, the $(0, 1/3, 0)$ spin density wave state is the ground state for both $x = 0$ and $x = 0.2$ since $E_{SDW} < E_{FM} < E_{PM}$. For $x = 0.4$, the paramagnetic state is the ground state since E_{PM} is the lowest. This indicates that the transition from the spin density wave to the paramagnetic ground

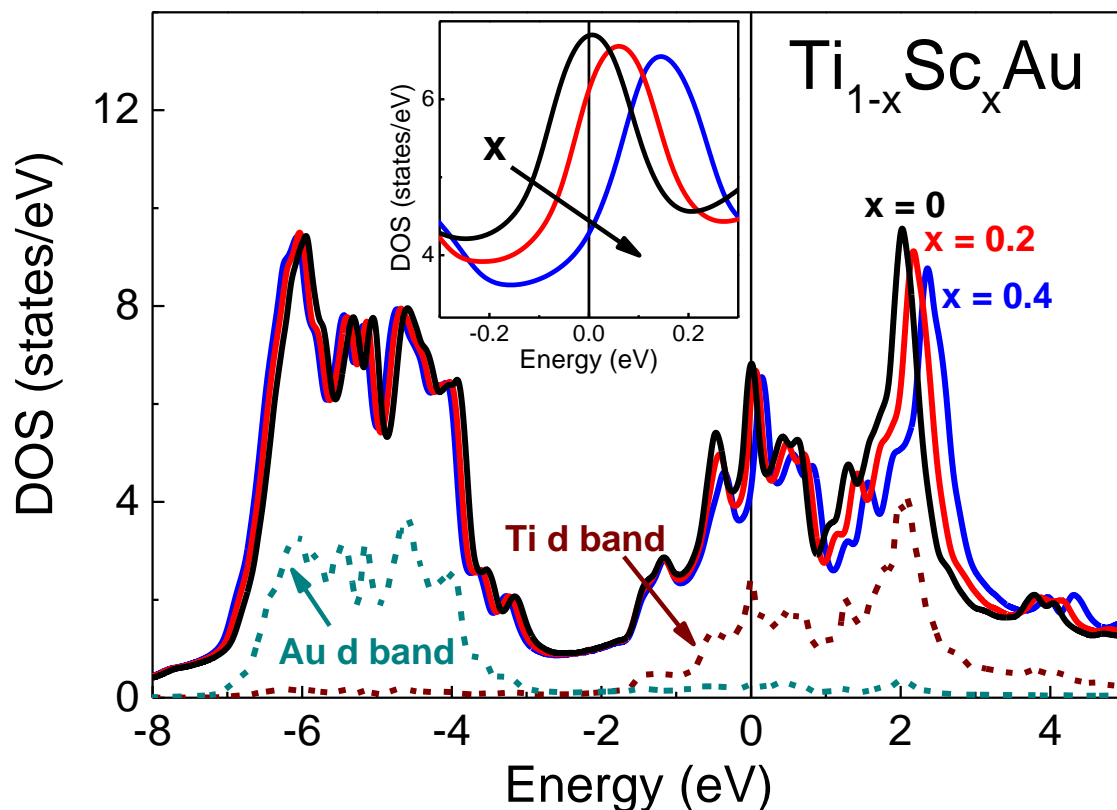


Figure 7.8: The total (solid lines) and partial (dashed lines) density of states in paramagnetic state for $\text{Ti}_{1-x}\text{Sc}_x\text{Au}$ where $x = 0, 0.2$ and 0.4 . In the $x = 0$ case, Ti bands (maroon) contribute more to the density of states at the Fermi level than the Au bands (cyan). The dashed densities of state are divided by a factor of two for ease of viewing. Inset: both position and magnitude of the peak at the Fermi level are affected by doping.

state occurs between $x = 0.2$ and $x = 0.4$. Experimentally, the critical doping is estimated to be $x_c = 0.13 \pm 0.01$. Although consistent with each other, the theoretical analysis is not able to correctly estimate the exact critical doping level, which likely indicates the importance of disorder for this quantum critical point. The decrease of the calculated ordered moments of the $(0, 1/3, 0)$ spin density wave state, listed in Table 7.1, is consistent with suppression of antiferromagnetic-paramagnetic transition to $T = 0$ K.

Total (solid lines) and partial (dashed lines) densities of states of the $\text{Ti}_{1-x}\text{Sc}_x\text{Au}$

compounds ($x = 0, 0.2$ and 0.4) in the paramagnetic state are shown in Fig. 7.8. As evident from the partial density of states for TiAu, the Au d bands lie mostly below the Fermi level while the Ti d bands contribute the most at the Fermi level. In TiAu, a sharp peak at the Fermi level indicates that the ground state is likely to be magnetic, a feature also seen in other itinerant magnets [261]. Upon addition of Sc doping, the peak shifts away from the Fermi level, as seen in the inset of Fig. 7.8. The direction of the shift indicates depletion of the valence band, which is consistent with the reduced number of valence electrons in Sc as compared with Ti.

Table 7.1: Summary of the band structure calculations for $\text{Ti}_{1-x}\text{Sc}_x\text{Au}$ with $x = 0, 0.2$ and 0.4 with paramagnetic, ferromagnetic, and spin density wave configuration.

x	PM	FM	SDW	
	Energy (meV)	Energy (meV)	Energy (meV)	μ_{ord} (μ_B)
0	0	-19	-76	0.5
0.20	0	-4.2	-45	0.35
0.40	0	44	23	$0.6 \cdot 10^{-5}$

The change in electronic properties induced by Sc doping in TiAu is also evident from the Fermi surface evolution. Firstly, the $(0, 1/3, 0)$ Fermi surface nesting present in TiAu (Fig. 7.9a) disappears in $\text{Ti}_{0.6}\text{Sc}_{0.4}\text{Au}$ (Fig. 7.9b). As stated previously [359], Fermi surface nesting is a critical feature of the electronic state for itinerant antiferromagnets. Therefore, loss of Fermi surface nesting indicates change of the ground state from the spin density wave state to the paramagnetic one. Additionally, while four bands cross the Fermi level in the TiAu case (Fig. 7.9a), only three do so for the case of $\text{Ti}_{0.6}\text{Sc}_{0.4}\text{Au}$ (Fig. 7.9b).

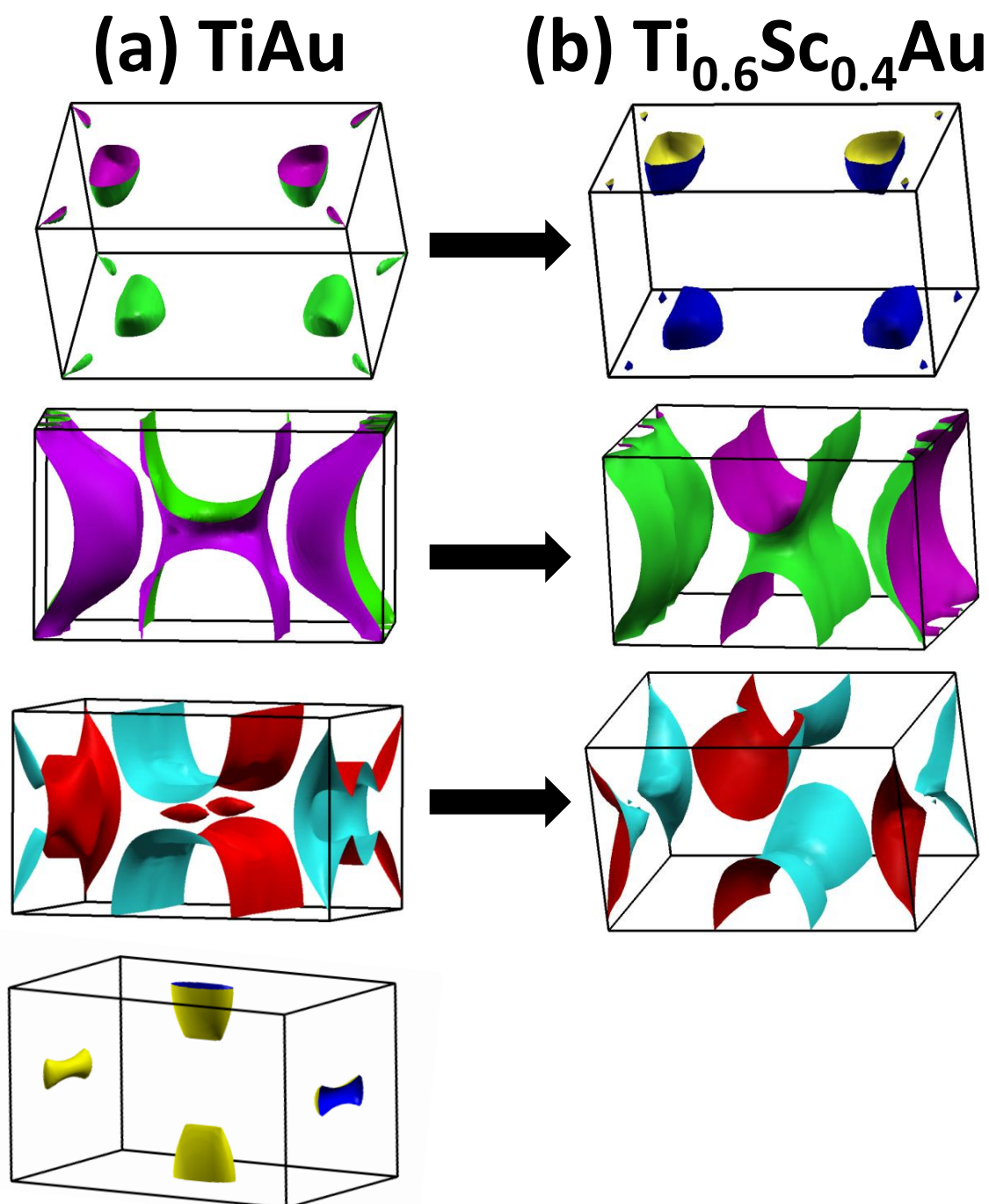


Figure 7.9: The evolution of the Fermi surface in TiAu with doping. While four bands contribute to the Fermi level in $x = 0$, only three bands are present for the $x = 0.4$ compound.

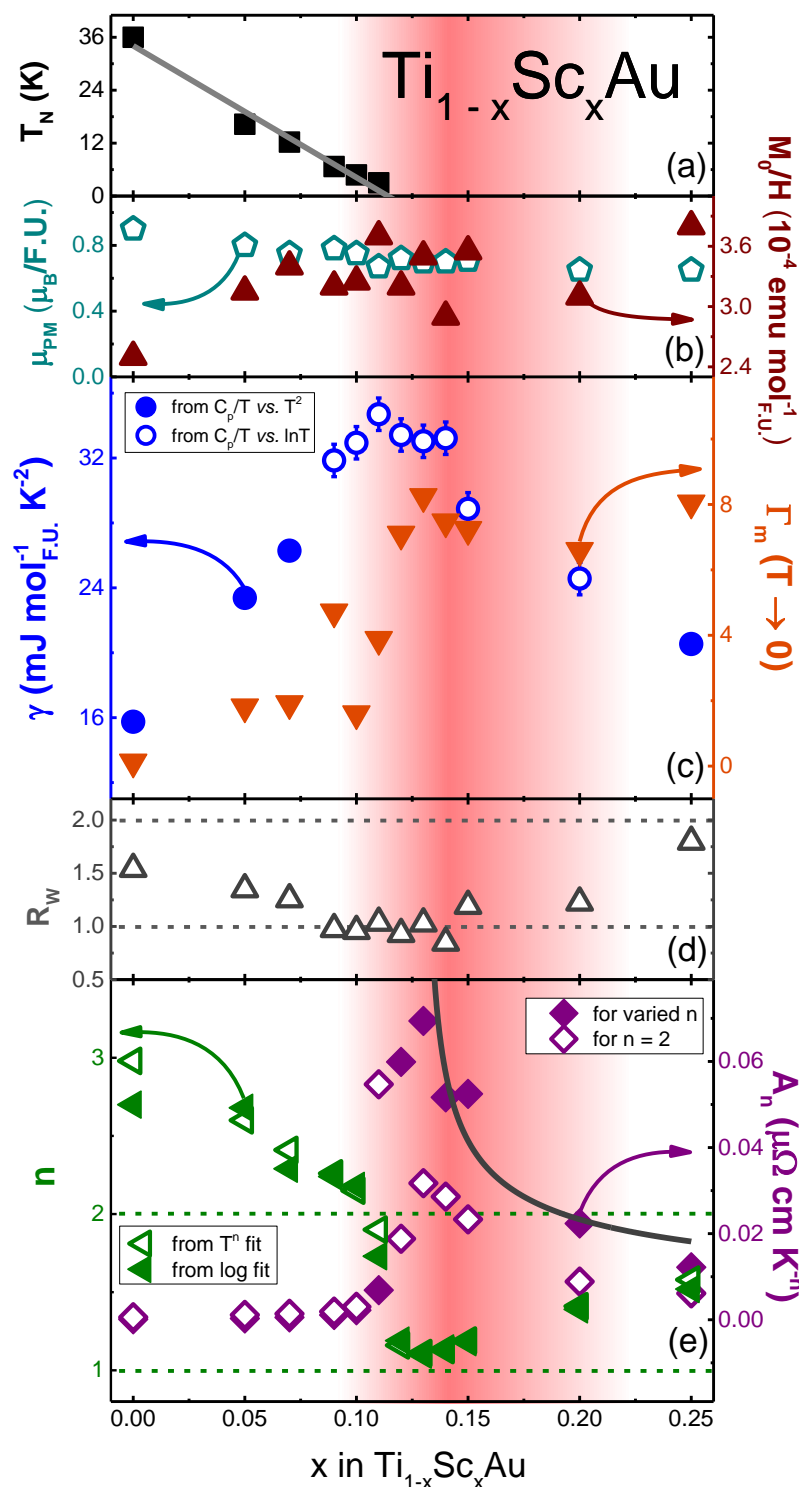


Figure 7.10: (a) Evolution of the Néel temperature T_N and (b) paramagnetic moment $\mu_{\text{P.M.}}$ with doping x . (c) Left axis: the Sommerfeld coefficient γ extracted from C_p/T vs. T^2 (Fermi liquid region, full circles) and from C_p/T vs. $\log T$ (non-Fermi liquid region, open circles). Right axis: The Grüneisen ratio Γ_{mag} . (d) Wilson's ratio R_W . (e) Left axis: The exponent n , extracted from $\Delta\rho$ vs. T^n (open triangles) and $\log\Delta\rho$ vs. $\log T$ (full triangles). Right axis: The resistivity coefficient A_n for varied n (full diamonds) and $n = 2$ (open diamonds).

7.4 Conclusion and Open Questions

In this work, the suppression of the antiferromagnetic order to $T = 0$ in a quantum critical regime was possible *via* partial substitution of Ti with Sc in $\text{Ti}_{1-x}\text{Sc}_x\text{Au}$. The critical doping estimate $x_c = 0.13 \pm 0.01$ is consistent across all measurements (Fig. 7.10), indicating collective quantum critical phenomenon. Moreover, the scaling behavior of $\text{Ti}_{1-x}\text{Sc}_x\text{Au}$ clearly indicates the 2D antiferromagnetic nature of magnetic spin fluctuations [268]. The suppression of the spin density wave-paramagnetic transition to absolute zero with Sc doping is also confirmed *via* band structure calculations, where a gradual shift of the peak in the density of states at the Fermi level as well as the loss of the Fermi surface nesting are expected. While the critical doping level extracted from the band structure calculations is larger than $x_c = 0.13 \pm 0.01$, the quantitative discrepancy is expected to decrease if the effects of disorder are taken into account. Such analysis is currently underway and will be reported elsewhere.

Although 2D antiferromagnetic quantum critical points have been reported for f electron systems [129, 206, 207], quantum critical point in $\text{Ti}_{1-x}\text{Sc}_x\text{Au}$ is the first among the filled shell d electron materials. Understanding the properties of this system will serve as a stepping stone towards explaining anomalous properties of solids in general and itinerant magnets in particular. Neutron scattering experiments are currently underway, targeted towards fully understanding the dimensionality of spin fluctuations and Fermi surface evolution as a function of Sc doping. However, possible complications may arise due to the small ordered moment of these weakly antiferromagnetic materials along with polycrystalline sample form, making single crystal synthesis highly desirable. Further doping experiments can elucidate the role of spin fluctuations, in particular it has been noted that 2D systems are more favorable for spin fluctuation-induced superconductivity, as compared with the 3D candidates [370]. This may potentially shed light on the intimate relation between

antiferromagnetism and d -wave superconductivity [391]. In general, it is commonly accepted that the comprehensive understanding of antiferromagnetic quantum phase transitions is essential for studying unconventional superconductivity [182]. It has also been suggested that the mechanism of the antiferromagnetic spin density wave quantum critical point is relevant to the heavy fermion quantum critical points, the description of which is still incomplete [77, 267]. Moreover, a detailed analysis of antiferromagnetic spin fluctuations for systems close to a quantum critical point could provide a microscopic mechanism for the marginal Fermi liquid [30, 388].

Mechanical Properties of Ti-Au Alloys

The search for new hard materials is often challenging from both theoretical and experimental points of view. Furthermore, using materials for biomedical applications calls for alloys with high biocompatibility which are even more sparse. The $\text{Ti}_{1-x}\text{Au}_x$ ($0.22 \leq x \leq 0.8$) alloys exhibit extreme hardness values, elevated melting temperatures (compared to those of constituent elements), reduced density compared to Au, high malleability, bulk metallicity, high biocompatibility, low wear, reduced friction, potentially high radio opacity, as well as osseointegration. All these properties render the $\text{Ti}_{1-x}\text{Au}_x$ alloys particularly useful for orthopedic, dental, and prosthetic applications, where they could be used as both permanent and temporary components. Additionally, the ability of $\text{Ti}_{1-x}\text{Au}_x$ alloys to adhere to ceramic parts could reduce the weight and cost of these components.

8.1 Introduction

Hardness is generally understood as a measure of resistance that a material offers against penetration by another object. Often, hardness is closely related to the response of surfaces to wear and the effectiveness of various tools, making hard materials highly utilized and valued by many industries. Advances of material science in this area have played an important role in the progress of civilization, from the first tools fashioned out of bone to chemically vapor deposited diamonds [134]. A good example is evolution of the cutting speed with hardness, shown in Fig. 8.1.

While diamond is certainly the hardest known material, it is not applicable everywhere; for example it is not effective for cutting ferrous metals, such as steel, because of a chemical reaction that produces iron carbide [189]. Other synthetic materials must be produced under high pressure and temperature, thus making the search for new hard materials not only scientifically interesting but also technologically useful.

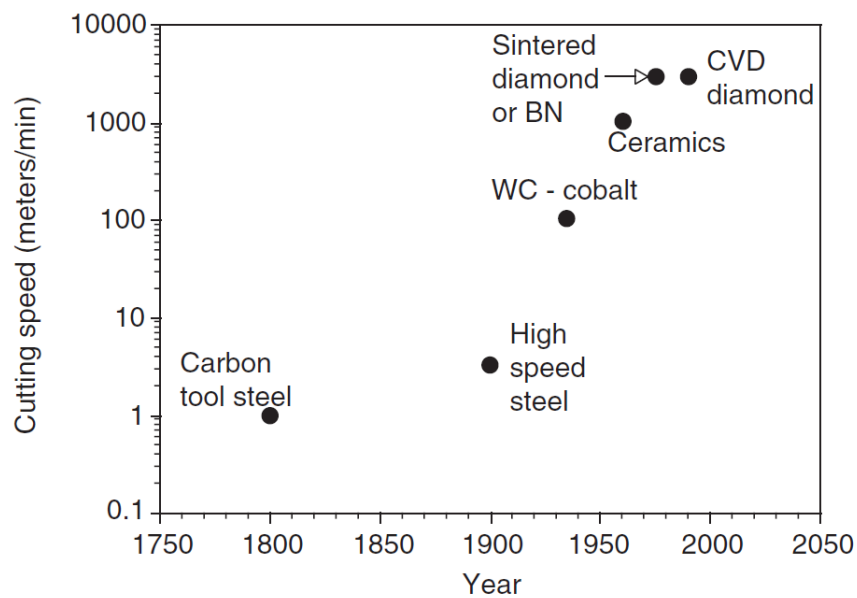


Figure 8.1: Cutting speed as a function of time [134].

8.2 Material Selection and Ashby Diagrams

Material selection is a significant part in the process of designing any physical object. This task becomes more involved given the large number of available materials and their properties. Out of all mechanical and thermal properties, about 30 are most important for both material characterization and engineering design [26]: hardness, strength, density, price, wear rate, melting point, thermal conductivity, electrical resistivity and such. In most cases, the performance of a component depends on a combination of material's properties. This suggests the idea of plotting properties against one another, so the materials may be separated into classes and families, now referred to as Ashby diagrams [26]. Examples of such Ashby diagrams include Young's modulus *vs.* density (Fig. 8.2(a)), strength *vs.* density, fracture toughness *vs.* Young's modulus, thermal conductivity *vs.* electrical resistivity, wear rate *vs.* hardness, and strength *vs.* relative cost (Fig. 8.2(b)). The underlying microstructure, shared by materials from the same family (*i. e.* ceramics, metal polymers, *etc.*), forces them to cluster together on the Ashby diagram. The elongated bubbles are the result of heat treatment and mechanical working, often used to alter physical properties of a material [26].

The Ashby diagrams condense a lot of information into a manageable form, aiding with material selection as well as further material development [26]. All Ashby diagrams have parts that are not populated with materials. While some empty regions can be explained by fundamental causes such as atom sizes and binding, there are regions that, in principle, should be accessible [26]. The new materials that belong to those regions will open new design possibilities.

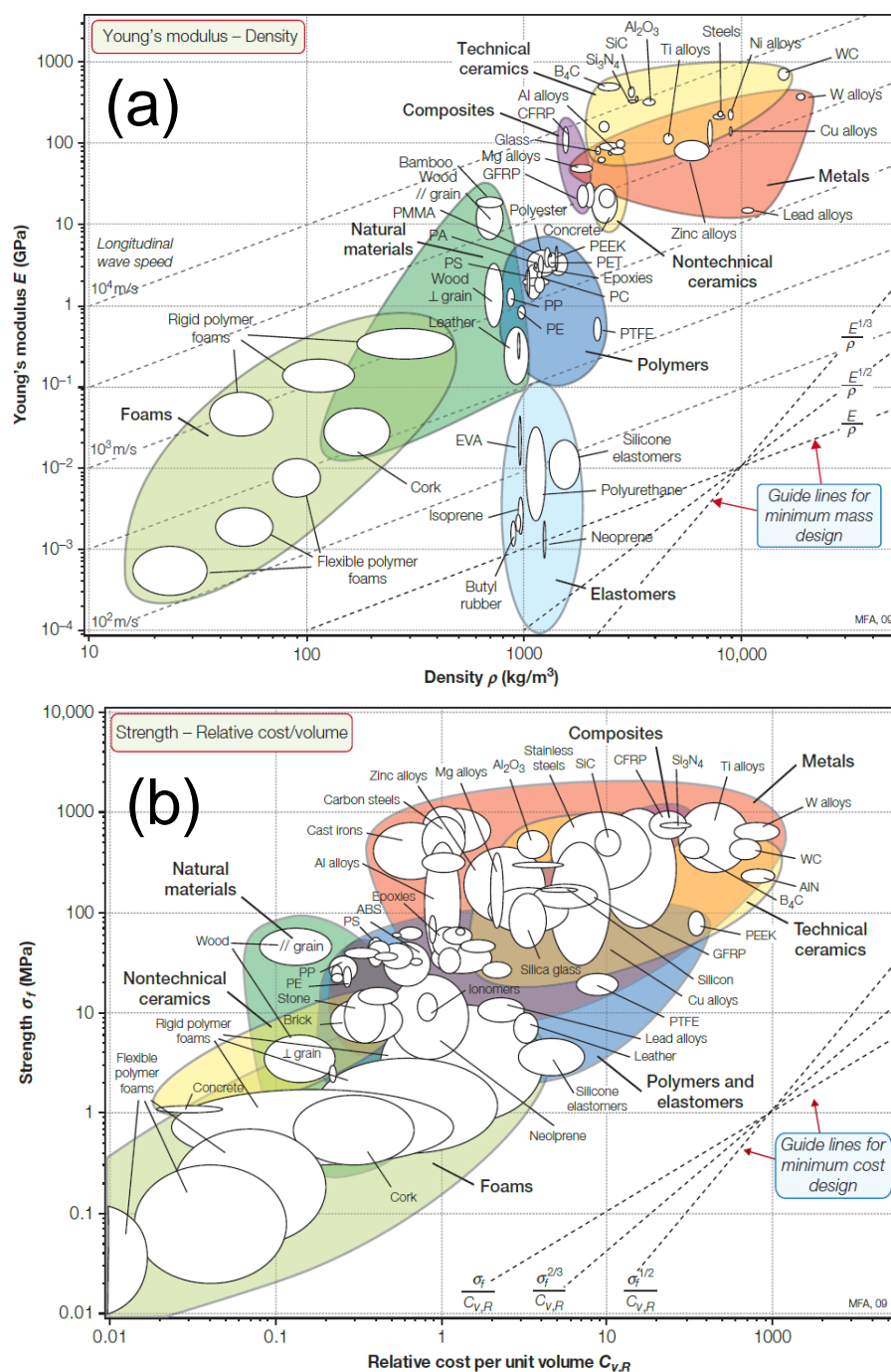


Figure 8.2: An example of Ashby plots [26] for (a) Young's modulus *vs.* density and (b) strength *vs.* relative cost per unit volume. The guide lines are used to select materials better suited for minimum weight design and minimum cost for desired strength, respectively.

8.3 Designing and Improving Hard Materials

Even though the physical difference between a hard and a soft material is intuitively simple and can be quantified by measurement rather easily, no model exists for predicting hardness of a given material [134]. In crystalline compounds, mechanical hardness is a direct consequence of the chemical structure, atom packing, and bond type, with the latter being the most important. For example, it is the strong covalent bonding in three dimensions that gives diamond its superior hardness properties. A clear dependence of hardness on the type of chemical bonding as well as the crystal structure can be seen from Table 8.1 [157, 333], for all Mohs's scale standards. As bonding changes from ionic (weak) to covalent (strong), hardness increases. Atom configurations with higher symmetry and packing coefficients also lead to increased hardness.

While covalent bonds in minerals such as diamond and corundum are strong, in metals, the bonds are generally weaker, as showcased by soft high purity crystals [134]. However, more factors are at play for alloys. For example, a common

Table 8.1: Crystal structure for the Mohs's scale reference materials [157, 333].

Mohs's Hardness	Reference Mineral	Chemical Composition	Crystal Lattice Type	Type of Bonding
1	Talc	$\text{Mg}_3\text{Si}_4\text{O}_{10}(\text{OH})_2$	Monoclinic	Ionic
2	Cement	$\text{CaSO}_4 \cdot 2\text{H}_2\text{O}$	Monoclinic	Ionic
3	Calcite	CaCO_3	Trigonal or hexagonal	Ionic
4	Fluorite	CaF_2	Cubic	Ionic
5	Apatite	$\text{CaF}(\text{PO}_4)_3$	Trigonal or hexagonal	Ionic
6	Orthoclase	KAlSi_3O_8	Monoclinic lattice	Ionic
7	Quartz	SiO_2	Trigonal or hexagonal	Covalent
8	Topaz	$\text{Al}_2\text{F}_2\text{SiO}_4$	Orthorhombic	Covalent
9	Corundum	Al_2O_3	Trigonal or hexagonal	Covalent
10	Diamond	C	Cubic	Covalent

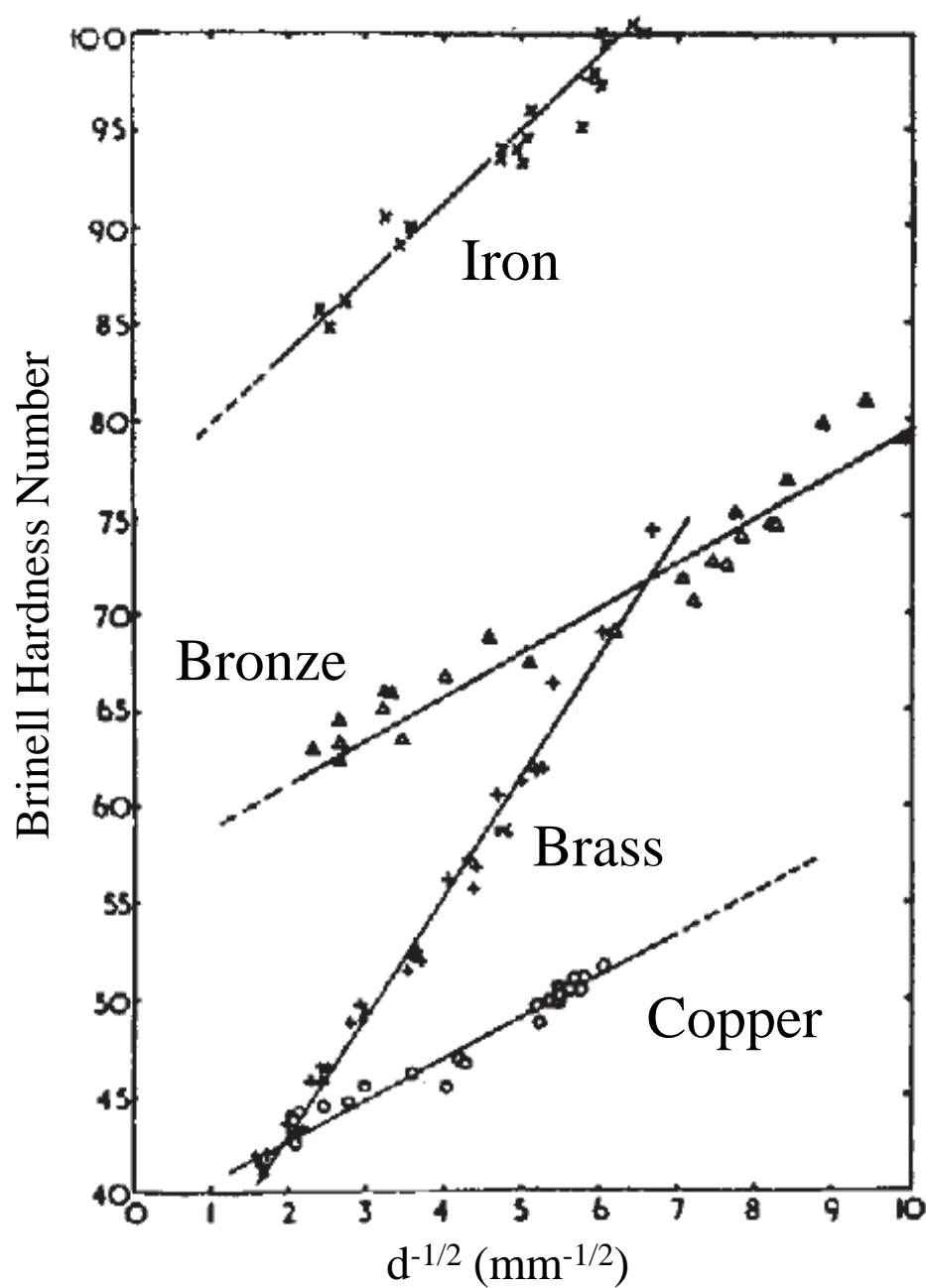


Figure 8.3: Hardness as a function of inverse grain diameter d for various metals and alloys [147].

property widely observed in metallurgy is the increased hardness of metallic alloys as compared with that of the constituent elements, hence the addition of foreign elements to a metal, such as carbon to iron [85]. The increase in hardness happens because forces between similar sized atoms are smaller than those between atoms of a different size [157]. The hardness of a metal also depends on the grain size: the smaller the grain size, the higher the hardness (Fig. 8.3) [147, 157]. This fact has been attributed to the number of grain boundaries, which act as barriers to dislocation motion, strengthening the material [134]. Moreover, homogeneous materials with small grain sizes lack defects and dislocations, which are usually required for a deformation to occur. Exceptionally high-hardness metals exhibit grain sizes in the nm range [157].

In efforts to increase hardness, cold working (also known as work hardening or strain hardening) is frequently implemented. The process entails deforming the material, usually by rolling at room temperature, which results in the increase of dislocations [58]. Moreover, the grains become distorted, trying to align with the direction of rolling, and eventually fracture into even smaller grains. This process has its drawbacks - while the hardness and strength are increased, ductility decreases and preferred orientation emerges [58]. The solution is to subject the material to annealing, a heat treatment at an elevated temperature for an extended period of time, followed by slow cooling. The increase in thermal energy, brought on by elevated temperature, reduces the energy stored in the material by applied deformation [58]. The annealing process (Fig. 8.4) is usually understood in terms of three stages:

1. **Recovery:** the name refers to the recovery of the original physical properties observed before cold working. During this step the internal strain and residual stress are relieved as the dislocations rearrange into lower-energy configurations. Moreover, the excess point defects such as vacancies are annihilated. Since grain

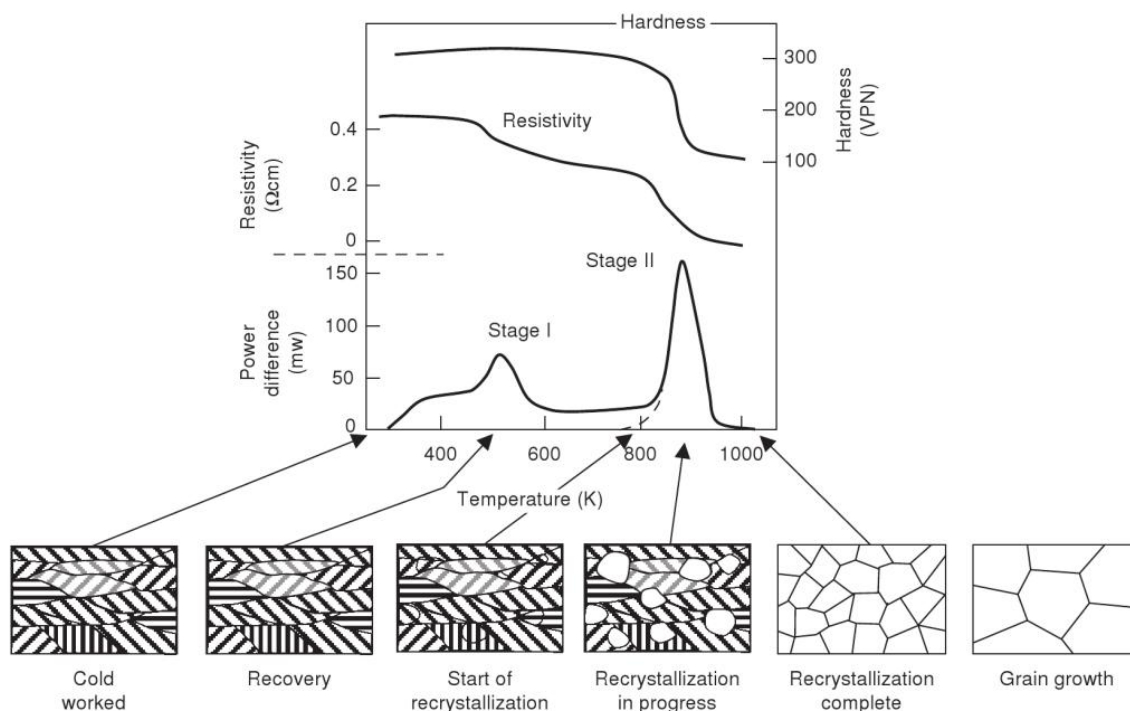


Figure 8.4: An example of an annealing process for cold-worked nickel [58,334]. The energy released on annealing was compared with that of a non-deformed sample.

orientations, shapes and sizes remain the same, the strength and ductility are not affected.

2. **Recrystallization:** this is a process of nucleation and growth of new grains when the badly deformed grains are replaced by the strain-free ones with new orientation, shape and size. Therefore, the strength is decreased and ductility is increased, returning to the pre-cold-working values. The rate of recrystallization depends largely on the temperature, duration, the purity of the specimen, the original grain size, and, most importantly, the degree of cold work.
3. **Grain growth:** this is an undesirable process given that increased grain size leads to decreased strength. The process involves migration of grain boundaries - grains with 6 or more sides grow at the expense of other ones.

When two or more materials are combined in the melt, additional steps in

the process of heat treatment need to be taken is order to optimize the mechanical properties. A method known as precipitation hardening is commonly used in magnesium, aluminum, beryllium-copper alloys, stainless steels, and nickel-base superalloys to significantly enhance hardness [58]. During precipitation hardening small particles (for example particles of carbon in steels) are dispersed throughout the matrix, creating a barrier against dislocations and providing resistance to slip, thus increasing overall hardness and strength. It has been determine that for optimal results, particles should be as hard as possible and the matrix should be soft and ductile [58]. Moreover, the particles should be spherical rather than needle-like, as small as possible, well-separated, and large in number. Similar to the treatment method described above for pure metals, alloys undergo a number of heat treatments to improve hardness and ductility:

1. **Solution annealing:** this initial step is aimed at producing a supersaturated metastable solid solution. The material is heated below the melting temperature (0.5 of T_m) for a short period of time ($2 - 4$ min/cm³), long enough to ensure a nearly homogeneous solid solution *via* diffusion. The profile temperature needs to be carefully selected so as to dissolve maximum amount of solute while preventing grain boundaries from melting. Solution annealing is commonly used in steels [58] to improve the distribution of carbides and thus hardness [68]. For non-ferrous alloys this is the first step in the hardening process.
2. **Quenching:** the temperature of the specimens is rapidly decreased to room temperature [68], preserving the supersaturated solid solution. Rapid quenching often results in high residual stresses and distortion, which is often accounted for by carefully selecting the quenching medium (water and other aqueous solutions, oil, air, glycol). After this step, materials are very ductile, thus forming into a desired part or straightening of metal sheets are conducted as soon as possible

after quenching.

3. **Aging:** a precipitate is formed from the alloying element, increasing strength and hardness dramatically [58]. The aging process is classified into two types: artificial, which requires reheating to a temperature well below melting (0.3 of T_m), and natural, which takes place at room temperature ($T = 27\text{ }^{\circ}\text{C}$). Since aging significantly increases hardness, straightening and forming need to be completed prior to precipitation. The solution is to suppress the natural aging by treatment at low temperatures (about $-18\text{ }^{\circ}\text{C}$) for several days.

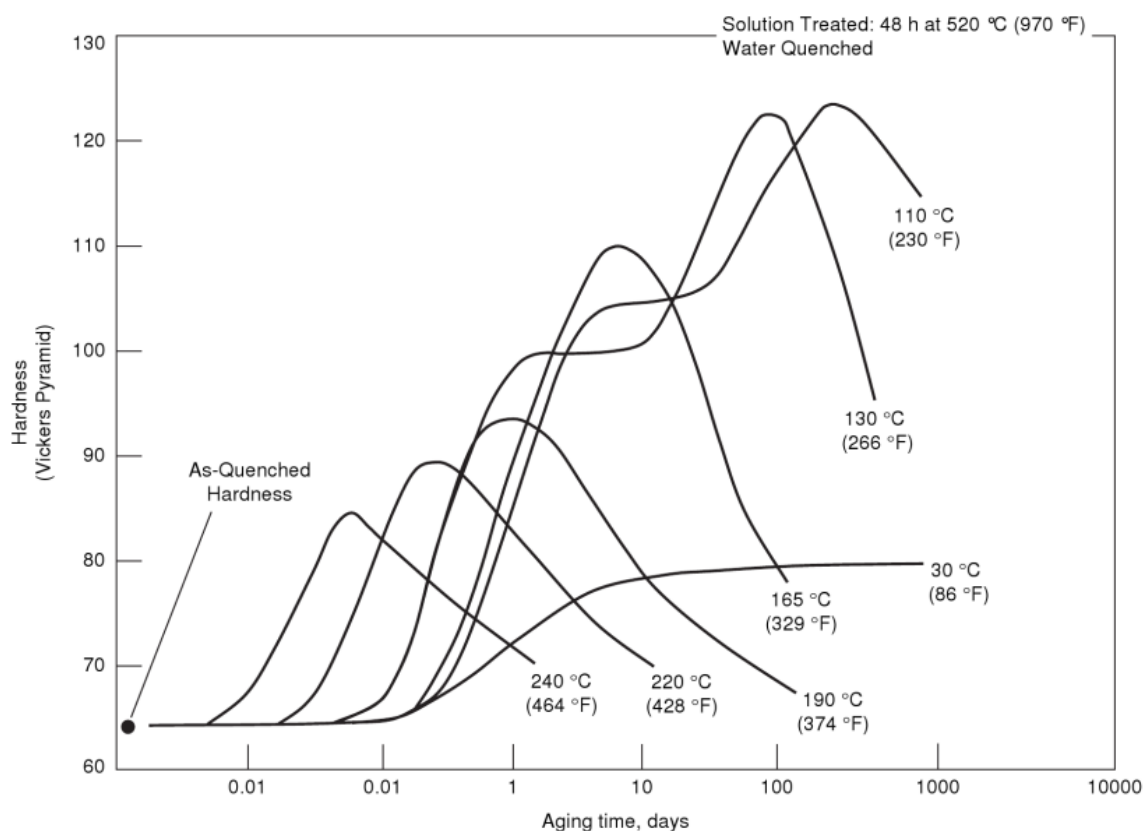


Figure 8.5: The effects of various precipitation hardening methods on hardness of the Al-4%Cu alloy [58]

Numerous studies have been conducted in efforts to perfect precipitation hardening for commercially available alloys. The drastic differences in hardness result from changing one or more parameters of the treatment, as can be seen from Fig. 8.5. Ad-

ditionally, a number of properties besides hardness can also be affected by the above process: tensile strength, formability, corrosion resistance, exfoliation corrosion, ductility, and stress resistance.

Many other heat treatment methods aim to improve other mechanical properties of alloys [58]:

1. **Tempering** requires heating to an intermediate temperature in an aim to improve ductility. It is most often used in steels which are too brittle to be used for most applications. While tempering significantly improves ductility and toughness, the hardness and strength are diminished.
2. **Oxide dispersion strengthening** yields higher strength materials due to the addition of oxides (yttria, alumina and others) during alloying.
3. **Differential hardening** employs different heat treatments for different parts of a single object. By using an insulation layer, only certain areas are left exposed to fully harden. This process is commonly used for knives and swords.
4. **Surface hardening:**
 - **Induction hardening:** a no-contact induction heating increases surface temperature very quickly. Consequent quenching results in a very hard, wear-resistant surface layer of martensite.
 - **Flame hardening** results in a layer of martensite being formed on top of a softer interior core. This process is mostly used for steels.
 - **Case hardening** is a thermochemical diffusion process during which atoms of carbon and nitrogen are absorbed by the outermost surface layer. Depending on the materials, this process is often referred to as carburizing, cyaniding, nitriding and carbonitriding.

5. **Cryogenic treating** requires cooling to extremely low temperatures (-192 °C) in order to improve hardness and wear resistance. It is usually only effective for materials that contain more than 10% austenite after quenching [68].

8.4 Properties of Ti and its Alloys

Titanium possesses high strength (Titans of Greek mythology are the inspiration behind the name) and low density, which has paved its way into a variety of fields. Like many other materials, Ti occurs in two different crystallographic structures, with a structural transition between two occurring at 882 °C in the pure metal. Below this temperature, Ti has a hexagonal close packed structure (α -Ti, $P6_3/mmc$ space group) while above it the structure is body centered cubic (β -Ti, $Im\bar{3}m$ space group). When selecting a Ti alloy for a certain application, it is important to differentiate between three main groups of titanium alloys [233]:

1. Hexagonal α alloys weld well, have low to medium strength, good toughness and ductility. While these alloys can be stress relieved and annealed, aging, solution treatment, quenching or any other heating methods do not affect the strength.
2. $\alpha - \beta$ alloys exhibit medium to high strength levels, respond well to heat treatment and are generally rather weldable. This type of Ti alloys is the most common one.
3. Cubic β alloys have high strength and are readily affected by heat treatment. Both stress-relieving and aging are very effective in improving the overall hardness.

The transition temperature between α - and β -Ti can be altered by either doping or heat treatment [233]. If the additive element increases the transition tem-

perature, it is referred to as the α -stabilizer. Some examples include Al, O, N, Sn, Zr and C. Similarly, β -stabilizers such as Cr, Mn, Fe, Mo, Nb, V, Ta, H and Au, decrease the transformation temperature. Most often, the β phase is sought after due to its superior strength values, hot and cold working properties and susceptibility to heat treatment [233]. To further improve the strength of Ti alloys, solution treating and aging are commonly implemented [398], as can be seen from Table 8.2.

Table 8.2: Temperature range and time typically used for stress relief in Ti and Ti-based alloys [307].

Ti Phase	Alloy	Temperature range (°C)	Time (hours)
	Pure Ti	480-590	1/4 - 4
α alloys	Ti-8Al-1Mo-1V	590-700	1/4 - 4
	Ti-6Al-2C-1Ta-0.8Mo	600-650	1/4 - 2
$\alpha - \beta$ alloys	Ti-6Al-4V	485-645	4 - 4
	Ti-3Al-2.5V	540-650	1/2 - 2
	Ti-8Mn	480-590	1/4 - 2
β alloys	Ti-13V-11Cr-3Al	710-730	1/2 - 1/4
	Ti-10V-2Fe-3Al	680-700	1/2 - 2

In addition to numerous applications in the industrial, automotive and aerospace fields, Ti has been widely used for implant devices that replace patients' hard tissues [105, 327]. After a number of toxic effects were reported in permanent implants [105], the use of V- and Al-containing Ti alloys was discontinued. A number of *in vivo* and *in vitro* experiments with various grades of Ti concluded that commercially pure Ti is a highly biocompatible material [105, 179] due to the spontaneous build-up of an inert and stable oxide layer. Additional properties that make Ti suitable for biomedical applications include low electronic conductivity, low ion-formation levels in aqueous environments, low pH value and dielectric constant, comparable to that of water [105]. Moreover, Ti is one of a few materials capable of osseointegration - mechanical retention of the implant by the host bone tissue - which stabilizes

the implant without any soft tissue layers between the two [52]. That is why Ti has been widely used for devices such as artificial knee and hip joints, screws and shunts for fracture fixation, bone plates, pacemakers and cardiac valve prosthesis that require high biocompatibility and corrosion resistance as well as high strength and low density [240, 317]. Not surprisingly, the dental applications of Ti are just as common for implants and their components, inlays, crowns, overdentures, and bridges [67, 105, 192, 193, 392]. The one drawback is the poor machineability of pure Ti, which reduces tool life, increases the processing time and is problematic when the elimination of a dental Ti prosthesis is necessary [278, 290]. This can be improved by adding a softer material to Ti. The addition of Ag and Cu has been rather successful in improving hardness and machineability of Ti [195–197, 363]. Since both of the dopants are α -stabilizers, α -Ti was produced. It can be expected that, if it were possible to form the equivalent β -Ti alloys, its hardness may increase β [362]. Au, which is located in the same group as Ag and Cu, is likely to increase the hardness, given that it is a β -stabilizer. Moreover, the high biocompatibility and corrosion resistance of Au may yield an alloy suitable for biomedical purposes [192]. While the machineability would decrease with increased hardness, the relatively low melting temperatures of Ti-Au alloys will allow for the majority of parts to be used in as-cast form.

Additionally, pure Ti is not strong enough for a number of medical devices [107, 159], calling for the development of a more superior alloy [152, 222, 290, 361, 363]. While hardness can be improved by alloying Ti with another element [105], care must be taken to preserve biocompatibility. Presently, only a two-fold increase in hardness has been possible in Ti [195–197, 363], achieved by alloying it with Cu or Ag. Using an alloying element with the same valence electron number as Cu and Ag, but with higher density, will result in a higher valence electron density of the alloy, which will likely lead to higher bond strength, and, consequently, higher hardness [123, 145]. This

immediately identifies Au as a suitable alloying candidate for increasing hardness. An already wide use of Au and Au-doped implant devices [111,122,164,364] ensures biocompatibility and corrosion resistance [192]. Furthermore, the ability of these alloys to adhere to a ceramic surface [111,351] along with a reduction in density upon dilution of Au with Ti can lessen overall weight and cost of medical components.

8.5 Ti - Au Alloys

8.5.1 Previous Work: From Dental Implants to "Iron Man"

While the rarity of gold has secured its position as the world's main currency for many centuries, its role in technology has been rather small. High biocompatibility, corrosion resistivity, and the melting temperature of pure Au make it extremely well suited for dental applications; however it is too soft and expensive to be used for components on its own [111]. In past studies, it was observed that the addition of small quantities of Ti ($< 10\%$ Ti) into pure Au improved the overall hardness [111,122,164,364] and corrosion resistance [111]. The enhanced hardness is particularly useful for jewelry, minting [122] and integrated circuitry [164] applications, diminishing the wear of these components. Additionally, the Ti-Au alloy can adhere to a ceramic surface, making it convenient for a number of biomedical applications, reducing the overall weight and cost of the corresponding parts [111,351]. The appeal of Ti-Au alloys for strength applications has even been acknowledged by the movie industry, listing the Ti-Au alloy as the material for Iron Man's face mask [1].

As for the Ti-rich Ti-Au alloys, the mechanical properties and grindability were also previously examined in search for the optimal dental alloy [362]. Despite the fact that Au is a β -stabilizer in Ti, it has been observed that the alloys (60 – 95% Ti) form two microstructures: α Ti and a mixture of α Ti and Ti_3Au . Higher

Ti concentrations were not attempted since it was believed that the intermetallic compound Ti_3Au caused the 60% Ti alloy to become brittle [362]. However, the Young's modulus increased as the concentration of Ti decreased to 60% possibly because of the Ti_3Au precipitation. The Young's moduli of the Ti-Au alloys are higher than those typically used for dental applications [362].

8.5.2 Current Study

Biomedical applications of the alloys from both Ti-rich and Au-rich sides of the Ti-Au phase diagram were previously explored in detail [102, 111, 362, 363]. While hardness values were increase in both regions, the effect was comparable to that seen in Ti-Ag and Ti-Cu systems. Interestingly enough, hardly anything has been reported on the hardness of intermediate compositions. In this manuscript, a series of $\text{Ti}_{1-x}\text{Au}_x$ ($0.22 \leq x \leq 0.8$) alloys was prepared, spanning the whole composition range. A remarkable nearly four-fold increase in hardness, as compared to pure Ti, is registered for the $\text{Ti}_{0.75}\text{Au}_{0.25}$ alloy, placing the hardness of this material above that of most biocompatible alloys currently used in the medical field [26]. The coefficient of friction and, consequently, wear rates, of this material are improved significantly in comparison with Ti, suggesting longer component life and less debris accumulation. These properties indicate that the $\text{Ti}_{0.75}\text{Au}_{0.25}$ alloy is suitable for a number of biomedical applications, particularly where Ti is already employed [67, 105, 192, 193, 240, 317, 392].

As mentioned above, hardness measurements reveal a non-monotonous change of hardness with x – the hardness reaches maximum values for $0.22 \leq x \leq 0.35$ (Fig. 8.7, red symbols). Those values are up to three or four times higher than that of pure Ti. Among surveyed nominal compositions, the $x = 0.25$ alloy exhibits the highest hardness value of ≈ 800 HV, higher than that of pearlitic steels [149, 305] and similar to both drawn pearlite and high carbon martensitic steels [85]. While

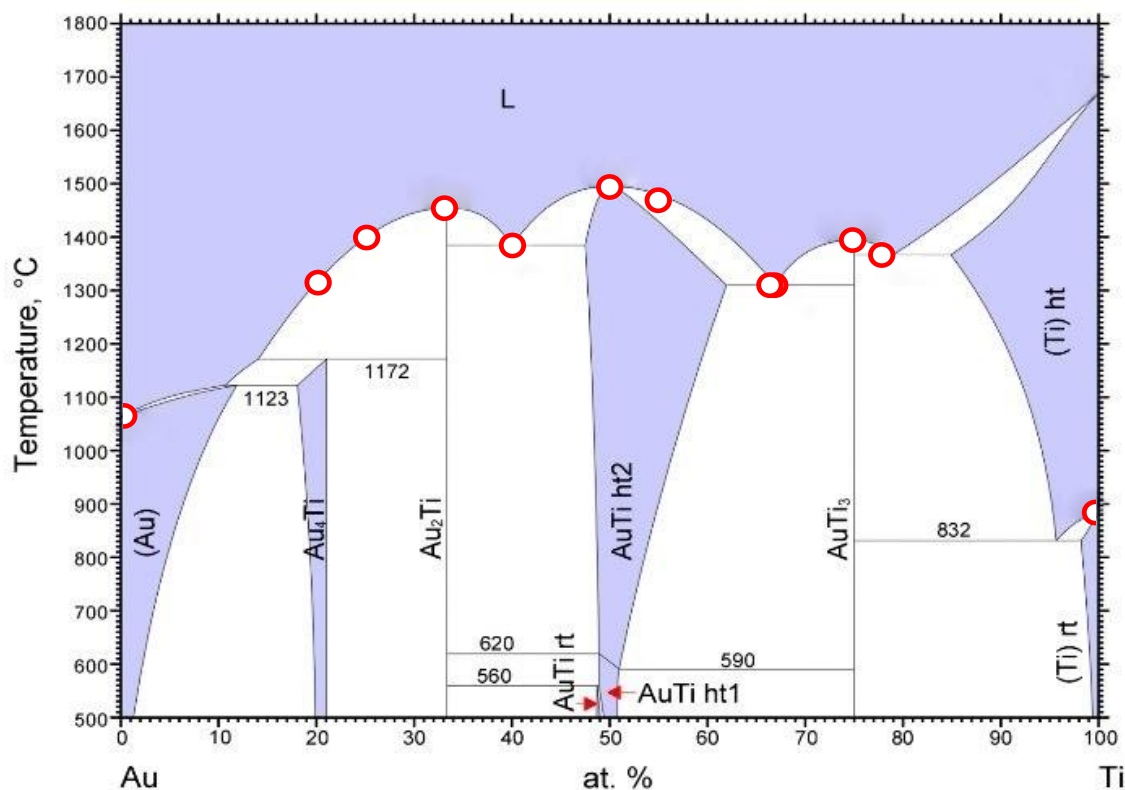


Figure 8.6: Binary phase diagram of Ti-Au with the open circles representing the compositions of the $\text{Ti}_{1-x}\text{Au}_x$ alloys for the current study ($0 \leq x \leq 1$) [389].

other metallic alloys such as WC, cBN, and high-carbon steels show higher hardness values, they are often not desirable for medical applications due to high toxicity. As mentioned above, both Ti and Au are biocompatible and have high resistance to *in vivo* corrosion, suggesting that the resulting alloys are suitable for biomedical applications [105, 179, 192]. In order to compare hardness and density of $\text{Ti}_{1-x}\text{Au}_x$ alloys with those of materials typically used for medical applications, an hardness *vs.* density diagram [26] was constructed (Fig. 8.7). As can be seen, $\text{Ti}_{0.75}\text{Au}_{0.25}$ offers a nearly four-fold increase in hardness while the density is comparable to commonly used implant materials. Moreover, it was noticed that melting $\text{Ti}_{1-x}\text{Au}_x$ samples in Al_2O_3 crucibles resulted in the intermetallic alloy adhering to the walls of the container. This property can reduce both the weight and cost of medical components

even further, if $\text{Ti}_{1-x}\text{Au}_x$ material is used as a coating for a ceramic part. Moreover, the values of the melting temperatures T_m for the $\text{Ti}_{1-x}\text{Au}_x$ alloys [389], are lowered upon Ti dilution with Au. The reduction in the melting temperature will allow for the preparation of components *via* casting, avoiding costly machining process [196].

A full theoretical understanding of the hardness mechanism remains challenging due to the inherent complexity and large number of parameters that affect it [70].

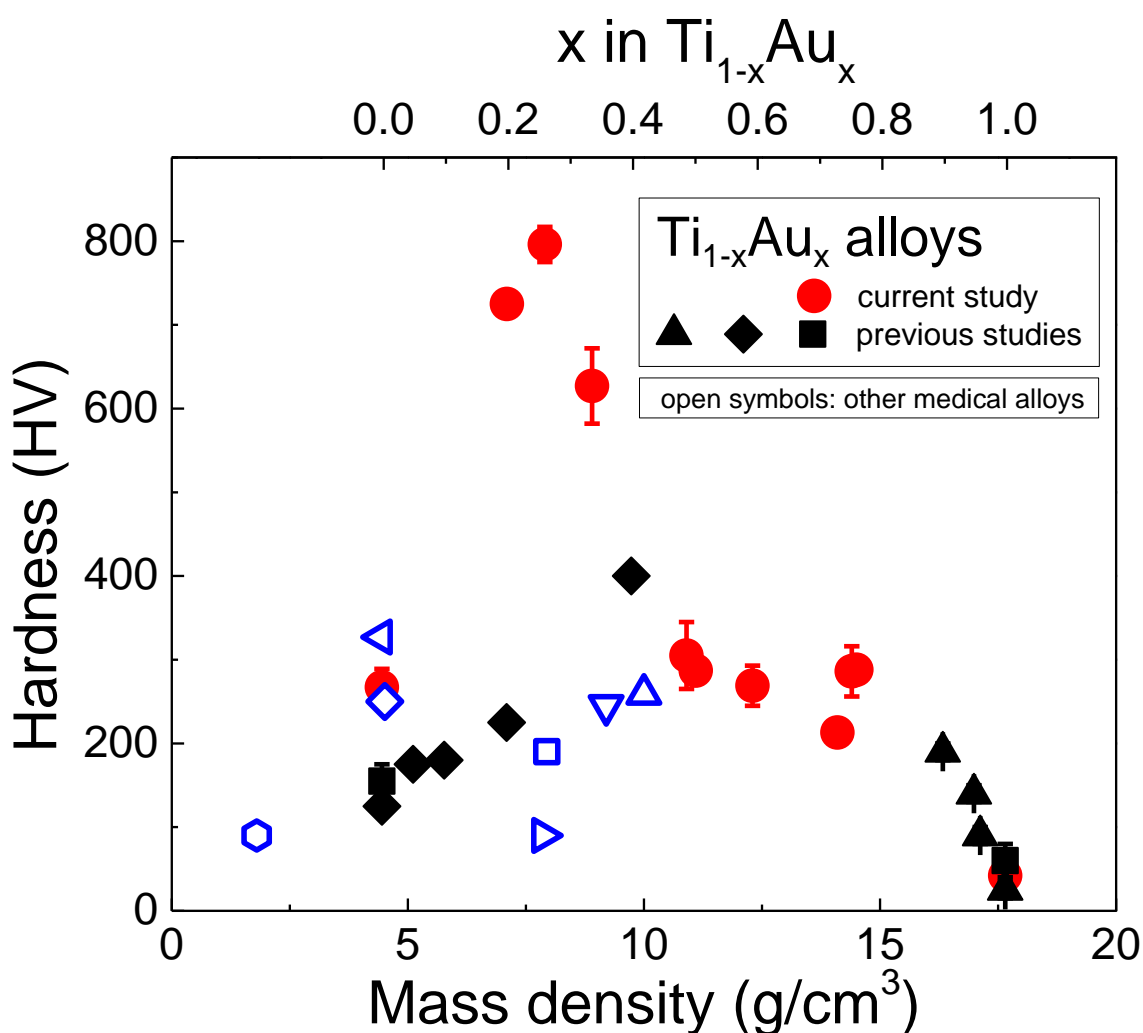


Figure 8.7: Hardness as a function of composition (top axis) and density (bottom axis) for $\text{Ti}_{1-x}\text{Au}_x$ and other medical alloys. Current study is represented by red circles. Previous studies of $\text{Ti}_{1-x}\text{Au}_x$ alloys are shown in full black symbols while other medical alloys are represented by open symbols.

Table 8.3: Summary of parameters for as-cast $\text{Ti}_{1-x}\text{Au}_x$ alloys.

x	Melting temperature T_m [389] (°C)	Mass density ρ (g/cm ³)	As-cast hardness (HV)
0	882	4.5	267 ± 22
0.22	1367	7.1	725 ± 12
0.25	1395	7.9	796 ± 21
0.33	1310	8.9	627 ± 45
0.45	1470	10.9	305 ± 40
0.50	1495	11.1	287 ± 9
0.60	1385	12.3	269 ± 24
0.67	1455	14.1	213 ± 5
0.75	1400	14.4	286 ± 30
0.80	1315	14.5	288 ± 8
1.00	1064	17.7	42 ± 4

In alloys, hardness is determined by the underlying crystal structure [123], making structural analysis of high importance. As summarized in Table 8.3, SEM and XRD analysis clearly indicate that all of the samples are composed of multiple phases. In $\text{Ti}_{0.75}\text{Au}_{0.25}$, the XRD analysis (Fig. 8.8(c)) revealed that the majority phase is $Pm\bar{3}n$ Ti_3Au and the minority phase is $Pm\bar{3}m$ Ti_3Au , accompanied by minor inclusions of αTi . Samples studied with scanning electron microscopy (SEM) were polished and examined in a field emission gun scanning electron microscope Zeiss 1540 esB. Samples for transmission electron microscopy (TEM) analysis were prepared *via* grinding and ion milling. The microstructures of the samples were investigated by a probe aberration corrected JEOL-JEMARm200cF at 200 kV. Microstructural TEM data are consistent with XRD results (Fig. 8.8(a)), indicating that during the solidification, intermetallics with chemistry close to $\text{Ti}_{0.75}\text{Au}_{0.25}$ form dendritic structure first, rejecting the Ti to the liquid between the dendrites. At lower temperature, solid solution of Ti is formed between the dendrites. TEM bright field image of the $\text{Ti}_{0.75}\text{Au}_{0.25}$ sample is shown in Fig. 8.8(b), consistent with the SEM data – the darker features in

Fig. 8.8(b) correspond to α Ti, which are marked by arrows in Fig. 8.8(a). This dendritic nature of Ti has also been observed in Ni-treated Ti [271], with higher hardness corresponding to the dendritic regions of the alloy.

The lifetime of a medical component within live tissue is determined by the wear rate with which it degrades. In particular, knee and hip replacements can only last on the order of a decade, making additional component replacement necessary [26]. Tribological experiments were conducted using a pin-on-disk tribometer (CSM Instruments). The diamond-SiC disk was selected for its durability. The ingot samples of $\text{Ti}_{1-x}\text{Au}_x$ ($x = 0.25, 0.3$ and 0.50) were used as a pin with a Ti ingot used as a reference. An example of the $\text{Ti}_{0.75}\text{Au}_{0.25}$ sample used for wear tests is shown in the inset of Fig. 8.9(a). In order to simulate wear during walking, a linear reciprocal motion was used with a sliding speed of 3.15 cm sec^{-1} and an applied load of 2N. The sliding distance of wear tests was set at 4 mm per stroke, with the total of 40 000 cycles. A synthetic body fluid was used as the test medium. Details of wear of diamond-SiC disk have been reported previously [405–407]. Comparison of the time-dependent coefficient of friction for $\text{Ti}_{1-x}\text{Au}_x$ ($x = 0, 0.25, 0.30$ and 0.50) alloys is shown in Fig. 8.9(a). The reference sample is Ti (black) with an average coefficient of friction (COF = 0.35) persistent for about 700 seconds. All of the $\text{Ti}_{1-x}\text{Au}_x$ alloys show $\text{COF} < 0.1$ after an initial running-in period of 100 seconds. These results indicate that the addition of Au to Ti is effective in reducing friction in $\text{Ti}_{1-x}\text{Au}_x$ alloys. Wear volumes of the $\text{Ti}_{1-x}\text{Au}_x$ pin and a diamond disk composite are shown in Fig. 8.9(b). To identify the wear modes, SEM analysis was conducted, with the pin and disk results shown in Fig. 8.10. In the SEM images of the wear of $\text{Ti}_{1-x}\text{Au}_x$ and SiC, the bright and groove-like features correspond to abrasion (from diamond grits) while the darker spots result from adhesion wear. The wear of SiC is also reduced for $\text{Ti}_{1-x}\text{Au}_x$ alloys as compared with Ti. This is consistent with the results in wear volume of both pin and disk as well, summarized in Table 8.3.

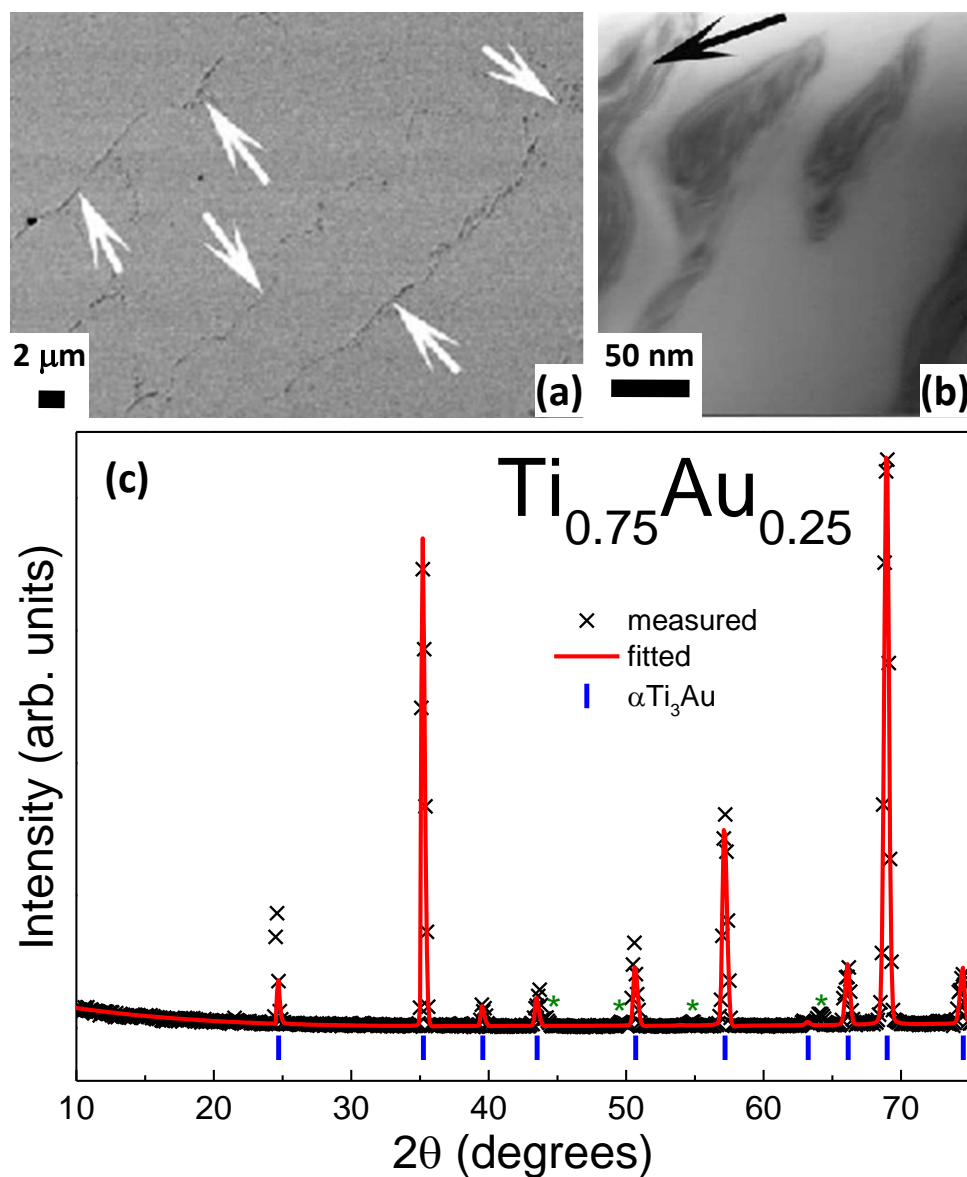


Figure 8.8: (a) In an SEM image, arrows indicate second phase particles which form between the dendrites of the material. Those particles are a Ti-rich solid solution. (b) The dark contrasted features in the TEM bright field image are the second phase Ti particles, one of which is indicated by an arrow. (c) X-ray diffraction pattern indicates that the $\alpha\text{-Ti}_3\text{Au}$ phase (blue vertical symbols) main phase accompanied by small inclusions of $\beta\text{-Ti}_3\text{Au}$ and $\alpha\text{-Ti}$ (marked by asterisks).

The stabilization of Ti by Au is indicated by the reduced adhesion of the $x = 0.50$ sample. The SEM and TEM images, shown in Fig. 8.8(a) and (b), indicate the secondary Ti-rich solid solution, thus the adhesion is Ti or Ti-rich. The wear modes on the pin (Fig. 8.10, images on the left) are given in Table 8.3 for all samples. The $\text{Ti}_{1-x}\text{Au}_x$ alloys have some features shown that seem to be worn less. Those are likely the microstructural hardening of the matrix. These features are more pronounced in the $\text{Ti}_{0.75}\text{Au}_{0.25}$ sample. The disk wear (Fig. 8.10, images on the right) show visible flattened diamond grits that indicate tribochemical interactions. This is, however, only true for Ti (Fig. 8.10(b)) rather than $\text{Ti}_{1-x}\text{Au}_x$ alloys (Fig. 8.10(d), (f) and (h)).

For metallic materials, the valence electron density (VED) has been suggested to improve phase stability, and, therefore, hardness [123, 145]. The VED value for Ti_3Au is 0.2 \AA^{-3} , which is higher than that of any other Ti-Au binaries (Table 8.6). Another possible origin of high hardness in $\text{Ti}_{0.75}\text{Au}_{0.25}$ is the reduction in the density of states (DOS) at the Fermi level (E_F), which has been referred to as a pseudogap [241, 257]. If such a pseudogap is formed across the Fermi level,

Table 8.4: Summary of composition analysis for as-cast $\text{Ti}_{1-x}\text{Au}_x$ alloys.

x	Phase(s) determined	
	from TEM	from XRD
0.22	$\text{Ti}_3\text{Au} + \alpha\text{Ti}$	$\alpha\text{Ti}_3\text{Au} + \alpha\text{Ti}$
0.25	$\alpha\text{Ti}_3\text{Au}$	$\alpha\text{Ti}_3\text{Au} + \beta\text{Ti}_3\text{Au} + \alpha\text{Ti}$
0.33	$\text{Ti}_3\text{Au} + \text{TiAu}$	$\alpha\text{Ti}_3\text{Au} + \beta\text{Ti}_3\text{Au} + \beta\text{TiAu}$
0.45		$\beta\text{TiAu} + \alpha\text{Ti}$
0.50	$\beta\text{TiAu} + \text{Ti}$	$\beta\text{TiAu} + \alpha\text{Ti} + \beta\text{Ti}_3\text{Au}$
0.60	$\text{TiAu} + \text{TiAu}_2$	$\beta\text{TiAu} + \text{TiAu}_2 + \alpha\text{T}$
0.67		$\text{Ti}_3\text{Au} + \text{TiAu}_2$
0.75		$\text{TiAu}_2 + \text{TiAu}_4$
0.80	$\text{TiAu}_2 + \text{TiAu}_4$	$\text{TiAu}_2 + \text{TiAu}_4$

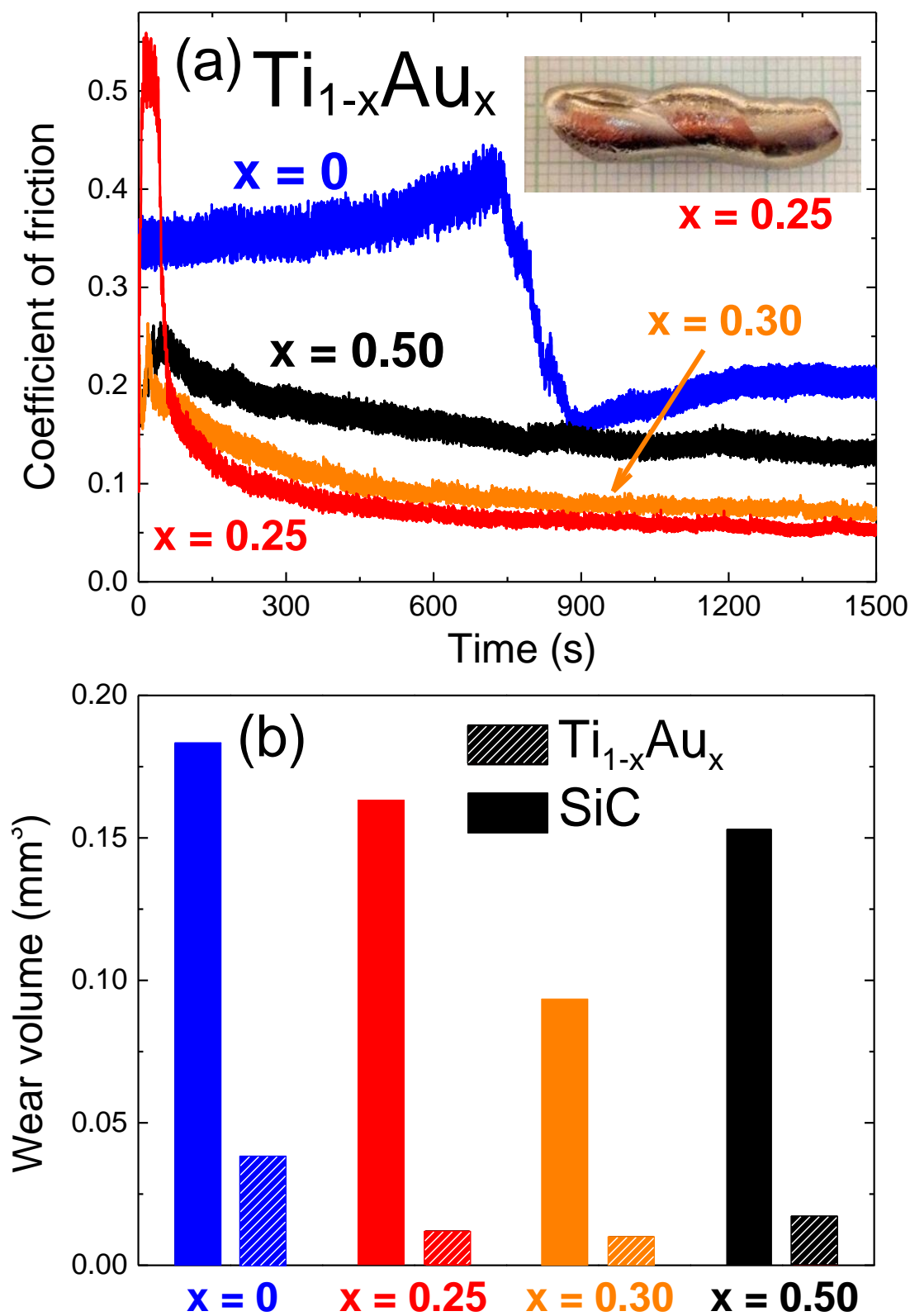


Figure 8.9: (a) Coefficient of friction as a function of time for $\text{Ti}_{1-x}\text{Au}_x$ with $x = 0, 0.25, 0.30$ and 0.50 . Inset: the $x = 0.25$ sample used for wear tests. (b) Wear volumes of the $\text{Ti}_{1-x}\text{Au}_x$ pin (dashed bars) and a SiC disk (full bars).

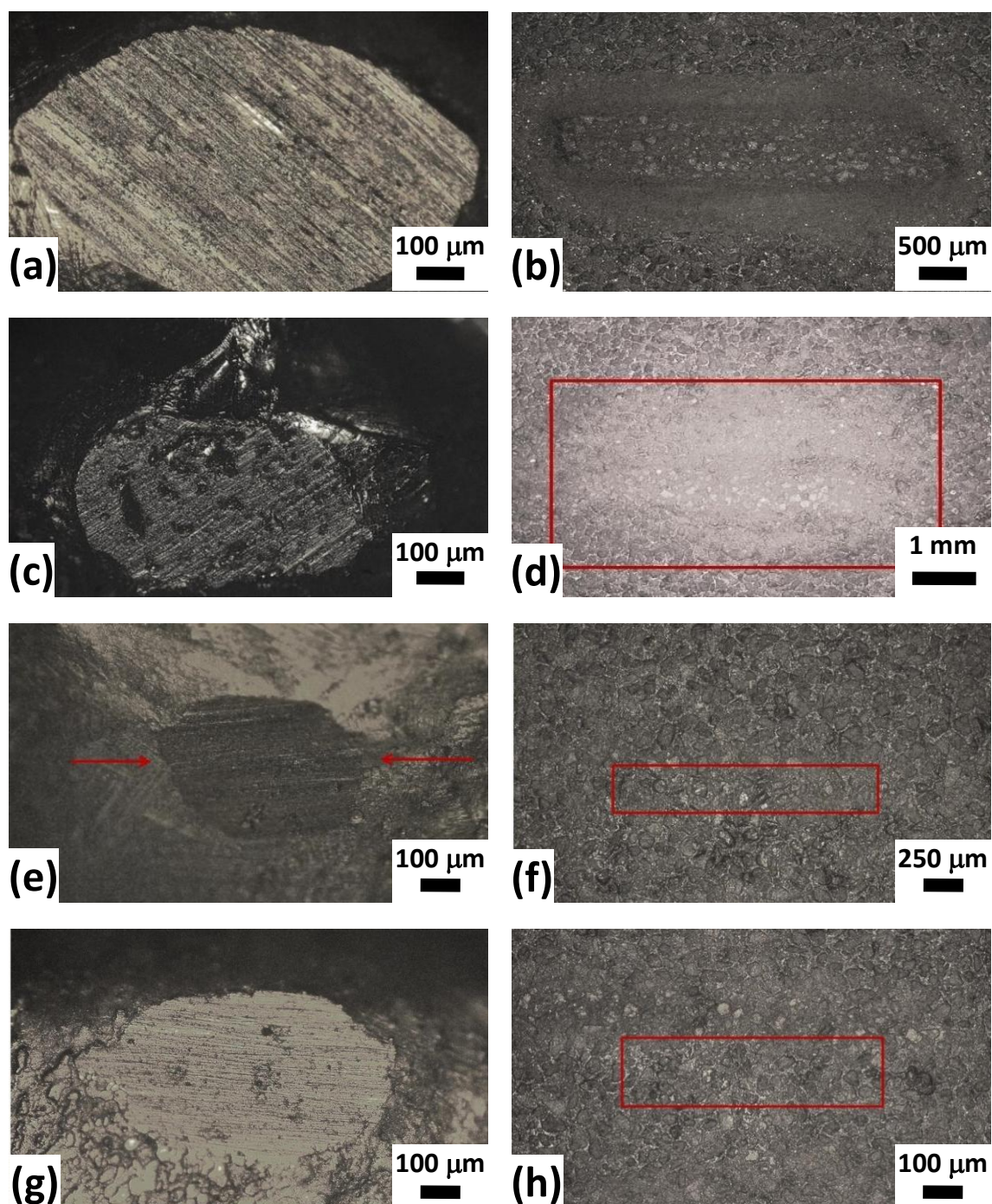


Figure 8.10: SEM images of the pin and disk wear test: (a) Ti reference ingot, (b), (d), (f) and (h) SiC disk. $\text{Ti}_{1-x}\text{Au}_x$ pins for $x = 0.25$ (c), $x = 0.30$ (e) and $x = 0.50$ (g) samples.

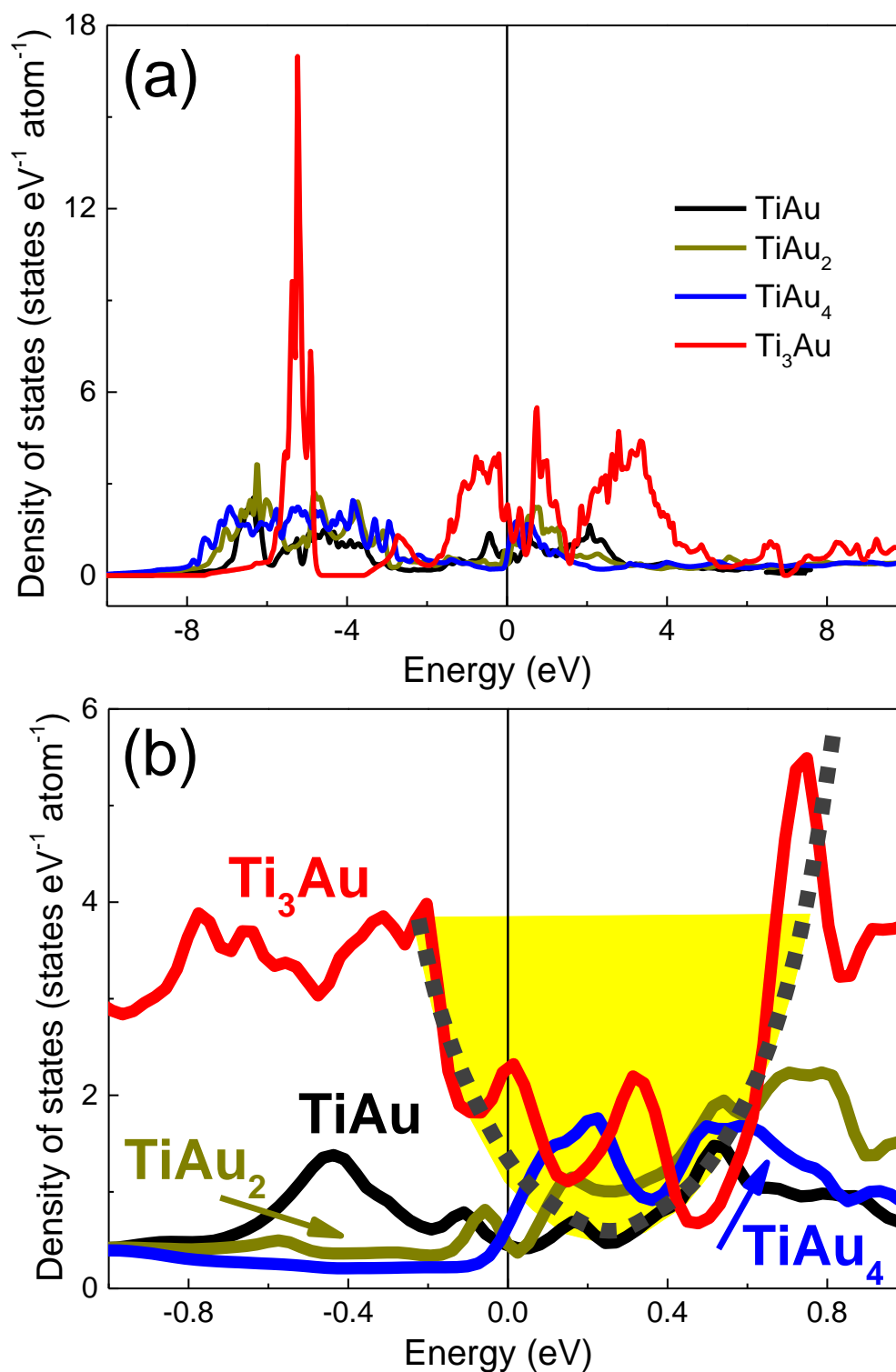


Figure 8.11: (a) Density of states as a function of energy for TiAu (black), TiAu₂ (yellow), TiAu₄ (blue) and Ti₃Au (red). Ti₃Au exhibits a pronounced valley around the Fermi energy, marked by a dashed gray line in (b).

Table 8.5: Wear parameters of the $\text{Ti}_{1-x}\text{Au}_x$ alloys.

x	$\text{Ti}_{1-x}\text{Au}_x$		SiC	
	wear volume (mm^3)	wear type	wear volume (mm^3)	wear type
0	0.038	abrasive, adhesive	0.183	adhesive
0.25	0.012	abrasive, adhesive	0.163	abrasive, adhesive
0.30	0.010	abrasive, adhesive	0.153	adhesive
0.50	0.017	abrasive	0.093	adhesive

the electronic energy is lowered, stabilizing the phase and, consequently, improving the hardness [257]. The pseudogap feature has been observed in a large number of materials for which either covalent or metallic bonds are dominant [257]. Typically, to affect the crystallographic phase significantly, the pseudogap must have a width W of 0.5 - 1.5 eV and height ratio $H/H_0 > 0.5$ [257]. As can be seen in Fig. 8.11, TiAu, TiAu_2 , and Ti_3Au exhibit pseudogaps around E_F . The parameters for those are listed in Table 8.6, from which it is obvious that the pseudogap for Ti_3Au is the most pronounced one (inset of Fig. 8.11), with $W \approx 1$ eV and $H/H_0 \approx 4$. This is again consistent with the highest hardness value of the $\text{Ti}_{0.75}\text{Au}_{0.25}$ alloy.

Table 8.6: Crystallographic and pseudogap parameters for Ti-Au phases.

Phase	Space group	VED (\AA^{-3})	ρ (g/cm^3)	Pseudogap	
				W (eV)	H/H_0
Ti_3Au	$Pm\bar{3}n$	0.20	7.87	1	4
TiAu	$Pmma$	0.15	11.05	1	0.4
TiAu_4	$I4/m$	0.10	14.52	—	—
TiAu_2	$I4/mmm$	0.12	14.09	0.2	2

8.5.3 Effects of Heat Treatment

Given that Ti alloys are frequently heat-treated to improve both hardness and ductility, two types of annealing were carried out for Ti-Au alloys. The first one consisted of heating the samples to 900 °C and dwelling for 7 days. The second annealing profile was based on the melting temperature, similar to what has been done for other Ti-base alloys, as shown in Table 8.2. The samples were heated to $0.5T_m$ for 1 hour and then annealed at $0.3T_m$ for 8 hours. The resulting hardness values are listed in Table 8.7. The hardness values of as-cast and annealed samples are very similar, which might be caused by variation in microstructure homogeneity which can mask the true annealing effects.

Alternative temperature treatments can be implemented in conjunction with plastic deformation. Cold- or hot-rolling these alloys can increase both plasticity and provide a more homogeneous material for further annealing. Consequently, hardness enhancement might decrease but increased plasticity could pave the way for additional applications.

Table 8.7: Comparison of hardness for different annealing profiles of $\text{Ti}_{1-x}\text{Au}_x$ alloys.

x	As-cast (GPa)	First anneal (GPa)	Second anneal (GPa)
0.22	7.11 ± 0.12	7.26 ± 0.10	6.73 ± 0.32
0.25	7.81 ± 0.21	7.51 ± 0.08	7.55 ± 0.18
0.335	6.56 ± 0.20	6.30 ± 0.29	6.36 ± 0.11
0.50	2.34 ± 0.24	2.51 ± 0.09	2.91 ± 0.17
0.60	2.64 ± 0.24	2.31 ± 0.15	2.14 ± 0.36
0.67	2.09 ± 0.05	2.68 ± 0.08	2.63 ± 0.04
0.80	2.83 ± 0.08	1.71 ± 0.07	1.80 ± 0.05

8.5.4 Conclusion and Future Endeavors

A series of $\text{Ti}_{1-x}\text{Au}_x$ alloys ($0.22 \leq x \leq 0.8$) has been investigated due to their extreme hardness values, elevated melting temperatures (compared to those of constituent elements), reduced density compared to pure Au, bulk metallicity, and high biocompatibility. Previously, radio opacity of other $\text{Ti}_{1-x}\text{Au}_x$ alloys has been reported [48, 49], allowing for differentiation between implants and live tissue. These properties make medical applications especially favorable with examples including replacement parts and components (both permanent and temporary), dental prosthetics and implants. The ability to adhere to ceramic components along with osseointegration are also beneficial, as they are able to reduce component weight and cost. Possible additional applications include circuit wires, hard coatings for tools and other medical equipment, drill head bits, as well as sporting goods.

Among biomedical materials, hardness of the $\text{Ti}_{0.75}\text{Au}_{0.25}$ alloy is clearly superior. Moreover, comparison with Ti indicates improved coefficient of friction and wear rates, reduced melting temperatures, and biocompatibility, making this compound particularly well suited for applications where Ti is already employed [67, 105, 192, 193, 240, 317, 392], with examples including replacement parts and components (both permanent and temporary), dental prosthetics and implants. The reduced density along with an ability to adhere to ceramic components and osseointegration will aid in reducing both component weight and cost.

An increase in the hardness can potentially be achieved by strengthening the covalent bonding, possible *via* addition of a dopant that is small enough so that the volume would stay nearly the same. Suitable choices include C and B, as their valence electron density values are similar to that of Ti_3Au [135]. Consequently, the biocompatibility might have to be sacrificed in order to achieve even higher hardness values, making $\text{Ti}_{1-x}\text{Au}_x$ alloys more suitable for industrial applications.

Type I Superconductivity in ScGa_3 and LuGa_3

Superconductivity in single crystals of ScGa_3 and LuGa_3 is observed from magnetization, specific heat and resistivity measurements: low critical temperatures $T_c = 2.1 - 2.2$ K, field-induced second-to-first order phase transition in the specific heat, critical fields less than 240 Oe and low Ginzburg-Landau coefficients ($\kappa \approx 0.23$ and 0.30 for ScGa_3 and LuGa_3 , respectively) all suggest that these crystals have a Type I superconducting ground state. These observations render ScGa_3 and LuGa_3 two of only several Type I superconducting compounds, with most other superconductors being Type II (compounds and alloys) or Type I (elemental metals and metaloids).

9.1 Motivation and Background

Despite the large number of known conventional and unconventional superconductors, new findings still emerge even from simple, binary intermetallic systems. The majority of the metallic elements are superconducting with small values of the critical temperatures T_c [311]. It has been noted [186], that intermetallic compounds often have T_c values higher than those of the constituent elements, as is the case in Nb_3Sn [247], V_3Si [243], ZrB_2 and NbB_2 [127]. Thermodynamic and transport measurements performed on single crystals of $R\text{Ga}_3$ ($R = \text{Sc}$ or Lu), formed with superconducting Ga with $T_c = 1.09$ K [311] and either non-superconducting Sc or superconducting Lu whose critical temperature is $T_c = 0.1$ K [311], place ScGa_3 and LuGa_3 among the aforementioned intermetallic superconductors.

Past studies focused on the synthesis of polycrystalline samples of $R\text{Ga}_3$, with reports on single crystals limited to de Haas-van Alphen measurements [302].

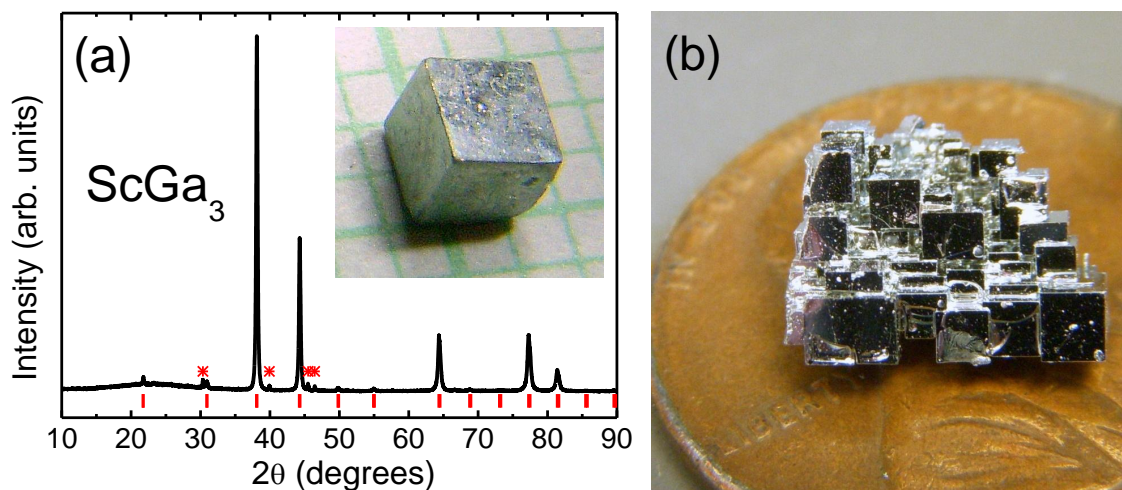


Figure 9.1: (a) Powder x-ray diffraction pattern for ScGa_3 (black), with calculated peak positions (vertical red marks) for space group $Pm\bar{3}m$ and lattice parameter $a = 4.0919$ Å. Minute amounts of residual Ga flux are marked by asterisks. Inset: a picture of a single crystal of ScGa_3 . (b) A cluster of ScGa_3 crystals, prepared from a molten solution.

Pluzhnikov *et. al.* characterized the geometry of the Fermi surface of three related intermetallic compounds, RGa_3 ($R = \text{Sc, Lu}$) and LuIn_3 . Together with findings from band structure calculations [161] on the same systems, these reports suggested great similarities between the electronic properties of ScGa_3 and LuGa_3 . Superconductivity below 2.3 K in LuGa_3 had already been mentioned [153], but thermodynamic and transport properties measurements of both ScGa_3 and LuGa_3 so far have been limited to $T > 4.2$ K [202, 204]. The similarities in the electronic structures of ScGa_3 and LuGa_3 suggest that if the superconductivity in the latter compound is confirmed, the former is also likely to display a superconducting ground state. Physical properties summarized below evidence that indeed both RGa_3 ($R = \text{Sc and Lu}$) are superconducting. The low critical temperatures T_c around 2.2 K and small critical fields $H_c < 240$ Oe point to Type I superconductivity in both compounds. Additional supporting evidence for the Type I superconductivity is provided by the field-dependent specific heat and low values of the Ginzburg-Landau (GL) coefficient $\kappa \approx 0.23$ and 0.3 for ScGa_3 and LuGa_3 , respectively.

The RGa_3 compounds ($R = \text{Sc, Dy-Tm, Lu}$) crystallize in the cubic $Pm\bar{3}m$ space group, a structure suggested by Matthias [244] to be favorable for superconductivity. Single crystals of ScGa_3 and LuGa_3 were prepared using a self flux method, as described in Section 3.1. Powder x-ray diffraction data, shown in Fig. 9.1 for ScGa_3 , were collected for both compounds, as described in Section 3.2. The patterns for ScGa_3 and LuGa_3 were refined with the cubic space group $Pm\bar{3}m$, with lattice parameters $a = 4.09$ Å and $a = 4.19$ Å, respectively. A picture of a ScGa_3 crystal and a cluster of crystals is also shown in Fig. 9.1. Traces of residual Ga flux are apparent in the powder pattern, and are marked with asterisks in Fig. 9.1. Additional single crystal x-ray diffraction measurements confirmed the crystals structure, stoichiometry and purity of the ScGa_3 crystals.

9.2 Physical Properties

As-measured susceptibility data $\chi = M/H$ for $R\text{Ga}_3$ in various applied magnetic fields H was scaled by 4π and corrected for demagnetizing effects (see Section 2.4 and Eq. 2.124):

$$4\pi\chi_{eff} = \frac{4\pi\chi}{(1 - N_d\chi)} \quad (9.1)$$

where N_d is the demagnetizing factor associated with the geometry of a crystal. For a cubic system, $N_d \approx 1/3$ [10, 292], yielding data shown in Fig. 9.2. As anticipated from their electronic properties [302], both $R = \text{Sc}$ (Fig. 9.2(a)) and Lu (Fig. 9.2(b)) compounds display similar superconducting ground states below 2.2 - 2.3 K. Increasing magnetic field suppresses the transition for ScGa_3 (Fig. 9.2(a)), such that T_c becomes smaller than 1.8 K for $H \approx 80$ Oe. Fig. 9.2(b) illustrates the similarity between the $H = 5$ Oe $M(T)$ data for ScGa_3 (squares) and LuGa_3 (triangles), for both zero-field cooled (full) and field-cooled (open) data. The critical field H_c for each compound can also be estimated from the $M(H)$ data, shown in Fig. 9.3. Taking the demagnetization effect into consideration, a more accurate estimate of the field H is:

$$H_{eff} = H - N_d M \quad (9.2)$$

where, as before, for a cube and $H||a$, $N_d \approx 1/3$. The resulting $M(H_{eff})$ isotherms are displayed in Fig. 3 (full symbols, bottom axes) along with as-measured $M(H)$ for $T = 1.8$ K (open symbols, top axes). The critical field values H_c , corresponding to the entrance to the normal state ($M = 0$), are not changed when demagnetizing effects are taken into account for $H||a$. The critical fields are remarkably low, H_c reaching only about 90 Oe at 1.8 K, the lowest temperature available for the magnetization

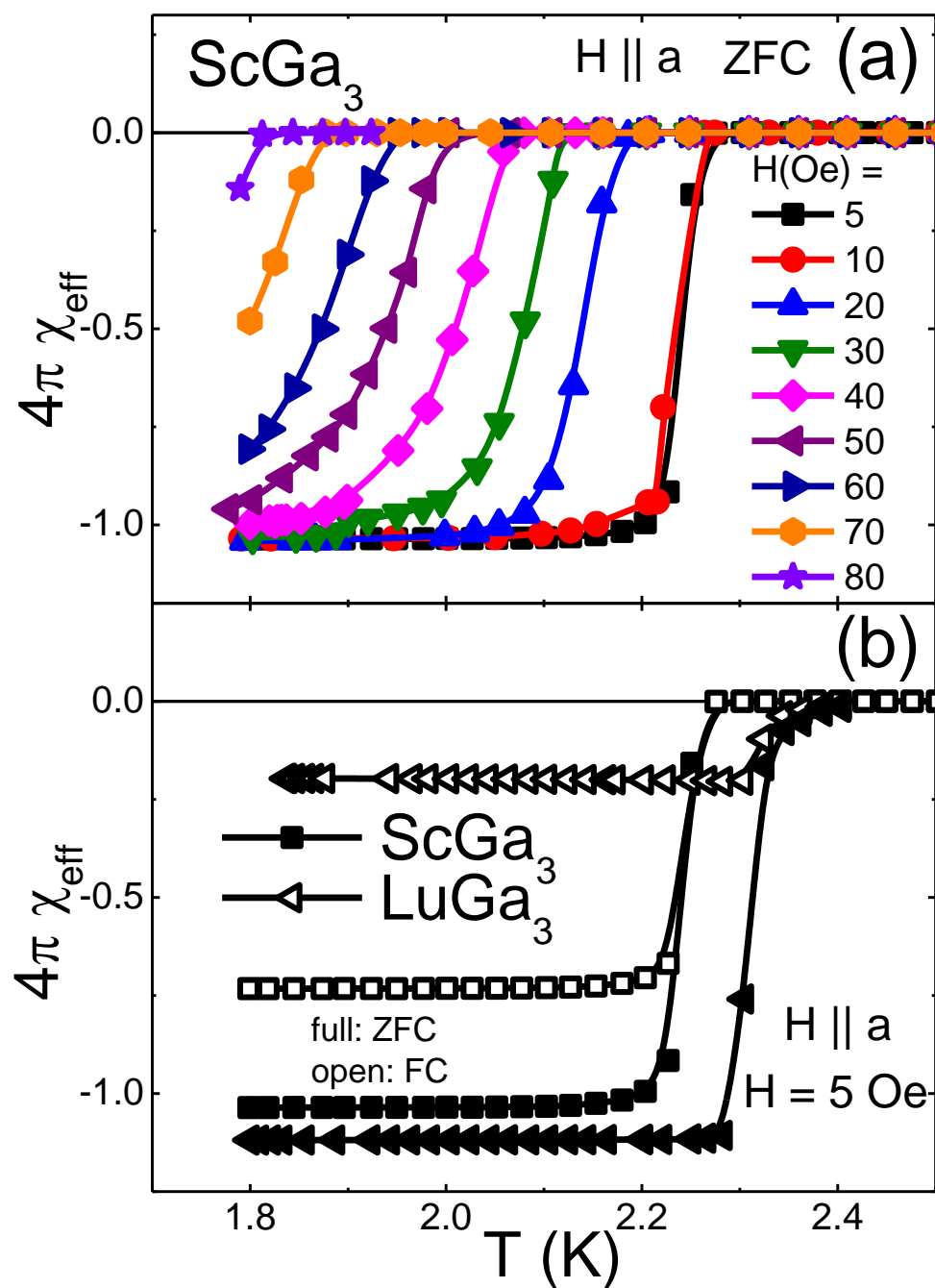


Figure 9.2: (a) Zero-field cooled temperature-dependent susceptibility data, scaled by 4π and corrected for demagnetizing effects (see text), for ScGa_3 in applied magnetic fields up to 80 Oe. (b) $H = 5$ Oe zero-field cooled (full symbols) and field-cooled (open symbols) scaled susceptibility $4\pi\chi_{\text{eff}}$ data for ScGa_3 (squares) and LuGa_3 (triangles).

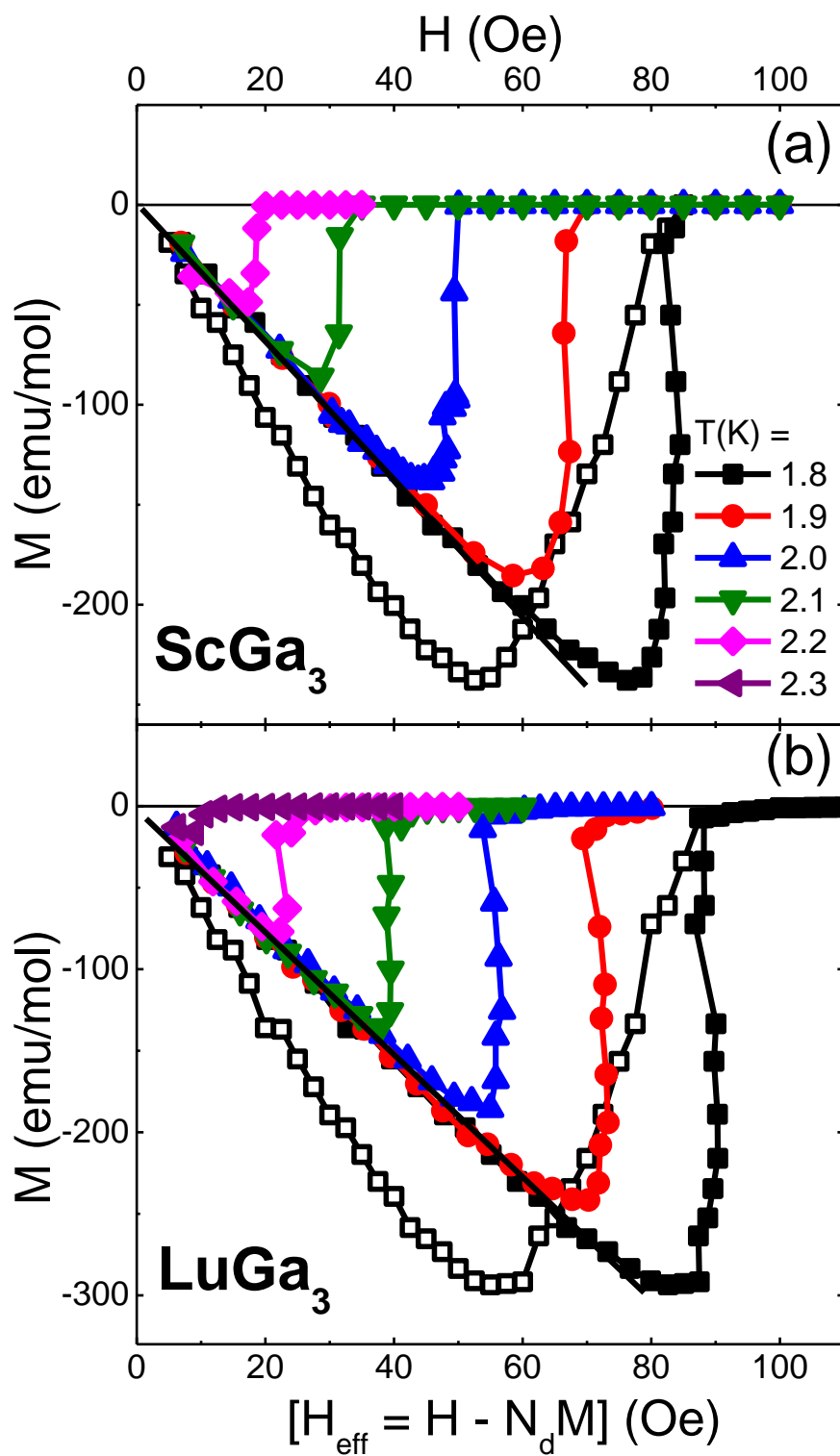


Figure 9.3: (a) ScGa_3 and (b) LuGa_3 $M(H_{\text{eff}})$ for temperatures between 1.8 K and 2.3 K. Open squares: $M(H)$ isotherms for $T = 1.8$ K, where H is the applied magnetic field.

measurements. Moreover, as will be shown below, the critical fields for both compounds remain small down to 0.4 K. This observation, along with the small critical temperatures and the shape of the $M(H)$ isotherms, indicate Type I superconductivity in both ScGa_3 and LuGa_3 . While most elemental superconductors are Type I, this is a rare occurrence in superconducting compounds, making ScGa_3 and LuGa_3 two of only a few such known systems [17,376,393,413,418]. It is therefore imperative to fully characterize the superconducting state in the $R\text{Ga}_3$ superconductors. Specific heat and resistivity measurements extend the findings from magnetization data down to lower temperatures.

Field-dependent specific heat measurements for ScGa_3 and LuGa_3 were carried out in fields up to 240 Oe, as shown in Fig. 9.4. As expected, a sharp peak is observed for field values $H < 240$ Oe, from which the critical temperature T_c can be determined as the point halfway between the peak and the normal state specific heat signal. Type I superconductivity in both compounds is confirmed by the increase of the jump in specific heat between zero and non-zero applied magnetic field H , indicating second-to-first order phase transition. T_c for ScGa_3 and LuGa_3 is suppressed from 2.1 K (open squares, Fig. 9.4(a)) and 2.0 K (open squares, Fig. 9.4(b)), respectively, at $H = 0$ to below 0.4 K at $H = 240$ Oe (solid line, Fig. 9.4(c) and (d)). The normal state electronic specific heat coefficient γ_n and phonon specific heat coefficient β were estimated from the linear fit of the normal state ($H = 240$ Oe) specific heat below 8 K, plotted as C_p/T vs. T^2 (not shown). Very similar γ_n values, $7.11 \text{ mJ mol}^{-1} \text{ K}^{-2}$ and $8.46 \text{ mJ mol}^{-1} \text{ K}^{-2}$, were obtained for ScGa_3 and LuGa_3 , respectively.

The superconducting electronic specific heat coefficient γ_s can also be determined from γ_n and the residual electronic specific heat coefficient γ_{res} . The latter coefficient, γ_{res} , estimated from C_e/T at $T = 0.4$ K and $H = 0$ (Fig. 9.4(c) and (d)), is much smaller than γ_n for both compounds. This results in $\gamma_s = \gamma_n - \gamma_{res} \approx \gamma_n$

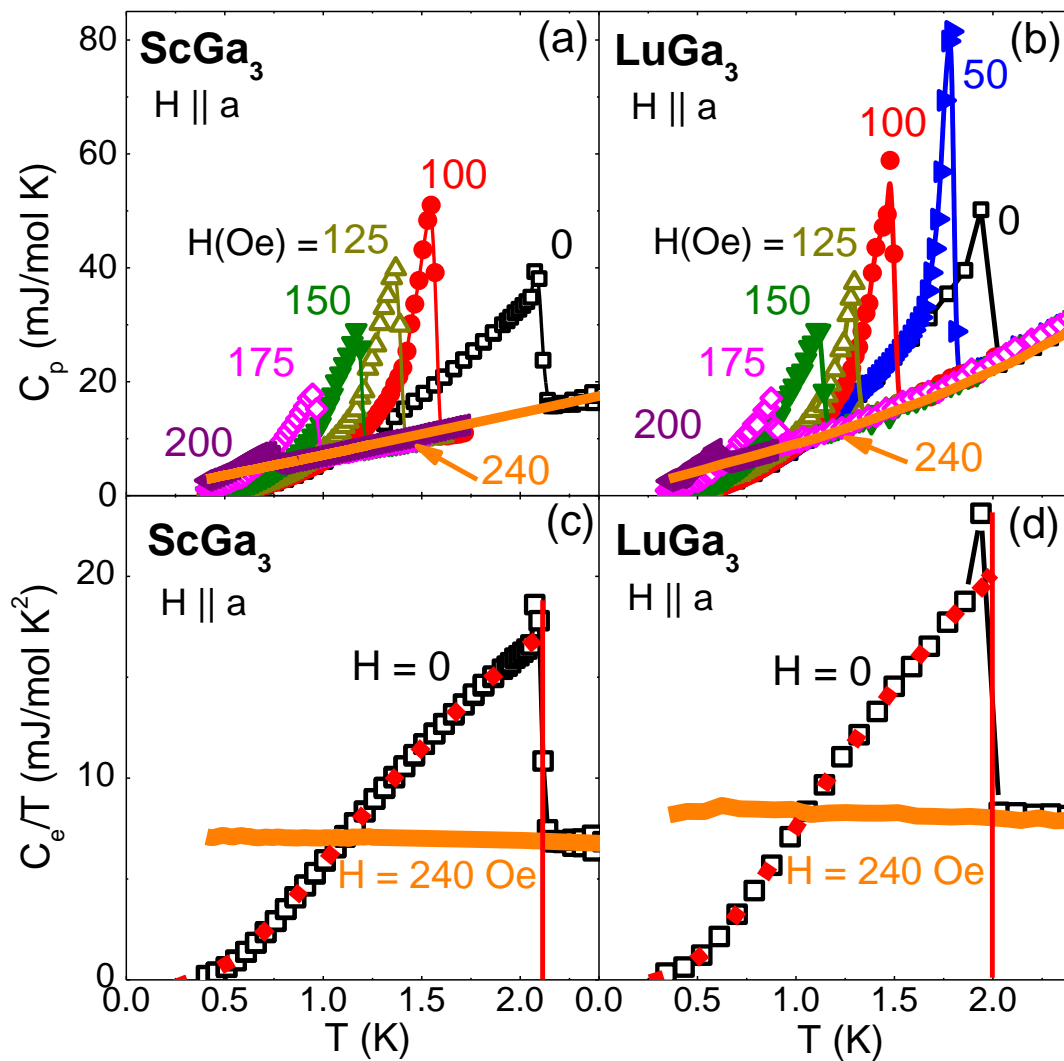


Figure 9.4: Specific heat data for (a) ScGa_3 and (b) LuGa_3 in applied magnetic fields up 240 Oe. (c) and (d) Normal ($H = 240$ Oe) and superconducting ($H = 0$) electronic specific heat C_e , scaled by temperature T . The entropy conservation construct gives the ratio $\Delta C_{es}/\gamma_n T_c \approx 1.44$ for both ScGa_3 and LuGa_3 , with the dashed line representing a fit of C_e/T to the expected BCS electronic specific heat.

for both ScGa₃ and LuGa₃. The entropy-conservation construct shown in Fig. 9.4(c) and (d) for ScGa₃ and LuGa₃, respectively, yields the same value for the jump in the electronic specific heat C_e at T_c , $\Delta C_e/\gamma_n T_c \approx 1.44$, consistent with BCS-Type superconductivity [32]. One more similarity between the two compounds is the minimum excitation energy $\Delta(0)$: from the low-temperature fit of the electronic specific heat $C_e \propto e^{-\Delta/k_B T}$ (dashed lines in Fig. 9.4(c) and (d)), $\Delta(0)$ is estimated to be 0.18 meV for ScGa₃ and 0.17 meV for LuGa₃. The Debye temperature:

$$\theta_D = \left(\frac{12N_A r k_B}{5\beta\pi^4} \right)^{1/3}, \quad (9.3)$$

where $r = 4$ is the number of atoms per formula unit, can be determined using the phonon specific heat coefficient β (Table 9.1), also estimated from the linear fit of C_p/T vs. T^2 (not shown). This yields $\theta_D = 660$ K for ScGa₃ and 232 K for LuGa₃. Moreover, the electron-phonon coupling constant λ_{el-ph} , can be determined using McMillan's theory [251]:

$$\lambda_{el-ph} = \frac{1.04 + \mu^* \ln \left(\frac{\theta_D}{1.45T_c} \right)}{(1 - 0.62\mu^*) \ln \left(\frac{\theta_D}{1.45T_c} \right) - 1.04} \quad (9.4)$$

where μ^* represents the repulsive screened Coulomb potential and is usually between 0.1 and 0.15. Setting $\mu^* = 0.13$, results in $\lambda_{el-ph} = 0.45$ and 0.55 for ScGa₃ and LuGa₃, respectively, implying that both compounds are weakly coupled superconductors.

From the specific heat data for both the superconducting ($H = 0$) and the normal ($H = 240$ Oe) states, an estimate of the thermodynamic critical field H_c can be obtained using the free energy relation [372]. The thermodynamic critical field values $H_c = 209 \pm 10$ Oe for ScGa₃ and 226 ± 10 Oe for LuGa₃ are consistent with what has been observed in magnetization and specific heat data. The field- and

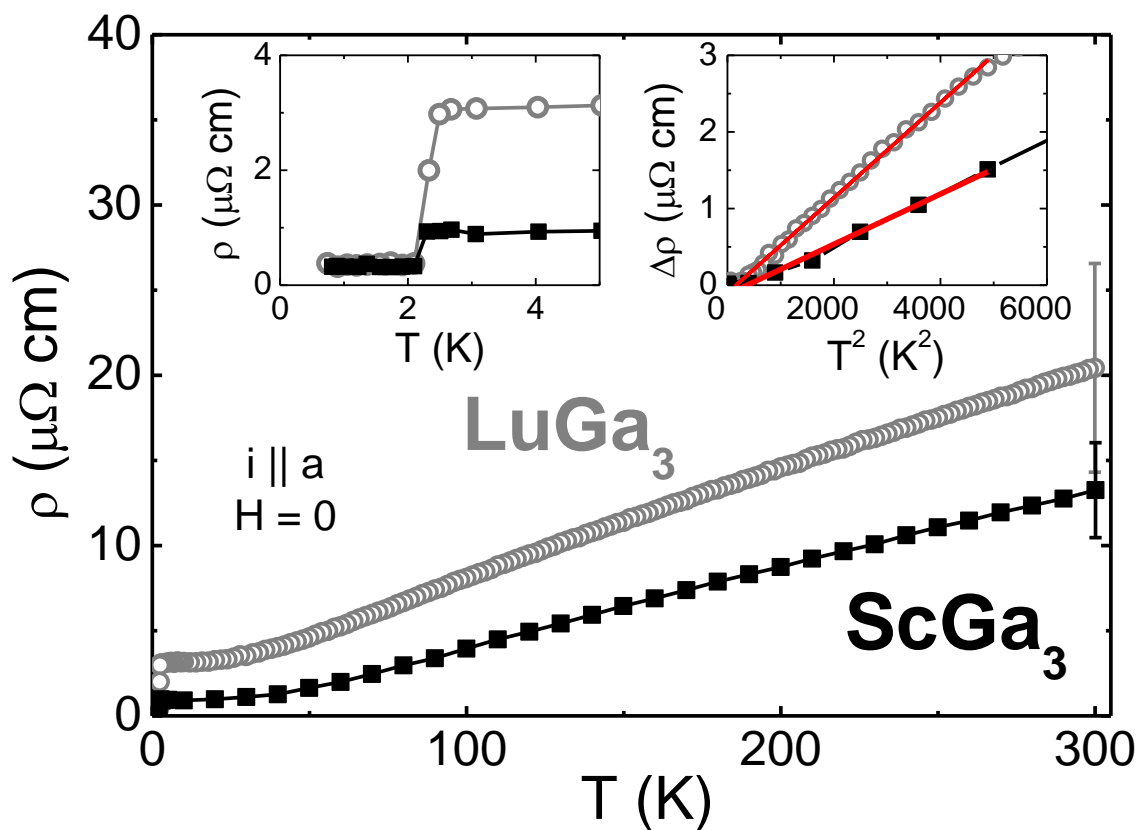


Figure 9.5: $H = 0$ temperature-dependent resistivity for ScGa_3 (full black symbols) and LuGa_3 (open gray symbols), with Bloch-Grüneisen-Mott fits (solid lines) for $n = 2$ (ScGa_3) and $n = 3$ (LuGa_3). Left inset: low-temperature $\rho(T)$ around T_c . Right inset: $\Delta\rho = \rho - \rho(0)$ vs. T^2 , with solid lines representing linear fits up to 80 K for ScGa_3 and 70 K for LuGa_3 .

temperature-dependent data can be summarized in the $H - T$ phase diagram, shown in Fig. 9.7 and discussed below.

Previously reported resistivity measurements [202,204] on LuGa_3 were limited to temperatures above 4.2 K, while similar data had not been presented for ScGa_3 . Figure 9.5 displays the $H = 0$ resistivity data for ScGa_3 and LuGa_3 (full and open symbols, respectively). The superconducting transition (left inset) is around 2.2 - 2.3 K for both compounds. The apparently finite resistivity in the superconducting state is likely an artifact of the measurement: the overall resistivity values are very small for both compounds; below T_c , the contact resistance, albeit small, might alter the mea-

sured voltage, which is very close to the instrument resolution. Above the transition and below 80 K for ScGa₃ or 70 K for LuGa₃, $\rho(T)$ exhibits Fermi liquid behavior, as illustrated by the $\Delta\rho \propto AT^2$ plot (right inset, Fig. 9.5), with $A = 3.4 \cdot 10^{-4}$ and $6.1 \cdot 10^{-4} \mu\Omega\text{cm K}^{-2}$, respectively. At higher temperatures a slight curvature of the resistivity is apparent. Solid line fits are obtained by using the Bloch-Grüneisen-Mott (BGM) relation [39]:

$$\rho = \rho_0 + A\left(\frac{T}{\theta_D}\right)^n \int_0^{\theta_D/T} \frac{x^n dx}{(e^x - 1)(1 - e^{-x})} - kT^3 \quad (9.5)$$

with $n = 2$ for ScGa₃ and $n = 3$ for LuGa₃ describe the data well up to room temperature, even higher than $\theta_D/4$. This points to significant $s-d$ band scattering, while the different exponents n suggest underlying differences in the electron-phonon scattering in the two compounds. The fits shown in Fig. 9.5 were performed using the θ_D values determined from specific heat; the other BGM parameters were determined to be $A = 38.5$ and $28.6 \mu\Omega\text{cm}$ and $k = 1.3 \cdot 10^{-7}$ and $0.3 \cdot 10^{-7} \mu\Omega\text{cm K}^{-3}$, for ScGa₃ and LuGa₃, respectively. If the parameter θ is also released for the BGM fits, equally good fits for $n = 2$ and $n = 3$ are achieved for ScGa₃, for θ_R values between 320 and 460 K, significantly smaller than the Debye temperature $\theta_D = 660$ K. For LuGa₃, the parameters remain nearly unchanged, with the best fit for $n = 3$ and $\theta_R = 230$ K, virtually identical to $\theta_D = 232$ K.

Based on the Sommerfeld coefficient extracted from the specific heat data, it is possible to estimate the London penetration depth $\lambda_L(0)$ (Eq. 2.120), the coherence length $\xi(0)$ (Eq.) and the GL parameter (Eq. 2.122).

Since both ScGa₃ and LuGa₃ have one formula unit per unit cell, the conduction electron density n , due to three electrons contributed by Sc and Lu, can be estimated as $n = 3/V$ where V is the volume of the unit cell. It results that

Table 9.1: Summary of parameters describing properties of ScGa₃ and LuGa₃.

	ScGa ₃	LuGa ₃
T_c (K)	2.1 ± 0.2	2.2 ± 0.25
H_c (Oe)	209 ± 10	226 ± 10
γ_n (mJ mol ⁻¹ K ⁻²)	7.03 ± 0.08	8.52 ± 0.06
β (mJ mol ⁻¹ K ⁻⁴)	0.027	0.621
A ($\mu\Omega\text{cm K}^{-2}$)	$3.4 \cdot 10^{-4}$	$6.1 \cdot 10^{-4}$
RRR	14.0	6.5
$\frac{\Delta C_e(T_c)}{\gamma_n T_c}$	1.44	1.44
λ_{el-ph}	0.45	0.55
$m^* m_0$	3.03	3.49
λ (nm)	59	63
ξ (μm)	0.26	0.21
κ	0.23	0.30

$n = 4.39 \cdot 10^{-2} \text{ \AA}^{-3}$ and $n = 4.08 \cdot 10^{-2} \text{ \AA}^{-3}$ for ScGa₃ and LuGa₃, respectively. If a spherical Fermi surface is assumed for both compounds, the Fermi wave vector k_F can be roughly calculated as $k_F = (3n\pi^2)^{1/3} = 1.09 \text{ \AA}^{-1}$ for ScGa₃ and 1.07 \AA^{-1} for LuGa₃. The effective electron mass can then be expressed in terms of the free electron mass m_0 :

$$m^* = \frac{\hbar^2 k_F^2 \gamma_n}{\pi^2 n k_B^2}, \quad (9.6)$$

yielding $m^* = 3.03m_0$ and $3.49m_0$ for ScGa₃ and LuGa₃, respectively. The London penetration depth, given by Eq. 2.120, has values of 59 nm for ScGa₃ and 63 nm for LuGa₃. The coherence length, calculated from Eq. 9.2, also has similar values for the two compounds: 0.26 μm for the former and 0.21 μm for the latter. The GL parameter, given by Eq. 2.122, is therefore 0.23 for ScGa₃ and 0.30 for LuGa₃. This indicates that both compounds are Type I superconductors, since $\kappa < 1/\sqrt{2}$. In comparison, a Type II superconductor MgB₂ has $\kappa(0)$ value close to 26 [109], while

$\kappa(0)$ for Type I superconductor LaRhSi_3 is close to 0.25 [17].

9.3 Band Structure Calculations

Using Eq. 3.30, previously reported band structure calculations for both ScGa_3 and LuGa_3 [161] predict smaller values of γ_n , compared to those obtained experimentally ($\gamma_{n,PPW} = 2.4 \text{ mJ mol}^{-1} \text{ K}^{-2}$ and $1.2 \text{ mJ mol}^{-1} \text{ K}^{-2}$ and Table 9.1). Since the above band structure calculations are based on the Pseudo-Potential Plane Wave approximation [161], a better estimate of γ_n can be achieved by using the Full-Potential Linear Augmented Plane Wave method (FP-LAPW) [41,296], as described in the Experimental Methods Section 3.11. The density of states, shown in Fig. 9.6, exhibits a

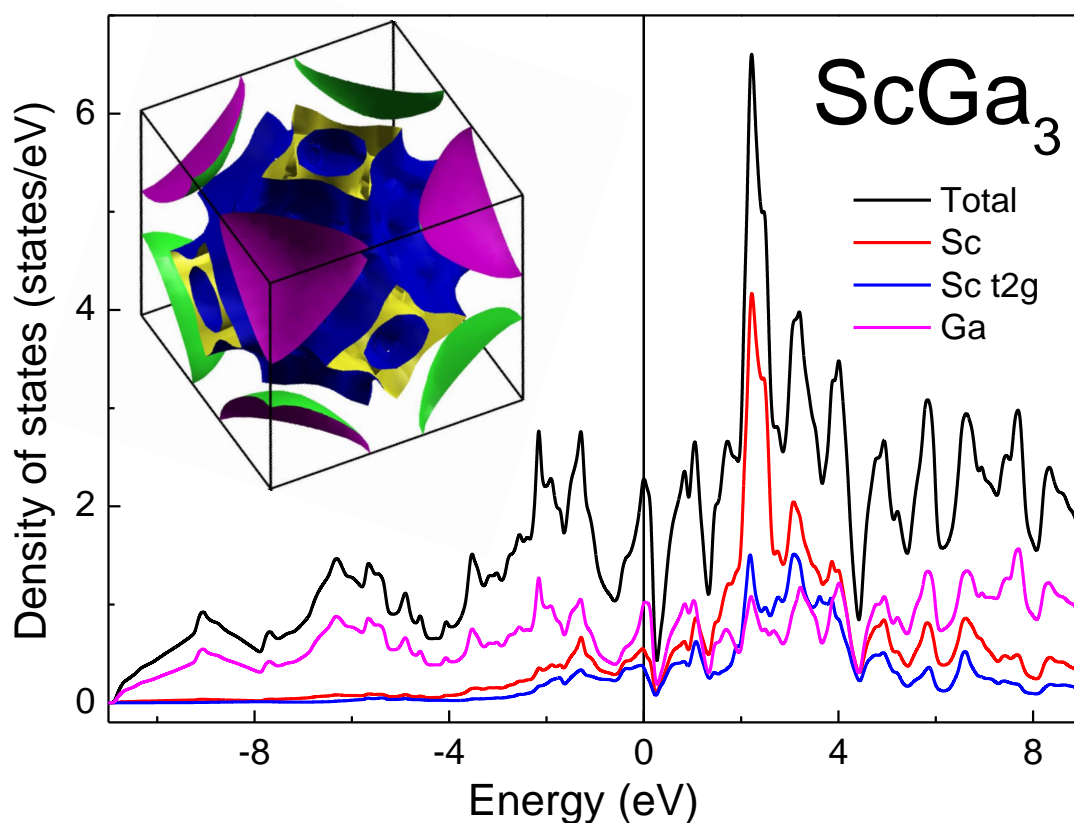


Figure 9.6: Density of states for ScGa_3 exhibits a peak at the Fermi surface. Inset: the Fermi surface of ScGa_3 .

peak at the Fermi surface, as is the case for previous calculations [161]. However, the magnitude of the peak is larger, yielding $N(E_F) \approx 2$ states eV^{-1} , and, consequently, $\gamma_{n,FPLAPW} = 7.1 \text{ mJ mol}^{-1} \text{ K}^{-2}$ for ScGa_3 , identical with the experimental value of $7.11 \text{ mJ mol}^{-1} \text{ K}^{-2}$.

9.4 Conclusion

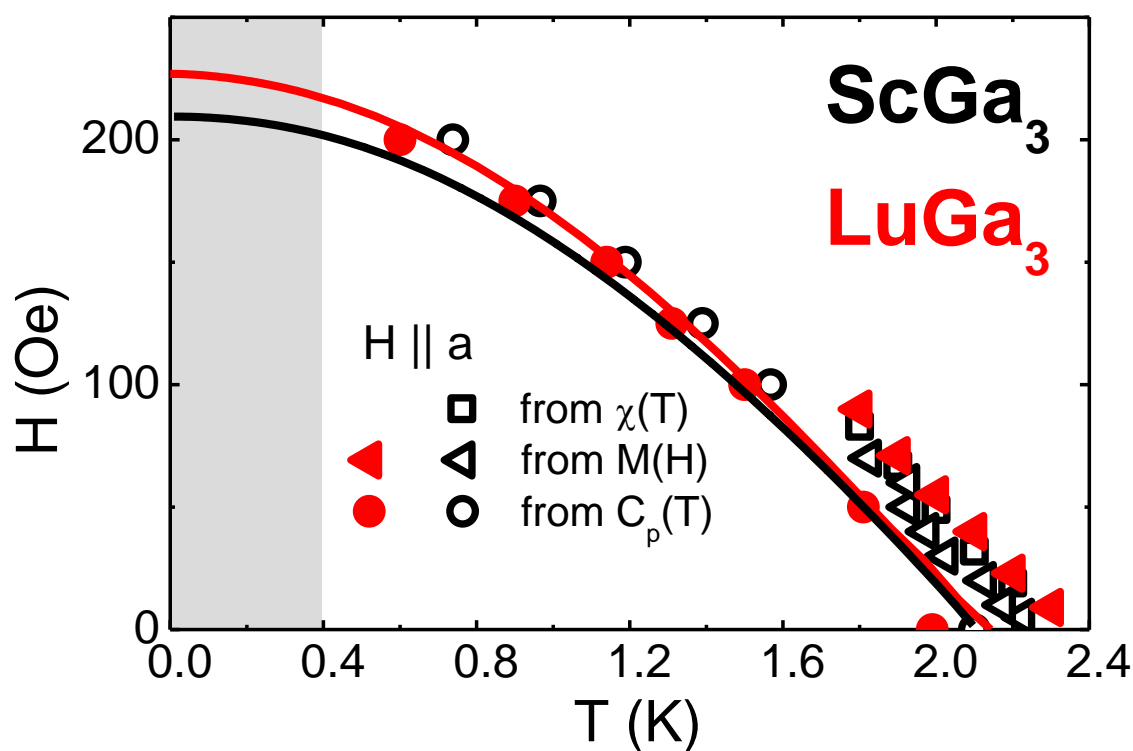


Figure 9.7: $H - T$ phase diagram for ScGa_3 (open black symbols) and LuGa_3 (full red symbols). The values of the critical fields H_c are determined from $\chi(T)$ data (squares), $M(H)$ data (triangles) and $C_p(T)$ data (circles).

In summary, Type I superconductivity in ScGa_3 and LuGa_3 is reported, with the parameters characteristic of the superconducting state, shown in Table 9.1. The shape of the $M(H)$ isotherms (Fig. 9.3), field-induced second-to-first order phase

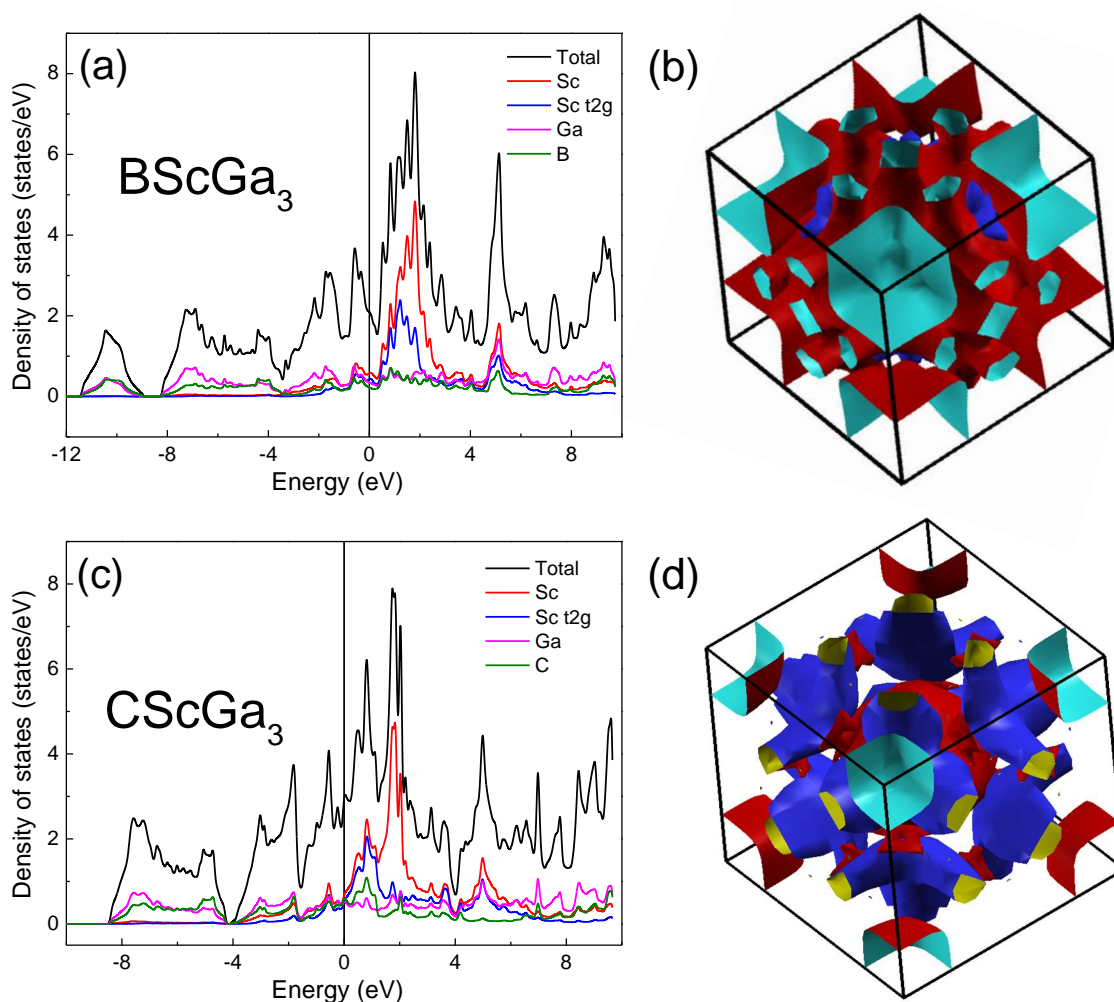


Figure 9.8: Doping of ScGa_3 with C and B shifts the peak away from the Fermi surface (a) and (c). The respective Fermi surface is plotted in (b).

transition in specific heat (Fig. 9.4), low T_c , H_c and κ values (Table 9.1) suggest that ScGa_3 and LuGa_3 are both Type I superconducting compounds. This is reflected also in the $H - T$ phase diagram (Fig. 9.7), where the symbols represent experimental points from $M(T)$ (squares), $M(H)$ (triangles) and C_P (circles). These data are in good agreement with the thermodynamic critical field H_c temperature dependence (solid lines). As suggested by the electronic properties [302], the superconducting parameters for the two compounds are very similar, as are their $H - T$ phase diagrams. A careful analysis of the crystal structure on one hand, and the thermodynamic and transport properties of the Type I superconducting compounds on the other hand,

may offer valuable insights into the rare occurrence of Type I superconductivity in binary or ternary systems. The relatively small electron-phonon coupling parameter λ_{el-ph} indicates that both compounds are weakly-coupled BCS superconductors.

For a number of superconductors, the superconducting temperature T_c can be raised by doping or application of pressure. Given face-centered crystal structure of both ScGa_3 and LuGa_3 , doping inside the cage with B and C was investigated. It was not possible to introduce the dopant either by flux or by armelting, which is likely caused by immiscibility of B and C in Ga and Sc. Moreover, according to the band structure calculations, shown in Fig. 9.8 for B- and C-doped ScGa_3 , the peak is shifted away from the Fermi level, suggesting a stable non-superconducting ground state.

Summary

While magnetism is certainly one of the most common and well studied condensed matter phenomena, not all its properties are yet fully understood. In particular, investigation of itinerant magnets composed of non-magnetic constituents has been the topic of this dissertation.

The only two compounds previously known to exhibit itinerant magnetism without any local moment contribution – ferromagnets Sc_3In and ZrZn_2 – were compared. Both systems have been known for over 60 years but only ZrZn_2 has been studied in depth. In particular, a quantum critical point in Sc_3In has remained elusive until present work. It was possible to suppress the ordering temperature to zero in a quantum critical regime by partially substituting Sc with Lu in $\text{Sc}_{3.1}\text{In}$. In-depth analysis of this quantum critical point *via* Arrott-Noakes method has indicated non-mean-field nature of $\text{Sc}_{3.1}\text{In}$, different from the mean-field behavior of ZrZn_2 . It was postulated that these differences between seemingly analogous systems can possibly be attributed to the dimensionality of spin fluctuations.

In order to further investigate this hypothesis, additional ferro- and antiferromagnetic compounds are necessary. In this work, a systematic method of finding

itinerant systems composed of non-magnetic constituents was proposed. By examining band structures and phase diagrams of known materials, it was possible to discover the first itinerant antiferromagnet composed of non-magnetic constituents – TiAu. In-depth analysis of physical properties and band structure calculations has indicated a spin-density wave ground state below 36 K.

The TiAu system was perturbed *via* application of pressure, high fields and doping. It was found that by substituting Ti with Sc, a quantum critical point can be achieved. Onset of non-Fermi liquid behavior close to the quantum critical point is evident from several physical properties. Scaling analysis has indicated a 2D character of this quantum phase transition, accompanied by enhanced spin fluctuations and electron-electron correlations.

Further investigation of Ti-Au alloys resulted in the discovery of a four-fold increase in hardness in Ti₃Au, as compared with pure Ti. Combination of biocompatibility, low wear and high hardness in this material make it well-suited for biomedical applications where Ti is already used. The origin of high hardness in Ti₃Au still remains puzzling, with possible origin of high valence electron concentration or pseudogap formation.

Bibliography

- [1] <http://suitupscene.com/scenes/iron-man/iron-man-becasue-gold-titanium-alloy-man-is-just-too-damn-long>. 2008. 8.5.1
- [2] Jara - jlich aachen research alliance. www.jara.org, 2013. (document), 3.28
- [3] chemwiki.ucdavis.edu, 2014. (document), 2.1
- [4] A. Abanov, A. V. Chubukov, and A. M. Finkel'stein. Coherent vs. incoherent pairing in 2D systems near magnetic instability. *Europhysics Letter*, 54:488, 2001. 7.1, 7.2
- [5] S. Abe, M. Matsumoto, T. Kaneko, H. Yoshida, H. Morita, and T. Kanomata. Magnetic properties of ordered alloy AuMn₂. *Journal of Magnetism and Magnetic Materials*, 140:103, 1995. 2.1.9
- [6] S. C. Abrahams. A neutron diffraction study of ZrZn₂ at 298 K and at 5 K. *Zeitschrift fur Kristallographie*, 112:427, 1959. 4.2.4
- [7] A. A. Abrikosov. On the magnetic properties of superconductors of the second group. *Zhurnal Eksperimental'noi i Teoreticheskoi Fiziki*, 32:1442, 1957. 2.4, 2.4
- [8] A.A. Aczel, E. Baggio-Saitovitch, S.L. Budko, P.C. Canfield, J.P. Carlo, G.F. Chen, Pengcheng Dai, T. Goko, W.Z. Hu, G.M. Luke, J.L. Luo, N. Ni, D.R. Sanchez-Candela, F.F. Tafti, N.L. Wang, T.J. Williams, W. Yu, and Y.J. Uemura. Muon-spin-relaxation studies of magnetic order and superfluid density in antiferromagnetic NdFeAsO, BaFe₂As₂, and superconducting Ba_{1-x}K_xFe₂As₂. *Physical Review B*, 78:214503, 2008. 6.2.3
- [9] A. Aguayo and D. J. Singh. Itinerant ferromagnetism and quantum criticality in Sc₃In. *Physical Review B (R)*, 66:020401, 2002. 4.1
- [10] A. Aharoni. Demagnetizing factors for rectangular ferromagnetic prisms. *Journal of Applied Physics*, 83:3432, 1998. 9.2

-
- [11] A. Aharoni. *Introduction to the Theory of Ferromagnetism*. T. J. International Ltd., Padstow, Cornwall, 2000. 2.1.1, 2.1.1
 - [12] A. M. Alsmadi, S. Alyones, C. H. Mielke, R. D. McDonald, V. Zapf, M. M. Altarawneh, A. Lacerda, S. Chang, S. Adak, K. Kothapalli, and H. Nakotte. Radio-frequency measurements of UNiX compounds ($X = \text{Al, Ga, Ge}$) in high magnetic fields. *Journal of Magnetism and Magnetic Materials*, 321:3712, 2009. 3.9, 3.9, 3.9
 - [13] A. Amato. Heavy-fermion systems studied by μSR technique. *Reviews of Modern Physics*, 69:1119, 1997. 3.8
 - [14] A. Amato, M. J. Graf, A. Visser, H. Amitsuka, D. Andreica, and A. Schenck. Weak-magnetism phenomena in heavy-fermion superconductors: selected μSR studies. *Journal of Physics: Condensed Matter*, 16:4403, 2004. 3.8
 - [15] V. K. Anand, D. T. Adroja, and A. D. Hillier. Ferromagnetic cluster spin-glass behavior in PrRhSn_3 . *Physical Review B*, 85:014418, 2012. 2.3.1, 5.2, 5.3, 5.3, 5.3
 - [16] V. K. Anand, D. T. Adroja, A. D. Hillier, and J. Taylor. Signatures of spin-glass behavior in the induced magnetic moment system PrRuSi_3 . *Physical Review B*, 84:064440, 2011. 2.3
 - [17] V. K. Anand, A. D. Hillier, D. T. Adroja, A. M. Strydom, H. Michor, K. A. McEwen, and B. D. Rainford. Specific heat and μsr study on the noncentrosymmetric superconductor LaRhSi_3 . *Physical Review B*, 83:064522, 2011. 1, 2.4, 9.2, 9.2
 - [18] P. W. Anderson and J. M. Rowell. Probable observation of the Josephson superconducting tunneling effect. *Physical Review Letters*, 10:230, 1963. 2.4, 3.3
 - [19] J. Androulakis, N. Katsarakis, and J. Giapintzakis. Coexistence of ferromagnetic and glassy behavior in semiconducting $\text{LaNi}_{0.2}\text{Co}_{0.8}\text{O}_3$. *Journal of Applied Physics*, 91:9952, 2002. 5.3, 5.3
 - [20] J. Annett. *Superconductivity, Superfluids and Condensates*. Oxford University Press, NY, 2003. (document), 2.4, 2.4, 2.4, 2.4, 2.31
 - [21] D. Aoki, A. Huxley, E. Ressouche, D. Braithwaite, J. Flouquet, J. P. Brison, E. Lhotel, and C. Paulsen. Coexistence of superconductivity and ferromagnetism in URhGe . *Nature*, 413:613, 2001. 2.1.9
 - [22] A. Arrott. Criterion for ferromagnetism from observations of magnetic isotherms. *Physical Review*, 108:1394, 1957. 2.2.3, 4.2.2
 - [23] A. Arrott. Equations of state along the road to the Arrott's last plot. *Journal of Magnetism and Magnetic Materials*, 322:1047, 2010. 2.2.3

-
- [24] A. Arrott and J. E. Noakes. Approximate equation of state for Nickel near its critical temperature. *Physical Review Letters*, 19:786, 1967. 2.2.3, 4.2.2
 - [25] M. Asanuma and T. Yamadaya. Magnetic properties and nuclear magnetic resonance of diluted (Gd, Zr)Zn₂. *Journal of Applied Physics*, 39:1244, 1968. 1, 2.1.9, 5.1, 5.2, 5.3, 5.4
 - [26] M. F. Ashby. *Materials Selection in Mechanical Design*. Butterworth-Heinemann, 2011. (document), 3.18, 3.7, 8.2, 8.2, 8.5.2, 8.5.2, 8.5.2
 - [27] N. W. Ashcroft and N. D. Mermin. *Solid State Physics*. Brooks Cole, Belmont, CA, 1976. (document), 1, 2, 3, 2.1.4, 2.1.4, 2.1
 - [28] G. J. Athas, J. S. Brooks, S. J. Klepper, S. Uji, and M. Tokumoto. Tunnel diode oscillator application to high sensitivity de Haas-van Alphen and superconducting critical field studies of anisotropic organic conductors. *Review of Scientific Instruments*, 64:3248, 1993. (document), 3.9, 3.23, 3.9, 3.9
 - [29] R. Ballou, B. Barbara, Z. Gamishidze, R. Lemaire, R. Z. Levitin, and A. S. Markosyan. A spin-glass state in the itinerant magnet systems Yttrium-Cobalt-Manganese Y(Co_{1-x}Mn_x)₂ and Lutetium-Cobalt-Manganese Lu(Co_{1-x}Mn_x)₂. *Journal of Magnetism and Magnetic Materials*, 119:294, 1993. 2.1.9
 - [30] W. Bao, C. Broholm, G. Aeppli, S. A. Carter, P. Dai, T. F. Rosenbaum, J. M. Honig, P. Metcalf, and S. F. Trevino. Magnetic correlations and quantum criticality in the insulating antiferromagnetic, insulating spin liquid, renormalized Fermi liquid, and metallic antiferromagnetic phases of the Mott system V₂O₃. *Physical Review B*, 58:24, 1998. 2.1.6, 7.1, 7.2, 7.4
 - [31] N. V. Baranov, A. N. Titov, V. I. Maksimov, N. V. Toporova, A. Daoud-Aladine, and A. Podlesnyak. Antiferromagnetism in the ordered subsystem of Cr ions intercalated into Titanium Diselenide. *Journal of Physics: Condensed Matter*, 17:5255, 2005. 2.1.7, 6.2.5
 - [32] J. Bardeen, L. N. Cooper, and J. R. Schrieffer. Theory of superconductivity. *Physical Review*, 108:1175, 1957. 2.4, 9.2
 - [33] E. D. Bauer, V. A. Sidorov, S. Bobev, D. J. Mixson, J. D. Thompson, J. L. Sarrao, and M. F. Hundley. High-pressure investigation of the heavy-fermion antiferromagnet U₃Ni₅Al₁₉. *Physical Review B*, 71:014419, 2005. 7.2
 - [34] E. D. Bauer, V. S. Zapf, P. C. Ho, N. P. Butch, E. J. Freeman, C. Sirvent, and M. B. Maple. Non-fermi-liquid behavior within the ferromagnetic phase in URu_{2-x}Re_xSi₂. *Physical Review Letters*, 94:046401, 2005. 7.1
 - [35] E. D. Bauer, V. S. Zapf, P.-C. Ho, N. P. Butch, E. J. Freeman, C. Sirvent, and M. B. Maple. Non-Fermi-liquid behavior within the ferromagnetic phase in URu_{2-x}Re_xSi₂. *Physical Review Letters*, 94:046401, 2005. 4.2.3

-
- [36] J. G. Bednorz and K. A. Muller. Possible high T_c superconductivity in the Ba-La-Cu-O system. *Zeitschrift fur Physik B*, 64:189, 1986. 2.4
 - [37] D. Belitz and T. R. Kirkpatrick. First order transitions and multicritical points in weak itinerant ferromagnets. *Physical Review Letters*, 82:4707, 1999. 6.2.3
 - [38] D. Belitz, T. R. Kirkpatrick, and Jörg Rollbühler. Tricritical behavior in itinerant quantum ferromagnets. *Physical Review Letters*, 94:247205, 2005. 7.1
 - [39] A. Bid, A. Bora, and A. K. Raychaudhuri. Temperature dependence of the resistance of metallic nanowires of diameter $\geq 15\text{nm}$: Applicability of Bloch-Grüneisen theorem. *Physical Review B*, 74:035426, 2006. 9.2
 - [40] K. Binder. Spin glasses: Experimental facts, theoretical concepts, and open questions. *Reviews of Modern Physics*, 58:801, 1986. 2.3, 2.3.1, 2.3.2, 5.3
 - [41] P. K. Blaha, K. Schwarz, G. Madsen, D. Kvasnicka, and J. Luitz. An augmented plane wave + local orbitals program for calculating crystal properties. *WIEN2K package*, <http://www.wien2k.at>, 2001. 3.11, 6.3, 9.3
 - [42] S. Blundell. *Magnetism in Condensed Matter*. Oxford University Press, NY, 2009. (document), 2.1.1, 2.4, 2.1.4, 2.1.5, 2.2.2, 2.2.2, 2.2, 2.2.2
 - [43] S. J. Blundell. Spin-polarized muons in condensed matter physics. *Contemporary Physics*, 40:175, 1999. (document), 3.8, 3.8, 3.8, 3.21, 3.8, 3.8, 3.8
 - [44] H. J. Blythe. Paramagnetic susceptibility of ZrZn_2 . *Physical Letters*, 21:144, 1966. (document), 2.14, 2.1.9
 - [45] G. S. Boebinger, Y. Ando, A. Passner, T. Kimura, M. Okuya, J. Shimoyama, K. Kishio, K. Tamasaku, N. Ichikawa, and S. Uchida. Insulator-to-metal crossover in the normal state of $\text{La}_{2-x}\text{Sr}_x\text{CuO}_4$. *Physical Review Letters*, 77:5417, 1996. 1, 4.1
 - [46] N. Bohr. Collected works (1905-1911). *Elsevier B. V.*, 1:163, 1972. 2.1.1
 - [47] M. Born and R. Oppenheimer. Zur Quantentheorie der Molekeln. *Annalen der Physik*, 389:457, 1927. 3.11
 - [48] J. F. Boylan, W. Cornish, and J. A. Simpson. Radiopaque markers and medical devices comprising binary alloys of Titanium. *United States Patent and Trademark Office*, US20090099645 A1, 2009. 8.5.4
 - [49] J. F. Boylan and J. A. Simpson. Radiopaque markers comprising binary alloys of Titanium. *United States Patent and Trademark Office*, US20080288056 A1, 2008. 8.5.4
 - [50] M. Braden, O. Friedt, Y. Sidis, P. Bourges, M. Minakata, and Y. Maeno. Incommensurate magnetic ordering in $\text{Sr}_2\text{Ru}_{1-x}\text{Ti}_x\text{O}_4$. *Physical Review Letters*, 88:197002, 2002. 6.2.3, 6.2.3

-
- [51] M. Brando, W. Duncan, D. Moroni-Klementowicz, C. Albrecht, D. Grüner, R. Ballou, and F. Grosche. Logarithmic Fermi-Liquid Breakdown in NbFe₂. *Physical Review Letters*, 101:3, 2008. 7.1
 - [52] P. I. Branemark. Osseointegration and its experimental background. *The Journal of Prosthetic Dentistry*, 50:399, 1983. 8.4
 - [53] G. E. Brodale, R. A. Fisher, W. E. Fogle, N. E. Phillips, and J. Curen. The effect of spin-glass ordering on the specific heat of CuMn. *Journal of Magnetism and Magnetic Materials*, 31:1331, 1983. (document), 2.25
 - [54] S. L. Bud'ko and P. C. Canfield. Field-induced quantum criticality in YbAgGe. *Physica B*, 403:1230, 2008. 1
 - [55] S. L. Bud'ko and P. C. Canfield. Field-induced quantum criticality in YbAgGe. *Physica B*, 403:1230, 2008. 4.1
 - [56] J. C. Burley, J. F. Mitchell, and S. Short. Competing electronic ground states in La_{1-x}Ca_xCoO₃. *Physical Review B*, 69:054401, 2004. (document), 2.3.1, 2.23
 - [57] N. P. Butch and M. B. Maple. Evolution of critical scaling behavior near a ferromagnetic quantum phase transition. *Physical Review Letters*, 103:076404, 2009. 1, 4.1, 4.2.1, 4.2.2, 4.2.2, 4.2.2, 4.3
 - [58] F. C. Campbell. *Elements of Metallurgy and Engineering Alloys*. ASM International, Material Park, Ohio, 2008. (document), 8.3, 8.4, 8.3, 1, 3, 8.5, 8.3
 - [59] F. Canepa, M. Napoletano, A. Palenzona, O. Moze, and W. Kockelmann. Ferromagnetic and incommensurate antiferromagnetic order in a multi-sublattice itinerant magnet: Y₃Co₈Sn₄. *Journal of Physics: Condensed Matter*, 17:373, 2005. 2.1.9
 - [60] P. C. Canfield. Fishing the Fermi sea. *Nature Physics*, 4:167, 2008. 3.1
 - [61] P. C. Canfield and I. R. Fisher. High-temperature solution growth of intermetallic single crystals and quasicrystals. *Journal of Crystal Growth*, 225:155, 2001. 3.1
 - [62] P. C. Canfield and Z. Fisk. Growth of single crystals from metallic fluxes. *Philosophical Magazine B*, 65:1117, 1992. 3.1, 3.1, 3.1, 3.1
 - [63] V. Cannella and J. A. Mydosh. Magnetic ordering in Gold-Iron alloys. *Physical Review B*, 6:4220, 1972. (document), 2.3, 2.24, 2.3.1
 - [64] G. Cao, W. H. Song, Y. P. Sun, and X. N. Lin. Violation of the Mott-Ioffe-Regel limit: high-temperature resistivity of itinerant magnets Sr_{n+1}Ru_nO_{3n+1} (n = 2,3) and CaRuO₃. *Solid State Communications*, 131:331, 2004. 2.1.9
 - [65] J. P. Carlo, T. Goko, I. M. Gat-Malureanu, P. L. Russo, A. T. SAvici, A. A. Aczel, G. J. MacDougall, J. A. Rodrigues, T. J. Williams, G. M. Luke, C. R.

- Wiebe, Y. Yoshida, S. Nakatsuji, Y. Maeno, T. Taniguchi, and Y. J. Uemura. New magnetic phase diagram of $(\text{Sr}, \text{Ca})_2\text{RuO}_4$. *Nature Materials*, 11:323, 2012. 4.2.4, 6.2.3, 6.2.3, 6.4, 6.2.3, 6.2.3
- [66] A. Carrington, I. J. Bonalde, R. Prozorov, R. W. Giannetta, A. M. Kini, J. Schlueter, H. H. Wang, U. Geiser, and J. M. Williams. Low-temperature penetration depth of $\kappa\text{-(ET)}_2\text{Cu}[\text{N}(\text{CN})_2\text{Br}]$ and $\kappa\text{-(ET)}_2\text{Cu}(\text{NCS})_2$. *Physical Review Letters*, 83:4172, 1999. 3.9
- [67] P. J. Cascone. Dental prosthesis method and alloys. *United States Patent and Trademark Office*, US 7892480 B2, 2011. 8.4, 8.5.2, 8.5.4
- [68] H. Chandler. *Heat Treater's Guide: Practices and Procedures for Nonferrous Alloys*. ASM International, Material Park, Ohio, 1996. 1, 2, 5
- [69] M. Chefki, M. M. Abd-Elmeguid, H. Micklitz, C. Huhnt, and W. Schlabititz. Pressure-induced transition of the sublattice magnetization in EuCo_2P_2 : Change from local moment Eu (4f) to itinerant Co (3d) magnetism. *Physical Review Letters*, 80:802, 1998. 5.1
- [70] X. Chen, H. Niu, and Y. Li. Modeling hardness of polycrystalline materials and bulk metallic glasses. *Intermetallics*, 19:1275, 2011. 8.5.2
- [71] E. Choi, G. Chern, and N. B. Perkins. Helimagnons in a chiral ground state of the pyrochlore antiferromagnets. *Europhysics Letters*, 101:37004, 2013. 2.1.9
- [72] C. W. Chu, L. Gao, F. Chen, Z. J. Huang, R. L. Meng, and Y. Y. Xue. Superconductivity above 150 K in $\text{HgBa}_2\text{Ca}_2\text{Cu}_3\text{O}_{8+}$ at high pressures. *Nature*, 365:323, 1993. 2.4
- [73] C. C. Chusuei and D. W. Goodman. *X-ray Photoelectron Spectroscopy*. Academic Press, NY, 2002. 3.6, 3.6, 3.6, 6.2.1
- [74] R. B. Clover and W. P. Wolf. Magnetic susceptibility measurements with a tunnel diode oscillator. *Review of Scientific Instruments*, 41:617, 1970. 3.9, 3.9
- [75] T. Coffey, Z. Bayindir, J. F. DeCarolis, M. Bennett, G. Esper, and C. C. Agosta. Measuring radio frequency properties of materials in pulsed magnetic fields with a tunnel diode oscillator. *Review of Scientific Instruments*, 71:12, 2000. 3.9, 3.9, 3.9
- [76] P. Coleman. Theories of non-Fermi liquid behavior in heavy fermions. *Phys. B*, 259:353, 1999. 4.1
- [77] P. Coleman, C. Pepin, Q. Si, and R. Ramazashvili. How do Fermi liquids get heavy and die? *Journal of Physics: Condensed Matter*, 723:723, 2001. 7.4
- [78] P. Coleman and A. J. Schofield. Quantum criticality. page 226, 2005. 7.2
- [79] B. R. Coles. Transitions from local moment to itinerant magnetism as a function of composition in alloys. *Physica B*, 91:167, 1977. 5.1

-
- [80] Planck Collaboration. Planck 2013 results. overviews of products and scientific results. *Astronomy and Astrophysics*, 571:A1, 2014. 2.4
 - [81] E. W. Collings. *Applied Superconductivity, Metallurgy, and Physics of Titanium Alloys*. Plenum Press, NY, 1985. 2, 3
 - [82] V. B. Compton and B. T. Matthias. The crystal structure of Sc_3In . *Acta Crystallographica*, 15:94, 1962. 4.2, 5.2
 - [83] M. Continentino. On the zero temperature critical point in heavy fermions. *Physica B*, 101:197, 1996. 4.1
 - [84] R. A. Cooper, Y. Wang, B. Vignolle, O. J. Lipscombe, S. M. Hayden, Y. Tanabe, T. Adachi, Y. Koike, M. Nohara, H. Takagi, C. Proust, and N. E. Hussey. Anomalous criticality in the electrical resistivity of $\text{La}_{2-x}\text{Sr}_x\text{CuO}_4$. *Science*, 323:603, 2009. 7.1
 - [85] L. Cui, H. Fujii, N. Tsuji, and K. Nogi. Friction stir welding of a high Carbon steel. *Scripta Materialia*, 56:637, 2007. 8.3, 8.5.2
 - [86] B. D. Cullity and S. R. Stock. *Elements of X-ray Diffraction*. Prentice Hall, Upper Saddle River, NJ, 2001. (document), 3.2, 3.2, 3.6, 3.2
 - [87] P. Curie. Proprietes magnetiques des corps a diverses temperatures. *Annales de Chimie et de Physique*, 5:289, 1895. 2.1.2
 - [88] S. Curtarolo, D. Morgan, K. Persson, J. Rodgers, and G. Ceder. Predicting crystal structures with data mining of quantum calculations. *Physical Review Letters*, 91:135503, 2003. 2.1.9, 5.1
 - [89] S. Curtarolo, W. Setyawan, S. Wang, J. Xue, K. Yang, R. H. Taylor, L. J. Nelson, G. L. W. Hart, S. Sanvito, M. Buongiorno-Nardelli, N. Mingo, and O. Levy. AFLOWLIB.ORG: a distributed materials properties repository from high-throughput ab initio calculations. *Computational Materials Science*, 58:227, 2012. 2.1.9
 - [90] Y. F. Dai, H. Zhang, S. Y. Zhou, B. Y. Pan, X. Qiu, X. C. Hong, T. Y. Guan, J. K. Dong, Y. Chen, and S. Y. Li. Unveiling the quantum critical point of an Ising chain. *arXiv:1103.0095v1*, 2011. 1, 4.1
 - [91] J. R. L. de Almeida nad D. J. Thouless. Stability of the Sherrington-Kirkpatrick solution of a spin glass model. *Journal of Physics A*, 11:983, 1978. (document), 2.3.2, 2.28, 2.3.2
 - [92] C. de la Cruz, Q. Huang, J. W. Lynn, J. Li, W. Ratcliff II, J. L. Zarestky, H. A. Mook, G. F. Chen, J. L. Luo, N. L. Wang, and P. Dai. Magnetic order close to superconductivity in the iron-based layered $\text{LaO}_{1-x}\text{F}_x\text{FeAs}$ systems. *Nature*, 453:899, 2008. 6.3
 - [93] C. T. Van Degrift. Tunnel diode oscillator for 0.001 ppm measurements at low temperatures. *Review of Scientific Instruments*, 46:599, 1975. 3.9, 3.9

-
- [94] A. del Moral, K. Kulakowski, C. de la Fuente, C. Abadia, A. Z. Maksymowicz, M. Magdon, and J. I. Arnaudas. Anisotropic magnetostriction of an amorphous itinerant magnet Y_2Fe and a simple random crystal-field model. *Physical Review B*, 57:5320, 1998. 2.1.9
 - [95] H. T. Diep. *Frustrated Spin Systems*. World Scientific Publishing, Danvers, MA USA, 2004. 2.3
 - [96] S. Doniach. The Kondo lattice and weak antiferromagnetism. *Physica B+C*, 91:231, 1977. 1, 4.1
 - [97] H. C. Donkersloot and J. H. N. van Vucht. Martensitic transformations in Gold-Titanium, Palladium-Titanium and Platinum-Titanium alloys near the equiatomic composition. *Journal of the Less Common Metals*, 20:83, 1970. 6.2.1
 - [98] J. L. Dormann, L. Bessais, and D. Fiorani. A dynamic study of small interacting particles: superparamagnetic model and spin-glass laws. *Journal of Physics C: Solid State Physics*, 21:2015, 1988. 5.3
 - [99] L. Drigo, F. Durantel, A. Audouardc, and G. Ballon. Tunnel diode oscillator-based measurement of quantum oscillations amplitude in pulsed high magnetic elds: a quantitative field-dependent study. *The European Physical Journal: Applied Physics*, 52:10401, 2010. (document), 3.23, 3.9
 - [100] L. Dudy, J. D. Denlinger, L. Shu, M. Janoschek, J. W. Allen, and M.B. Maple. Yb valence change in $\text{Ce}_{1-x}\text{Yb}_x\text{CoIn}_5$ from spectroscopy and bulk properties. *Physical Review B*, 88:165118, 2013. 6.2.1
 - [101] S. R. Dunsiger, J. P. Carloand T. Goko, G. Nieuwenhuys, T. Prokscha, A. Suter, E. Morenzoni, D. Chiba, Y. Nishitani, T. Tanikawa, F. Matsukura, H. Ohno, J. Ohe, S. Maekawa, and Y. J. Uemura. Spatially homogeneous ferromagnetism of $(\text{Ga}, \text{Mn})\text{As}$. *Nature Materials*, 9:2010, 2010. 3.8
 - [102] K. Edalati and Z. Horita. Universal plot for hardness variation in pure metals processed by high-pressure torsion. *Materials Transactions*, 51:1051, 2010. 8.5.2
 - [103] D. M. Edwards and E. P. Wohlfarth. Magnetic isotherms in the band model of ferromagnetism. *Proceedings of the Royal Society A*, 303:127, 1968. 2.1.8
 - [104] M. Elfresh. *Fundamentals of Magnetism and Magnetic Measurements*. Quantum Design Inc., 1994. 3.3
 - [105] C. N. Elias, J. H. C. Lima, R. Valiev, and M. A. Meyers. Biomedical applications of Titanium and its alloys. *Journal of Metals*, page 46, 2008. 8.4, 8.5.2, 8.5.2, 8.5.4
 - [106] H. Eschrig and K. Koepernik. $\text{Na}_{0.75}\text{CoO}_2$ - an itinerant magnet? *Physica C*, 460:495, 2007. 2.1.9

-
- [107] A. Faria, R. Rodrigues, Q. Claro, W. Mattos, and R. Ribeiro. Wear resistance of experimental titanium alloys for dental applications. *Journal of the Mechanical Behavior of Biomedical Materials*, 4:1873, 2011. 8.4
 - [108] E. Fawcett. Spin-density-wave antiferromagnetism in Chromium. *Reviews of Modern Physics*, 60:209, 1988. (document), 2.1.6, 2.11, 6.3
 - [109] D. K. Finnemore, J. E. Ostenson, S. L. Budko, G. Lapertot, and P. C. Canfield. Thermodynamic and transport properties of superconducting MgB_2 . *Physical Review Letters*, 86:2420, 2001. 9.2
 - [110] I. Fischer and A. Rosch. Field-tuned quantum critical point of antiferromagnetic metals. *Physical Review B*, 71:184429, 2005. 7.1
 - [111] J. Fischer. Mechanical, thermal, and chemical analyses of the binary system Au-Ti in the development of a dental alloy. *Journal of Biomedical Materials Research*, 52:678, 2000. 8.4, 8.5.1, 8.5.2
 - [112] K. H. Fischer. Static properties of spin glasses. *Physical Review Letters*, 34:1438, 1975. (document), 2.26, 2.3.2
 - [113] I. R. Fisher, M. C. Shapiro, and J. G. Analytis. Principles of crystal growth of intermetallic and oxide compounds from molten solutions. *Philosophical Magazine*, 92:2401, 2012. 3.1
 - [114] M. E. Fisher. Relation between the specific heat and susceptibility of an antiferromagnet. *Philosophical Magazine*, 7:1731, 1962. 6.2.2, 7.2
 - [115] M. E. Fisher and J. S. Langer. Resistive anomalies at magnetic critical points. *Physical Review Letters*, 20:665, 1968. 6.2.2, 7.2
 - [116] Z. Fisk and J. P. Remeika. *Growth of Single Crystals from Molten Metal Fluxes*. Elsevier Science Publishers B. V., Amsterdam, Netherlands, 1989. 3.1, 3.1
 - [117] G. C. Fletcher and R. P. Addis. The magnetic state of the ϵ phase of Iron. *Journal of Physics F: Metal Physics*, 4:1951, 1974. 6.2.6
 - [118] J. M. Franz and D. J. Sellmyer. Magnetic interactions and high-field magnetization in dilute magnetic alloys. *Physical Review B*, 8:2083, 1973. 6.2.5
 - [119] G. S. Fulcher. Analysis of recent measurements of the viscosity of glasses. *Journal of American Ceramic Society*, 8:339, 1925. 2.3.1, 5.3
 - [120] P. Fulde. *Electron Correlations in Molecules and Solids*. Springer-Verlag, Berlin, Heidelberg, 1995. 2.1.9
 - [121] M. Gabay and G. Toulouse. Coexistence of spin-glass and ferromagnetic ordering. *Physical Review Letters*, 47:201, 1981. (document), 2.28, 2.3.2
 - [122] G. Gafner. The development of 990 Gold-Titanium: its production, use and properties. *Gold Bulletin*, 22:112, 1989. 8.4, 8.5.1

-
- [123] F. Gao, J. He, E. Wu, S. Liu, D. Yu, D. Li, S. Zhang, and Y. Tian. Hardness of covalent crystals. *Physical Review Letters*, 91:015502, 2003. 8.4, 8.5.2, 8.5.2
 - [124] W. E. Gardner, T. F. Smith, B. W. Howlett, C. W. Chu, and A. Sweedler. Magnetization measurements and pressure dependence of the Curie point of the phase Sc_3In . *Physical Review*, 166:577, 1968. (document), 1, 2.15, 2.1.9, 4.1, 4.2.1, 4.2.2, 5.1, 6.2.6, 7.2
 - [125] M. Garst, L. Fritz, A. Rosch, and M. Vojta. Dimensional crossover in quantum critical metallic magnets. *Physical Review B*, 78:235118, 2008. 7.2
 - [126] V. A. Gasparov, A. Audouard, L. Drigo and A. I. Rodygin, C. T. Lin, W. P. Liu, M. Zhang, A. F. Wang X. H. Chen, H. S. Jeevan, J. Maiwald, and P. Gegenwart. Upper critical magnetic field of $\text{K}_x\text{Fe}_{2y}\text{Se}_2$ and $\text{Eu}_{0.5}\text{K}_{0.5}\text{Fe}_2\text{As}_2$ single crystals. *Physical Review B*, 87:094508, 2013. 3.9
 - [127] V. A. Gasparov, N. S. Sidorov, I. I. Zver'kova, S. S. Khassanov, and M. P. Kulakov. Electron transport in diborides: observation of superconductivity in ZrB_2 . *Journal of Experimental and Theoretical Physics Letters*, 73:532, 2001. 9.1
 - [128] I. M. Gat-Malureanu, J. P. Carlo, T. Goko, A. Fukaya, T. Ito, P. P. Kyriakou, M. I. Larkin, G. M. Luke, P. L. Russo, A. T. Savici, C. R. Wiebe, and K. Yoshimura nad Y. J. Uemura. Muon spin relaxation and susceptibility measurements of an itinerant-electron system $\text{Sr}_{1-x}\text{Ca}_x\text{RuO}_3$: quantum evolution from ferromagnet to paramagnet. *Physical Review B*, 84:224415, 2011. 4.2.4, 6.2.3, 6.2.3, 6.4, 6.2.3
 - [129] P. Gegenwart, J. Custers, C. Geibel, K. Neumaier, T. Tayama, K. Tenya, O. Trovarelli, and F. Steglich. Magnetic-field induced quantum critical point in YbRh_2Si_2 . *Physical Review Letters*, 89:056402, 2002. 1, 7.1, 7.1, 7.2, 7.4
 - [130] P. Gegenwart, J. Custers, Y. Tokiwa, C. Geibel, and F. Steglich. Ferromagnetic quantum critical fluctuations in $\text{YbRh}_2(\text{Si}_{0.95}\text{Ge}_{0.05})_2$. *Physical Review Letters*, 94:076402, 2005. 7.2
 - [131] P. Gegenwart, Q. Si, and F. Steglich. Quantum criticality in heavy-fermion metals. *Nature Physics*, 4:186, 2008. 4.1, 7.2
 - [132] D. J. W. Geldart and D. Neilson. Quantum critical behavior in the insulating region of the two-dimensional metal-insulator transition. *Physical Review B*, 76:193304, 2007. 1, 4.1
 - [133] M. Getzlaff. *Fundamentals of Magnetism*. Springer-Verlag, Berlin, Heidelberg, 2008. (document), 2.5, 2.1.2
 - [134] J. J. Gilman. *Chemistry and Physics of Mechanical Hardness*. John Wiley and Sons, Hoboken, NJ, 2009. (document), 3.7, 3.7, 3.19, 3.7, 8.1, 8.1, 8.3, 8.3
 - [135] J. J. Gilman, R. W. Cumberland, and R. B. Kaner. Design of hard crystals. *International Journal of Refractory Metals and Hard Materials*, 24:1, 2006. 8.5.4

-
- [136] V.L. Ginzburg and L.D. Landau. On the theory of superconductivity. *Zhurnal Eksperimental'noi i Teoreticheskoi Fiziki*, 20:1064, 1950. 2.4
 - [137] P. A. Goddard, J. Singleton, P. Sengupta, R. D. McDonald, T. Lancaster, S. J. Blundell, F. L. Pratt, S. Cox, N. Harrison, J. L. Manson, H. I. Southerland, and J. A. Schlueter. Experimentally determining the exchange parameters of quasi-two-dimensional Heisenberg magnets. *New Journal of Physics*, 10:083025, 2008. 3.3
 - [138] J. B. Goodenough. *Magnetism and the Chemical Bond*. John Wiley and Sons, NY, 1963. 2.1.3
 - [139] W. D. Gregory, T. P. Sheahen, and J. F. Cochran. Superconducting transition and critical field of pure Gallium single crystals. *Physical Review*, 150:315, 1966. 4.1, 4.2.1, 4.2.2
 - [140] J. Grewe, J. S. Schilling, K. Ikeda, and Jr. K. A. Gschneidner. Anomalous behavior of the weak itinerant ferromagnet Sc_3In under hydrostatic pressure. *Physical Review B*, 40:9017, 1989. (document), 1, 2.15, 2.1.9, 5.1, 6.2.6, 7.2
 - [141] R. B. Griffiths. Nonanalytical behavior above the critical point in a random Ising ferromagnet. *Physical Review Letters*, 23:1, 1969. 4.2.3
 - [142] S. A. Grigera, R. S. Perry, A. J. Schofield, M. Chiao, S. R. Julian, G. G. Lonzarich, S. I. Ikeda, Y. Maeno, A. J. Millis, and A. P. Mackenzie. Magnetic field-tuned quantum criticality in the metallic ruthenate $\text{Sr}_3\text{Ru}_2\text{O}_7$. *Science*, 294:329, 2001. 7.1, 7.2
 - [143] E. Grüneisen. Theorie des festen Zustandes einatomiger Elemente. *Annalen der Physik*, 344:257, 1912. 7.2
 - [144] R. Guinebretiere. *X-ray Diffraction by Polycrystalline Materials*. ISTE, Newport Beach, CA, 2007. (document), 3.7, 3.8
 - [145] S. Guo, C. Ng, J. Lu, and C. T. Liu. Effect of valence electron concentration on stability of fcc or bcc phase in high entropy. *Journal of Applied Physics*, 109:103505, 2011. 8.4, 8.5.2
 - [146] K. Hagdorn, D. Hohlwein, J. Ihringer, K. Knorr, W. Prandl, H. Ritter, H. Schmid, and T. Zeiske. Canted antiferromagnetism and magnetoelastic coupling in metallic $\text{Ho}_{0.1}\text{Ca}_{0.9}\text{MnO}_3$. *European Physics Journal*, 11:243, 1999. 3.8
 - [147] E. O. Hall. Variation of hardness of metals with grain size. *Nature*, 173:948, 1954. (document), 8.3
 - [148] A. Hamann, D. Lamago, Th. Wolf, H. von Löhneysen, and D. Reznik. Magnetic blue phase in the chiral itinerant magnet MnSi . *Physical Review Letters*, 107:037207, 2011. 2.1.9

-
- [149] K. Han, D. V. Edmonds, and G. D. W. Smith. Optimization of mechanical properties of high-Carbon pearlitic steels with Si and V additions. *Metallurgical and Materials Transactions A*, 32:1314, 2001. 8.5.2
 - [150] H. Hasegawa. Specific heat due to spin fluctuations in nearly and weakly antiferromagnetic metals. *Journal of the Physical Society of Japan*, 38:107, 1975. 7.2
 - [151] H. Hasegawa and T. Moriya. Effect of spin fluctuations on itinerant electron antiferromagnetism. *Journal of the Physical Society of Japan*, 36:1542, 1974. 2.1.8, 6.2.2, 7.2
 - [152] M. Hattori, K. Hasegawa, M. Yoshinari, E. Kawada, Y. Oda, and T. Okabe. The effect of fluoride and albumin on corrosion of titanium. *Dental Materials Journal*, 20:16, 2001. 8.4
 - [153] E. E. Havinga, H. Damsma, and M. H. van Maaren. Oscillatory dependence of superconductive critical temperature on number of valency electrons in Cu_3Au -type alloys. *Journal of Physics and Chemistry of Solids*, 31:2653, 1970. 9.1
 - [154] R. S. Hayano, Y. J. Uemura, J. Imazato, N. Nishida, T. Yamazaki, and R. Kubo. Zero- and low-field spin relaxation studied by positive muons. *Physical Review B*, 20:850, 1979. 3.8, 4.2.4, 6.2.3
 - [155] D. Heiman, E. D. Isaacs, P. Becla, and S. Foner. High-field magnetization of (Cd, Mn)Te. *Physical Review B*, 35:3307, 1987. 6.2.5
 - [156] W. Heisenberg. Zur Theorie des Ferromagnetismus. *Zeitschrift fur Physik*, 49:619, 1928. 1, 2.1.8, 6.1
 - [157] K. Herrmann. *Hardness Testing: Principles and Applications*. ASM International, Material Park, Ohio, 2011. (document), 8.3, 8.1, 8.3
 - [158] I. Hetel, T. R. Lemberger, and M. Randeria. Quantum critical behavior in the superfluid density of strongly underdoped ultrathin Copper Oxide films. *Nature Physics*, 3:700, 2007. 1, 4.1
 - [159] W. Ho, W. Chen, S. Wu, and H. Hsu. Structure, mechanical properties, and grindability of dental TiZr alloys. *Journal of Materials Science: Materials in Medicine*, 19:3179, 2008. 8.4
 - [160] P. C. Hohenberg and B. I. Halperin. Theory of dynamic critical phenomena. *Reviews of Modern Physics*, 49:435, 1977. 2.3.1
 - [161] <http://www.aflowlib.org/index.html>; S. Curtarolo, D. Morgan, K. Persson, J. Rodgers, and G. Ceder. Predicting crystal structures with data mining of quantum calculations. *Physical Review Letters*, 91:135503, 2003. 9.1, 9.3
 - [162] S. L. Huang, L. X. Guan, J. B. Yi, B. C. Zhao, Y. Wu, Z. C. Fan, T. C. Sum, J. Ding, and L. Wang. Magnetic and electric transport properties of $\text{Nd}_{0.75}\text{Sr}_{1.25}\text{Co}_{1-x}\text{Mn}_x\text{O}_4$. *Journal of Applied Physics*, 104:123904, 2008. 5.2

-
- [163] J. G. Huber, M. B. Maple, D. Wohlleben, and G. S. Knapp. Magnetic properties of ZrZn_2 under pressure. *Solid State Communications*, 16:211, 1975. 6.2.6
 - [164] G. Humpston and D. M. Jacobson. A new high strength Gold bond wire. *Gold Bulletin*, 25:132, 1992. 8.4, 8.5.1
 - [165] D. Huser, L. E. Wenger, A. J. van Duynveldt, and J. A. Mydosh. Dynamical behavior of the susceptibility around the freezing temperature in (Eu, Sr)S. *Physical Review B*, 27:3100, 1983. (document), 2.24, 2.3.1
 - [166] N. Huy, a. Gasparini, J. Klaasse, a. de Visser, S. Sakarya, and N. van Dijk. Ferromagnetic quantum critical point in URhGe doped with Ru. *Physical Review B*, 75:60, 2007. 7.2
 - [167] K. Ikeda and Jr. K. A. Gschneider. Disappearance of the heat capacity peak of Sc_3In around the Curie temperature in high magnetic fields. *Journal of Magnetism and Magnetic Materials*, 22:207, 1981. 1, 5.1, 5.2
 - [168] K. Ikeda and Jr. K. A. Gschneider. Disappearance of the heat capacity peak of Sc_3In around the Curie temperature in high magnetic fields. *Journal of Magnetism and Magnetic Materials*, 22:207, 1981. 4.1, 4.2.2
 - [169] A. Ishigaki and T. Moriya. On the theory of spin fluctuations around the magnetic instabilities effects of zero-point fluctuations. *Journal of the Physical Society of Japan*, 67:3924, 1998. 7.2
 - [170] A. Ishikawa. Electrical resistivity due to antiferromagnetic spin waves in Cr. *Journal of the Physical Society of Japan*, 51:441, 1982. 7.2
 - [171] Y. Ishikawa, Y. Noda, Y. J. Uemura, C. F. Majkrzak, and G. Shirane. Paramagnetic spin fluctuations in the weak itinerant-electron ferromagnet MnSi. *Physical Review B*, 31:5884, 1985. 7.2
 - [172] R. Jaramillo, Y. Feng, J. C. Lang, Z. Islam, G. Srajer, P. B. Littlewood, D. B. McWhan, and T. F. Rosenbaum. Breakdown of the Bardeen-Cooper-Schrieffer ground state at a quantum phase transition. *Nature*, 459:405, 2009. 7.1
 - [173] R. Jaramillo, Y. Feng, J. Wang, and T. F. Rosenbaum. Signatures of quantum criticality in pure Cr at high pressure. *Proceedings of the National Academy of Sciences*, 107:13631, 2010. 7.1
 - [174] A. Jayaraman, A. R. Hutson, J. H. McFee, A. S. Coriell, and R. G. Maines. Hydrostatic and uniaxial pressure generation using teflon cell container in conventional piston cylinder device. *Review of Scientific Instruments*, 38:44, 1967. 3.5
 - [175] J. R. Jeffries, N. A. Frederick, E. D. Bauer, Hikari Kimura, V. S. Zapf, K. D. Hof, T. A. Sayles, and M. B. Maple. Superconductivity and non-Fermi liquid behavior near antiferromagnetic quantum critical points in $\text{CeRh}_{1-x}\text{Co}_x\text{In}_5$. *Physical Review B*, 72:024551, 2005. 7.1, 7.1

-
- [176] T. Jeong. Electronic structure of nearly ferromagnetic compound HfZn_2 . *Solid State Communications*, 138:265, 2006. 2.1.9, 5.4
 - [177] T. Jeong and Y. Kwon. Magnetism and electronic structure of $\text{Sc}_{3.1}\text{In}$. *Journal of the Korean Physical Society*, 51:629, 2007. 4.2, 4.2.1, 4.2.2
 - [178] A. Jesche and P. C. Canfield. Single crystal growth from light, volatile and reactive materials using Lithium and Calcium flux. *Philosophical Magazine*, 94:2372, 2014. 3.1
 - [179] C. B. Johansson. *On Tissue Reactions to Metal Implants*. PhD Thesis, University of Gothenburg, Sweden, 1991. 8.4, 8.5.2
 - [180] B. D. Josephson. Possible new effects in superconductive tunneling. *Physics Letters*, 1:251, 1962. 2.4, 3.3
 - [181] S. R. Julian, C. Pfleiderer, F. M. Grosche, N. D. Mathur, G. J. McMullan, A. J. Diver, I. R. Walker, and G. G. Lonzarich. The normal states of magnetic d and f transition metals. *Journal of Physics: Condensed Matter*, 8:9675, 1996. 7.1, 7.2
 - [182] H. Kadowaki, K. Motoya, Taku J. Sato, J. W. Lynn, J. a. Fernandez-Baca, and J. Kikuchi. Quantum phase transition in the itinerant antiferromagnet $(\text{V}_{0.9}\text{Ti}_{0.1})_2\text{O}_3$. *Physical Review Letters*, 101:096406, 2008. 7.1, 7.4
 - [183] H. Kadowaki, Y. Tabata, M. Sato, N. Aso, S. Raymond, and S. Kawarazaki. Quantum critical point of itinerant antiferromagnet in the heavy fermion. *Physical Review Letters*, 96:016401, 2006. 4.1
 - [184] H. Kadowaki, Y. Tabata, M. Sato, N. Aso, S. Raymond, and S. Kawarazaki. Quantum critical point of itinerant antiferromagnet in the heavy fermion. *Physical Review Letters*, 96:1, 2006. 7.1, 7.2
 - [185] J. A. Kaeck. Electron-spin susceptibilities of the liquid binary alkali metal alloys. *Physical Review*, 175:897, 1968. 2.1
 - [186] S. L. Kakani. *Material Science*. New Age International, 2006. 9.1
 - [187] Y. Kamihara, H. Hiramatsu, M. Hirano, R. Kawamura, H. Yanagi, T. Makiya, and H. Hosono. Iron-based layered superconductor: LaOFeP . *Journal of the American Chemical Society*, 128:10012, 2006. 2.4
 - [188] M. G. Kanatzidis, R. Pöttgen, and W. Jeitschko. The metal flux: a preparative tool for the exploration of intermetallic compounds. *Angewandte Chemie International Edition*, 44:6996, 2005. 3.1
 - [189] R. B. Kaner, J. J. Gilman, and S. H. Tolbert. Designing superhard materials. *Science*, 308:1268, 2010. 8.1
 - [190] T. Kato and T. Saita. Multi-canonical Monte-Carlo simulation on ferromagnetism-cluster glass transition in Pd-Mn alloys. *Physica B*, 284:1347, 2000. 5.2

-
- [191] R. J. Keizer, A. Visser, A. A. Menovsky, J. J. M. Franse, A. Amato, F. N. Gygax, M. Pinkpank, and A. Schenck. Magnetism in heavy-fermion $\text{U}(\text{Pt},\text{Pd})_3$ studied by μSR . *Journal of Physics: Condensed Matter*, 11:8591, 1999. 3.8
 - [192] B. Kempf, H. M. Rigelstein, T. Baumgaerther, and L. Voelkl. Manufacture of cast Gold-Titanium alloy dental or jewelry parts. *European Patent Application*, EP 717118 A2 19960619, 1996. 8.4, 8.5.2, 8.5.2, 8.5.4
 - [193] B. Kempf, H. M. Rigelstein, A. Voelcker, and U. Birkholz. Dental construction element for use in a casting-on process. *European Patent Application*, EP 729739 A2 19960904, 1996. 8.4, 8.5.2, 8.5.4
 - [194] N. Kernavanois, S. Raymond, E. Ressouche, B. Grenier, J. Flouquet, and P. Lejay. Neutron diffraction study under pressure of the heavy-fermion compound CePd_2Si_2 . *Physical Review B*, 71:064404, 2005. 2.1.9
 - [195] M. Kikuchi, Y. Takada, S. Kiyosue, M. Yoda, M. Woldu, Z. Cai, O. Okuno, and T. Okabe. Grindability of cast Ti-Cu alloys. *Dental Materials*, 19:375, 2003. 8.4
 - [196] M. Kikuchi, Y. Takada, S. Kiyosue, M. Yoda, M. Woldu, Z. Cai, O. Okuno, and T. Okabe. Mechanical properties and microstructures of cast Ti-Cu alloys. *Dental Materials*, 19:174, 2003. 8.4, 8.5.2
 - [197] M. Kikuchi, M. Takahashi, T. Okabe, and O. Okuno. Grindability of cast Ti-Ag and Ti-Cu alloys. *Dental Materials*, 22:191, 2003. 8.4
 - [198] P. J. C. King, R. Renzi, S. P. Cottrell, A. D. Hillier, and S. F. J. Fox. ISIS muons for materials and molecular science studies. *Physica Scripta*, 88:068502, 2013. 3.8
 - [199] H. Kitagawa, N. Kojima, and T. Nakajima. Studies of mixed-valence states in three-dimensional halogen-bridged Gold compounds, $\text{Cs}_2\text{Au}'\text{Au}'''\text{X}_6$, ($\text{X} = \text{Cl}, \text{Br}$ or I). Part 2: x-ray photoelectron spectroscopic study. *Journal of the Chemical Society, Dalton Transactions*, 11:3121, 1991. 6.2.1
 - [200] C. Kittel. *Introduction to Solid State Physics*. John Wiley and Sons, Hoboken, NJ, 1996. 3.5
 - [201] O. Klein, S. Donovan, M. Dressel, and G. Gruner. Microwave cavity perturbation technique. *International Journal of Infrared and Millimeter Waves*, 14:2423, 1993. 3.9
 - [202] Z. Kletowski. Resistance of some Lanthanum and Lutetium compounds of the type $(\text{La},\text{Lu})\text{Me}_3$. *Physica Status Solidi*, 108:363, 1988. 9.1, 9.2
 - [203] Z. Kletowski, R. Cloots, M. Ausloos, M. Pekala, A. J. Hurd, and G. Vacquier. *Supermaterials, NATO Science Series*. Springer-Verlag, Berlin, Heidelberg, 2001. 3.1

-
- [204] Z. Kletowski, R. Fabrowski, P. Slawinski, and Z. Henkie. Resistance of some REMe_3 compounds, $\text{RE} = \text{La}$ and Lu , $\text{Me} = \text{Sn}$, Pb , In , and Ga . *Journal of Magnetism and Magnetic Materials*, 166:361, 1997. 9.1, 9.2
 - [205] W. Knafo, S. Raymond, J. Flouquet, B. Fak, M. A. Adams, P. Haen, F. Lapierre, S. Yates, and P. Lejay. Anomalous scaling behavior of the dynamical spin susceptibility of $\text{Ce}_{0.925}\text{La}_{0.075}\text{Ru}_2\text{Si}_2$. *Physical Review B*, 70:174401, 2004. 4.1
 - [206] G. Knebel, D. Aoki, J. P. Brison, and J. Flouquet. The quantum critical point in CeRhIn_5 : A resistivity study. *Journal of the Physical Society of Japan*, 77:114704, 2008. 1, 7.1, 7.1, 7.2, 7.4
 - [207] G. Knebel, D. Braithwaite, P. C. Canfield, G. Lapertot, and J. Flouquet. Electronic properties of CeIn_3 under high pressure near the quantum critical point. *Physical Review B*, 65:1, 2001. 1, 7.1, 7.1, 7.2, 7.2, 7.4
 - [208] W. Kohn and L. J. Sham. Self-consistent equations including exchange and correlation effects. *Physical Review*, 140:A1133, 1965. 3.11
 - [209] K. Kojima, Y. Fudamoto, M. Larkin, G.M. Luke, J. Merrin, B. Nachumi, Y.J. Uemura, N. Motoyama, H. Eisaki, S. Uchida, K. Yamada, Y. Endoh, S. Hosoya, B.J. Sternlieb, and G. Shirane. Reduction of ordered moment and Neel temperature of quasi one-dimensional antiferromagnets Sr_2CuO_3 and Ca_2CuO_3 . *Physical Review B*, 78:1787, 1997. 6.2.3, 6.2.3
 - [210] K. M. Kojima, J. Yamanobe, H. Eisaki, S. Uchida, Y. Fudamoto, I. M. Gat, M. I. Larkin, A. Savici, Y. J. Uemura, P. P. Kyriakou, M. T. Rovers, and G. M. Luke. Site-dilution in quasi one-dimensional antiferromagnet $\text{Sr}_2(\text{Cu}_{1-x}\text{Pd}_x)\text{O}_3$: reduction of Neel temperature and spatial distribution of ordered moment sizes. *Physical Review B*, 70:094402, 2004. (document), 6.2.3, 6.7
 - [211] J. D. Koralek, D. Meier, J. P. Hinton, A. Bauer, S. A. Parameswaran, A. Vishwanath, R. Ramesh, R. W. Schoenlein, C. Pfleiderer, and J. Orenstein. Observation of coherent helimagnons and Gilbert damping in an itinerant magnet. *Physical Review Letters*, 109:247204, 2012. 2.1.9
 - [212] M. Koyano, M. Suezawa, H. Watanabe, and M. Inoue. Low-field magnetization and ac magnetic susceptibility of spin- and cluster-glasses of itinerant magnet Fe_xTiS_2 . *Journal of the Physical Society of Japan*, 63:1114, 1994. 2.1.9
 - [213] J. Kubler. Spin fluctuations in ferromagnetic ZrZn_2 . *Physical Review B*, 70:064427, 2004. 2.1.9
 - [214] J. Kubler. *Theory of Itinerant Electron Magnetism*. Oxford University Press, NY, 2009. 2.1.6, 2.1.8, 6.3
 - [215] R. K  chler, P. Gegenwart, C. Geibel, and F. Steglich. Systematic study of the Gr  neisen ratio near quantum critical points. *Science and Technology of Advanced Materials*, 8:428, 2007. 7.2

-
- [216] R. K  chler, P. Gegenwart, K. Heuser, E. W. Scheidt, G. R. Stewart, and F. Steglich. Gr  neisen ratio divergence at the quantum critical point in $\text{CeCu}_{6-x}\text{Ag}_x$. *Physical Review Letters*, 93:93, 2004. 7.2
 - [217] R. K  chler, N. Oeschler, P. Gegenwart, T. Cichorek, K. Neumaier, O. Tegus, C. Geibel, J. A. Mydosh, F. Steglich, L. Zhu, and Q. Si. Divergence of the Gr  neisen ratio at quantum critical points in heavy fermion metals. *Physical Review Letters*, 91:066405, 2003. 7.2
 - [218] S. Kunkemoller, A. A. Nugroho, Y. Sidis, and M. Braden. Spin-density-wave ordering in $\text{Ca}_{0.5}\text{Sr}_{1.5}\text{RuO}_4$ studied by neutron scattering. *Physical Review B*, 89:045119, 2014. 6.2.3, 6.2.3
 - [219] L. D. Landau and E. M. Lifshitz. *Electrodynamics of Continuous Media*. Pergamon, Oxford, 1960. 3.9
 - [220] M. P. Langevin. Magnetism et Theory des Electrons. *Annales de Chimie et de Physique*, 5:70, 1905. 2.1.8
 - [221] M. P. Langevin. Sur la Theorie du Magnetisme. *Journal de Physique Thorique et Applique*, 4:678, 1905. 1, 2.1.2, 2.1.8
 - [222] E. P. Lautenschlager and P. Monaghan. Titanium and titanium alloys as dental materials. *International Dental Journal*, 43:245, 1993. 8.4
 - [223] M. Lee, A. Husmann, T. F. Rosenbaum, and G. Aeppli. High resolution study of magnetic ordering at absolute zero. *Physical Review Letters*, 92:187201, 2004. 2.1.6, 7.1
 - [224] D. X. Li, S. Nimori, Y. Shiokawa, Y. Haga, E. Yamamoto, and Y. Onuki. Ferromagnetic cluster glass behavior in U_2IrSi_3 . *Physical Review B*, 68:172405, 2003. 5.2
 - [225] D. X. Li, T. Yamamura, S. Nimori, K. Yubuta, and Y. Shiokawa. Spin-glass behavior in CeCu_2 -type uranium compound U_2AuGa_3 . *Applied Physics Letters*, 87:142505, 2005. 5.2
 - [226] H. v. L  hneysen, T. Pietrus, G. Portisch, H. G. Schlager, a. Schr  der, M. Sieck, and T. Trappmann. Non-Fermi-liquid behavior in a heavy-fermion alloy at a magnetic instability. *Physical Review Letters*, 72:3262, 1994. 7.1
 - [227] H. v. L  hneysen, A. Rosch, M. Vojta, and P. W  lfle. Fermi-liquid instabilities at magnetic quantum phase transitions. *Reviews of Modern Physics*, 79:1015, 2007. 2.1.6, 7.1, 7.1, 7.2
 - [228] G.G. Lonzarich. Band structure and magnetic fluctuations in ferromagnetic or nearly ferromagnetic metals. *Journal of Magnetism and Magnetic Materials*, 45:43, 1984. 7.2

-
- [229] G. M. Luke, A. Keren, K. Kojima, L. P. Le, B.J. Sternlieb, W. D. Wu, and Y.J. Uemura. Competition between magnetic order and superconductivity in CeCu_2Si_2 . *Physical Review Letters*, 73:1853, 1994. 3.8
 - [230] O. S. Lutes and J. L. Schmit. Low-temperature magnetic transitions in dilute Au-based alloys with Cr, Mn, and Fe. *Physical Review*, 134:A676, 1964. 2.3
 - [231] J. W. Lynn. *High temperature superconductivity*. Springer-Verlag, Berlin, Heidelberg, 1990. (document), 2.29, 2.4
 - [232] J. W. Lynn, Y. Chen, S. Chang, Y. Zhao, S. Chi, W. Ratcliff, B. G. Ueland, , and R. W. Erwin. Double focusing thermal triple axis spectrometer at the NCNR. *Journal of Research of NIST*, 117:61, 2012. 3.10
 - [233] Jr. M. J. Donachie. *Titanium: a Technical Guide*. ASM International, Metals Park, Ohio, 1988. 8.4, 8.4
 - [234] F. Ma, Z. Lu, and T. Xiang. Arsenic-bridged antiferromagnetic superexchange interactions in LaFeAsO . *Physical Review B*, 78:224517, 2008. 6.3
 - [235] User's Manual. *Magnetic Property Measurement System - MPMS XL*. Quantum Design Inc., 2011. (document), 3.6, 3.17, 3.6
 - [236] User's Manual. *Physical Property Measurement System*. Quantum Design Inc., 2011. (document), 3.13, 3.3, 3.4, 3.4, 3.15, 3.4, 3.16, 3.5
 - [237] N. Marcano, J. C. Gomez Sal, J. I. Espeso, L. Fernandez Barquin, and C. Paulsen. Cluster-glass percolative scenario in $\text{CeNi}_{1-x}\text{Cu}_x$ studied by very low-temperature AC susceptibility and DC magnetization. *Physical Review B*, 76:224419, 2007. 5.2, 5.3
 - [238] M. S. J. Marshall, D. T. Newell, D. J. Payne, R. G. Egdell, and M. R. Castell. Atomic and electronic surface structures of dopants in oxides: STM and XPS of Nb- and La-doped $\text{SrTiO}_3(001)$. *Physical Review B*, 83:035410, 2011. 6.2.1
 - [239] R. M. Martin. *Electronic Structure: Basic Theory and Practical Methods*. Cambridge University Press, Cambridge UK, 2008. 6.3
 - [240] S. K. S. Marya and R. K. Bawari. *Total Hip Replacement Surgery*. JP Medical Ltd., 2010. 8.4, 8.5.2, 8.5.4
 - [241] T. B. Massalski. Comments concerning some features of phase diagrams and phase transformations. *Materials Transactions*, 51:583, 2010. 8.5.2
 - [242] N. D. Mathur, F. M. Grosche, S. R. Julian, I. R. Walker, D. M. Freye, R. K. W. Haselwimmer, and G. G. Lonzarich. Magnetically mediated superconductivity in heavy fermion compounds. *Nature*, 394:39, 1998. 7.1, 7.2
 - [243] B. T. Matthias. Transition temperatures of superconductors. *Physical Review*, 89:884, 1953. 9.1

-
- [244] B. T. Matthias. Empirical relation between superconductivity and the number of valence electrons per atom. *Physical Review*, 97:74, 1954. 4.1, 4.2.2, 9.1
 - [245] B. T. Matthias and R. M. Bozorth. Ferromagnetism of a Zirconium-Zinc compound. *Physical Review*, 109:604, 1958. 1, 2.1.8, 2.1.9, 5.1, 6.1, 6.2.2
 - [246] B. T. Matthias, A. M. Clogston, H. J. Williams, E. Corenzwit, and R. C. Sherwood. Ferromagnetism in solid solutions of Scandium and Indium. *Physical Review Letters*, 7:7, 1961. (document), 1, 2.1.8, 2.15, 2.1.9, 3.1, 5.1, 5.2, 6.1, 6.2.2
 - [247] B. T. Matthias, T. H. Geballe, S. Geller, and E. Corenzwit. Superconductivity of Nb_3Sn . *Physical Review*, 95:1435, 1954. 9.1
 - [248] A. Matthiessen and C. Vogt. Ueber den Einfluss der Temperatur auf die Elektrische Leitungsfähigkeit der Legierungen. *Annalen der Physik*, 198:19, 1864. 2.4
 - [249] I. I. Mazin and M. D. Johannes. Fermi surface nesting and the origin of charge density waves in metals. *Physical Review B*, 77:165135, 2008. 6.3
 - [250] A. Poddar and C. Mazumdar. Cluster glass behaviour in Co-substituted double perovskite $\text{Ca}_2\text{FeMoO}_6$. *Materials Research Bulletin*, 46:682, 2011. 5.2
 - [251] W. L. McMillan. Transition temperature of strong-coupled superconductors. *Physical Review*, 167:331, 1968. 2.4, 9.2
 - [252] A. McNeillie, D. H. Brown, and W. E. Smith. X-ray photoelectron spectra of some Gold compounds. *Journal of the Chemical Society, Dalton Transactions*, 5:767, 1980. 6.2.1
 - [253] D. B. McWhan and T. M. Rice. Pressure dependence of itinerant antiferromagnetism in Chromium. *Physical Review Letters*, 19:846, 1967. 7.1
 - [254] W. Meissner and R. Ochsenfeld. Ein Neuer Effekt bei Eintritt der Supraleitfähigkeit. *Naturwissenschaften*, 21:787, 1933. 2.4
 - [255] D. Meschede, F. Steglich, W. Felsch, H. Maletta, and W. Zinn. Specific heat of insulating spin-glasses Eu, Sr near the onset of ferromagnetism. *Physical Review Letters*, 44:102, 1980. (document), 2.25
 - [256] A. J. Millis. Effect of nonzero temperature on quantum critical points in itinerant fermion systems. *Physical Review B*, 48:7183, 1976. 4.1
 - [257] U. Mizutani. *Hume-Rothery rules for structurally complex alloy phases*. Taylor and Francis Group, FL, 2011. 8.5.2
 - [258] P. Mohn. *Magnetism in the Solid State*. Springer-Verlag, Berlin, Heidelberg, 2006. 2.1.4, 2.1.5

-
- [259] A. F. J. Morgownik and J. A. Mydosh. Analysis of the high-temperature spin-glass susceptibility: determination of the local magnetic exchange. *Solid State Communications*, 47:321, 1983. (document), 2.3.1, 2.22
 - [260] T. Moriya. Recent developments in the theory of spin fluctuations in itinerant electron magnets. *Physica B*, 86:356, 1977. 1
 - [261] T. Moriya. *Spin Fluctuations in Itinerant Electron Magnetism*. Springer-Verlag, Berlin, Heidelberg, 1985. (document), 1, 2.1.6, 2.1.6, 2.1.6, 2.1.6, 2.12, 2.1.8, 2.13, 2.1.8, 2.2.2, 4.1, 5.2, 5.2, 6.2.2, 7.2, 7.2, 7.3
 - [262] T. Moriya. *Spin Fluctuations in Itinerant Electron Magnetism*. Springer-Verlag, Berlin, Heidelberg, 1985. 4.2.1, 4.3
 - [263] T. Moriya. Theory of itinerant electron magnetism. *Journal of Magnetism and Magnetic Materials*, 100:261, 1991. 2.1.8
 - [264] T. Moriya and A. Kawabata. Effect of spin fluctuations on itinerant electron ferromagnetism. *Journal of Physical Society of Japan*, 34:639, 1973. 2.1.8, 6.1, 6.2.2
 - [265] T. Moriya and A. Kawabata. Effect of spin fluctuations on itinerant electron ferromagnetism II. *Journal of Physical Society of Japan*, 35:669, 1973. 2.1.8, 6.1, 6.2.2
 - [266] T. Moriya and Y. Takahashi. Itinerant electron magnetism. *Annual Review of Materials Science*, 14:1, 1984. 1, 2.1.8, 2.1.9, 6.1
 - [267] T. Moriya and T. Takimoto. Anomalous properties around magnetic instability in heavy electron systems. *Journal of the Physical Society of Japan*, 64:960, 1995. 7.2, 7.2, 7.2, 7.4
 - [268] T. Moriya and K. Ueda. Spin fluctuations and high temperature superconductivity. *Advances in Physics*, 49:555, 2000. (document), 1, 2.2.2, 2.3, 2.4, 7.2, 7.2, 7.4
 - [269] T. R. Moriya and K. Ueda. Antiferromagnetic spin fluctuation and superconductivity. *Reports on Progress in Physics*, 66:1299, 2003. 7.1
 - [270] K. Morrison, A. Dupas, Y. Mudryk, V. K. Pecharsky, K. A. Gschneidner, A. D. Caplin, and L. F. Cohen. Identifying the critical point of the weakly first-order itinerant magnet DyCo₂ with complementary magnetization and calorimetric measurements. *Physical Review B*, 87:134421, 2013. 2.1.9
 - [271] S. Mridha and T. N. Baker. Crack-free hard surfaces produced by laser nitriding of commercial purity titanium. *Materials Science and Engineering A*, 188:229, 1994. 8.5.2
 - [272] C. A. M. Mulder, A. J. van Duynveldt, and J. A. Mydosh. Susceptibility of CuMn spin glass: frequency and field dependence. *Physical Review B*, 23:1384, 1981. (document), 2.24

-
- [273] J. A. Mydosh. *Spin Glasses: an Experimental Introduction*. Taylor and Francis Group, London, 1993. (document), 2.3, 2.3, 2.19, 2.3, 2.20, 2.21, 2.3, 2.3.1, 2.3.1, 2.3.1, 2.3.1, 2.5, 2.3.1, 2.3.1, 2.3.1, 2.3.2, 2.3.2, 2.3.2, 2.3.2, 2.3.2, 2.3.2, 2.3.2, 5.2, 5.3, 5.3
 - [274] J. A. Mydosh and P. J. Ford. Low temperature electrical resistivity of the spin glass: CuMn. *Physics Letters*, 49:189, 1974. 2.3
 - [275] J. A. Mydosh, P. J. Ford, M. P. Kawatra, and T. E. Whall. Electrical resistivity of AuFe alloys in the spin-glass, mictomagnetic, and ferromagnetic regimes. *Physical Review B*, 10:2845, 1974. 2.3
 - [276] K. Nagamine. *Introductory Muon Science*. Cambridge University Press, NY, 2003. 3.8, 3.8
 - [277] S. Nagata, P. H. Keesom, and H. R. Harrison. Low-dc-field susceptibility of CuMn spin glass. *Physical Review B*, 19:1633, 1979. (document), 2.3.1, 2.23
 - [278] H. Nakajima and T. Okabe. Titanium in dentistry: development and research in the U.S.A. *Dental Materials Journal*, 15:77, 1996. 8.4
 - [279] A. V. Naumkin, A. Kraut, and S. W. Gaare. *NIST X-ray Photoelectron Spectroscopy Database*. National Institute of Standards and Technology, Gaithersburg, 2000. 3.6, 6.2.1
 - [280] A. H. Castro Neto and B. A. Jones. Non-Fermi-liquid behavior in U and Ce alloys: Criticality, disorder, dissipation, and Griffiths-McCoy singularities. *Physical Review B*, 62:14975, 2000. 4.2.3
 - [281] M. Nicklas, M. Brando, G. Knebel, F. Mayr, W. Trinkl, and A. Loidl. Non-Fermi-liquid behavior at a ferromagnetic quantum critical point in $\text{Ni}_x\text{Pd}_{1-x}$. *Physical Review Letters*, 82:4268, 1999. 4.2.3, 7.2, 7.2, 7.2
 - [282] T. Nishioka, Y. Tabata, T. Taniguchi, and Y. Miyako. Canonical spin glass behavior in Ce_2AgIn_3 . *Journal of the Physical Society of Japan*, 69:1012, 2000. 5.2
 - [283] Z. Novotny, G. Argentero, Z. Wang, M. Schmid, U. Diebold, and G. S. Parkinson. Ordered array of single adatoms with remarkable thermal stability: Au/ $\text{Fe}_3\text{O}_4(001)$. *Physical Review Letters*, 108:216103, 2012. 6.2.1
 - [284] Y. Nozaki, K. Nakanl, T. Yajima, H. Kageyama, B. Frandsen, L. Liu, S. Cheung, T. Goko, Y. J. Uemura, T. S. J. Munsie, T. Medina, G. M. Luke, J. Munevar, D. Nishio-Hamane, and C. M. Brown. Muon spin relaxation and electron/neutron diffraction studies of $\text{BaTi}_2(\text{As}_{1-x}\text{Sb}_x)_2\text{O}$: absence of static magnetism and superlattice reflections. *Physical Review B*, 88:214506, 2013. 4.2.4, 6.4
 - [285] A. Schröder, G. Aeppli, E. Bucher, R. Ramazashvili, and P. Coleman. Scaling of magnetic fluctuations near a quantum phase transition. *Physical Review Letters*, 80:5623, 1998. 7.1

-
- [286] U. S. Department of Energy. Office of science. <http://science.energy.gov/>, 2014. (document), 2.33
- [287] E. Ohmichi, E. Komatsu, and T. Osada. Application of a tunnel diode oscillator to noncontact resistivity measurement in pulsed magnetic fields. *Review of Scientific Instruments*, 75:2094, 2004. 3.9
- [288] H. Okada, K. Koyama, K. Watanabe, Y. Kusakari, T. Kanomata, and H. Nishihara. Magnetic properties of heusler compounds Ru_2CrGe and Ru_2CrSn . *Applied Physics Letters*, 92:062502, 2008. 2.1.7, 6.2.5
- [289] K. Okumura. Systematic analysis of the magnetic susceptibility in the itinerant electron model. *Physical Review B*, 52:13358, 1995. 2.1.8
- [290] O. Okuno and H. Hamanaka. Application of β Titanium alloys in dentistry. *Dentistry in Japan*, 26:101, 1989. 8.4
- [291] J. Orenstein and A. J. Millis. Advances in the physics of high-temperature superconductivity. *Science*, 288:468, 2000. 1, 4.1
- [292] J. A. Osborn. Demagnetizing factors of the general ellipsoid. *Physical Review*, 67:351, 1945. 9.2
- [293] A. W. Overhauser. Spin density waves in electron gas. *Physical Review*, 128:1437, 1962. 2.1.6, 2.1.8
- [294] J. Paglione, M. A. Tanatar, D. G. Hawthorn, E. Boaknin, R. W. Hill, F. Ronning, M. Sutherland, L. Taillefer, C. Petrovic, and P. C. Canfield. Field-induced quantum critical point in CeCoIn_5 . *Physical Review Letters*, 91:246405, 2003. 7.1
- [295] R. E. Peierls. *Quantum Theory of Solids*. Oxford University Press, Oxford, 1955. 3
- [296] J. P. Perdew, K. Burke, and M. Ernzerhof. Generalized gradient approximation made simple. *Physical Review Letters*, 77:3865, 1996. 3.11, 6.3, 9.3
- [297] C. Pfleiderer, A. Faisst, H. von Löhneysen, S. M. Hayden, and G. G. Lonzarich. Field dependence of the specific heat of single-crystalline ZrZn_2 . *Journal of Magnetism and Magnetic Materials*, 226:258, 2001. 4.2.3
- [298] C. Pfleiderer, G. J. McMullan, S. R. Julian, and G. G. Lonzarich. Magnetic quantum phase transition in MnSi under hydrostatic pressure. *Physical Review B*, 55:8330, 1997. 7.2
- [299] C. Pfleiderer, M. Uhlarz, S. M. Hayden, R. Vollmer, H. v. Lhneysen, N. R. Bernhoeft, and G. G. Lonzarich. Coexistence of superconductivity and ferromagnetism in the d-band metal ZrZn_2 . *Nature*, 412:58, 2001. (document), 2.14

-
- [300] A. B. Pippard. An experimental and theoretical study of the relation between magnetic field and current in a superconductor. *Proceedings of the Royal Society A*, 216:547, 1953. 2.4
- [301] V.G. Pleschov, N.V. Baranov, A.N. Titov, K. Inoue, M.I. Bartashevich, and T. Goto. Magnetic properties of Cr-intercalated TiSe_2 . *Journal of Alloys and Compounds*, 320:13, 2001. 2.1.7, 6.2.5
- [302] V. B. Pluzhnikov, A. Czopnik, and I. V. Svechkarev. de Haas-van Alphen effect in ScGa_3 , LuGa_3 and YIn_3 . *Physica B*, 212:375, 1995. 9.1, 9.2, 9.4
- [303] R. Prozorov, M. D. Vannette, G. D. Samolyuk, S. A. Law, S. L. Budko, and P. C. Canfield. Contactless measurements of Shubnikov-de Haas oscillations in the magnetically ordered state of CeAgSb_2 and SmAgSb_2 single crystals. *Physical Review B*, 75:014413, 2007. 3.9, 3.9
- [304] R. Pynn. *Neutron Scattering Primer*. <http://www.ncnr.nist.gov>, 1990. (document), 3.10, 3.10, 3.25, 3.26, 3.27, 3.10
- [305] D. Raabe, P. Choi, Y. Li, A. Kostka, X. Sauvage, F. Lecouturier, K. Hono, R. Kirchheim, R. Pippan, and D. Embury. Metallic composites processed via extreme deformation: toward the limits of strength in bulk materials. *MRS Bulletin*, 35:982, 2010. 8.5.2
- [306] S. Rahman, J. Timlin, J. E. Crow, T. Mihalisin, and P. Schlottmann. Transitions between localized and itinerant antiferromagnetism in the Cerium-Lead-Indium ($\text{Ce}(\text{Pb},\text{In})_3$) and Cerium-Lead-Thallium ($\text{Ce}(\text{Pb},\text{Tl})_3$) systems. *Physica B*, 163:649, 1990. 2.1.9
- [307] T. V. Rajan, C. P. Sharma, and A. Sharma. *Heat Treatment: Principles and Techniques*. PHI Learning Private Limited, New Delhi, 1994. (document), 8.2
- [308] P. D. Reotier and A. Yaouanc. Muon spin rotation and relaxation in magnetic materials. *Journal of Physics: Condensed Matter*, 9:9113, 1997. 3.8
- [309] P. Rhodes and E. P. Wohlfarth. The effective Curie-Weiss constant of ferromagnetic metals and alloys. *Proceedings of the Royal Society A*, 273:247, 1963. 1, 2.1.7, 2.1.7, 5.3, 6.2.5, 6.2.5
- [310] S. Riyadi, S. Giriapura, R. A. de Groot, A. Caretta, P. H. M. van Loosdrecht, T. T. M. Palstra, and G. R. Blake. Ferromagnetic order from p-electrons in Rubidium Oxide. *Chemistry of Materials*, 23:1578, 2011. 5.2
- [311] B. W. Roberts. Survey of superconducting materials and critical evaluation of selected properties. *Journal of Physical and Chemical Reference Data*, 5:581, 1976. 9.1
- [312] E. E. Rodriguez, C. Stock, K. Krycka, C. F. Majkrzak, K. Kirshenbaum, N. P. Butch, S. R. Shanta, J. Paglione, and M. A. Green. Noncollinear spin-density wave antiferromagnetism in FeAs . *Physical Review B*, 83:134438, 2011. 2.1.9

-
- [313] A. Rosch. Interplay of disorder and spin fluctuations in the resistivity near a quantum critical point. *Physical Review Letters*, 82:4280, 1999. 7.2
 - [314] S. Sachdev. Quantum criticality: competing ground states in low dimensions. *Science*, 288:475, 2000. 1, 4.1
 - [315] A. S. Saleh, R. Al-Jaber, A. Malkawi, S. Mahmood, and I. Abu-Aljarayesh. Structural and magnetic studies of the alloy system $\text{CuAl}_{1-x}\text{Fe}_x$. *Journal of Magnetism and Magnetic Materials*, 99:152, 1991. 6.2.5
 - [316] E. V. Sampathkumaran, K. Hirota, I. Das, and M. Ishikawa. Interplay of the kondo effect and ferromagnetism in the Cerium-Nickel-Gallium ($\text{CeNi}_x\text{Ga}_{4-x}$) alloys. *Physical Review B*, 47:8349, 1993. 2.1.9
 - [317] G. V. Samsonov. *Handbook of the Physicochemical Properties of the Elements*. Springer-Verlag, Berlin, Heidelberg, 1968. 8.4, 8.5.2, 8.5.4
 - [318] K.G. Sandeman, G.G. Lonzarich, and A.J. Schofield. Ferromagnetic superconductivity driven by changing Fermi surface topology. *Physical Review Letters*, 90:167005, 2003. 6.2.2
 - [319] A.T. Savici, Y. Fudamoto, I.M. Gat, T. Ito, M.I. Larkin, Y.J. Uemura, G.M. Luke, K.M. Kojima, Y.S. Lee, M.A. Kastner, R.J. Birgeneau, and K. Yamada. Muon spin relaxation studies of incommensurate magnetism and superconductivity in stage-4 $\text{La}_2\text{CuO}_{4.11}$ and $\text{La}_{1.88}\text{Sr}_{0.12}\text{CuO}_4$. *Physical Review B*, 66:014524, 2002. 6.2.3
 - [320] S. S. Saxena, P. Agarwal, K. Ahilan, F. M. Grosche, R. K. W. Haselwimmer, M. J. Steiner, E. Pugh, I. R. Walker, S. R. Julian, P. Monthoux, G. G. Lonzarich, A. Huxley, I. Sheikin, D. Braithwaite, and J. Flouquet. Superconductivity on the border of itinerant-electron ferromagnetism in UGe_2 . *Nature*, 406:587, 2000. 2.1.9, 7.1
 - [321] R. W. Schmitt and I. S. Jacobs. Low-temperature electrical and magnetic behavior of dilute alloys: Mn in Cu and Co in Cu. *Journal of Physics and Chemistry of Solids*, 3:324, 1957. 2.3
 - [322] A. Schröder, G. Aeppli, R. Coldea, M. Adams, O. Stockert, H.v Löhneysen, E. Bucher, R. Ramazashvili, and P. Coleman. Onset of antiferromagnetism in heavy-fermion metals. *Nature*, 407:351, 2000. 1, 4.1, 7.1, 7.1
 - [323] K. Schubert, H. G. Meissner, M. Poetzschke, W. Rossteutscher, and E. Stolz. Einige Strukturdaten Metallischer Phasen VII. *Naturwissenschaften*, 49:57, 1962. 6.2.1
 - [324] S. Schultz and G. Dunifer. Observation of spin waves in Sodium and Potassium. *Physical Review Letters*, 18:283, 1967. 2.1
 - [325] R. T. Schumacher and C. P. Slichter. Electron spin paramagnetism of Lithium and Sodium. *Physical Review*, 101:58, 1956. 2.1

-
- [326] R. T. Schumacher and W. E. Vehse. The paramagnetic susceptibility of Sodium metal. *Journal of Physics and Chemistry of Solids*, 24:297, 1963. 2.1
- [327] M. Semlitsch. Titanium alloys for hip joint replacements. *Clinical Materials*, 2:1, 1987. 8.4
- [328] W. Setyawan and S. Curtarolo. High-throughput electronic structure calculations: challenges and tools. *Computational Materials Science*, 49:299, 2010. 2.1.9
- [329] R. D. Shannon. Revised effective ionic radii and systematic studies of interatomic distances in halides and chalcogenides. *Acta Crystallographica*, 32:751, 1976. 4.1, 5.1, 7.2, 7.2
- [330] D. Sherrington and S. Kirkpatrick. Solvable model of a spin-glass. *Physical Review Letters*, 35:1792, 1975. (document), 2.3.2, 2.27, 2.3.2
- [331] M. Shiga, H. Wada, K. Yoshimura, and Y. Nakamura. Transition from itinerant electron to local moment system in $\text{Y}(\text{Mn}_{1-x}\text{Al}_x)_2$. *Journal of Magnetism and Magnetic Materials*, 54:1073, 1986. 5.1
- [332] S. Shtrikman and E. P. Wohlfarth. The theory of the Vogel-Fulcher law of spin glasses. *Physica Letters*, 85:467, 1981. 2.3.1
- [333] A. Simunek and J. Vackar. Hardness of covalent and ionic crystals: first-principles calculations. *Physical Review Letters*, 96:085501, 2006. (document), 8.3, 8.1
- [334] V. Singh. *Physical Metallurgy*. Standard Publishers Distributors, 1999. (document), 8.4
- [335] J. C. Slater. Magnetic effects and the Hartree-Fock equation. *Physical Review*, 82:538, 1951. 2.1.6
- [336] J. C. Slater. An augmented plane wave method for the periodic potential problem. *Physical Review B*, 92:603, 1953. 3.11
- [337] R. P. Smith, M. Sutherland, G. G. Lonzarich, S. S. Saxena, N. Kimura, S. Tahashima, M. Nohara, and H. Takagi. Magnetinal breakdown of the Fermi-liquid state on the border of metallic ferromagnetism. *Nature*, 455:1220, 2008. 4.2.3
- [338] T. F. Smith, C. W. Chu, and M. B. Maple. Superconducting manometers for high pressure measurement at low temperature. *Cryogenics*, 9:53, 1969. 3.5
- [339] T. F. Smith, J. A. Mydosh, and E. P. Wohlfarth. Destruction of ferromagnetism in ZrZn_2 at high pressure. *Physical Review Letters*, 27:1732, 1971. 6.2.6
- [340] Casa Software. *Casa XPS Manual*. Casa Ltd., 2009. (document), 3.3, 3.11, 3.12

-
- [341] D. A. Sokolov, M. C. Aronson, W. Gannon, and Z. Fisk. Critical phenomena and the quantum critical point of ferromagnetic $\text{Zr}_{1-x}\text{Nb}_x\text{Zn}_2$. *Physical Review Letters*, 96:116404, 2006. 1, 2.1.9, 4.1, 4.2.2, 4.3, 5.1, 6.2.6, 7.1, 7.2
- [342] J. Solyom. *Fundamentals of the Physics of Solids*. Springer-Verlag, Berlin, Heidelberg, 2007. 3.2
- [343] J. Souletie and J. L. Tholence. Critical slowing down in spin glasses and other glasses: Fulcher versus power law. *Physical Review B*, 32:516, 1985. 2.3.1, 5.3
- [344] G. L. Squires. *Introduction to the Theory of Thermal Neutron Scattering*. Cambridge University Press, 2010. 3.10, 3.10
- [345] H. Srikanth, J. Wiggins, and H. Rees. Radio-frequency impedance measurements using a tunnel-diode oscillator (TDO) technique. *Review of Scientific Instruments*, 70:3097, 1999. 3.9, 3.9
- [346] J. P. Srivastava. *Elements of solid state physics*. PHI Learning Private Limited, New Delhi, 2011. 3
- [347] K. Stahl. Rietveld refinement framework. Technical University of Denmark, 2008. 3.2
- [348] G. R. Stewart. Non-Fermi-liquid behavior in d- and f- electron metals. *Reviews of Modern Physics*, 73, 2001. 1, 4.1, 4.1, 7.1
- [349] O. Stockert, J. Arndt, A. Schneidewind, H. Schneider, H. S. Jeevan, C. Geibel, F. Steglich, and M. Loewenhaupt. Magnetism and superconductivity in the heavy-fermion compound CeCu_2Si_2 studied by neutron scattering. *Physica B*, 403:973, 2008. 6.2.3
- [350] E. C. Stoner. Collective electron ferromagnetism. *Proceedings of the Royal Society A*, 165:372, 1938. 1, 2.1.8, 6.1
- [351] R. Strietzel. Burning alloy for the production of ceramically veneered dental restorations. *United States Patent and Trademark Office*, US 7491361 B2, 2009. 8.4, 8.5.1
- [352] A. Subedi and David J. Singh. Band structure and the itinerant magnetism in quantum critical NbFe_2 . *Physical Review B*, 81:024422, 2010. 4.1
- [353] S. Sullow, G. J. Nieuwenhuys, A. A. Menovsky, and J. A. Mydosh. Spin glass behavior in URh_2Ge_2 . *Physical Review Letters*, 78:354, 1997. 5.2
- [354] E. Svanidze, T. Besara, J. K. Wang, T. Siegrist, K. Han, and E. Morosan. Doping-induced quantum critical point in itinerant antiferromagnet TiAu . (in preparation), 2015. 7
- [355] E. Svanidze, L. Liu, B. Frandsen, B. D. White, T. Besara, T. Goko, T. Medina, T. J. S. Munsie, G. M. Luke, D. Zheng, C. Q. Jin, T. Siegrist, M. B. Maple, Y. J. Uemura, and E. Morosan. Non-Fermi liquid behavior close to a quantum critical point in a ferromagnetic state without local moments. *Physical Review*

-
- X, 5:011206, 2015. (document), 1, 2.15, 2.1.9, 4.2, 5.1, 5.2, 5.2, 5.3, 5.4, 6.2.3, 7.1, 7.2
- [356] E. Svanidze, C. A. McElroy, J. Singleton, V. S. Zapf, J. W. Kim, J. Leotin, M. B. Maple, and E. Morosan. High-field and pressure experiments on itinerant antiferromagnet TiAu. (in preparation), 2015. 7.2
- [357] E. Svanidze and E. Morosan. Type-I superconductivity in ScGa_3 and LuGa_3 single crystals. *Physical Review B*, 85:174514, 2012. (document), 3.1, 3.1, 3.9
- [358] E. Svanidze and E. Morosan. Cluster-glass behavior induced by local moment doping in the itinerant ferromagnet $\text{Sc}_{3.1}\text{In}$. *Physical Review B*, 88:064412, 2013. 1, 5.1
- [359] E. Svanidze, J. K. Wang, T. Besara, L. Liu, Q. Huang, T. Siegrist, B. Frandsen, J. W. Lynn, A. H. Nevidomskyy, M. B. Gamza, M. C. Aronson, Y. J. Uemura, and E. Morosan. Novel itinerant antiferromagnet TiAu. *Nature Communications*, accepted, 2015. 1, 6.2.4, 6.2.5, 6.2.6, 7.2, 7.2, 7.2, 7.3, 7.3
- [360] M. Szlowska, D. Gnida, and D. Kaczorowski. Magnetic and electrical transport behavior in the crystallographically disordered compound U_2CoSi_3 . *Physical Review B*, 84:134410/1, 2011. 2.3.1, 5.2
- [361] Y. Takada, H. Nakajima, O. Okuno, and T. Okabe. Microstructure and corrosion behavior of binary titanium alloys with beta-stabilizing elements. *Dental Materials Journal*, 20:34, 2001. 8.4
- [362] M. Takahashi, M. Kikuchi, and O. Okuno. Mechanical properties and grindability of experimental Ti-Au alloys. *Dental Materials Journal*, 23:203, 2004. 8.4, 8.5.1, 8.5.2
- [363] M. Takahashi, M. Kikuchi, Y. Takada, and O. Okuno. Mechanical properties and microstructures of dental cast Ti-Ag and Ti-Cu alloys. *Dental Materials*, 21:270, 2002. 8.4, 8.5.2
- [364] T. Takahashi, M. Kikuchi, Y. Takada, and O. Okuno. Basic compositions of Gold-Titanium alloys for dental casting. *Japanese Society for Dental Materials and Devices*, 17:126, 1998. 8.4, 8.5.1
- [365] Y. Takahashi. On the origin of the Curie-Weiss law of the magnetic susceptibility in itinerant electron ferromagnets. *Journal of the Physical Society of Japan*, 55:3553, 1986. 2.1.8, 2.1.8
- [366] Y. Takahashi and T. Moriya. Quantitative aspects of the theory of weak itinerant ferromagnetism. *Journal of the Physical Society of Japan*, 54:1592, 1985. 7.2
- [367] J. Takeuchi and Y. Masuda. Low temperature specific heat of itinerant electron ferromagnet Sc_3In . *Journal of the Physical Society of Japan*, 46:468, 1979. 4.1, 4.2.1, 4.2.2

-
- [368] J. Takeuchi, H. Sasakura, and Y. Masuda. Spin Fluctuations in Itinerant Electron Antiferromagnetic $\text{Cr}_{1-x}\text{V}_x$ System. *Journal of the Physics Society Japan*, 49:508, 1980. 7.1, 7.2
 - [369] M. Takigawa, H. Yasuoka, Y. J. Uemura, R. S. Hayano, T. Yamazaki, and Y. Ishikawa. Positive muon spin rotation and relaxation in the helically ordered state of MnSi. *Journal of Physical Society of Japan*, 49:1760, 1980. 6.2.3
 - [370] T. Takimoto and T. Moriya. Superconductivity and antiferromagnetism in three-dimensional hubbard model. page 8, 2002. 7.4
 - [371] J. L. Tholence. On the frequency dependence of the transition temperature in spin glasses. *Solid State Communications*, 35:113, 1980. 2.3.1, 2.3.1, 5.3, 5.3
 - [372] M. Tinkham. *Introduction to Superconductivity*. Dover Publications, 1996. (document), 2.4, 2.30, 2.4, 2.4, 2.32, 2.4, 2.4, 9.2
 - [373] Y. Tokiwa, E. D. Bauer, and P. Gegenwart. Zero-field quantum critical point in CeCoIn_5 . *Physical Review Letters*, 111:107003, 2013. 7.1
 - [374] Y. Tokiwa, T. Radu, C. Geibel, F. Steglich, and P. Gegenwart. Divergence of the magnetic Grüneisen ratio at the field-induced quantum critical point in YbRh_2Si_2 . *Physical Review Letters*, 102:066401, 2009. 7.2
 - [375] O. Trovarelli, C. Geibel, S. Mederle, C. Langhammer, F. M. Grosche, P. Gegenwart, M. Lang, G. Sparn, and F. Steglich. YbRh_2Si_2 : pronounced non-Fermi-liquid effects above a low-lying magnetic phase transition. *Physical Review Letters*, 85:626, 2000. 1, 4.1
 - [376] M. I. Tsindlekht, G. I. Leviev, V. M. Genkin, I. Felner, Y. B. Paderno, and V. B. Filippov. Glass-like low-frequency ac response of ZrB_{12} and Nb single crystals in the surface superconducting state. *Physical Review B*, 73:104507, 2006. 2.4, 9.2
 - [377] M. Tsvelik and M. Reizer. Phenomenological theory of non-Fermi-liquid heavy-fermion alloys. *Physical Review B (R)*, 48:9887, 1993. 4.1
 - [378] K. Ueda. Electrical resistivity of antiferromagnetic metals. *Journal of the Physical Society of Japan*, 43:1497, 1977. 7.2
 - [379] Y. J. Uemura, A. A. Aczel, Y. Ajiro, J. P. Carlo, T. Goko, D. A. Goldfeld, A. Kitada, G. M. Luke, G. J. MacDougall, I. G. Mihailescu, J. A. Rodriguez, P. L. Russo, Y. Tsujimoto, C. R. Wiebe, T. J. Williams, T. Yamamoto, K. Yoshimura, and H. Kageyama. MuSR studies of the frustrated quasi-2d square-lattice spin system $\text{Cu}(\text{Cl},\text{Br})\text{La}(\text{Nb},\text{Ta})_2\text{O}_7$: evolution from spin-gap to antiferromagnetic state. *Physical Review B*, 80:174408, 2009. 6.2.3
 - [380] Y. J. Uemura, T. Goko, I. M. Gat-Malureanu, J. P. Carlo, P. L. Russo, A. T. Savici, A. Aczel, G. J. MacDougall, J. A. Rodriguez, and G. M. Luke. Phase separation and suppression of critical dynamics at quantum transitions of itin-

-
- erant magnets: MnSi and $(\text{Sr}_{1-x}\text{Ca}_x)\text{RuO}_3$. *Nature Physics*, 3:29, 2007. 2.1.9, 3.8, 4.2.4, 6.2.3, 6.2.3, 6.4, 6.2.3
- [381] Y. J. Uemura, A. Keren, L. P. Le, G. M. Luke, W. D. Wu, Y. Kubo, T. Manako, Y. Shimakawa, M. Subramanian, J. L. Cobb, and J. T. Markert. Magnetic-field penetration depth in $\text{Tl}_2\text{Ba}_2\text{CuO}_{6+\delta}$ in the overdoped regime. *Nature*, 364:605, 1993. 3.8
- [382] Y. J. Uemura, W. J. Kossler, X. H. Yu, H. E. Schone, J. R. Kempton, C. E. Stronach, S. Barth, F. N. Gygax, B. Hitti, A. Schenck, C. Baines, W. F. Lankford, Y. Ooniki, and T. Komatsubara. Coexisting static magnetic order and superconductivity in $\text{CeCu}_{2.1}\text{Si}_2$ found by muon spin relaxation. *Physical Review B*, 39:4726, 1989. 6.2.3
- [383] Y. J. Uemura, T. Yamazaki, D. R. Harshman, M. Senba, and E. J. Ansaldo. Muon-spin relaxation in AuFe and CuMn spin glasses. *Physical Review B*, 31:546, 1985. 3.8, 3.8, 4.2.4, 6.2.3, 6.2.3, 6.2.3, 6.4, 6.2.3, 6.2.3
- [384] M. Uhlarz, C. Pfleiderer, and S. M. Hayden. Quantum phase transitions in the itinerant ferromagnet ZrZn_2 . 93:256404, 2004. 7.1
- [385] V. I. Valkov, A. V. Golovchan, V. P. Dyakonov, and H. Szymczak. Magnetic order-order phase transitions in itinerant magnets: $\text{Fe}_{2-x}\text{Mn}_x\text{As}$. *Low Temperature Physics*, 37:309, 2011. 2.1.9
- [386] M. D. Vannette, S. L. Bud'ko, P. C. Canfield, and R. Prozorov. Distinguishing local moment versus itinerant ferromagnets: dynamic magnetic susceptibility. *Journal of Applied Physics*, 103:07D302, 2008. (document), 3.9, 3.9, 3.9, 3.24, 5.1, 6.2.4
- [387] M. D. Vannette, A.S. Sefat, S. Jia, S.A. Law, G. Lapertot, S. L. Budko, P. C. Canfield, J. Schmaliana, and R. Prozorov. Precise measurements of radio-frequency magnetic susceptibility in ferromagnetic and antiferromagnetic materials. *Journal of Magnetism and Magnetic Materials*, 320:354, 2008. 3.9, 3.9, 5.1
- [388] C. M. Varma, P. B. Littlewood, S. Schmitt-Rink, E. Abrahams, and A. E. Ruckenstein. Phenomenology of the normal state of Cu-O high-temperature superconductors. *Physical Review Letters*, 63:1996, 1989. 7.4
- [389] P. Villars, H. Okamoto, and K. Cenzual. *ASM Alloy Phase Diagrams Center*. ASM International, Metals Park, Ohio, 2007. (document), 3.1, 3.1, 3.3, 3.4, 3.9, 8.6, 8.5.2, 8.3
- [390] T. Vojta. Quantum phase transitions in electronic systems. *Annals of Physics*, 9:403, 2000. 2.2.2
- [391] T. Vojta. Disorder-induced rounding of certain quantum phase transitions. *Physical Review Letters*, 90:107202, 2003. 7.1, 7.4

-
- [392] N. Vuilleme. Non-precious dental alloy. *United States Patent and Trademark Office*, US 6613275 B1, 2003. 8.4, 8.5.2, 8.5.4
 - [393] K. Wakui, S. Akutagawa, N. Kase, K. Kawashima, T. Muranaka, Y. Iwahori, J. Abe, and J. Akimitsu. Thermodynamic properties of the non-centrosymmetric Type-I superconductor Rh_2Ga_9 and Ir_2Ga_9 . *Journal of Physical Society of Japan*, 78:034710, 2009. 2.4, 9.2
 - [394] P. Walker and W. H. Tarn. *Handbook of Metal Etchants*. CRC Press, Boca Raton, FL USA, 1991. 3.1
 - [395] X. F. Wang, T. Wu, G. Wu, H. Chen, Y. L. Xie, J. J. Ying, Y. J. Yan, R. H. Liu, and X. H. Chen. Anisotropy in the electrical resistivity and susceptibility of superconducting BaFe_2As_2 single crystals. *Physical Review Letters*, 102:117005, 2009. 6.2.2
 - [396] R. C. Wayne and L. R. Edwards. Effects of pressure on the Curie temperature of ZrZn_2 . *Physical Review*, 188:1042, 1969. 6.2.6
 - [397] P. Weiss. L'hypothse du Champ Molculaire et la Propriet Ferromagnetique. *Radium*, 6:661, 1907. 1, 2.1.3, 2.1.8
 - [398] G. Welsch, R. Boyer, and E. W. Collings. *Materials Properties Handbook: Titanium Alloys*. ASM International, Material Park, Ohio, 2007. 8.4
 - [399] K. G. Wilson. The renormalization group: Critical phenomena and the Kondo problem. *Reviews of Modern Physics*, 47:773, 1975. 7.2
 - [400] E. P. Wohlfarth. Forced magnetostriction in the band model of magnetism. *Journal of Physics C: Solid State Physics*, 2:68, 1969. 6.2.6
 - [401] E. P. Wohlfarth. Thermodynamic aspects of itinerant electron magnetism. *Physica B+C*, 91:305, 1977. 6.2.6
 - [402] E. P. Wohlfarth and J. F. Cornwell. Critical points and ferromagnetism. *Physical Review Letters*, 7:342, 1961. 5.1
 - [403] M. K. Wu, J. R. Ashburn, C. J. Torng, P. H. Hor, R. L. Meng, L. Gao, Z. J. Huang, Y. Q. Wang, and C. W. Chu. Superconductivity at 93 K in a new mixed-phase Y-Ba-Cu-O compound system at ambient pressure. *Physical Review Letters*, 58:908, 1987. 2.4
 - [404] M. Wuttig. *Ultrathin Metal Films*. Springer-Verlag, Berlin, Heidelberg, 2004. (document), 2.10, 2.1.6
 - [405] H. Xiao, S. Kim, X. He, D. Zhou, C.M. Li, and H. Liang. Friction pair evaluation of cartilage-diamond for partial joint repair. *Carbon*, 80:551, 2014. 8.5.2
 - [406] H. Xiao, C. Lin, and H. Liang. In situ tribo-electrochemical evaluation of wear of diamond composites. *Journal of Electrochemical Society*, 161:E87, 2014. 8.5.2

-
- [407] H. Xiao, A. M. Sinyukov, X. He, C. Lin, and H. Liang. Silicon-oxide-assisted wear of diamond-containing composite. *Journal of Applied Physics*, 114:223505, 2013. 8.5.2
 - [408] Y. Yamaguchi, S. Waki, and K. Mitsugi. Superconductivity of YbSb₂. *Journal of Physical Society of Japan*, 56:419, 1987. 2.4
 - [409] L. F. Yamshchikov, V.A. Lebedev, I.F. Nichkov, S.P. Raspopin, and S.E. Puchinskis. Thermodynamics of the formation of Scandium alloys with Gallium, Indium, and Antimony. *Izvestiya Akademii Nauk SSSR*, 5:188, 1985. 4.1
 - [410] H. Yao, J. A. Robertson, E. A. Kim, and S. A. Kivelson. Theory of stripes in quasi two dimensional rare-earth tritellurides. *Physical Review B*, 74:245126, 2006. 6.3
 - [411] A. Yeh, Y. Soh, J. Brooke, G. Aeppli, T. F. Rosenbaum, and S. M. Hayden. Quantum phase transition in a common metal. *Nature*, 419:459, 2002. 2.1.6, 7.1, 7.2
 - [412] E. A. Yelland, S. M. Hayden, S. J. C. Yates, C. Pfleiderer, M. Uhlarz, R. Vollmer, H. v. Lhneysen, N. R. Bernhoeft, R. P. Smith, S. S. Saxena, , and N. Kimura. Superconductivity induced by spark erosion in ZrZn₂. *Physical Review B*, 72:214523, 2005. (document), 2.14
 - [413] S. Yonezawa and Y. Maeno. Type-I superconductivity of the layered Silver Oxide Ag₅Pb₂O₆. *Physical Review B*, 72:180504–1, 2005. 2.4, 9.2
 - [414] L. Yu, C. Qian, Q. Da-Wei, W. Ji-Liang, Z. Jing, W. Shuang, and G. Jing. Effects of fe doping on AC susceptibility of Pr_{0.75}Na_{0.25}MnO₃. *Chinese Physics B*, 20:117502, 2011. 5.3, 5.3
 - [415] P. Y. Yu and M. Cardona. *Electronic Band Structure*. Springer-Verlag, Berlin, Heidelberg, 2010. 3.11
 - [416] S. Zhang, S. Tan, L. Pi, and Y. Zhang. Strong correlation effects and new phase transition at high pressure-low temperature in La_{0.5}Ba_{0.5}FeO₃. *Journal of Magnetism and Magnetic Materials*, 322:3381, 2010. 5.2
 - [417] Y. Zhang, I. Opahle, H. O. Jeschke, and R. Valenti. Itinerant nature of magnetism in iron pnictides: A first-principles study. *Physical Review B*, 81:094505, 2010. 2.1.9
 - [418] Liang L. Zhao, S. Lausberg, H. Kim, M. A. Tanatar, M. Brando, R. Prozorov, and E. Morosan. Type-I superconductivity in YbSb₂ single crystals. *Physical Review B*, 85:214526, 2012. 2.4, 9.2
 - [419] R. Zhou, Z. Li, J. Yang, D. L. Sun, C. T. Lin, and G. Zheng. Quantum criticality in electron-doped BaFe_{2x}Ni_xAs₂. *Nature Communications*, 4:1, 2013. 7.1, 7.2

- [420] L. Zhu, M. Garst, A. Rosch, and Q. Si. Universally diverging Grüneisen parameter and the magnetocaloric effect close to quantum critical points. *Physical Review Letters*, 91:066404, 2003. 7.2